



**HAL**  
open science

# Development of new sensing materials to improve the sensitivity and selectivity of an optoelectronic nose

Charlotte Hurot

► **To cite this version:**

Charlotte Hurot. Development of new sensing materials to improve the sensitivity and selectivity of an optoelectronic nose. Biological Physics [physics.bio-ph]. Université Grenoble Alpes [2020-..], 2020. English. NNT : 2020GRALY064 . tel-03738042

**HAL Id: tel-03738042**

**<https://theses.hal.science/tel-03738042>**

Submitted on 25 Jul 2022

**HAL** is a multi-disciplinary open access archive for the deposit and dissemination of scientific research documents, whether they are published or not. The documents may come from teaching and research institutions in France or abroad, or from public or private research centers.

L'archive ouverte pluridisciplinaire **HAL**, est destinée au dépôt et à la diffusion de documents scientifiques de niveau recherche, publiés ou non, émanant des établissements d'enseignement et de recherche français ou étrangers, des laboratoires publics ou privés.

## THÈSE

Pour obtenir le grade de

### DOCTEUR DE L'UNIVERSITE GRENOBLE ALPES

Spécialité : **Physique pour les Sciences du Vivant**

Arrêté ministériel : 25 mai 2016

Présentée par

**Charlotte HUROT**

Thèse dirigée par

**Arnaud BUHOT, Ingénieur de Recherche, CEA Grenoble,**

et codirigée par

**Yanxia HOU-BROUTIN, Chargée de Recherche, CNRS,**

préparée au sein du **CEA Grenoble**

Institut de Recherche Interdisciplinaire de Grenoble (IRIG) / Département des Interfaces pour l'Energie, la Santé et l'Environnement (DIESE) / Service : Systèmes Moléculaires et nanoMatériaux pour l'Energie et la Santé (SyMMES) / Groupe : Chimie pour la Reconnaissance et l'Etude des Assemblages Biologiques (CREAB)

Dans **l'École Doctorale de Physique**

### **Development of new sensing materials to improve the sensitivity and selectivity of an optoelectronic nose**

Thèse soutenue publiquement le **17 Novembre 2020**,  
devant le jury composé de :

**Mme. Carole CHAIX**

Directrice de Recherche CNRS à l'Institut des Sciences Analytiques, Rapportrice

**Mr. Yann CHEVLOT**

Directeur de Recherche CNRS à l'Institut des Nanotechnologies de Lyon, Examineur

**Mr. Jérôme GOLEBIOWSKI**

Professeur à l'Université Nice Sophia Antipolis, Rapporteur

**Mr. Jean-Michel GUILLOT**

Professeur à l'IMT Mines d'Alès, Examineur

**Mr. Christophe MOREAU**

Directeur de Recherche CNRS à l'Institut de Biologie Structurale, Président

**Mme. Valérie STAMBOULI-SENE**

Chargée de Recherche CNRS au Laboratoire des Matériaux et du Génie Physique,  
Examinatrice





## Remerciements

Je tiens tout d'abord à remercier tous les membres du jury qui ont accepté de prendre connaissance et d'évaluer mon travail. La séance de questions qui a suivi la soutenance a été véritablement intéressante, malgré le contexte particulier de cette année. J'ai une reconnaissance toute particulière pour Christophe Moreau et Valérie Stambouli-Sene, qui ont suivi mon projet de thèse dès la fin de la première année et qui se sont toujours montrés d'un grand soutien. Merci également à Yann Chevolut et Jean-Michel Guillot pour leur grande réactivité qui a rendu possible cette soutenance.

Je remercie chaleureusement mes directeurs de thèse Yanxia Hou-Broutin et Arnaud Buhot. Merci Yanxia pour l'immense liberté que tu m'as accordée. C'était une grande chance de bénéficier de ta confiance. J'ai beaucoup appris sur le métier de chercheur. Merci Arnaud pour ton enthousiasme permanent et pour les conversations scientifiques qui ont fait énormément progresser le projet. D'un point de vue humain, vous avez tous les deux été d'une gentillesse immense.

Ma gratitude va également à tous ceux avec qui j'ai travaillé au cours de cette thèse. Merci à Sophie Brenet, qui m'a transmis avec talent et rigueur les rudiments de la chimie et qui a construit les solides fondations du projet. Jonathan Weerakkody, toujours positif et inspirant, ce fut un grand plaisir de te côtoyer. Marielle, qui reprend le flambeau et à qui je souhaite beaucoup de réussite. Noël Scaramozzino, qui a beaucoup aidé aux expériences de *phage display*, et a toujours été présent pour répondre à nos questions. Loïc Briand et Christine Belloir pour m'avoir fourni des protéines de grande qualité et tout le support associé. Raphaël Mathey, la force vive du labo.

Merci à tout le CREAB. C'était un plaisir de venir travailler le matin. J'espère que le laboratoire gardera longtemps cet esprit de convivialité. Je regretterai tout particulièrement mes co-bureaux, qui ont été d'un grand soutien au cours de cette thèse : Sophie, Eric et Elise.

Je tenais aussi à saluer tous les enseignants qui m'ont menée jusqu'ici en me transmettant une partie de leur passion.

Rien de tout cela n'aurait été possible sans tous ceux qui m'ont fait me sentir à la maison à Grenoble. Morgan et François, les colocs de la première heure. Julie et Geoffroy, vous êtes devenus de véritables amis et des sources d'inspiration pour moi par votre bienveillance, votre générosité et votre justesse. Marie, l'étincelle de joie vive à la maison. Chris, avec qui chaque instant du quotidien ressemble à des vacances. Brandade et son sens de l'accueil au réveil ou en rentrant du boulot. Les improvisateurs, les danseurs de swing, les holimovers, les joggers, les skieurs, les joueurs de squashes et de jeux de société, les yogis, ...

Je terminerai par remercier ma famille. Vous êtes pour moi l'ancre immuable à laquelle je sais pouvoir me raccrocher. Je suis consciente de la chance que j'ai de vous avoir et extrêmement fière de chacun d'entre vous.



# Table of contents

<b>TABLE OF CONTENTS</b>	<b>2</b>
<b>NOMENCLATURE OF THE DIFFERENT PROBES</b>	<b>10</b>
<b>INDEX</b>	<b>12</b>
<b>ABBREVIATIONS</b>	<b>18</b>
<b>NOTATIONS</b>	<b>22</b>
<b>INTRODUCTION</b>	<b>24</b>
<b>CHAPTER 1 STATE OF THE ART: BIOMIMETIC STRATEGIES TO IMPROVE THE SENSITIVITY AND SELECTIVITY OF ARTIFICIAL NOSES</b>	<b>30</b>
<b>1.1. WHAT IS AN ARTIFICIAL NOSE?</b>	<b>30</b>
1.1.1. VOLATILE ORGANIC COMPOUNDS	30
1.1.2. THE BIOLOGICAL NOSE: A SOURCE OF INSPIRATION	31
1.1.3. WORKING PRINCIPLE AND PERFORMANCES OF AN ARTIFICIAL NOSE	32
<b>1.2. DESIGN OF BIOMIMETIC SENSING MATERIALS</b>	<b>34</b>
1.2.1. BIO-SOURCED MATERIALS	34
1.2.2. BIOMATERIALS BY COMPUTATIONAL DESIGN	36
1.2.3. NOVEL MATERIALS BASED ON HIGH-THROUGHPUT SELECTION METHODS	37
<b>1.3. IMMOBILIZATION OF THE SENSING MATERIAL ON THE SENSOR SURFACE</b>	<b>40</b>
1.3.1. IMPROVEMENT OF THE SELECTIVITY	40
1.3.2. INCREASE OF THE SENSITIVITY	41
<b>1.4. STRATEGIES INSPIRED BY THE PERIRECEPTOR EVENTS</b>	<b>43</b>
1.4.1. FLOW DYNAMICS	44
1.4.2. HYDRATED SENSING ENVIRONMENT	44
1.4.3. CHROMATOGRAPHIC EFFECTS	45
<b>1.5. TRANSDUCTION SYSTEMS</b>	<b>46</b>
1.5.1. BIOINSPIRED AMPLIFICATION AND TRANSDUCTION	47
1.5.2. MULTIPLEXING FOR LARGE ARRAYS OF SENSORS	48
<b>1.6. DATA PROCESSING</b>	<b>50</b>
1.6.1. A MODEL OF NEURONS: TOWARD SPIKE-BASED NEUROMORPHIC APPROACHES	50
1.6.2. ARTIFICIAL NEURAL NETWORKS AND HARDWARE MODELS OF OLFACTORY BULB	51

1.6.3.	FEEDBACK INHIBITORY LOOPS AND LEARNING ALGORITHMS TAKING INSPIRATION FROM THE CORTEX	53
<b>1.7.</b>	<b>POSITIONING OF THE THESIS PROJECT</b>	<b>54</b>

**CHAPTER 2 AN OPTOELECTRONIC NOSE FOR THE DETECTION OF VOLATILE ORGANIC COMPOUNDS IN THE GAS PHASE** **60**

---

<b>2.1.</b>	<b>SENSING MATERIALS</b>	<b>61</b>
2.1.1.	HISTORICAL PROBES	61
2.1.2.	NEW PROBES DEVELOPED IN THIS PROJECT	63
<b>2.2.</b>	<b>IMMOBILIZATION OF PROBES</b>	<b>64</b>
2.2.1.	PREPARATION OF CHIPS BY SPOTTING AN ARRAY OF SENSING MATERIALS	64
2.2.2.	DRIFT CONTROL STRATEGIES	66
<b>2.3.</b>	<b>SAMPLING OF VOLATILE ORGANIC COMPOUNDS</b>	<b>68</b>
2.3.1.	FLUIDIC CIRCUIT	68
2.3.1.	PRECISE DILUTION OF VOCs	70
2.3.2.	HUMIDITY CONTROL	70
<b>2.4.</b>	<b>TRANSDUCTION SYSTEM: SURFACE PLASMON RESONANCE IMAGING</b>	<b>73</b>
2.4.1.	WORKING PRINCIPLE OF SPRI	73
2.4.2.	CONDUCT OF A SAMPLE ANALYSIS	75
<b>2.5.</b>	<b>DATA PROCESSING AND ANALYSIS</b>	<b>76</b>
2.5.1.	ANALYSIS OF AN INDIVIDUAL INJECTION	77
2.5.2.	PRINCIPAL COMPONENT ANALYSIS	78

**CHAPTER 3 CHARACTERIZATION AND ASSESSMENT OF THE PERFORMANCE OF THE DEVICE** **86**

---

<b>3.1.</b>	<b>AFFINITY EVALUATION OF A FREE PROBE FOR A TARGET VOC IN SOLUTION</b>	<b>86</b>
3.1.1.	COMPUTER MODELLING: DETERMINATION OF THE STRUCTURE AND AFFINITY OF A PEPTIDE FOR A TARGET VOC	86
3.1.2.	ISOTHERMAL TITRATION CALORIMETRY: EXPERIMENTAL MEASUREMENT OF THE AFFINITY BETWEEN OBPs AND VOCs	88
<b>3.2.</b>	<b>SURFACE CHARACTERIZATION OF THE SENSING MATERIALS ON THE SPRI CHIP</b>	<b>90</b>
3.2.1.	THEORETICAL MODEL BASED ON SPRI IMAGES	91
3.2.2.	EXPERIMENTAL SURFACE CHARACTERIZATION METHODS	97
<b>3.3.</b>	<b>OPTOELECTRONIC TONGUE FOR VOC DETECTION IN THE LIQUID PHASE WITH IMMOBILIZED PROBES</b>	<b>103</b>
3.3.1.	WORKING PRINCIPLE OF LIQUID-PHASE SPRI	103
3.3.2.	AMPLIFICATION STRATEGIES FOR THE DETECTION OF SMALL MOLECULES IN THE LIQUID PHASE	104

<b>3.4. PERFORMANCE ASSESSMENT OF THE OPTOELECTRONIC TONGUE AND NOSE</b>	<b>105</b>
3.4.1. CHARACTERIZATION OF THE SENSITIVITY	105
3.4.2. CHARACTERIZATION OF THE SELECTIVITY	111

---

**CHAPTER 4 PROTEIN ENGINEERING: USING ODORANT BINDING PROTEINS AS SENSING MATERIALS** **120**

<b>4.1. FABRICATION OF OBP-CHIPS</b>	<b>122</b>
4.1.1. GENERAL INFORMATION ON THE OBPs USED IN THIS PROJECT	122
4.1.2. IMMOBILIZATION OF OBPs ON THE CHIP	124
<b>4.2. OBP-BASED OPTOELECTRONIC TONGUE</b>	<b>126</b>
4.2.1. PARTICULARITIES OF THE PROTOCOL AND DATA PROCESSING	126
4.2.2. DETECTION OF VOCs IN SOLUTION	127
4.2.3. REGENERATION PROCEDURE	130
4.2.4. PERFORMANCES OF THE OPTOELECTRONIC TONGUE	132
<b>4.3. OBP-BASED OPTOELECTRONIC NOSE: TOWARD THE DETECTION OF VOCs IN THE GAS PHASE</b>	<b>135</b>
4.3.1. DETECTION OF VOCs IN DRY AIR	135
4.3.2. STRATEGIES TO INCREASE THE SPECIFIC BINDING OVER NON-SPECIFIC BINDING RATIO	137
4.3.3. DETECTION OF VOCs IN HUMID AIR	139
<b>4.4. PERFORMANCE OF THE OBP-BASED OPTOELECTRONIC NOSE</b>	<b>142</b>
4.4.1. SELECTIVITY	142
4.4.2. ANALYSIS OF THE DISCRIMINATION MECHANISMS	144
4.4.3. OTHER PERFORMANCES	147
<b>4.5. TRANSFER TO THE NeOse Pro</b>	<b>147</b>
4.5.1. PERFORMANCE OF THE OBP CHIPS INTEGRATED IN THE NeOse Pro	147
4.5.2. ANALYSIS OF THE DISCRIMINATION MECHANISMS	149

---

**CHAPTER 5 PHAGE DISPLAY: IN VITRO SCREENING OF HIGH-AFFINITY PEPTIDES** **156**

<b>5.1. PHAGE DISPLAY WORKING PRINCIPLE</b>	<b>156</b>
5.1.1. PHAGE LIBRARY	158
5.1.2. IMMOBILIZATION OF THE TARGET ON A SOLID SURFACE	160
5.1.3. SELECTION PROCEDURE	162
5.1.4. PHAGE TITRING AND CLONE ISOLATION	163
<b>5.2. SELECTION OF THREE PEPTIDES FOR THE DETECTION OF PHENYL COMPOUNDS</b>	<b>164</b>
5.2.1. FIRST RESULTS OF THE PHAGE DISPLAY EXPERIMENT	164



5.2.2.	CHARACTERIZATION OF THE AFFINITY OF THE FREE PEPTIDES IN SOLUTION FOR PHENYL COMPOUNDS	166
<b>5.3.</b>	<b>PEPTIDE-BASED OPTOELECTRONIC TONGUE: DETECTION OF VOCs IN THE LIQUID PHASE</b>	<b>172</b>
5.3.1.	SIGNAL AMPLIFICATION BY THE DETECTION OF NANOPARTICLES FUNCTIONALIZED WITH VOCs	172
5.3.2.	COMPETITIVE ASSAY	175
<b>5.4.</b>	<b>PEPTIDE-BASED OPTOELECTRONIC NOSE: DETECTION OF VOCs IN THE GAS PHASE</b>	<b>177</b>
5.4.1.	INFLUENCE OF HUMIDITY ON THE OPTOELECTRONIC NOSE	178
5.4.2.	PERFORMANCE OF THE PEPTIDE-BASED OPTOELECTRONIC NOSE	181
5.4.3.	INDIVIDUAL SELECTIVITY OF THE DIFFERENT PEPTIDE BIOSENSORS	182
<b>5.5.</b>	<b>PERSPECTIVES FOR THE OPTIMIZATION OF THE SELECTION PROTOCOL</b>	<b>184</b>
5.5.1.	PHAGE-HRP DISPLAY	185
5.5.2.	PHAGE DISPLAY MONITORED BY SPRi	187
 <b>CHAPTER 6 PROSPECTIVE WORK: POTENTIAL INPUT OF COMPUTATIONAL SIMULATIONS</b>		<b>194</b>
<b>6.1.</b>	<b>VIRTUAL SCREENING OF PENTAPEPTIDES FOR OPTOELECTRONIC NOSE DEVELOPMENT</b>	<b>194</b>
6.1.1.	SELECTION OF THE PROBES USED IN THIS PROJECT	195
6.1.2.	PREPARATION OF THE CHIP	196
6.1.3.	VOC ANALYSIS BY THE OPTOELECTRONIC NOSE	197
6.1.4.	CONCLUSION	199
<b>6.2.</b>	<b>EXPLORATORY WORK ON LONGER PEPTIDES</b>	<b>199</b>
6.2.1.	DESCRIPTION OF THE PROTOCOL	200
6.2.2.	INFLUENCE OF THE PEPTIDE PROPERTIES ON THEIR BINDING AFFINITY	202
6.2.3.	INFLUENCE OF THE VOC PROPERTIES ON THE BINDING AFFINITY	203
6.2.4.	CHEMICAL RESOLUTION	204
6.2.5.	CONCLUSION	207
<b>6.3.</b>	<b>SUPPORT TO <i>IN VITRO</i> SELECTION</b>	<b>207</b>
 <b>CONCLUSIONS AND PERSPECTIVES: THINKING TOOL FOR IMPROVING THE PERFORMANCE OF THE ARTIFICIAL NOSE</b>		<b>212</b>
	DESCRIPTION OF THE TOOL	212
	OVERVIEW OF THE ACTIONS CARRIED OUT DURING THIS THESIS	213
	PERSPECTIVES	215
 <b>APPENDIX</b>		<b>218</b>
	A-1 ANGULAR SENSITIVITY	218

A-2 <i>IN SILICO</i> SCREENING OF HPDNA	219
<b>REFERENCES</b>	<b>222</b>
<b>LIST OF SCIENTIFIC PRODUCTION</b>	<b>248</b>
<b>RESUME - SUMMARY</b>	<b>251</b>



## Nomenclature of the different probes

R0 to R19	historical peptides
OBP3-w, OBP3-a and OBP3-c	odorant binding protein mutants
B5, B6 and B7	peptides selected by Ju <i>et al.</i> by phage display for the detection of BTX compounds [1]
P1, P2 and P3	peptides selected for VOC with a phenyl ring by phage display, with a consensus, synthesized
PhD1 to PhD12	peptides selected for VOC with a phenyl ring by phage display, without a consensus, not synthesized
OH-AuNP and P-AuNP	gold nanoparticle functionalized with PEG OH or phenylethylamine (respectively)
IHRIC, KSDSC, LGFDC, TGKFC, LAWHC and WHVSC	pentapeptides selected by virtual screening
X6 and X12	peptide containing 6 or 12, respectively, repeated amino acids X



## Index

**affitin** Artificial proteins, derived from a DNA binding protein found in a bacteria living in extreme environmental conditions, which can be directed to selectively bind biomolecules (classically antigens).

**alpha helix ( $\alpha$ -helix)** Common motif in the secondary structure of proteins, right hand-helix conformation in which every backbone N–H group hydrogen bonds to the backbone C=O group of the amino acid located three or four residues earlier along the protein sequence.

**analyte** In this thesis, VOC of interest, or molecules being detected by the system.

**angular sensitivity** In this thesis, derivative of the plasmon curve of a biosensor at the working angle.

**aptamer** Oligonucleotide that binds to a specific target molecule.

**artificial nose** Device intended to detect VOCs in the gas phase, with a biomimetic design based on array of cross-reactive sensors and a pattern recognition system.

**artificial tongue** Device intended to detect VOCs or flavors in the liquid phase, with a biomimetic design based on array of cross-reactive sensors and a pattern recognition system.

**association phase** In this thesis, phase of the kinetic response of the biosensors during which the VOC molecules reached the prism surface and bound to the sensing materials.

**beta sheet ( $\beta$ -sheet)** Common motif in the secondary structure of proteins, beta strands connected laterally by backbone hydrogen bonds, forming a generally twisted, pleated sheet.

**biosensor** In this thesis, a single system composed of a given sensing material and the SPRi transducer.

**blank injection** In this thesis, liquid-phase or gas-phase SPRi analysis performed without VOC, on the running buffer or the carrier gas, to verify the cleanliness of the fluidic system and identify potential incorrect settings.

**chemical resolution** In this thesis, characteristic of an artificial nose or tongue that qualifies its ability to discriminate between similar VOCs.

**cross-reactivity** Quality of several biosensors that have the ability to bind several VOCs each with different affinities. Conversely, one VOC will bind to several biosensors.

**dendrimer** Repetitively branched molecules.

**dissociation phase** In this thesis, phase of the kinetic response of the biosensors during rinsing, where the VOC molecules were flushed from the sensing materials and the biosensor regenerated.

**disulphide bridge** Functional group with the structure R-S-S-R', usually derived by the coupling of two thiol groups. Disulfide bridges formed between two cysteine residues are an important component of the secondary and tertiary structure of proteins.

**docking simulation** Computational method which predicts the preferred orientation of two bound molecules to form a stable complex. The binding affinity can then be predicted thanks to scoring functions.

**drift** Long-term variation of the baseline signal provided by a sensor, in our case, of the reflectivity of the biosensors.

**dynamic PCA** In this thesis, PCA carried out on a kinetic database

**equilibrium** In this thesis, phase of the kinetic response of the optoelectronic nose or tongue during an analyte injection in which the signal was stable for all the biosensors.

**G-protein coupled receptors** Family of receptor proteins that detect molecules outside the cell and activate internal signal transduction pathways and, ultimately, cellular responses. They have seven transmembrane domains and couple with G proteins.

**hairpin DNA** Artificial DNA molecule with a stem loop structure that can be used to target biomolecules.

**helical peptide** Peptide with an  $\alpha$ -helix secondary structure.

**individuals** (PCA) One observation of all the variables used for PCA, represented as one line in the correlation matrix, and one point on the plot in the (PC1; PC2) plan.

**kinetic response** In this thesis, variation of reflectivity in time of a given biosensor corresponding to an analyte injection.

**limit of detection (LOD)** In this thesis, lowest detectable concentration of VOC with a reliable signal (SNR > 3).

**linear peptide** Peptide with no  $\alpha$ -helix or  $\beta$ -sheet.

**lipocalin** Family of proteins that transport small hydrophobic molecules, with a common tertiary structure architecture: eight stranded antiparallel  $\beta$ -barrel enclosing an internal ligand binding site.

**molecular modelling** All methods, theoretical and computational, used to model or mimic the behavior of molecules, from an atomistic level description.

**negative selection** In this thesis, phase during which the probe candidates that are likely to bind unwanted compounds are eliminated, notably in phage display and virtual screening methods.

**non-specific adsorption** In this thesis, unwanted adsorption of molecules on the sensor surface, outside of the probes.

**non-specific binding** In this thesis, adsorption or binding of molecules on the probes that does not involve a specific binding site, with a weak affinity.

**olfactory receptors (ORs)** G-protein coupled receptors present on the olfactory neurons that are responsible for the detection of odorants.

**odorant binding proteins (OBPs)** Small shuttle proteins secreted in the nasal mucus of many vertebrate species and the sensillar lymph of insects. They reversibly bind VOC molecules to deliver them to olfactory receptors.

**oligonucleotide** Short DNA or RNA molecules.

**optoelectronic nose or tongue** The artificial nose or tongue that we develop in our laboratory, based on protein or peptide probes and SPRi transduction.

**principal component analysis (PCA)** Eigenvector-based multivariate analysis that enables to identify and represent the dimensions that best explain the variance in the data.

**peptide** Short chains of amino acids linked by peptide bonds.

**perireceptor events** In olfaction, ensemble of interactions occurring between odorant molecules and the olfactory system before they bind to the olfactory receptors.

**phage** Virus that infects bacteria to replicate, composed of a capsid enclosing genetic material.

**phage display** *In vitro* method based on genetically-modified phages for the high-throughput screening of peptides or proteins selective to a target.

**phenyl ring** Aromatic cyclic group of atoms with six carbon bonded together in a hexagonal planar ring.

**plasmon curve** In this thesis, curve representing the reflectivity of a ROI as a function of the incident angle in an SPRi setup, used for the determination of the best working angle and of the angular sensitivity.

**probes** In this thesis, biomolecules that interact with VOC molecules. Once fixed on the surface of the SPRi chip in dense assembly, they constitute the sensing materials.

**region of interest (ROI)** Range of pixels whose intensity will be averaged to get the signal of a sensing area.

**response profile at equilibrium** In this thesis, diagram representing  $\Delta R$  at equilibrium for every sensing material.



**self-assembled monolayers (SAM)** Ordered assembly of molecules formed spontaneously on a surface by adsorption and re-organization. In this thesis, the molecules possess a thiol group that has a strong affinity to gold to form a well-organized thin layer.

**selectivity** In this thesis, quality of a biosensor that has a very different binding affinity with VOC molecules of different families, or even VOCs with very similar structures.

**sensing material** In this thesis, thin layer of probes after immobilization on the sensor surface, sometimes mixed with one or more other molecules for reasons of hydration, dilution or passivation.

**sensitivity** In this thesis, each sensing material  $i$  would have its own sensitivity  $\eta_i$  defined as  $\eta_i = \partial R / \partial C$  with  $\partial R$  an infinitesimal variation of reflectivity, and  $\partial C$  an infinitesimal variation of VOC concentration.

**sensorgram** Plot of the response of a SPR or SPRi sensor against time.

**signature of a VOC** In this thesis, ensemble of signals obtained with all the biosensors upon their contact and interaction with the VOC molecules, which will be fed to the pattern recognition system to identify the sample.

**site-directed mutagenesis** Method used to make specific changes to the DNA sequence of a gene, and so to any gene products.

**static PCA** PCA conducted on an equilibrium database.

**surface plasmon resonance (SPR)** Resonant oscillation of electrons stimulated by light at the interface between a metal and a dielectric, at the basis of SPRi.

**surface plasmon resonance imaging (SPRi)** Label free analytical tool that combines SPR (see above) with imaging of the metallic surface to monitor simultaneously interactions between different sensing materials and an analyte.

**thiol** Organosulfur compound with a  $-SH$  functional group (named thiol group), which has a strong affinity with gold. Many thiols have strong odors.

**transduction** Conversion of a signal from one type to another. For example, olfactory neurons convert a chemical recognition into an action potential. SPRi converts a change in refractive index into an electrical signal.

**variables (PCA)** Feature selected to characterize the individuals in a PCA, represented as a column in the correlation matrix, and one vector in the (PC1;PC2) plan.

**virtual screening** Computational technique to identify the best binders to a target among a library of biomolecules thanks to molecular docking.

**volatile organic compound (VOC)** Organic molecule with a high vapor pressure at ordinary room temperature.



## Abbreviations

AFM	atomic force microscopy
AuNP	gold nanoparticle
BSA	bovine serum albumin
BTX	benzene, toluene, and the three xylene isomers
cAMP	adenosine 3,5-cyclic monophosphate
CCD	charge coupled device
CEA	French Alternative Energies and Atomic Energy Commission
CNRS	French National Center for Scientific Research
DLS	dynamic light scattering
DMSO	dimethyl sulfoxide
DNA	deoxyribonucleic acid
<i>E. coli</i>	<i>Escherichia Coli</i>
EDC	1-ethyl-3-(3-dimethylaminopropyl)carbodiimide hydrochloride)
ELISA	enzyme-linked immunosorbent assay
FET	field-effect transistor
GC/MS	gas chromatography coupled with mass spectroscopy
GRAVY	grand average of hydropathy
hpDNA	hairpin DNA
HRP	horseradish peroxidase
IBMP	3-Isobutyl-2-methoxypyrazine
INRAE	French National Research Institute for Agriculture, Food and Environment
IPTG	isopropyl $\beta$ -D-1-thiogalactopyranoside
ITC	isothermal titration calorimetry
KPFM	kelvin probe force microscopy
LC-MS grade	solvent with a high purity for liquid chromatography - mass spectroscopy
LDA	linear discriminant analysis
LOD	limit of detection

LED	light-emitting diode
MDGC	multidimensional gas chromatography
MFC	mass flow controller
MOS	metal oxide semiconductor
NHS	N-hydroxysulfosuccinimide
OBP	odorant binding protein
OR	olfactory receptor
PC	pressure controller
PC1 and PC2	first two principal components
PCA (FR: ACP)	principal component analysis
PCR	polymerase chain reaction
PEEK	polyetheretherketone
PEG	poly(ethylene glycol)
PEG COOH	HS-(CH <sub>2</sub> ) <sub>11</sub> (EG) <sub>6</sub> -COOH
PEG OH	HS-(CH <sub>2</sub> ) <sub>11</sub> (EG) <sub>3</sub> -OH
PFA	perfluoroalcoxy
PID	photo ionization detector
ppb	part per billion
ppm	part per million
ppt	part per trillion
PTFE	polytetrafluoroethylene
QCM	quartz crystal microbalance
RH	relative humidity
RIU	refractive index unit
RNA	ribonucleic acid
ROI	region of interest
SAM	self-assembled monolayers
SAW	surface acoustic wave
SDS	sodium dodecyl sulfate

SELEX	systematic evolution of ligands by exponential enrichment
SNR	signal-to-noise ratio
SPPS	solid phase peptide synthesis
SPR	surface plasmon resonance
SPRi	surface plasmon resonance imaging
TAAR	trace-amine associated receptor
TBS	tris-buffered saline
TE	transverse electric
TM	transverse magnetic
ToF-SIMS	time-of-flight secondary ion mass spectroscopy
VOC (FR: COV)	volatile organic compound
Xgal	5-bromo-4-chloro-3-indolyl-beta-D-galactopyranoside
XME	xenobiotic metabolizing enzymes
XPS	x-ray photoelectron spectroscopy
(v/v)	volume-to-volume ratio
3D	tridimensional



## Notations

$E_{\text{bind}}$	binding energy
$K_d$	dissociation constant at equilibrium
$M$	molecular weight
$n$	refractive index
OD600	optical density at 600 nm
$P$	pressure
PC $x$	$x^{\text{th}}$ principal component
pfu	plaque forming unit
$R^2$	coefficient of determination
$R_i(t)$	percentage of reflectivity of the ROI $i$ at time $t$
$S_{\text{phenyl}}$	selectivity for phenyl compounds
$\Delta R$	variation of reflectivity measured by SPR $i$
$\Delta R_{\text{eq}}$	variation of reflectivity at equilibrium
$\varepsilon$	extinction coefficient of gold nanoparticles at 520 nm
$\eta$	sensitivity of a sensing material
$\theta$	angle of incidence
$\theta_w$	working angle
$\lambda$	penetration depth of the SPR excitatory evanescent wave inside the dielectric
$\sigma$	surface density of the probes
$\chi_R$	contrast in reflectivity between a sensing material and gold at the working angle





## Introduction

Biomimicry is becoming widespread as a tool for the development of advanced technological devices that meet industrial and societal needs. Supported by an increased knowledge of biological mechanisms, and by the development of new technologies such as bioengineering and nanotechnology, this approach stands out in the current circumstances of limited resources through its sobriety and efficiency. Notably, in our digital society, many of our decisions are informed by the accumulation and processing of data collected by an ever-increasing number of sensors. In nature, this perception is based on physical senses: sight, hearing, touch; and chemical senses: smell and taste. Yet this second component is largely neglected when it comes to developing reliable and objective technological equivalents.

Nowadays, the detection and identification of odors is a real industrial need. Indeed, a device that mirrors the sense of smell would address many applications: in the food industry, for quality control or pathogen detection, in cosmetics, in the environmental field for air quality monitoring, or even for medical diagnosis. In this context, a new class of biomimetic sensors is emerging: artificial noses, inspired by their biological counterpart. They offer a portable, low-cost, easy-to-use analysis tool, which can virtually detect any volatile organic compound (VOC), the main constituents of odors. Moreover, the recovered information is similar to the sensory perception of a smell: a mixture of VOCs is identified as a whole by its unique signature. However, despite much recent progress, the performance of artificial noses is still far from matching that of the biological nose. Especially in terms of sensitivity and selectivity, whereas to adapt to the needs of its potential users, the device requires to be customizable to allow for detection of an odor of interest in a complex and variable environment, sometimes at a very low concentration.

Since 2012, our team has been developing an optoelectronic nose relying on the association of a range of peptide sensing materials and surface plasmon resonance imaging transduction. Upon exposure to a VOC, the different sensing materials bind the molecules with different affinity. A pattern recognition algorithm processes the resulting signals to identify the sample. My thesis project is a continuation of this work. It aims at evaluating the interest of three different strategies for the development of novel high-performance sensing materials, with tunable binding properties. Namely, protein engineering, phage display and virtual screening will be the subject of three different chapters.

Chapter 1 is a review of biomimetic strategies reported in the literature to improve the sensitivity and selectivity of artificial noses. It positions our project within the state of the art.

The Chapter 2 describes the optoelectronic nose device in details, along with the precise objectives of this thesis project. Several modifications were brought to the existing experimental setup to meet new requirements implied by the good function of the new sensing materials.

Theoretical models and advanced characterization were key to validate successive milestones toward the qualification of new constituents for our optoelectronic nose. The Chapter 3 presents the validation procedure and these different methods.

In Chapter 4, we considered the integration of proteins naturally present in the nose as sensing materials in our optoelectronic nose. We used three mutants of odorant binding proteins designed and produced by Dr. Loïc Briand. The sensitivity of these proteins was expected to be particularly high. We verified this point through the evaluation of the performance of the resulting artificial nose.

In parallel, we optimized the protocol of phage display to identify the most selective heptapeptide binders for VOCs with a phenyl group. Phage display, presented in Chapter 5, is an *in vitro* high-throughput selection method. Three peptides were synthesized at the conclusion of these experiments, which were subsequently tested as new sensing materials for our device.

Eventually, we led prospective studies to evaluate the potential input of computational assays for the development of new sensing materials in Chapter 6.

This leads to the conclusions and perspectives of this thesis project, underpinned by a recapitulative diagram.

## CHAPTER 1

State of the art: biomimetic strategies to improve the sensitivity and selectivity of artificial noses



## **Résumé du chapitre 1 - Etat de l'art : stratégies biomimétiques pour améliorer la sélectivité et la sensibilité des nez artificiels**

La biologie est une grande source d'inspiration pour la conception de dispositifs technologiques de pointe répondant aux défis sociétaux et industriels actuels. Notamment, une nouvelle classe de capteurs biomimétiques émerge : les nez artificiels. En s'inspirant du fonctionnement du nez biologique, ils détectent et identifient des composés organiques volatils (COV), les principaux constituants des odeurs, pour adresser un grand nombre d'applications industrielles.

De tels dispositifs seraient en effet utiles dans le domaine agro-alimentaire, pour le contrôle qualité ou la détection de pathogènes, en cosmétique, dans le domaine de l'environnement pour le suivi de la qualité de l'air, ou même pour le diagnostic médical. Plusieurs pathologies sont en effet accompagnées d'une modification de la composition des sécrétions du patient : air exhalé, urine, selles...

Les nez artificiels sont plus portables, moins coûteux, plus faciles d'utilisation que les méthodes traditionnellement employées pour ces applications. De plus, ils analysent un échantillon comme un tout. En cela, l'information récupérée se rapproche de la perception sensorielle d'une odeur.

Cependant, malgré beaucoup de progrès récents, les performances des nez artificiels sont encore loin d'égaliser celles du nez biologique. En particulier pour ce qui est de la sensibilité et de la sélectivité. Ces dispositifs doivent être sélectifs pour savoir détecter et identifier avec certitude un COV cible dans un échantillon complexe. De plus, pour des applications médicales notamment, la détection de traces de COV est cruciale.

Ce chapitre dresse un état de l'art des stratégies biomimétiques proposées pour pallier à ces limitations. Il commence par une introduction au fonctionnement général d'un nez artificiel.

Les performances exceptionnelles du nez biologique sont rendues possibles par son organisation systémique et multi-échelle. Dans la suite du chapitre, nous verrons comment chaque niveau d'organisation du système olfactif peut inspirer des développements technologiques pour améliorer la sensibilité et la sélectivité des nez artificiels. Il évoque ainsi, pour commencer, le développement de matériaux sensibles spécialisés dans la détection d'un COV cible, et les stratégies pour les immobiliser efficacement sur la surface d'un capteur. Par la suite, il propose une réflexion sur les méthodes d'échantillonnage des COV et sur l'environnement du capteur. Pour finir, il aborde les méthodes de transduction et de traitement de données biomimétiques.

Toutes ces notions fournissent les clés de compréhension pour la suite de ce projet de thèse.



# CHAPTER 1      State of the art: biomimetic strategies to improve the sensitivity and selectivity of artificial noses

Biology is a great source of inspiration for the design of cutting-edge technological devices that meet current societal and industrial challenges. In particular, a new class of biomimetic sensors is emerging: artificial noses. Inspired by the functioning of the biological nose, these are devices intended to detect odorant compounds. Such systems could address many industrial applications: in the food industry for quality control or pathogen detection, in cosmetics, in the environmental field for air quality monitoring, or even for medical diagnosis. This thesis will not discuss about medical devices designed to replace a patient's defective nose.

Artificial noses are more portable, less expensive and easier to use than traditional methods for these applications. In addition, they analyze a sample as a whole. In this way, the information recovered is closer to the sensory perception of a smell. They can also be referred to as electronic noses, without necessarily relying on an electronic detection method.

## 1.1. WHAT IS AN ARTIFICIAL NOSE?

---

Artificial noses aim at the detection and identification of volatile organic compounds (VOCs), the main components of odors. Unlike most of the biosensors developed for other applications, artificial noses do not target a specific molecule through a lock-and-key recognition, but rather intend to cover the broadest possible spectrum of VOCs. For this, just like their biological counterparts, artificial noses rely on the combination of an array of cross-selective chemical sensors or biosensors and a pattern recognition system [2]. Artificial noses must be distinguished from artificial tongues. In contrast to the latter dedicated for the analysis of samples in the liquid phase, they strive for the detection of VOCs in the gas phase.

### 1.1.1. Volatile organic compounds

An odor is caused by one or more volatilized chemical compounds, generally in low concentrations, that humans and animals can perceive by their sense of smell. Some of these molecules are inorganic (like hydrogen sulphide or ammonia), but the main constituents of odors are volatile organic compounds. They are small molecular weight organic molecules (<300 g/mol) with a high vapor pressure at room temperature (>0.01 kPa at 20°C) [3]. They are carbon-containing compounds, which may or may not display a particular chemical function. Most of the chemical families (alcohols, aldehydes, esters, *etc.*) and structures (linear, branched, aromatic, *etc.*) are represented among the VOCs. They therefore form a large and diverse group. VOCs have two main sources of emission: natural and anthropogenic.



At first, they are naturally rejected by living organisms, for instance as chemical messages between individuals [4,5]. For many species, these VOCs notably play a crucial role in feeding [6], reproduction, and breeding. On another note, VOCs are waste products of metabolic pathways of numerous living being. For example, humans reject more than one thousand different VOCs [7]. It is known that their smell is representative of humans' health status. Several pathologies are in fact accompanied by a change in the composition of the patient's secretions [8]: exhaled air, urine, feces, and sweat. Bacteria also reject VOCs, the nature and proportion of which depend on the species. Obviously, the detection of these "natural" VOCs have many applications in the food [9] and health [10] industry.

The second major source of VOCs is human activity. They are produced by chemical processes, like organic synthesis, fermentation, refinery, organic solvent evaporation, incomplete combustion, *etc.* Their rapid detection could facilitate the monitoring of these processes. As we know, olfaction is also very efficient to find narcotics and explosives. On the other hand, because of their high volatility, anthropogenic VOCs propagate easily and are responsible for air, soil and water contamination. As a result, artificial noses are interesting tools to monitor this pollution [11].

### **1.1.2. The biological nose: a source of inspiration**

Artificial noses are bioinspired and designed to mimic the olfactory system of animals. It is thus interesting to comprehend the working principle of biological nose to understand the design of their artificial counterpart (Figure 1-1).

Biological olfaction rests on the interaction between VOCs and olfactory receptors (ORs) [12] (Figure 1-1 (a)). ORs are transmembrane proteins at the tips of the cilia of olfactory neurons, bathed in mucus or lymph (Figure 1-1 (b)). The VOCs enter the nasal cavity with breathing, and pass through this hydrophilic layer rich in proteins before reaching the receptor (Figure 1-1 (c)). All the perireceptor events occurring during this step contribute to the detection and identification of VOCs [13]. Notably, since most odorants are hydrophobic, the transport of molecules through aqueous mucus sometimes requires small shuttle proteins called odorant binding proteins (OBPs).

Olfactory neurons are the transducers of the biological nose (Figure 1-1 (d)). Their function is to convert the chemical signal imputable to the binding of VOCs on ORs into an electrical signal. This nerve impulse is then transmitted to the olfactory bulb. In the olfactory bulb, several layers of neurons process the signal (Figure 1-1 (e)). Eventually, the brain analyses the data and identify the smell. All the scales of organization of this olfactory system are great sources of inspiration to improve the performances of artificial noses, as we will demonstrate in this chapter.

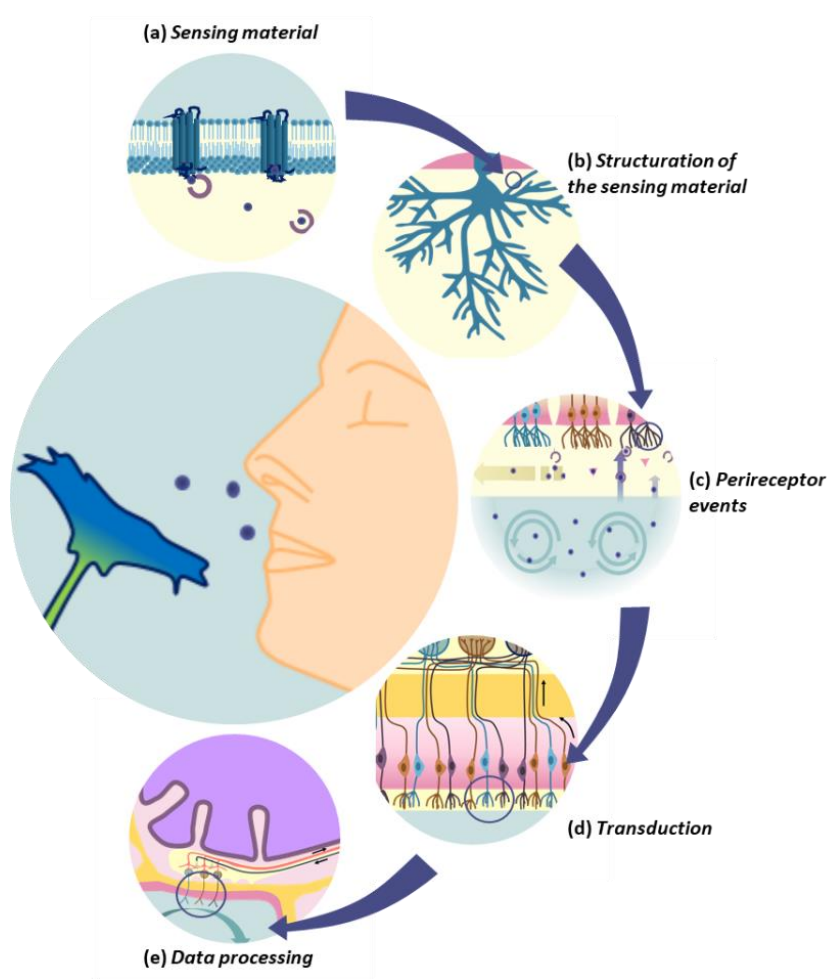


Figure 1-1 Main constituents and functions involved in the biological olfaction.

The remarkable characteristic of the biological nose is its cross-reactivity mode of operation. Illustratively, the human olfactory system possesses around 400 types of functional olfactory receptors; however, it can recognize hundreds of thousands of odors. In fact, an odorant molecule can generally bind to several receptors. Reversely, olfactory receptors are able to bind different odorants, with different affinities. The brain does not interpret the single response of an olfactory receptor, but rather the pattern resulting from their collective interaction with the VOCs to identify an odor. This requires a training phase to associate a detection pattern to an object (flower, coffee, etc.).

### 1.1.3. Working principle and performances of an artificial nose

The Figure 1-2 is the general scheme of the structure of an artificial nose. Taking inspiration from the olfactory system described above, its main constitutive elements are sensing materials (the “olfactory receptors”) to bind the species of interest, a transduction system (the “neuron”) to convert this chemical event into a measurable physical signal and a computer (the “brain”) which processes the data to identify the odor. Just like its biological counterpart, an artificial nose

recognizes VOCs on the principle of cross-reactivity. That is why several sensing materials are necessary. A VOC molecule can bind to multiple sensing materials, and reversely, a sensing material can interact with different VOCs. The resulting interaction pattern is a “signature” of the sample. The computer compares this signature with a database to identify the sample.

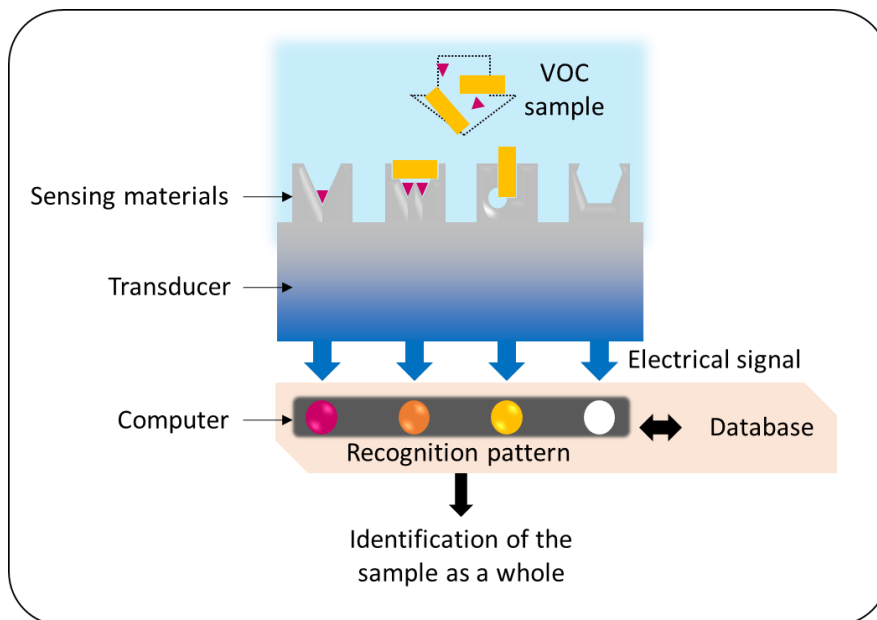


Figure 1-2 General scheme of an artificial nose.

The physicochemical properties of a sensing material change when a VOC binds to its surface, in a way that depends on the nature of the VOC and its concentration. Most of the artificial nose systems use a metal-oxide semiconductor layer or conducting polymers as sensing materials [14]. In both cases, the adsorption of a chemical component at their surface leads to a change in their conductance. Various other synthetic sensing materials have been developed, like dyes with varying color or fluorescence properties [15], molecular imprinted polymers [16], *etc.* Nevertheless, it seems increasingly clear that the use of biological materials and biomolecules as sensitive elements is necessary to approach the performance of the biological nose in terms of odor detection and identification. Systems using whole animals, organs, tissues or cells were investigated for fundamental purpose, but they are very complicated to industrialize, mainly due to a poor stability [17,18]. Although, achievements in the field of biology, genetic engineering and biotechnology provide a possibility to use biomolecules as probes (peptides, proteins, DNA...), and we will explore this direction in this thesis.

Despite a great number of advances in the last forty years, the performances of the artificial noses developed to date are still far from those of the biological nose. In particular, when it comes to sensitivity and selectivity. For many applications, artificial noses must enable the identification of a target VOC in a complex milieu with certainty. Therefore, selectivity is a key feature. It qualifies the ability to detect a target analyte in a sample containing other admixtures and

contaminants [19]. Besides, in several medical applications, an artificial nose is required to trace sub-ppm (parts-per-million) concentrations of VOC [20]. The minimum amount of analyte detectable with a sensor defines its limit of detection or sensitivity.

In the rest of this chapter, we will review the technical solutions proposed in the literature to improve the sensitivity and selectivity of artificial noses, covering various aspects including the nature of the sensing material used, their structure, their complementarity with the transduction system, as well as the data processing.

## 1.2. DESIGN OF BIOMIMETIC SENSING MATERIALS

---

The deorphanization of human olfactory receptors helped to understand how our nose is able to sense tens of thousands of odorant compounds while being highly discriminating. In fact, some of the ORs are “generalist”, whereas the others are “specialist” and strictly directed toward a limited number of structurally related VOC [21,22]. It can also happen that a given receptor presents both a high specificity for a molecular feature and cross-reactivity for others [23]. Relying on this observation, the design of narrowly tuned sensing material appears to be the first logical step towards an increase in selectivity. As in the biological nose, these specific materials could be coupled with more “generalist” ones to maintain a wide detection spectrum. Here, we focus on the main strategies that can be adopted to reach this goal. More detailed reviews are available that list the sensors developed so far with this approach [17,24,25].

### 1.2.1. Bio-sourced materials

The use of proteins from the olfactory system as sensing material is the strategy that directly results from this reasoning. Indeed, the biological nose is able to detect some VOCs at parts-per-trillion (ppt) concentration [12]. Studies suggest that it could even have a lower detection threshold than gas chromatography coupled to mass spectroscopy (GC/MS) for given VOCs [26]. To date, the detection performances of three main families of proteins, presented on Figure 1-3, were investigated.

ORs are the first candidates that come to mind, by direct mimicry of the olfactory system. Indeed, when successfully immobilized on a sensor, they can greatly improve the selectivity and sensitivity to target VOCs [27,28]. Nevertheless, they are proteins from the G protein-coupled receptor family, composed of seven transmembrane alpha helices, which causes real technological challenges. First, their structure is essential for their binding function, and a lipid environment is necessary to preserve it. Membrane fractions [29,30], then nanovesicles or nanoliposomes [31–34], and eventually nanodiscs (Figure 1-3 (b)) [35–37] have been used to achieve their efficient immobilization on sensors. Second, the fact that they are not soluble makes their production

challenging. However, high throughput expression of ORs in heterologous cells [38–41] and cell-free [42,43] strategies exist now.

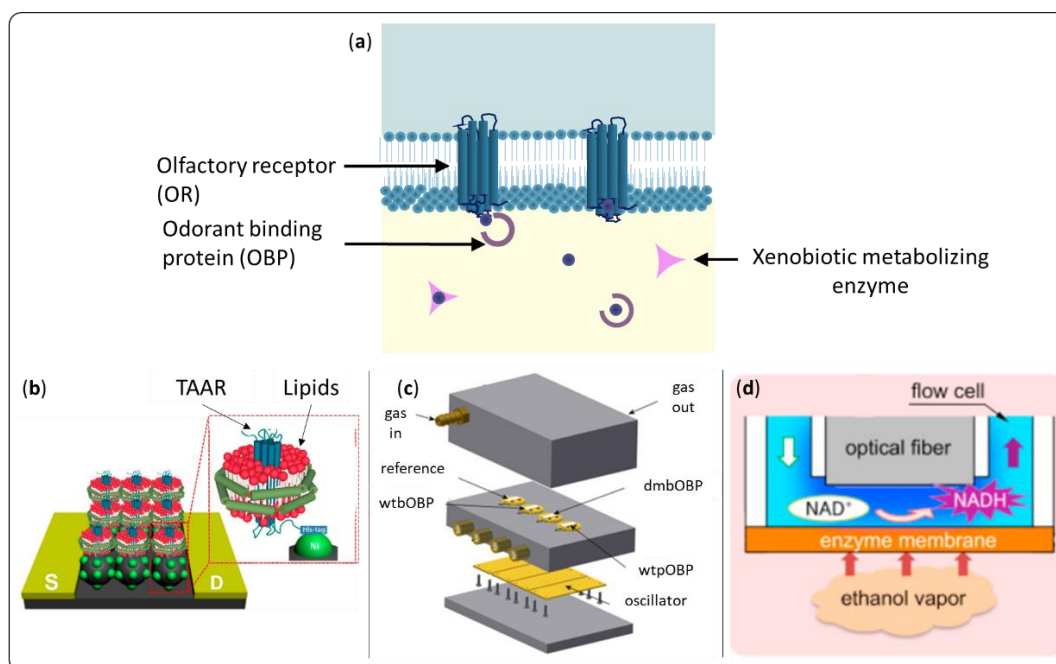


Figure 1-3 Proteins interacting with VOCs in the human nose (a) and examples of olfactory sensors designed from biosourced materials. (b) Trace amine associated receptors (TAAR) in lipid nanodiscs grafted on a field-effect transistor for the detection of cadaverine (adapted from [35]). (c) Three different kind of OBPs deposited on surface acoustic wave sensors for carvone sensing (adapted from [44]). (d) Optical sensor for the detection of ethanol based on an alcohol dehydrogenase membrane [45].

Odorant binding proteins are shuttle proteins for the transport of hydrophobic VOCs through the aqueous mucus for vertebrates, or the sensillar lymph for insects. They are smaller than ORs with a molecular weight of approximately 20 kDa and much more stable to temperature change, pH variations, and organic solvents. Moreover, they are soluble, which greatly facilitates their expression by bacteria and their use in sensors [46–48]. Mammalian OBPs belong to the lipocalin family. They bind VOCs with affinities in the micromolar range, with relatively low specificity. However, it is possible to tune their binding properties by site-directed mutagenesis [49]. Insect OBPs have a more rigid structure composed of six  $\alpha$ -helices stabilized with three disulfide bridges [50]. OBPs' function requires humidity, and most of the olfactory sensors developed with these proteins to date perform detection in liquid. However, some results show that their use in artificial noses may be possible (Figure 1-3 (c)) [44,51–55].

To date, very few sensor designs used enzymes for the detection of volatile organic compounds. However, these proteins have a proven high specificity and selectivity, and offer the advantage of not requiring regeneration. One could think in particular of olfactory xenobiotic metabolizing enzymes (XMEs), which are present in the olfactory endothelium and very likely to bind to VOCs [46]. This direction may be worth exploring. Arakawa *et al.* [45] recently developed gas-phase ethanol biosensors using alcohol dehydrogenase as shown in Figure 1-3 (d). Other

liquid-based enzyme sensors have been reported for flavor detection [56,57], or water quality determination [58].

### 1.2.2. Biomaterials by computational design

Although promising, the industrial application of bioelectronic noses relying on proteins is still very challenging. The immobilization of these molecules on the sensor surface is difficult to perform without a loss of their structure and activity, and in a reproducible manner. The computational design of high affinity peptides could help to overcome these limitations [59]. Peptides are much more robust than proteins, cheaper to synthesize, and could potentially be integrated into industrial devices. On top of that, they can reach similar affinity to those of proteins through rational design. Several methods commonly used for drug discovery could be adapted for this purpose, including molecular modeling and molecular docking, quantitative structure-activity relationship, *de novo* design, virtual screening, and molecular dynamics simulation [60]

#### 1.2.2.1. From proteins to high-affinity peptides

First, several teams have been trying to extract the sequences responsible for VOC recognition in ORs [61–65], OBPs [66–69] or antibodies [70]. As an example, presented in Figure 1-4, Wasilewski *et al.* [69] used docking simulations on an OBP to extract peptides selective for octanal, and tested the influence of the chain length on the selectivity. In accordance with experimental results obtained with a piezoelectric sensor, the longest peptide mimicking the binding pocket of the protein was the best candidate. Knowledge of the three-dimensional structure of these proteins is a staple for a successful simulation. Class A G-protein-coupled receptors of known structures provide a pattern to compensate for the lack of high-resolution 3D structures of ORs in most cases [71]. Docking simulations are then carried out on the obtained molecular model.

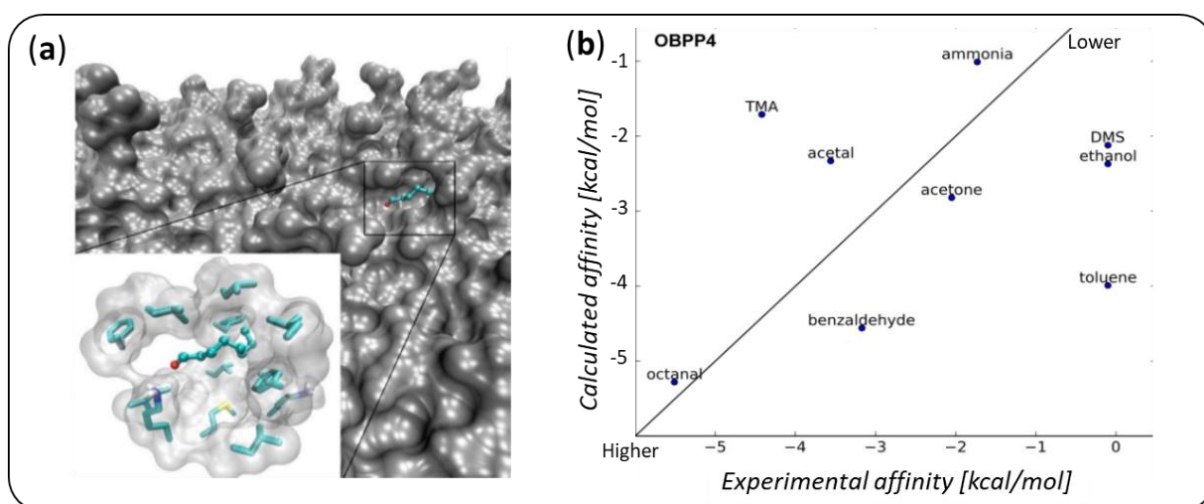


Figure 1-4 (a) Docking simulations performed on an OBP 3D structure model enable to identify a binding site for octanal for obtaining specific peptides accordingly. (b) The experimental and calculated affinities are consistent and show that one of the peptides has a high affinity for octanal [69].

#### 1.2.2.2. Virtual screening

The previous approach can be limited when there is no natural ligand inventoried for a target molecule. In this context, virtual screening represents an interesting alternative. Blanco *et al.* [72] paved the way to molecular modeling of peptides binding to VOCs. Later, Pizzoni *et al.* [73] designed five peptides with various physicochemical properties and predicted their binding scores with 14 VOCs from different chemical classes. The comparison with experimental quartz crystal microbalance (QCM) gas sensing proved that the forecasts were accurate. DNA can also be used for the design of gas sensors [74–76], with sequence dependent selectivity [77]. Recently, Mascini *et al.* [78] reported the use of hairpin DNA screened *in silico* against different chemical classes of VOCs. Their use on QCM and surface plasmon resonance imaging (SPRi) chips was successful for gas sensing [79].

### 1.2.3. Novel materials based on high-throughput selection methods

Natural evolution provided us with a method to carry out this screening process *in vitro* [80]. Several screening methods inspired by this mechanism made it possible to identify specific molecular binders from a library, experimentally [81]. Among them, phage display and SELEX (Systematic Evolution of Ligands by Exponential Enrichment) represent promising tools for the design of peptides and proteins or oligonucleotides (respectively) with a high affinity and specificity toward a target VOC.

#### 1.2.3.1. Phage display

Phage display is a laboratory technique that enables the selection of peptides or proteins with a high affinity for a target [80]. It uses bacteriophages, viruses that infect bacteria. In this technique, a random genetic sequence is inserted into a phage gene coding for a coat protein, causing the phage to "display" a random peptide or protein on its envelope. It results in a connection between genotype (the gene) and phenotype (the peptide or protein). A whole library of phages, each displaying a different peptide is constituted. The target, here a VOC, is immobilized on a surface, which is put in contact with the phage library. In this way, the phages that display a peptide with a high affinity for the target will bind to the surface. After incubation, the unbound viruses are rinsed off, while the bounded ones are eluted and amplified through the infection of bacteria. As a result, an enriched library of phages with a high affinity for the target is obtained. This library is used for the next selection round. Commonly, 3 to 5 rounds are carried out, at the end of which the strongest binders are retrieved, isolated and their genetic material sequenced. Thus, the corresponding peptide sequence can be traced back.

Although phage display has been widely used to discover binders for large molecules [82,83], the literature is scarcer for smaller targets. Interesting examples are the detection of explosives

[84–87] and pesticides [88,89]. Indeed, the screening of peptides selective to a VOC is particularly challenging, since it requires immobilizing the odorant molecule on a surface. Besides, the affinity between a short peptide and a VOC is relatively low. Still, Sawada *et al.* [90] identified a naphthalene-specific peptide from a commercial library of M13 phages exhibiting 12-mer peptides. It exhibits good sensitivity and selectivity in solution, but the team did not test the detection in the gas phase.

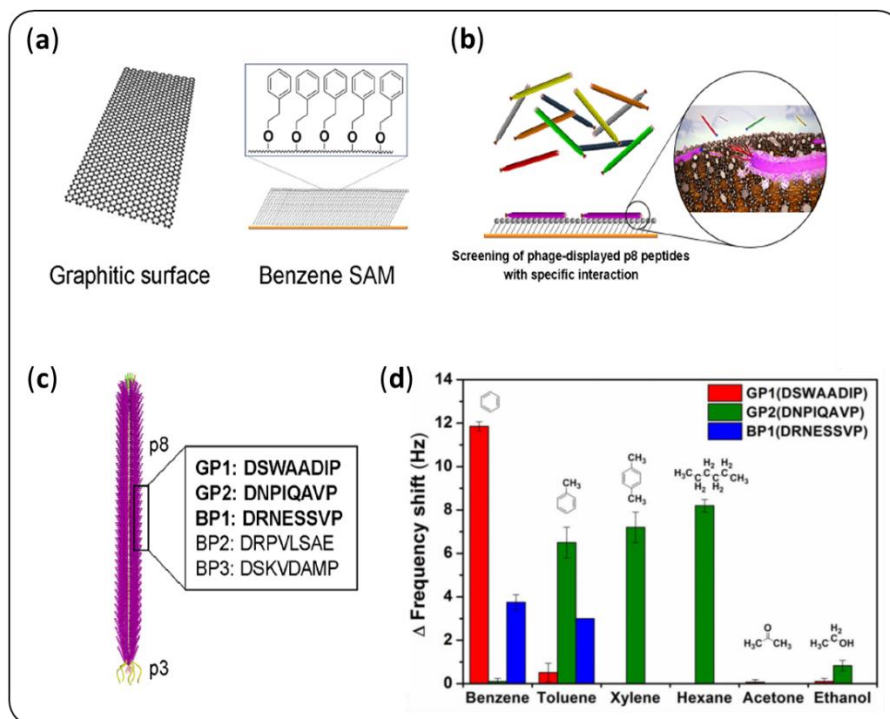


Figure 1-5 Example of a phage display protocol proposed by Ju *et al.* [91]. A library of M13 phages with random peptides displayed on the p8 coat protein was screened (b) against a graphene surface or a benzene SAM (a) to identify ligands specific to benzene. The selected peptides (c) allow for single-carbon discrimination (d).

The use of peptides or proteins from the phage display for gas detection represents an additional challenge, since the selection is carried out in solution. Ju *et al.* [91] screened a phage library against benzene, as depicted in Figure 1-5. Their results are very promising: the three selected peptides showed high selectivity for benzene, even in the gas phase. To achieve such a performance, they chose to work with a custom phage library with p8 proteins displaying random peptides [92]. This made selection possible, even with weaker affinities [93]. However, Tanaka *et al.* [94] recently managed to perform the highly sensitive detection of benzaldehyde in solution and in the gas phase with a peptide selected from a 7-mer commercial library. Nonetheless, they did not clearly demonstrate the selectivity of this peptide.

The phage display protocol would therefore require additional adaptations to be feasible on small targets. The selection of VOC-specific proteins by this method would be worth exploring [95]. It is noteworthy that Nakamura *et al.* [96] proposed an on-bead selection to identify



pentapeptides binding selectively to dioxin. This could represent an interesting cell-free alternative to phage display.

#### 1.2.3.2. SELEX

Speaking of cell-free screening methods, SELEX is probably the most common one. It allows the selection of nucleic acid aptamers, which have the combined advantages of being cheap, robust and reusable, and can have high sensitivity and specificity to a target [97]. New sensing strategies rely on their conformational changes upon target binding.

The selection process begins with the synthesis of a very large oligonucleotide library consisting of randomly generated sequences of fixed length flanked by constant 5' and 3' ends that serve as primers [98]. Just like in phage display, the library is incubated with the target. Oligonucleotides with a weak affinity to it are removed. The bound sequences are eluted and amplified by polymerase chain reaction (PCR) to prepare for subsequent rounds of selection. After few cycles, the best binders are sequenced. The detection of small molecules, and so of VOCs is made easier by the use of Capture-SELEX, which enables the selection of DNA aptamers for solute targets [99]. In this method, the same docking sequence is added to all the oligonucleotides, to enable their immobilization on magnetic beads bearing the complementary strand. Then during selection, oligonucleotides with high affinity to the target will preferentially bind to it, and so be released from the beads. The weak binders are easy to remove with a magnet.

Nevertheless, to date, all of the aptamers developed for VOC sensing were only tested in the liquid phase. Examples include the work of Komarova *et al.* [100] for the detection of furaneol and Kuznetsov *et al.* [101] for the detection of vanillin. In both papers, the selected aptamers were coupled with an ion-sensitive field-effect transistor. The latter integrated an air-to-liquid interface (see 1.4.2)).

In summary, there are many strategies to design sensing materials with a high affinity to a target, which can be very helpful to design sensors dedicated to a given application. These high-affinity materials can be integrated in an artificial nose, in association with more “generalist” ones to keep a wide spectrum of detection. Nevertheless, we have to keep in mind that increasing the affinity between a probe and a target will ineluctably make the regeneration and the reuse of the sensor more difficult [102]. Even in the biological nose, the signal termination is a complex problem. Enzymes, proteins and a continuous renewal of the mucus and the cells are probably involved in this mechanism [13,46]. For this reason, it is worth combining this strategy with a systemic biomimetic design to increase the selectivity and sensitivity of a sensor, which we will discuss in the next parts.

### 1.3. IMMOBILIZATION OF THE SENSING MATERIAL ON THE SENSOR SURFACE

Once the probes selected, their arrangement and structuration upon immobilization on the sensor surface is crucial. In this part, we will review the functionalization strategies that lead to improved sensitivity and selectivity of an artificial nose (Figure 1-6).

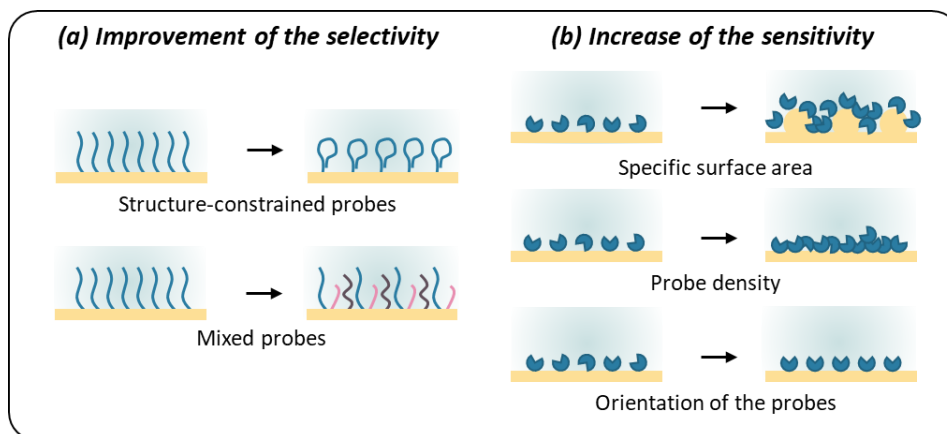


Figure 1-6 The immobilization of the sensing material on the surface of the sensor is key to make full use of its sensing potential and to ensure the highest sensitivity and selectivity.

#### 1.3.1. Improvement of the selectivity

At the molecular level to begin with, ORs and OBPs are highly structured, which ensures their activity. When switching to synthetic probes, a similar structure mimicking "binding pockets" of these proteins is most likely desirable to increase specificity. The fact that most of the peptides selected by phage display to date exhibit a secondary structure reinforces this hypothesis. Indeed, in the work of Sawada *et al.* [90], circular dichroism spectroscopy showed that the selected peptide folds in  $\beta$ -turn. For Tanaka *et al.* [94], the best binders included a proline, which can contribute to a bent or twisted conformation. In both cases, the authors considered the structuration of the peptides was partly responsible for the molecular recognition.

Giebel *et al.* [103] were the first to voluntarily constrain the conformation of peptides by flanking them with two cysteine which would result in disulfide bond formation. The cyclic peptides selected by phage display had a three-order-of-magnitude higher affinity to streptavidin than linear ones. Moreover, they are on the rise for drug development [104]. Structures mimicking antibodies are also emerging in drug discovery [105,106], which could be very interesting for the selection or maturation of peptides by phage display. Since a secondary structure is only possible for primary sequences of more than 4-5 amino acids, the length of the peptides could become a key feature when it comes to the improvement of the selectivity [69,107].

Mascini *et al.* [78] used the same reasoning to develop hairpin-DNA probes whose loops recreate structured "binding sites". *In silico* simulations in Figure 1-7 showed that saddle-shaped

binding pockets lead to higher binding scores than planar ones, which the team explained by a higher synergic cooperation.

Interestingly, this idea can also be useful to improve a natural binder. Kotlowski *et al.* [108] produced mutants of the Italian honeybee OBP 14 with an additional disulfide bond, reducing its dynamics and leading to a higher affinity for eugenol.

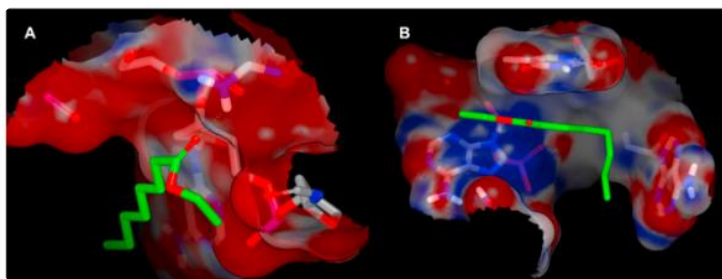


Figure 1-7 Electrostatic molecular surfaces of the single strand DNA CTGCAA, with a planar interaction surface (binding score -2.26 Kcal/mol) (A), and ATAATC with a saddle shaped binding pocket (binding score -6.28 Kcal/mol) (B) in complex with ethyl octanoate (highlighted in green) [78].

Our team [109–112] proposed another approach to improve the selectivity of artificial tongues, which could be adapted to artificial noses. It relies on mimicking the biological properties of glycosaminoglycans based on a combinatorial approach. Two disaccharides, lactose and sulfated lactose, were used as building blocks, mixed in different proportions and self-assembled on the sensor so as to reproduce the charged topography of these polysaccharides. In a similar way, peptides could be mixed to fabricate “binding-pocket like” surfaces in a cheap and easy to produce way.

### 1.3.2. Increase of the sensitivity

At the tissue level, the structure of the olfactory epithelium plays a key role in the sensitivity of the biological nose [113]. For instance, in humans, ten million olfactory neurons project five to fifty cilia each into the mucus (schematic representation in Figure 1-8 (a)). As a result, the total sensing area can reach about 70 cm<sup>2</sup> [107]. Similarly, in artificial sensors, a nano-structuration of the sensing surface leads to an increase in the sensitivity. As a first example, the team of Dr. D. Compagnone [78,114,115] deposited functionalized nanoparticles on their sensors to increase the specific surface, as shown in Figure 1-8 (b). Zine *et al.* [116] generated them directly *in situ*. Recently, Tanaka *et al.* [94] immobilized selective peptides on ZnO nanowires, Figure 1-8 (c).

Similarly, the shape of insect antennae extends a very large sensitive surface. Besides, this configuration is adapted to the diffusion of VOCs in air. For example, a molecule encountering the antenna of *Bombyx mori* would hit and bounce on its surface about 100 times [117]. In such a way, it acts as a physical amplifier [118], which could be a great source of inspiration for sensor design. Spencer *et al.* [119] mirrored the structure of moth antennae thanks to an additive fabrication

process. This system developed for fundamental understanding purposes could inspire technological devices, as pointed in the review of Jaffar-Bandjee *et al* [120] (Figure 1-8 (d)).

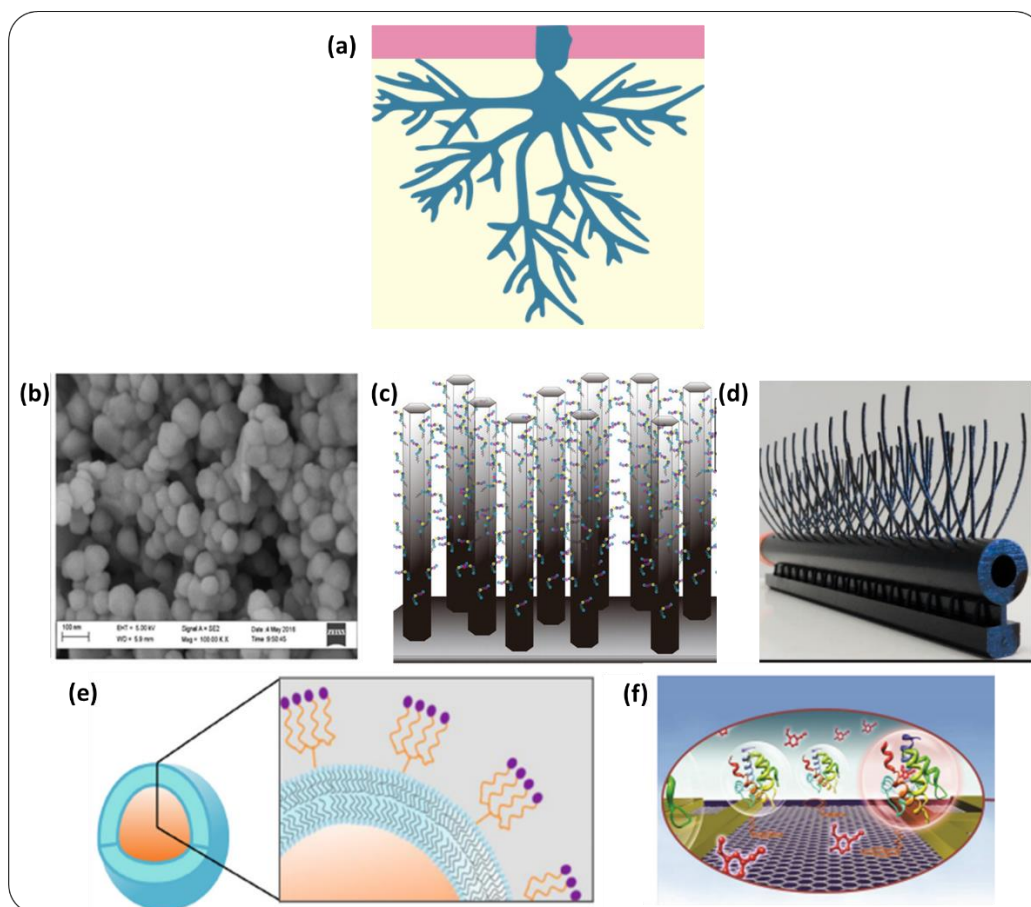


Figure 1-8 (a) Olfactory neurons deploy a large specific surface area in the mucus through their cilia. To mimic this strategy, (b) Mascini *et al.* [115] modified ZnO nanoparticles with peptides, (c) Tanaka *et al.* [94] immobilized peptides specific to benzaldehyde on ZnO nanowires. (d) Jaffar-Bandjee *et al.* [120] fabricated artificial “moth antennae” (e) Gray *et al.* [121] proposed liposomes displaying tetrameric peptides to enable cooperative binding (f) Larisika *et al.* [122] used a bi-functional linker to optimize the orientation of OBPs on a graphitic surface.

The density of sensing molecules on the sensor surface is also a very important point when it comes to the sensitivity. With an optimal density, the sensitivity can be improved. Moreover, multivalency is indeed a proven approach to improve affinity between a probe and a target [123,124]. This is particularly relevant for peptides selected by phage display. When isolated, they may actually exhibit considerably lower affinity than when presented on the phages, where they can attach multivalently to targets. For example, dendritic architectures inspired from the phage structure (Figure 1-8 (e)) can typically improve the affinity by two orders of magnitude [121,125]. Alternatively, Hou *et al.* used a Langmuir-Blodgett technique to create a dense layer of OBPs [51].

Besides the strict number of probes per surface unit discussed above, their orientation is also key to ensure an optimized binding, especially when it comes to proteins. In the literature, various ingenious strategies have been developed for this purpose. OBPs can be immobilized using a cysteine [49] or histidine tag [108,126] at their N-terminus so as to keep a good access of the VOCs

to the binding pocket. Larisika *et al.* [122] and Zhang *et al.* [127] proposed a solution with a bi-functional linker (Figure 1-8 (f)). Du *et al.* [128] employed aptamers to graft olfactory receptors onto their sensor. Interestingly, Kuang *et al.* [129] used a graphene-binding peptide as an anchor.

#### 1.4. STRATEGIES INSPIRED BY THE PERIRECEPTOR EVENTS

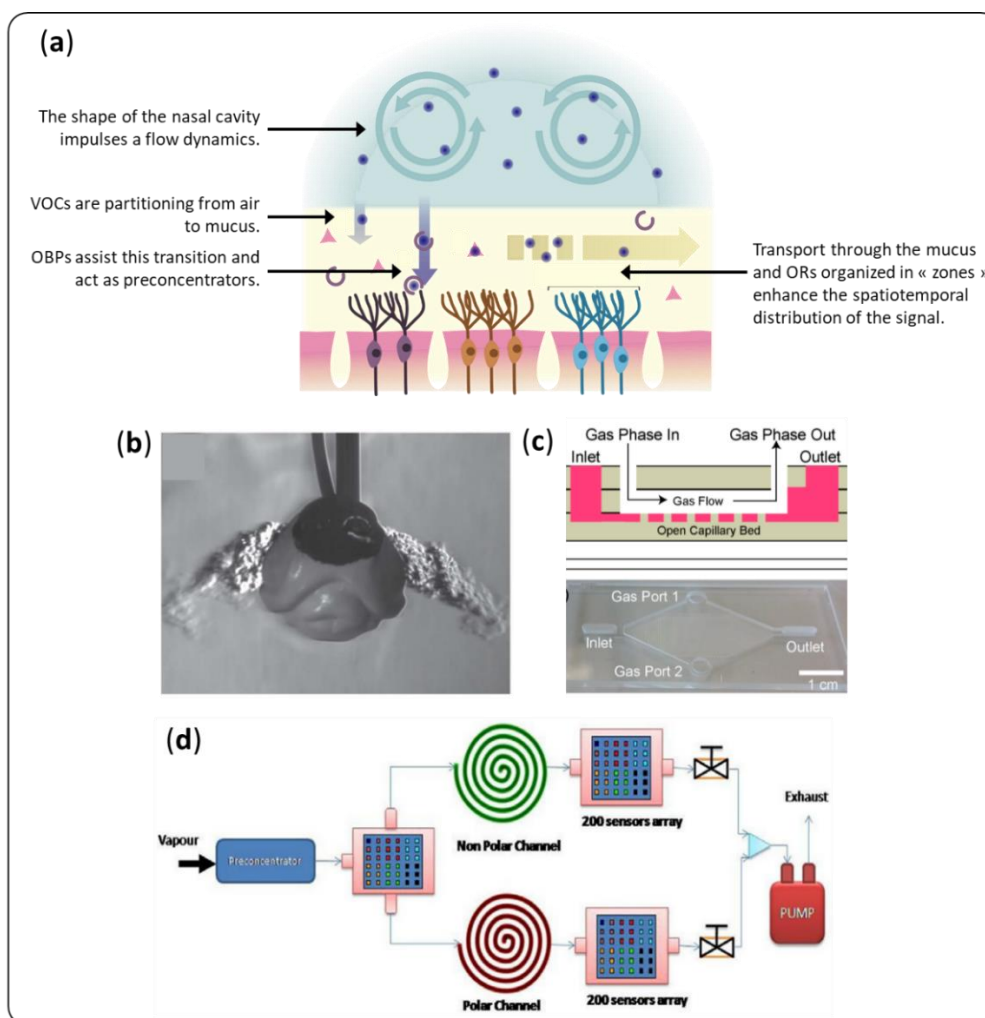


Figure 1-9 (a) Main perireceptor events in the biological olfaction. (b) 3D printed model of a dog nose enabled Staymates *et al.* [130] to visualize, understand and reproduce the sniffing process. (c) Warden *et al.* [131] proposed an open channel microfluidic card for gas-to-liquid extraction. (d) The design proposed by Che Harun *et al.* [132] helped to separate a sample spatially and temporally.

The biological nose is a much more complex system than just an array of cross-selective sensors. Prior to reach olfactory receptors, VOCs have first to enter the nasal cavity through breathing. Then, they pass through an aqueous layer: the nasal mucus in vertebrates or the sensillar lymph in insects. This milieu is constantly renewed and rich in proteins that interact with VOCs. Perireceptor events, described roughly in Figure 1-9 (a), include all biochemical interactions that occur during these two stages. They are necessary to ensure the good performances of the natural nose, and they affect the perception of smells. When it comes to

artificial noses, the sampling of VOCs plays a crucial role [133]. The perireceptor events become an important source of inspiration for their sensitive and selective detection.

#### **1.4.1. Flow dynamics**

In the biological noses of vertebrates, breathing conveys the VOCs to the olfactory epithelium. The airflow dynamics plays a role in olfaction. First, the shape of the nasal cavity directs most of the flux towards the olfactory epithelium, acting as a pre-concentrator [134]. Furthermore, it distributes spatially the VOCs depending on their physicochemical properties, which facilitates their identification. Sniffing could reinforce this effect [135].

Dr. D. R. Walt's team was the first team to take inspiration from this observation [136]. They improved the discrimination capacity of a fiber optic sensor using a replica of canine nasal cavity in which they placed identical sensors at different positions. The spatial distribution of the VOCs due to flow dynamics in this chamber provided useful supplementary data. Chang *et al.* [137] adopted a similar strategy and designed a fluidic cell on the model of the human nasal turbinate to facilitate the discrimination of VOCs. A good understanding of the flow dynamics in the analysis chamber can also result in the improvement of the sensitivity of the sensor. Scott *et al.* [138] used a computational fluid dynamic model to position their QCM sensor in a way to collect most of the sample. It is also a way to limit the effects of position and the response time of the sensors [139].

Some teams have even mimed sniffer-induced flow modulations to improve the sensitivity and discrimination capabilities of their sensors. El Barbri *et al.* [140] used a peristaltic pump to modulate the flow of the carrier gas in their artificial nose. It resulted in an improvement of the classification accuracy for five volatile organic compounds. The implementation of this method required dedicated data processing such as discrete wavelet transform or Deep-Q network. The latter, when integrated into a feedback loop, can help to optimize the flow modulation [141]. The breathing frequency is indeed a proven important parameter in artificial sniffing devices [142]. Staymates *et al.* [130] coupled the two previous approaches using both a simulated 3D printed dog's nose and sniffing. This system, presented in Figure 1-9 (b), resulted in a 16-fold improvement of the sensitivity of a commercially available explosive detector.

#### **1.4.2. Hydrated sensing environment**

In vertebrates, before reaching the olfactory epithelium, inspired VOCs must first penetrate a mucus layer. It plays an important role in the transport of VOCs, their metabolization, and their interaction with olfactory receptors [13]. Moreover, thanks to the presence of large glycoproteins (mucins), mucus provides a hydrated environment, which is very favorable for fragile proteins. It guarantees the integrity of their structure, and therefore their function. In insects, this function is

assured by the sensillar lymph. Similarly, humidity is most probably a key factor for the design of selective and sensitive sensors.

Although OBPs are more stable than other proteins, they can lose their active conformation in harsh conditions. Thus, an aqueous medium is required to ensure their function [48]. Humidity remains an important issue when it comes to peptides, although less structured and thus more robust than proteins when dried. The water molecules seem to play a role in the specific interaction between peptides and a target VOC. Indeed, the sensitivity and specificity of selected peptides can be lost at low ambient humidity [91,143].

To circumvent this problem, several teams have recently elaborated designs by integrating an air-to-liquid extraction interface to an artificial tongue. Lee *et al.* [144] and Kuznetsov *et al.* [101] used a porous membrane made in polycarbonate and  $\text{SiO}_2/\text{Si}_3\text{N}_4/\text{SiO}_2$ , respectively. This membrane acts similarly to the cuticle in insect antennae. It prevents the evaporation of water while allowing the diffusion of odorant molecules. Warden *et al.* [131] proposed another strategy with open microfluidic channels relying on capillarity (Figure 1-9 (c)). Alpha-cyclodextrin added in the capture liquid enabled reasonable capture efficiency, up to 30% for hexanal at 16 ppm.

Although interesting, these approaches pose the problem of the transition of VOCs from a gaseous phase to a liquid phase, which can drastically increase the detection time and the limit of detection. In the biological nose, this limitation turns to an asset: OBPs assist the partitioning of hydrophobic VOCs from air to the mucus, and this acts as a pre-concentration step of the chemical message. In the absence of these carrier proteins, artificial devices integrating an air-to-liquid interface would likely require a first step of pre-concentration of VOCs [145,146].

### **1.4.3. Chromatographic effects**

Mucus presents another advantage for the selective detection of VOCs. Indeed, molecules travel differently through it, depending on their physicochemical properties, as they would in a chromatographic column. Thereby, it creates a spatial and temporal separation, which greatly facilitates the discrimination of VOCs [147–149].

Gas chromatography coupled with mass spectroscopy (GC/MS) is a reference technique for analyzing VOCs in industry. It is very reliable and sensitive with a limit of detection below the part per billion. Moreover, it can provide the exact composition of a complex mixture, component by component and sometimes in a quantitative way. The analysis of samples for food quality, health or environment monitoring is made complex by 1) the wide range of masses of the constituents of these complex mixtures, 2) the chemical resolution needed to distinguish between two VOCs with very similar structure. Nevertheless, the development of multidimensional gas chromatography (MDGC) provides a partial solution to these problems [150]. It is based on the

series connection of several columns with stationary phases of orthogonal properties. Notably, heart-cut MDGC is particularly adapted to the analysis of VOCs in real samples [151]. Another option is to analyze the resulting spectrum, not by identifying the single peaks, but as a signature for the whole mixture. It can be considered as an artificial nose in which the different sensors are chromatographic peaks. Notably alpha-MOS (Toulouse, France) is selling a flash gas chromatography electronic nose, used in many studies [152].

It is also possible to integrate a spatial separation on conventional artificial noses to improve their performance. Mimicking the chromatographic behavior of the mucus, Covington *et al.* [153] integrated a microfluidic channel coated with a polymer onto an array of chemoresistive microsensors. They noticed improvements in the selectivity of their artificial nose thanks to the temporal retention of VOCs. Later on, the same team [132,154] used a combination of three chemosensor arrays, as drawn in Figure 1-9 (d). The first one provided spatial information and separated the sample between two chromatography columns. Like in MDGC, one column was coated with a polar stationary phase, and the other with a non-polar one. These columns ensured temporal separation of the samples, and conveyed them to two other sensor arrays. The system gained in ability to discriminate between complex odors thanks to spatiotemporal response. In both designs, the polymer used to mimic mucus was unrelated with real molecules present in the nose. It could be interesting to put these works in perspective with Yabuki *et al.* [155], who studied the separation of VOCs through a chromatography column coated with OBPs.

However, adding these elements (water, artificial mucus) on the chip is not without risk. A poor design could lead to a dramatic increase of the non-specific adsorption (see 2.2.2 and Figure 3-15). Woodka *et al.* [156] ingeniously designed a low volume analysis chamber combined with a low vapor flow to separate the VOCs directly by adsorption on the sensors, without adding a stationary phase and obtained very good discrimination results as well. Another option is to consider strategies to block non-sensitive surfaces beforehand.

## 1.5. TRANSDUCTION SYSTEMS

---

Once a VOC molecule finally reaches the olfactory epithelium and interacts with an OR, the olfactory neuron responds with an electrical output signal. Different transduction pathways may coexist [157,158]. One example is the adenosine 3, 5-cyclic monophosphate (cAMP) signaling (Figure 1-10 (a)). Briefly, the activation of the OR, coupled to a G protein and adenylyl cyclase results in the production of cAMP, a second messenger. cAMP opens Ca<sup>2+</sup> ion channels, creating a current, which is amplified by Ca<sup>2+</sup>-gated Cl<sup>-</sup> channels. Some cell-based olfactory sensors exploit this complex mechanism [159]. However, "industrializable" artificial noses must rely on transduction methods that are easier to manufacture, more stable over time and better controlled. Classical methods can be mechanical (QCM, microcantilever, surface acoustic wave...), electronic



(pellistor, field effect transistor (FET)...) or optical (SPR, absorbance, fluorescence...). Several reviews previously described their principle and applications [160–163]. This chapter focuses on biomimetic strategies to improve their sensitivity and selectivity.

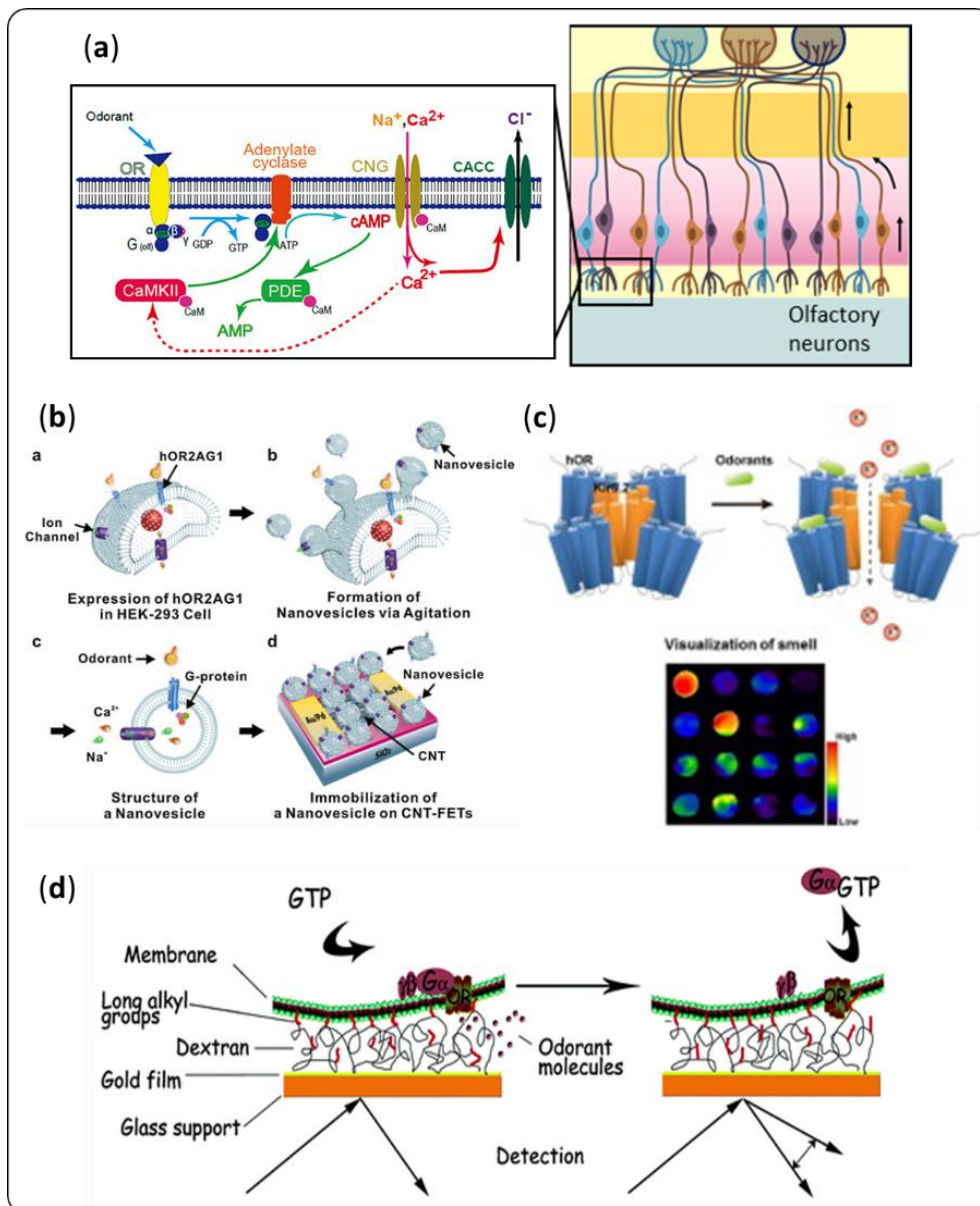


Figure 1-10 (a) The olfactory neurons are the biological transducers of the olfactory signal. On the left is a schematic representation of the cAMP signaling pathway [164]. This process inspired different designs to achieve highly sensitive detection of VOCs. (b) Jin et al. [32] integrated nanovesicles containing ORs and ion channels on field-effect transistors to enhance the potential difference caused by VOC binding. (c) Oh et al. [165] designed ion channel-coupled ORs for fundamental research purpose that could be integrated in biosensors. (d) The design proposed by Vidic et al. [31] used the desorption of the G protein upon VOC binding to enhance an SPR signal.

### 1.5.1. Bioinspired amplification and transduction

The binding of a VOC molecule to a sensor causes a very weak raw electrical, mechanical or optical variation, and so it is interesting to consider adding an amplification system to the design. This is where olfactory neurons come into play as sources of inspiration [166].

It is possible to enhance the measurable potential difference due to the recognition of a VOC molecule by an OR using ion channels, just like in the biological nose. Jin *et al.* [32] immobilized nanovesicles containing both ORs and ion-channels on a field-effect transistor (Figure 1-10 (b)). They obtained a sensitivity two orders of magnitude higher than that of a similar bioelectronic nose without calcium ion channels. Oh *et al.* [165] coupled human ORs with an ion-channel to monitor the binding of odorant with a membrane potential dye (Figure 1-10 (c)). This technique was developed for more fundamental research purposes, but these ion-channel coupled receptors could be used in biosensors.

As far as optical transducers are concerned, when binding an odorant, some proteins can undergo a change in their optical properties that can act as an amplifier. As a first example, OBPs conformation can change [167,168]. This event can lead to a variation in their refractive index [169], which Hurot *et al.* [49] exploited to amplify an SPR signal. Secondly, tryptophan and tyrosine fluoresce when excited at a correct wavelength. This phenomenon can quench in the close vicinity of a VOC. Thus, if one of those residues is located in the binding pocket of a receptor, it can act as a binding reporter. It is the case for most natural insect OBPs [48]. Based on this principle, Wei *et al.* [170] designed a specific mutant of porcine OBP adding a tryptophan residue in its binding pocket. This engineered protein could be used in a biosensor, using direct fluorescence measurements. Returning to the primary inspiration of olfactory neurons, Vidic *et al.* [31] co-expressed an OR and a G protein in a yeast, and used some membrane extract on an SPR sensor (Figure 1-10 (d)). When an odorant binds to the receptor, the G subunit is desorbed, leading to a much bigger change in refractive index. In 2008, the same team immobilized ORs-containing nanosomes on an SPR chip. Those receptors bound specifically a kind of OBP. Upon injection of the receptor preferential VOC, the OBPs were released, providing the same amplification effect on the SPR signal [171].

It is interesting to note that, in the two latter cases, an important variation in mass accompanied the change in optical properties. It could be adapted to mechanical transducers. It is also the case for aptamers: Andrianova *et al.* [172] designed an aptamer, which releases its complementary DNA strand during VOC binding. They used an ion sensitive field effect transistor as a transducer, but similar probes could also be interesting for amplifying optical or mechanical detection.

### **1.5.2. Multiplexing for large arrays of sensors**

However, designing the best transducers is not enough to optimize the sensitivity and selectivity of an artificial nose. To mimic the function of the biological nose, it is necessary to multiplex them in order to obtain the largest possible array of sensors, in term of both variety and number of sensors [173]. Indeed, humans express about 400 different types of functional ORs

[21]. One olfactory neuron carries about one million replicates of the same kind, with the olfactory epithelium being composed of 10 million olfactory neurons. This layout has several advantages. First, the variety of binding properties among the ORs increases the range of perceptible VOCs. Second, a greater number of chemical "pixels" allows a finer pattern and therefore better identification of these compounds. Third, a large number of replicates increases drastically the signal to noise ratio while smoothing out signals from defective receptors. Finally, it allows taking full advantage of the spatial and temporal separation permitted by an artificial mucus or a fluidic chamber (see 1.4). This last point also requires a transduction method that provides kinetic signals.

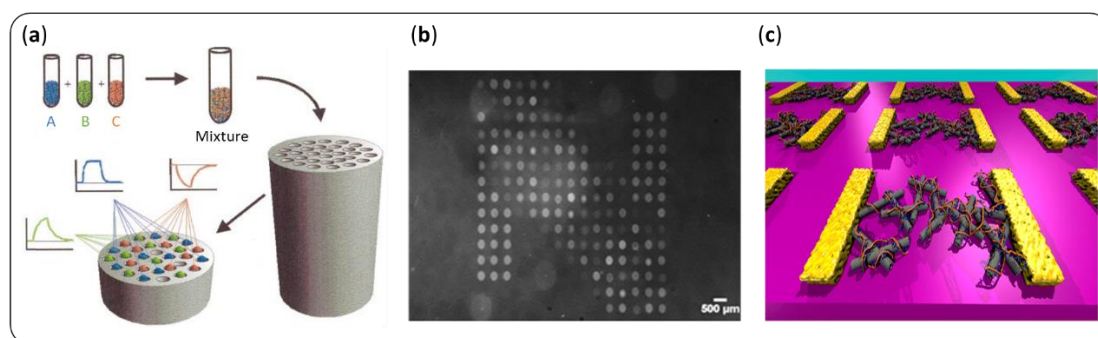


Figure 1-11 Multiplexing the sensors is key to achieve high sensitivity and selectivity of an artificial nose. (a) Dickinson et al. [174] proposed a fiber optic bead sensor array. (b) Brenet et al. [175] constructed a microarray and used SPRi for VOC sensing in the gas phase. (c) Kybert et al. [75] integrated numerous graphene FETs on a small chip.

Concerning the choice of a transduction method, care must be taken to ensure that it does not induce interference and distortion between signals from different sensors [176]. In this respect, optical transduction methods are particularly suitable for the development of sensitive and reliable artificial noses. Moreover, contrary to multiplexed electronic transducers or mechanical resonators, some of them offer the possibility of versatile, small scale and repeatable functionalization with biomolecules. For instance, since 1999, Walt group [174] developed a fiber optic bead-based sensor with thousands of microspheres in a very easy to produce way (Figure 1-11 (a)). These sensors provide spectral and temporal responses and are suitable for on-site analysis. A review for all other microbeads sensors is available [177]. Our group [175] used SPRi to monitor simultaneously 4 replicates of 18 different sensing materials deposited in a microarray format (Figure 1-11 (b)). A spotting robot achieved the functionalization of the sensing surface simply, via thiol chemistry. Again, this transduction method provides a label-free, kinetic response. Even more simple, colorimetric and fluorometric sensors are gaining attention [15].

Multiplexing electrical transducers may be more complex, especially for wiring reasons, and because the resulting sensors will be independent from each other, making their comparison less straightforward. Nevertheless, nanotechnology is a key ally to design highly sensitive olfactory sensors [178,179]. Indeed, nanoscale materials combine their high conductivity with a high

surface-to-volume ratio, which allows the dense functionalization of their surface with biomolecules (see 1.3.2). As a result, the most sensitive olfactory sensors developed to date relied on an electronic transduction, and measured a change in current, conductivity, or electric potential in a biomolecule upon the binding of a VOC. Moreover, nanofabrication holds out hope for progress in scalability. For instance, Kybert *et al.* [76] developed a photolithography method to integrate 112 graphene-based FETs with good performances on a single chip with the size of a coin (Figure 1-11 (c)). It is then easy to graft biomolecules onto graphene by means of  $\pi$ - $\pi$  stacking. In this paper, DNA strands permitted the selective detection of VOCs in vapor. For the record, Larisika *et al.* [122] attached OBPs on the same kind of device, for the detection of VOCs in solution. Carbon nanotubes are commonly used for the development of olfactory sensors with an enhanced sensitivity [180]. They were notably decorated with olfactory receptors [37] or specific peptides [68,129]. On top of that, the development of micro-fabrication techniques made these sensors more scalable [181]. As a final example, Gao *et al.* [182] designed a highly sensitive olfactory sensor with silicon nanowires conjugated with OBPs. Its fabrication relied on a top-down approach, which is much cheaper and easier to implement in a large scale than the classical bottom-up strategy.

## 1.6. DATA PROCESSING

---

The interaction of a sample with all the sensors of a large array will give a vector of high dimension that we will call “signature”. The aim is then to identify the sample from its signature. First of all, the signatures of a large number of known samples are collected in a database and used for the training phase. Later on, when an unknown sample is analyzed, its signature is compared with the database to identify it. Multidimensional analysis methods are particularly suited to large data, above all when the difference between samples can be subtle. These methods reduce the number of dimensions to be observed in a way to represent the variability of the data at best. Principal component analysis (PCA) and linear discriminant analysis (LDA) are classically used. Several reviews [183,184] provided a detailed description of the classical pattern recognition methods implemented in artificial olfaction. Here, we focus on the biomimetic data processing strategies used to improve the sensitivity and selectivity of artificial noses [173,185,186]. Most of the work presented below was performed on MOS or conductive polymer artificial noses, but the same computing principles could be used for bioelectronic systems.

### 1.6.1. A model of neurons: toward spike-based neuromorphic approaches

As the front-end of the olfactory pathway, olfactory neurons use time as a dimension for coding [187]. Odor information is transmitted to the higher brain areas in the form of spike trains. The firing rate of olfactory neurons and the variations of this feature encode part of the

information about the nature of an odor. Similarly, the temporal component of the signals given by the transducer of an artificial nose conveys additional information that is useful for improving its performance [109]. For instance, during her PhD thesis in our group, Sophie Brenet [175] improved greatly the classification of alcohols and carboxylic acids by integrating kinetic descriptors in PCA and hierarchical clustering on principal components. Nevertheless, adding features to the data processing increases the dimensionality of the problem and can lengthen the recognition time.

Concerning the detection time, it is possible to identify VOCs with a good accuracy using only transient information. Several approaches were considered for arrays of MOS [188,189]. Interestingly, Luo *et al.* [190] proposed a gradient tree-boosting algorithm that only needed the first 6 seconds of the raw signals to achieve the classification of six gases. This solution is interesting, since it does not require feature extraction from the data. Rodriguez *et al.* [191] achieved a similar result with a deep multilayer perceptron neural network to identify wine spoilage in less than three seconds. Munoz-Mata *et al.* [192] held the same reasoning with QCM sensors.

To tackle the high dimensionality, it is crucial to select the optimal set of features to cover most of the information. Calculating the correlation between them is a classical method to do so [193,194]. Perera *et al.* [195] chose a bioinspired technique, which allowed a robust classification, even with a small number of samples. Clusters (signals) from different features (OR types) converged to feature groups (glomeruli), and this redundancy enabled noise reduction and VOC discrimination. This feature selection can also be interesting to get rid of the drift or defective sensors [196,197]. Remarkably, Magna *et al.* [198] also developed a self-repairing algorithm dedicated to this purpose.

Besides, the reduction of dimensionality itself leads to expensive and power-consuming data processing. The requirement for large computing devices limits the portability of the devices. This leads us to neuromorphic methods, which take the comparison with the functioning of neurons one-step further and code only the necessary information in the form of spikes [185,199]. They combine the advantage of requiring low power, simplifying the data processing, and enabling learning algorithm, as we will see in the next part.

### **1.6.2. Artificial neural networks and hardware models of olfactory bulb**

In the biological nose of mammalian, several layers of neurons are involved in the processing of the signal [200,201]. All the olfactory neurons carrying the same type of olfactory receptors converge on the same spatial area called the glomerulus, where they synapse with mitral cells. Then, mitral cells will send the averaged signal through their axons to the olfactory cortex. The

dendrites of mitral cells contact granule cells, which by some theories produces lateral inhibition between mitral cells (Figure 1-12 (a)). The function of the olfactory bulb is crucial to take advantage of large sensor arrays (see 1.5.2). A very similar structure evolved in insects, called antennal lobe, where projection neurons are the equivalent of mitral cells [202]. Logically, most of the solutions considered for artificially reproducing these structures relied on artificial neural networks [185].

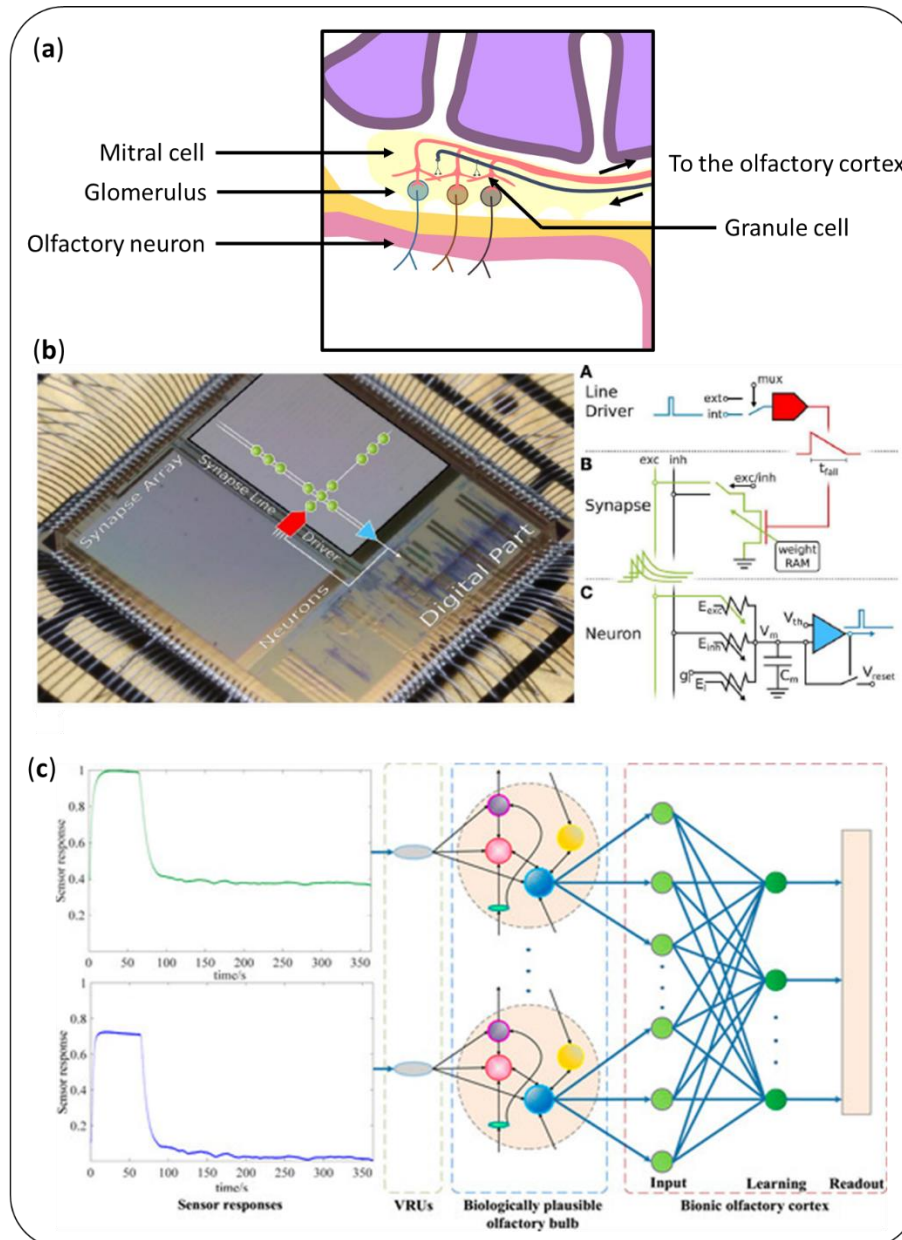


Figure 1-12 (a) Several layers of cells are involved in the biological processing of odor signals. To reproduce their functions, (b) Pfeil et al. [203] proposed a hardware model of the olfactory bulb. (c) Liu et al. [204] coupled a computational model of the olfactory bulb with one of the olfactory cortex.

Initially, several teams carried out computer simulations of the architecture of the olfactory bulb [205–207]. Notably, Martinelli *et al.* [208] described an original work with a colorimetric sensor. With a single layer of spiking neurons, they showed that the latency enables quick

discrimination of VOCs. Jing *et al.* [209] developed a neural network that mimicked olfactory neurons, mitral cells and granule cells to classify raw data from an artificial nose with a 93% accuracy.

Interestingly, spike-based neuromorphic approaches are compatible with analog data processing, and so with hardware implementation. Koickal *et al.* [210] demonstrated the first example of a hardware model of olfactory bulb to process spike signal coming from an olfactory sensor. They implemented a time-dependent learning circuit, which adapted the weights of the model in a dynamic fashion. Besides lowering the power consumption of the data processing unit, it enabled to get rid of the variations between the different MOS sensors. This was further improved by including onset latency for a better classification [211]. Pfeil *et al.* [203] introduced supervised learning based on reward-depending plasticity with an accuracy ranging from 87% to 96% (Figure 1-12(b)). Recently, Vanarse *et al.* [212] deployed a spiking neural network hardware with a 96.5% accuracy in the identification of target gases.

### **1.6.3. Feedback inhibitory loops and learning algorithms taking inspiration from the cortex**

In the mammalian nose though, the olfactory bulb is only a “secondary transduction” which acts as a signal-conditioning step. The olfactory cortex performs the identification of the odor [201]. Similarly, in insects, the higher brain centers include the mushroom body and the lateral protocerebrum.

Ratton *et al.* [213] were the first to use a simulation integrating both an olfactory bulb and an olfactory cortex connected by a feedback loop. This model analyses a VOC in a hierarchical fashion. This can be very interesting when it comes to analyzing unknown samples. Still, its linearity resulted in a poor success rate. Subsequently, different teams focused on making their solution suitable for real-world applications. The NEUROCHEM project [214] proposed a very large-scale sensor array (65,536 elements) using conducting polymers. The European universities involved in this project explored different neuromorphic algorithms implemented in a platform suitable for robotic integration. Diamond *et al.* [215] proposed a model of the insect antennal lobe, able to process noisy signals in real time. Recently, Borthakur *et al.* [216] utilized an external plexiform layer to enable online training without risk of forgetting and integrating a confidence indicator. The Figure 1-12 (c) shows the design of Liu *et al.* [204], who used squared cosine receptive fields to improve the classification performance.

The olfactory cortex is also very useful for the habituation capacity of the nose, through its inhibitory feedback. Granule cells could indeed act as a feedback loop between it and the mitral cells. The solution proposed by Li and Hertz [217] intended to mimic the habituation of the biological nose. In particular, the aim was to identify a variation in a mixture over time. Guttierrez-

Osuna *et al.* proposed several other algorithms in his wake, one of them based on the KIII model of the cortex, which is more biologically plausible [218,219].

## 1.7. POSITIONING OF THE THESIS PROJECT

---

Artificial noses developed to date are not yet as sensitive and selective as the biological nose. However, such performances are desirable to address biomedical, industrial or public safety applications. It is the multi-scale and systemic organization of the biological nose that allows it to reach detection limits in the order of ppt and to distinguish several hundred thousand odors. This includes special binding properties of olfactory receptors, the appropriate structuring of the olfactory epithelium, relevant perireceptor events, the unique functioning of neurons and the different neuronal layers involved in data processing. To improve the performances of the artificial noses, it is therefore relevant to draw inspiration from all these elements in order to propose ingenious biomimetic solutions, as summarized in this first chapter.

Our laboratory has been working on the development of an optoelectronic nose based on SPRi since 2012. This strategy has proven successful enough to distinguish molecules from different chemical families [175]. Nevertheless, like most of the artificial noses developed to date, it lacked sensitivity and chemical resolution for VOCs with similar structures. In this context, this project addressed most of the points evoked in the literature and listed in this first chapter to improve the performance of our optoelectronic nose.

Primarily, several strategies were implemented for the development of more selective sensing materials, either by using biological proteins or by screening novel probes *in vitro* or *in silico*. In order to exploit the full potential of these new sensing materials, particular care was taken in their immobilization on the sensor surface, which allowed a higher sensitivity and selectivity. Indeed, the structuration of the probes, their density and their appropriate orientation were essential. Besides, the biomolecules under consideration were more delicate. Different technical solutions for their efficient immobilization on the sensor and their regeneration were therefore envisaged to lengthen the lifetime of the device. In addition, not to be overlooked was the importance of VOC sampling in terms of fluid dynamics and hydration. Finally, as far as data transduction and processing was concerned, we worked with large arrays of sensors, which generated a large amount of data. As a result, we had to implement statistical methods to assess the performance of our device, in terms of sensitivity and selectivity. The next chapter will explain in details all these points.





## CHAPTER 2

An optoelectronic nose for the detection of volatile organic compounds in the gas phase



## Résumé du chapitre 2 - Un nez optoélectronique pour la détection de composés organiques volatils en phase gazeuse

L'équipe CREAB du laboratoire SyMMES (UMR 5819 CEA-CNRS-UGA, Grenoble, France) développe depuis 2012 un nez optoélectronique pour la détection de composés organiques volatils (COV) en phase gazeuse. Dans le système initial, des matériaux sensibles à base de peptides courts ou de molécules organiques simples sont responsables de la reconnaissance des COV. Ils sont immobilisés sur le prisme par auto-assemblage sous forme de réseau. Cette étape est réalisée par un robot de micro dépôt, ce qui permet d'obtenir une grande densité de matériaux sensibles (300 plots sur 64 mm<sup>2</sup>). Le prisme est ensuite monté dans une chambre d'analyse connectée à un circuit fluide. Ce circuit génère les échantillons de COV et les achemine jusqu'à la chambre d'analyse dans de l'air sec, de manière contrôlée et reproductible. Ces échantillons sont ensuite analysés par imagerie par résonance de plasmons de surface. Cette méthode de transduction permet le suivi cinétique en temps réel de l'interaction du COV avec les différents matériaux sensibles. Les signaux issus de l'ensemble de ces interactions forment la signature de l'échantillon. Elle est analysée, soit individuellement, soit statistiquement par analyse en composantes principales (ACP) pour finalement identifier l'échantillon.

Ce chapitre décrit en détail la construction de ce nez optoélectronique et son fonctionnement. Ce système a démontré de bonnes performances de détection lors de travaux précédents. Cependant, pour des molécules de structures très proches, il manque parfois de sensibilité et de sélectivité. Cette thèse vise à pallier à ces limitations.

Pour cela, de nouveaux matériaux sensibles biomimétiques ont été développés et testés. Les stratégies mises en œuvre feront l'objet des chapitres suivants. Les deux types de matériaux utilisés sont d'une part des protéines liant les odorants (OBP), et d'autre part des peptides dont la séquence a été rationalisée pour augmenter leur sensibilité à un COV ou une famille de COV cible. Dans les deux cas, leur sensibilité et leur sélectivité vis-à-vis des odorants nécessitent des conditions de fonctionnement optimisées. Dans ce cadre, plusieurs modifications ont été apportées au banc de mesure initial. Ces modifications, détaillées dans ce chapitre, concernent le dépôt des matériaux sensibles sur les puces, l'introduction contrôlée d'humidité dans le système fluide, et la dilution des COV.



## CHAPTER 2 An optoelectronic nose for the detection of volatile organic compounds in the gas phase

This PhD thesis was carried out in SyMMES laboratory (UMR 5819, Grenoble, France). It is a joint research unit between Grenoble Alps University, the French National Center for Scientific Research (CNRS) and the French Alternative Energies and Atomic Energy Commission (CEA). The CREAB team from SyMMES focuses on the development of: 1) bio-inspired and bio-hybrid architectures using biopolymers like DNA and its analogues, DNA origamis, *etc.*, 2) biosensors and biochips for the analysis of interactions from the molecular scale up to more complex biological objects (cells, bacteria, *etc.*). In particular, the team has extensive expertise in surface chemistry and surface plasmon resonance imaging (SPRi). In the last decade, CREAB launched a new research theme to develop artificial tongues and noses.

In this context, our project started in 2008 with the design of an optoelectronic tongue to analyze proteins and complex mixtures in the liquid phase based on SPRi [109–112]. Since 2012, the laboratory has been working on the development of an optoelectronic nose, to detect VOCs in the gas phase, based on the same working principle. It is noteworthy that, for the first time, we have demonstrated that SPRi was very efficient for such application. Briefly, the chips are glass prisms coated with a thin gold film, on which an array of various sensing materials is deposited. When a VOC interacts with these sensing materials, the resulting changes in their local refractive index are simultaneously monitored in real time, thanks to SPRi. The pattern signals resulting from the interaction between the VOC and all the sensing materials generates a “signature” of the odorant compound. Eventually, a pattern recognition analysis enables its identification. In this chapter, we will detail the design of this optoelectronic nose, as well as its operating principle.

In the past years, several patents have been filed on this device [220–223]. Furthermore, thanks to the originality and great potential of our work, the startup Aryballe technologies was founded in 2014 based on a licensed patent. Since then, this company is working on the miniaturization and commercialization of the optoelectronic nose. A compact industrial device, the NeOse Pro, is commercialized by the company, which will be used in this project (Figure 2-1).



Figure 2-1 The NeOse Pro from Aryballe [224].

## 2.1. SENSING MATERIALS

### 2.1.1. Historical probes

As explained in the first chapter, the sensing materials are responsible for the chemical recognition of a VOC. They are the first brick for the construction of an artificial nose system.

The development of high-performance sensing materials is the core of this thesis project. First of all, the vocabulary to be used needs to be clarified. The Figure 2-2 backs these definitions. We will use the term "probe" to refer to a single sensing molecule, which will interact with the VOC molecules and constitute the sensing material. It can be for example a peptide or a protein. The "sensing material" is the thin layer of these probes after immobilization on the sensor surface, sometimes mixed with one or more other molecules for reasons of hydration, dilution or passivation, as we will see later. A "biosensor" or "olfactory biosensor" is the single system composed of a given sensing material and the transducer, here SPRi. Finally, the "artificial tongue" or "artificial nose" is the whole device, including all the olfactory biosensors for the detection of VOCs in the liquid or in the gas phase, respectively.

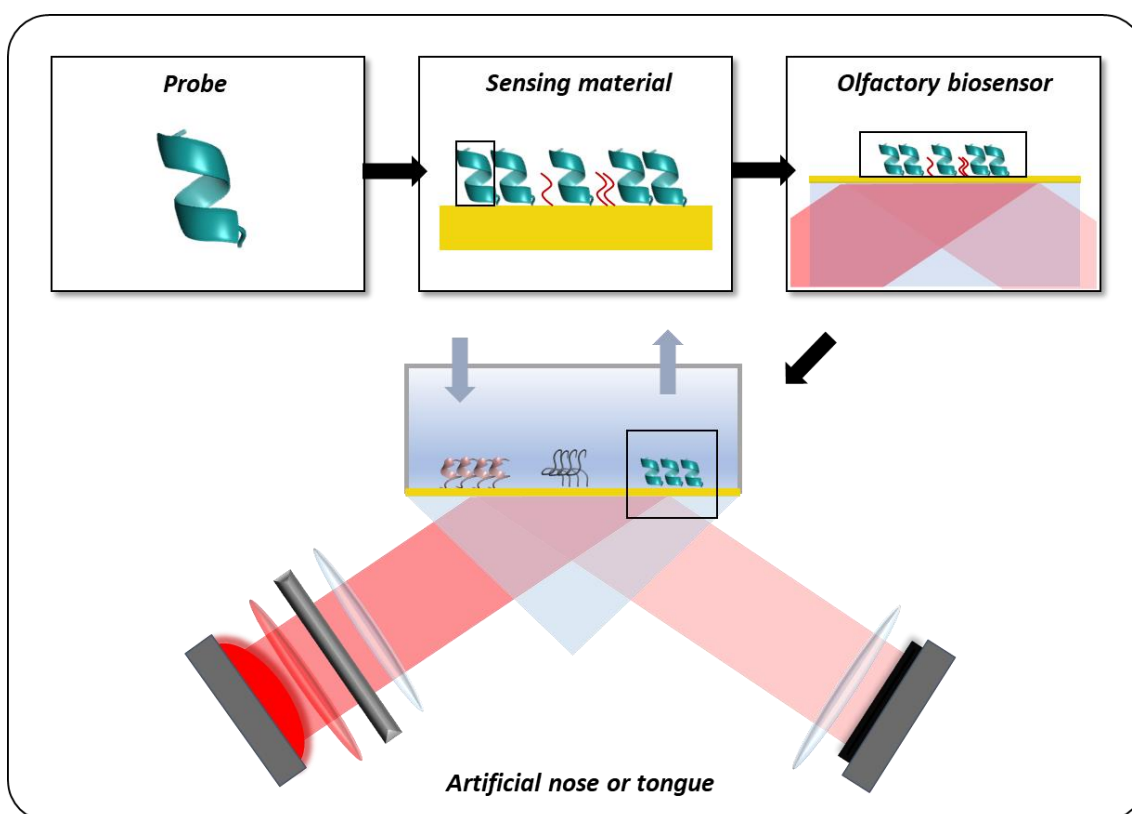


Figure 2-2 Graphical definition of the terms "probe", "sensing material", "olfactory biosensor" and "artificial nose" or "artificial tongue" used in this thesis project.

Several criteria are determining for the choice of sensing materials. They include the diversity of probes to enable the design of a large array of sensors with a wide detection spectrum, their structuration for a better sensitivity and selectivity, their robustness when immobilized on the

sensor surface to ensure a long lifetime and a resistance to environmental changes, and their cost that is usually linked to the production difficulties, *etc.*

Peptides meet most of the above criteria. These biopolymers are the basic components of proteins, and consist of a short sequences of amino acids linked together by peptide bonds [225]. There are 20 natural amino acids with various physicochemical properties (Figure 2-3). For example, with only six variable amino acids,  $6.4 \times 10^7$  sequences are possible. Peptides can exhibit a secondary structure, essentially  $\alpha$ -helices. A short, structured peptide can show high affinity for a target [105]. They are much more robust than whole proteins, thanks to their smaller size, and can be dried. On top of that, they are easy to produce synthetically, for example using the solid phase peptide synthesis (SPPS) method [226], which makes them relatively inexpensive.

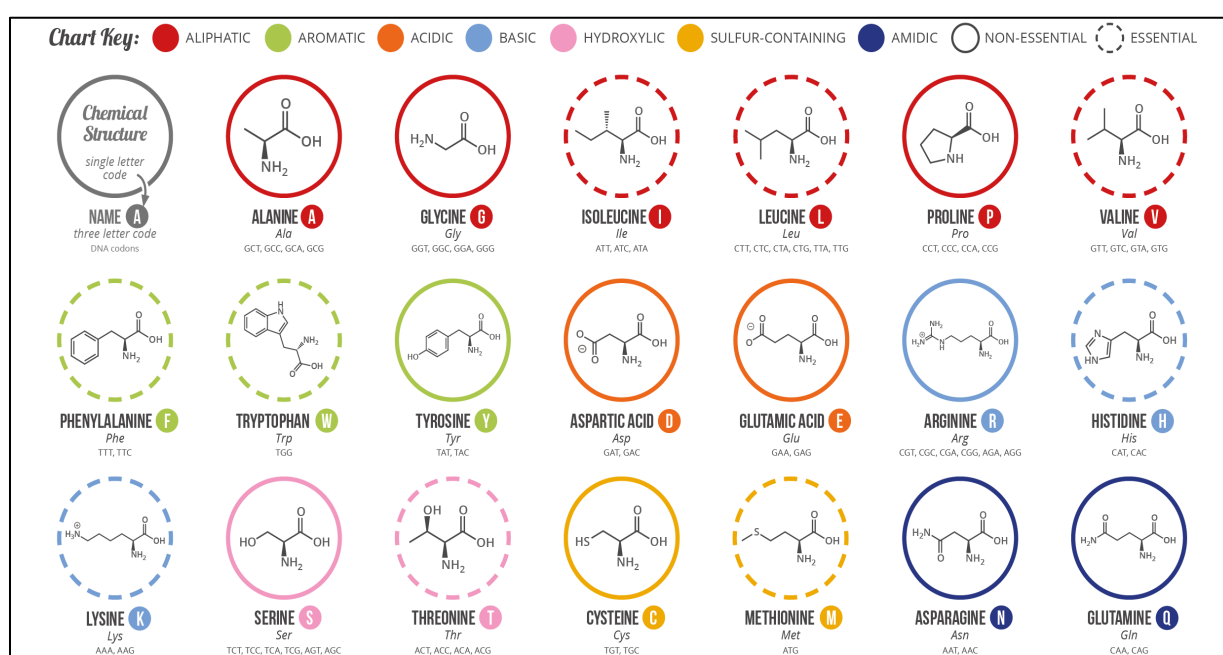


Figure 2-3 Chemical structure of the twenty common amino acids [227]

For all these reasons, our team historically chose to work with a variety of short peptides (8 amino acids) and organic molecules (<550 g.mol<sup>-1</sup>) (Figure 2-5 (a) and (b)). All these probes comprised three parts: a terminal group for their immobilization (thiol for organic molecules and cysteine in the case of peptides), a flexible and short linker, and a variable sensing part. The thiol anchor enables a one-step immobilization of all the probes on the chip, as we will see in 2.2. Basically, one sensing material is the result of the self-assembly of one of these probes on the sensor surface. Since all the probes have similar molecular weights, it is possible to achieve SPRI measurement at a fixed angle while working in the linear zone of all the sensing materials (see 2.4).

At the beginning of this thesis project, the existing 27 probes were quite simple. Their sequence was not rationalized for a particular application. Rather, the idea was to have non-



specific interactions and the widest possible detection spectrum. Identification of VOCs was possible by cross-reactivity. This strategy has proven successful enough to distinguish molecules from different chemical families [175]. Nevertheless, in some cases, it lacked chemical resolution for VOCs with similar structures. For instance, with our existing laboratory setup, it was impossible to distinguish between the three xylenes (Figure 2-4).

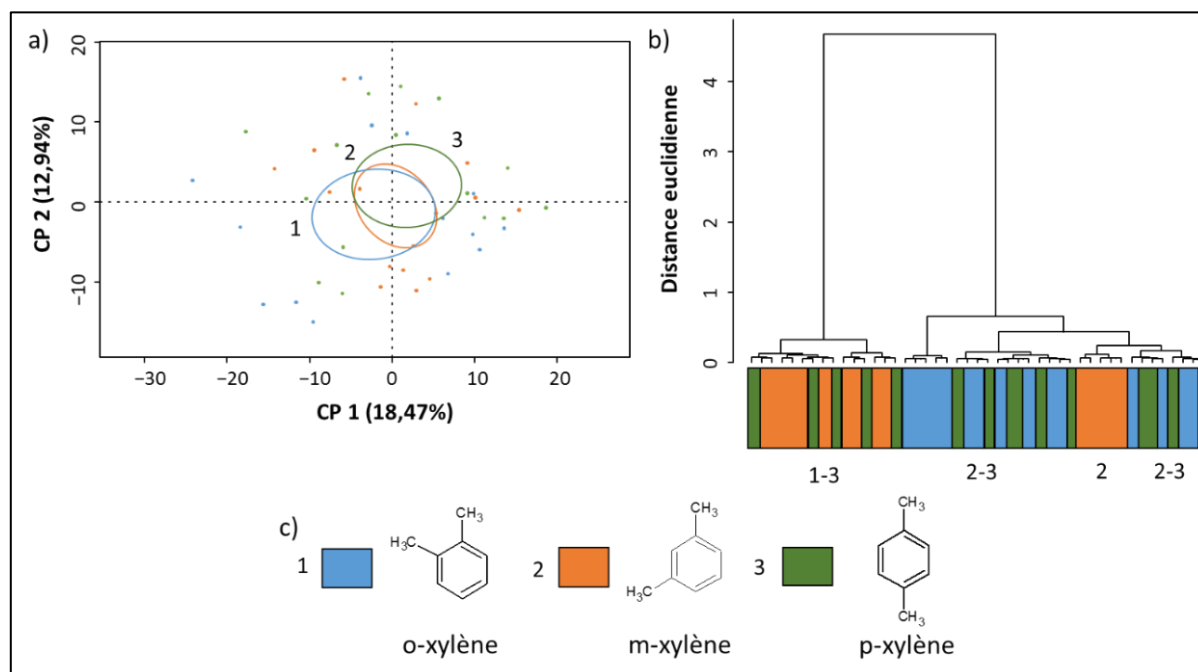


Figure 2-4 a) Analysis of 45 samples of *o*-xylene, *m*-xylene, and *p*-xylene. b) Hierarchical clustering on the same data. Both show that no discrimination was possible. c) Chemical formula of these molecules. [228]

### 2.1.2. New probes developed in this project

In this context, the main objective of my thesis was to set up different strategies to develop novel sensors with improved performance dedicated to a given application. That is to say with an exacerbated sensitivity and selectivity for a VOC or a family of target VOCs. As in the human nose, these new sensing materials might be combined with the existing materials in order to maintain a broad detection spectrum.

On the one hand, to facilitate this association, the new sensing materials we will examine must have some similarities and good compatibility with the previous ones. Firstly, the surface chemistry for grafting them to the sensor must be the same, so that the previously optimized one-step protocol can be maintained. Secondly, their chemical nature and molecular weight must be comparable to that of the original materials, to be able to work with the same transduction system. This point will be detailed later. On the other hand, as mentioned in the first chapter, to increase the selectivity of the probes, their arrangement and structuration upon immobilization on the sensor surface is crucial.

In this thesis, the adopted solution was therefore to look for longer peptides that can have structures slightly more complex than a single  $\alpha$ -helix (Figure 2-5), or even for more complex biomolecules such as whole proteins. Adding a cysteine to the end of the selected sequences will preserve the thiol chemistry and promote the orientation of these probes. The original spacer will also be maintained to preserve flexibility and accessibility. Then we aim to be able to tailor the binding properties of these new probes for a given application. For this purpose, several strategies will be implemented to rationalize their amino acid sequence for a better selectivity for target VOCs. Each will be discussed in a separate chapter.

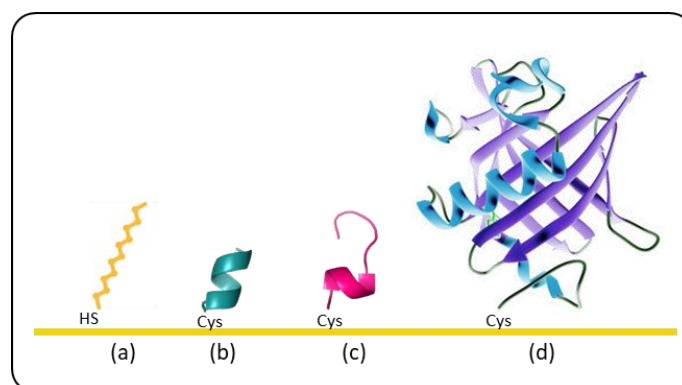


Figure 2-5 Structural models of the probes used for the development of sensing materials in our laboratory a) organic molecule, b) short peptide, c) longer and more structured peptide, and d) mammalian odorant binding protein. Among them, a) and b) were designed in the previous work; c) and d) are explored in this thesis.

We explored in chapter 4 the possibility of incorporating odorant binding proteins (Figure 2-5 (d)) into our artificial nose. The small size of these proteins (17 kDa), their solubility, thus ease of production and handling, as well as the possibility of tuning their binding properties made them ideal candidates.

As for more structured peptides, two different strategies were proposed. In chapter 5, we used the phage display technique to screen new peptides with a high affinity for the phenyl ring. In chapter 6, we tested peptides selected *in silico* for their affinity for certain chemical families of VOCs.

However, these new materials are more fragile than the original ones and require more careful handling and a favorable environment. Especially because their selectivity performance is intimately linked to their structure. Therefore, it will be necessary to first optimize the protocol and the experimental set-up, which is the subject of the rest of this chapter.

## 2.2. IMMOBILIZATION OF PROBES

### 2.2.1. Preparation of chips by spotting an array of sensing materials

The immobilization method developed in the laboratory aims at fabricating large arrays of olfactory sensor in a simple and reproducible manner. As explained in the previous part, all the

probes used in this project possess a thiol function at one end, which enables their fixation on a gold surface via self-assembly, to form a dense thin layer. Organic molecules, peptides or OBPs were deposited on the gold-coated base of a prism to be used for SPRi detection.

To work in reproducible conditions, gold surfaces were priority cleaned with a Femto plasma cleaner (Diener Electronic, Germany) for 3 minutes using these parameters: 75% oxygen, 25% argon, 0.6 mbar, 80 W. This removed oxides and organic contamination from the surface. However, it made the surface too hydrophilic to spot localized droplets of probes, as our protocol requires. For this reason, a waiting time of 48h was then necessary before spotting an array of sensing materials.

A non-contact spotting robot sciFLEXARRAYER (Sciencion, Berlin, Germany) was used to fabricate the microarray (Figure 2-6). This robot ejects drops of probes in a spotting buffer at a controlled volume by deformation of a piezoelectric crystal. In this way, up to 300 biosensors in total can be integrated on the same prism, for a total surface of 64 mm<sup>2</sup>. Several replicates of the same sensing material were randomly distributed on the prism to limit positional effects. The chips were left to incubate for 18 hours to allow self-assembly of the probes at controlled temperature and humidity. The unfixed probes were subsequently rinsed off the prisms, which were dried and stored at 4°C before use.

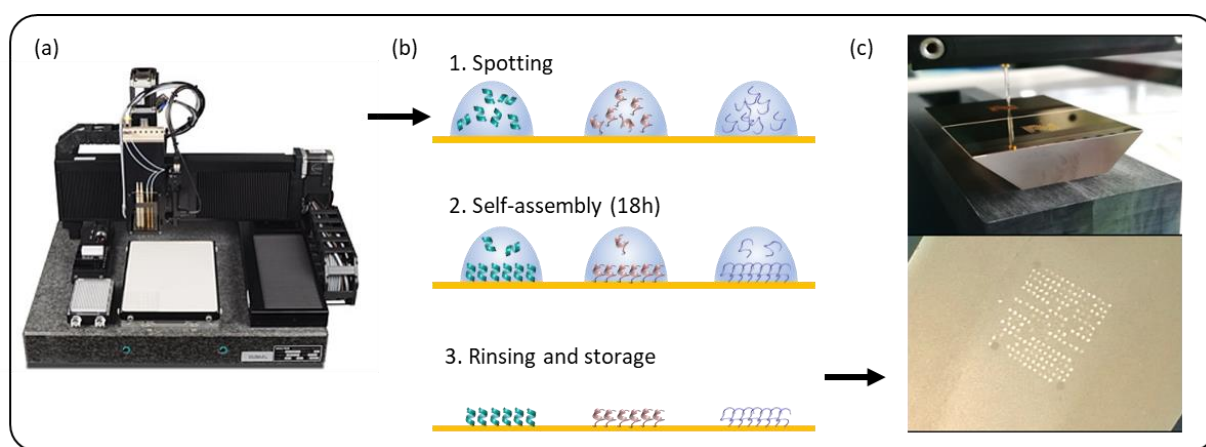


Figure 2-6 (a) The spotting robot used in this project [229] (b) Self-assembly of the probes (c) Example of a prism functionalized with a microarray of sensing materials (Credit: D. Morel/CEA).

For confidentiality reasons, the detailed protocols used to fabricate the chips are not given in the thesis. The Table 2-1 gives some of the parameters used to fabricate the chips. Very small spotting volumes were used to limit the chip's cost by saving precious sensing material. The original protocol 1 had to be adapted for the needs of this project. First of all, in order to preserve the activity of the proteins, they were spotted in an aqueous buffer with controlled pH and salinity (Protocol 3). The OBPs were handled as much as possible on ice or at low temperature to restrain

their activity and prevent their contamination by unwanted VOCs prior to the experiment. For the same reason, LC-MS grade water was used.

	Protocol 1	Protocol 2	Protocol 3
<b>Probes</b>	Short peptides and organic molecules	Peptides	OBPs
<b>Spotting buffer</b>	Optimized buffer 1 (confidential)	Optimized buffer 2 (confidential)	50 mM NaH <sub>2</sub> PO <sub>4</sub> 5% [v/v] glycerol in H <sub>2</sub> O - pH 7.5
<b>Probe concentration</b>	0.1 mM	0.1 mM	8 μM
<b>Drop volume</b>	1.2 nL	1.2 nL	6 nL
<b>Conditions of self-assembly</b>	18h – 25°C Controlled humidity	18h – 25°C	18h – 4°C Controlled humidity

Table 2-1 Functionalization protocols used in this project

Additionally, we observed that the density of peptides on the surface of the prism varied when using Protocol 1. This was notably reflected by the variations of contrast on the gold observed by SPRi, as explained in part 3.2.1 (Figure 2-7 (a)). The hypothesis that we retained to explain this observation is that the more hydrophobic and therefore less water-soluble peptides did not disperse completely in the spotting buffer that we used originally. By switching to Protocol 2, we were able to halve the contrast variations between the different sensing materials (Figure 2-7 (c)), and to obtain a clear, reproducible microarray (Figure 2-7 (b)).

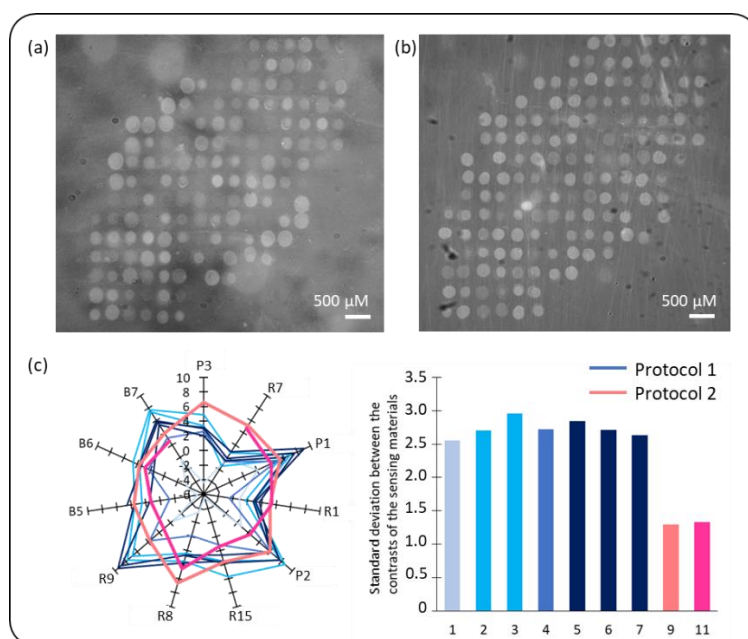


Figure 2-7 SPRi images of prisms spotted with (a) protocol 1 or (b) protocol 2. (c) Contrast of the different sensing materials on gold in percentage of reflectivity and associated standard deviation for prisms spotted with protocol 1 (blue) or protocol 2 (pink).

### 2.2.2. Drift control strategies

It is well known that all biosensors are subject to drift. This progressive and undesired deviation of the output signal originates from two main sources. First, “poisonous” compounds

can adsorb to the sensor surface in a more or less reversible manner, a phenomenon known as non-specific adsorption (see Figure 3-15). Second, the instruments used for the transduction of the signal can also have their own drift. It is thus important to control and limit this drift, and this involves working on the surface chemistry.

#### *2.2.2.1. Elaboration of a reference sensor*

Today the calibration for the noise and drift remains a main issue for the artificial nose development. Indeed, for biosensors and biochips based on key-and-lock recognition principle, usually a non-specific sensor is used for negative control. It allows determining the noise of the instrument and most importantly validating the obtained signal. In general, a signal is considered as reliable when the signal ratio between the sensor and the negative control is above three. In contrast, for cross-reactive multisensory systems such as artificial nose, each sensor interacts with VOCs with more or less affinity. Here, the signals obtained with all sensors are considered whether they are strong or weak. The combination of all these signals will generate a “signature” for the sample. Thus, so far, in all existing artificial nose systems, there is no reference sensor for negative control. It is then very difficult to determine the noise and the drift of the artificial nose for reliable analysis.

In a previous study (PhD thesis of Sophie Brenet [228]), for the first time, our laboratory has developed a reference sensor. For this, we have elaborated a patented process (FR1758547) by using special thiol molecules (perfluorothiol) which almost do not interact with most VOCs, namely inert to VOCs. The reference sensor was deposited on the chip by spotting, in the same way as for peptide sensors. With the help of this sensor as negative control, we could not only validate the signals obtained with all the cross-reactive sensors but also determine the instrumental drift.

#### *2.2.2.2. Surface background passivation*

Moreover, we have determined that the main drift source of our optoelectronic nose system was the contamination of bare gold on the chip. Indeed, the gold surface is very active and can be easily contaminated by organic compounds. Consequently, VOC molecules may not only bind onto the probes, but are also likely to adsorb on the free gold surface of the chip (Figure 2-8 (c)). This is, for instance, especially true with sulphur-containing or amine-containing VOCs. In this case, the contrast between the signals obtained with the sensing materials and with the background of the chip can be severely reduced, resulting in a loss of sensitivity, selectivity and reproducibility. In addition, if the sensing materials are not perfectly dense, the signal measured over a sensing area is not entirely attributable to the interaction between the probes and the VOC molecules (Figure 2-8 (a)), but also to the adsorption of VOC molecules on the accessible gold surface (Figure 2-8 (b)). It limits the understanding of these interactions.

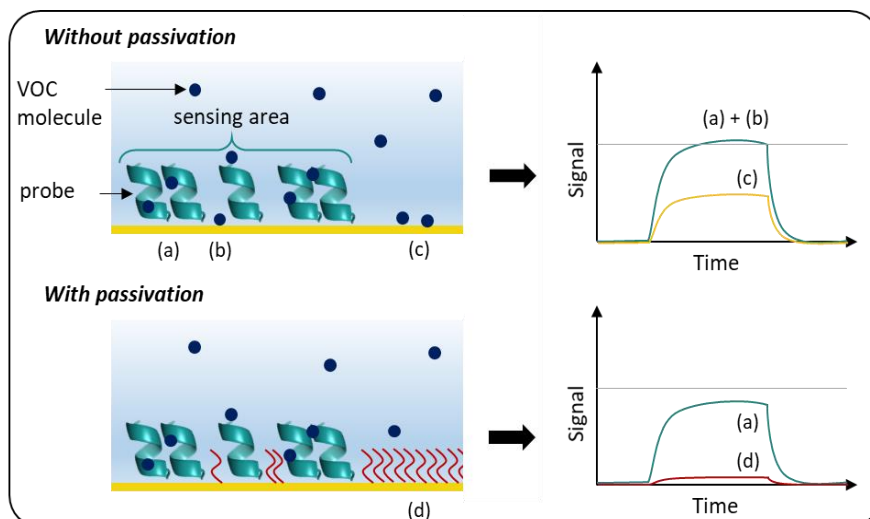


Figure 2-8 Schematic illustration of the interaction between sensing materials and VOCs and the corresponding signals. Without passivation, the desired signal due to the interaction between the probe and the VOC (a) can be altered by the adsorption of the molecules on the bare gold surface of the chip, either outside (c) or inside (b) sensitive areas. With passivation, an anti-fouling molecule (d) is used to block the surface background.

The problem of non-specific adsorption is common in the domain of biosensors, and passive and active methods exist to remedy this issue [230]. The most common strategy is to block the surface with an anti-fouling molecule. Typically, bovine serum albumin (BSA) or poly (ethylene glycol) (PEG) are often used to prevent the non-specific adhesion of proteins to the sensors. However, to the best of our knowledge, there is no mention in the literature of such coatings for artificial noses.

In this context, an innovative passivation process was developed based on surface chemistry. We blocked the bare gold surface using, again, inert perfluorothiol molecules [221]. For peptide chips, a passivation was therefore carried out after the deposition of the probes. In her PhD thesis [228], Sophie Brenet showed that the passivation reduced significantly the non-specific adsorption, as well as the chemical drift of the chip, enabling a greater repeatability, a higher signal-to-noise ratio, and an extended lifetime of the sensors.

On the contrary, OBP chips were not passivated for fear of damaging or blocking the binding sites of the proteins. It is to note that, in the perspective of this project, we will also talk about “non-specific binding”. This refers to the interaction between the OBP envelope and VOCs. In contrast, selective binding takes place in the binding pocket of the proteins. All these terms are illustrated in the following chapter in Figure 3-15.

## 2.3. SAMPLING OF VOLATILE ORGANIC COMPOUNDS

### 2.3.1. Fluidic circuit

Once the chip ready, it was placed in an analysis chamber sealed with silicon (Figure 2-9 (a)), connected to a fluidic circuit. This fluidic circuit was responsible for the generation and the

transport of VOC samples to the analysis chamber. At the beginning of this project, the existing setup was the one presented on Figure 2-9 (b). All the tubing was made of polytetrafluoroethylene (PTFE), an anti-fouling plastic. All the connectors and valves were made of stainless steel (Swagelok, France).

The sample generation was performed in dry air ( $O_2$ :  $20.9 \pm 1\%$ , 0% relative humidity (RH), Air Products, USA). The total flow was divided into two lines: the VOC line to evaporate and transport the sample, and a clean line for sample dilution and rinsing. Hence, the baseline was performed in dry air, which also served as carrier gas for sample injection. A valve mounted before the analysis chamber enabled to switch from one line to the other, or to mix them. Pressure and mass flow controllers (Bronkhorst, Netherlands) enabled to work in stable and reproducible conditions (1.05 bar, 100 mL/min). Moreover, to avoid any temperature effect, the whole analysis chamber was put in a Peltier controlled incubator at 25 °C.

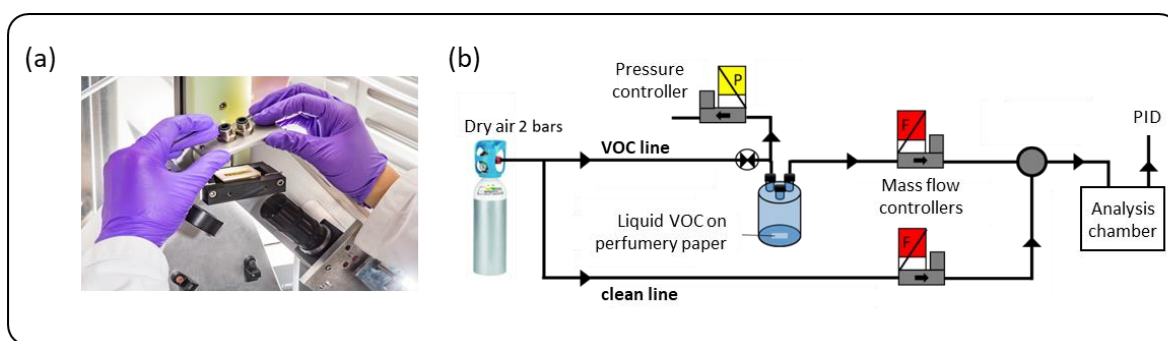


Figure 2-9 (a) The analysis chamber with air inlet and outlet (Credit: D. Morel/CEA). (b) Simplified scheme of the initial fluidic circuit [228].

A blank injection was systematically performed before any sample analysis to check that the fluidic circuit was clean. Then, a reference compound was injected before any session of experiment to ensure that the performances of the prisms were still acceptable, and that the setup was correct.

To perform a sample injection, 50  $\mu$ L of pure VOC in liquid form was deposited on perfumery paper in a three-neck glass flask. The airflow passing through this flask evaporated the sample and conveyed it to the analysis chamber. The concentration of the VOC could be modified by mixing the VOC line and the clean line, and adjusting their respective flows. In this way, the concentration could be divided by approximately up to one order of magnitude. It was precisely measured at the end of the line using a photo-ionization detector (PID), (ppbRAE300, RAE Systems, USA). A typical injection lasted about 10 minutes. Then, the valve was switched, and a flow of clean air regenerated the prism, until the PID measured 0 ppb at the output of the analysis chamber. A clean flask replaced the used one for the next sample injection.

### 2.3.1. Precise dilution of VOCs

As we will see in chapter 3, the estimation of the sensitivity and selectivity of our artificial nose requires making wide and accurate dilution ranges of VOCs. In this respect, the existing bench was not precise enough and we made the following adjustments.

We installed a computerized calibration system (CGM 2000, Umwelttechnik MCZ GmbH, Germany) that enables the dilution and the release of a span gas in dry air. This system also works with two mass flow controllers enabling to adjust the relative flows of a clean line and a span gas line, with a greater precision. The span gas line is connected to a bottle of gaseous VOC at a known concentration in dry air (Air Products, USA). The precision controllers enable a range of dilution with an accuracy of  $\pm 1\%$ . Naturally, the resulting VOC concentration depends on the concentration of the span gas in the bottle. For instance, with a bottle of butanol at 5 ppm, we could reach concentrations ranging from 0.1 ppb to 2.5 ppm. This system controlled by a computer offers the possibility to program jumps of concentration.

In parallel, we took inspiration from a process used in the industry [231]. The liquid VOCs were diluted in mineral oil before their introduction in the evaporation flask. In Figure 2-10 (a), we can see that mineral oil alone does not give any signal by SPRi. In Figure 2-10 (b), we see that there is a good linearity between the dilution ratio by volume of a liquid VOC in mineral oil and the final concentration that reach the analysis chamber, measured with the PID in part per billion (ppb). This method is very easy to put in place. Its only limitation is the solubility of the different VOCs in mineral oil.

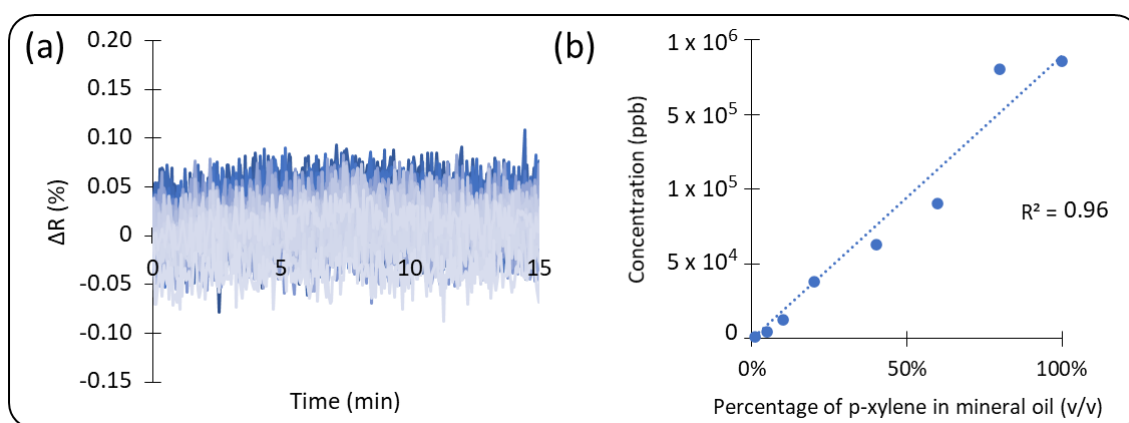


Figure 2-10 (a) Variation of reflectivity measured for all the sensing materials upon the injection of mineral oil. (b) Example of correspondence between the VOC concentrations measured with the PID and the dilution percentages in mineral oil.

### 2.3.2. Humidity control

In the light of our preliminary experiments and the literature, it became increasingly clear that a certain level of humidity was essential to maintain the high affinity that some probes have



for VOCs [48,143]. Indeed, this affinity, especially for proteins, depends largely on the structure of the probes and their ability to make hydrogen bonds. The use of dry air as carrier gas was therefore no longer suited to our needs and the bench had to be adapted accordingly. However, the introduction of humidity had to be done in a well-controlled manner since water has a high impact on the SPRi signal. First, the humidity reaching the prism had to be highly stable in time to avoid drift. Second, the humidity in the clean line and in the VOC line had to be the same, so that the baseline corresponded to humid air and the signal measured during injections was only due to the interaction between the VOC and the probes.

Great effort was made during this PhD to optimize the new fluidic circuit, as depicted on Figure 2-11. To meet the specifications, a “humidity stage” (boxed in yellow), was added before the existing gas bench (in blue). To reach the desired humidity level, two lines were mixed with different relative flows. The “dry line” with air coming straight from the source, and the “wet line”, which passed through a water bubbler beforehand (custom-made, Swagelok, France). A pressure controller was also added after this humidity stage, with a command pressure of 1.5 bar to prevent backflow. A humidity sensor (HumidIcon HIH6100, Honeywell, USA) in the analysis chamber enabled the measurement of the exact relative humidity (RH), as well as the precise temperature. Finally, since dry air was no longer required, a zero-air generator (Umwelttechnik MCZ GmbH, Germany) was installed as an alternative source of clean air. This apparatus pumped the ambient air, filtered it and dried it before pushing it into the fluidic circuit. As a result, it turned to be cheaper than dry air bottles in the long term, although the air obtained was not completely dry. We measured a mean value of 8% RH at the output of the zero-air generator.

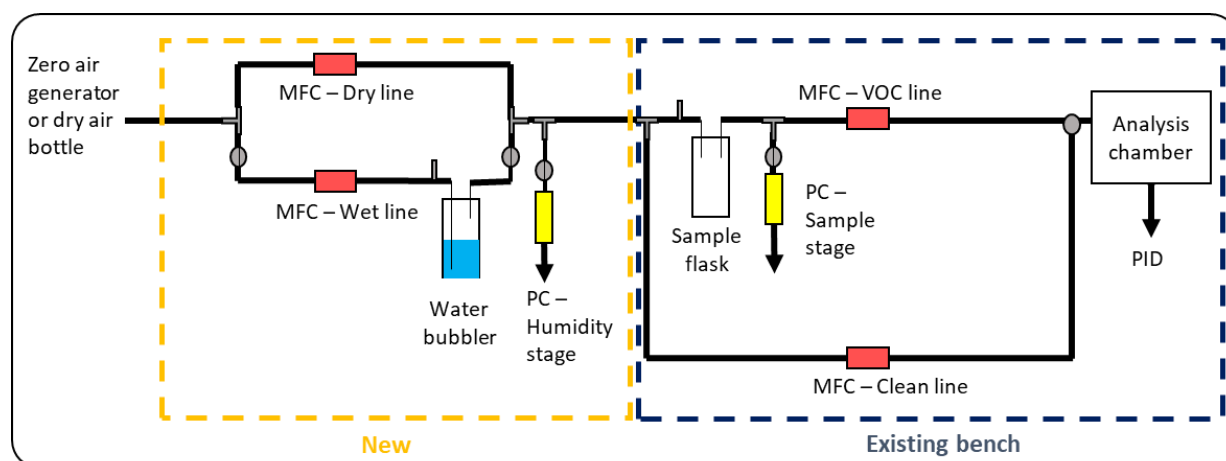


Figure 2-11 Optimized fluidic circuit with a controlled humidity. PC = pressure controller, MFC = mass-flow controller.

Furthermore, we have calibrated this extended fluidic circuit. To do so, we varied the relative flows between the dry line and the wet line, while keeping a total (sum) flow rate of 250 mL/min. We measured the resulting RH after the pressure controller of the humidity stage. The results, presented in Figure 2-12, showed that this setup was quite reactive, since the equilibrium was

reached in less than 2 minutes after the modification of the flows (dotted lines). Moreover, there was a good linearity between the relative flows and the RH, as seen in the insert, with a  $R^2$  of one. Nevertheless, the maximum RH, reached when the dry line flow was zero and the wet line flow was 250 mL/min was only 96%. This could be for two reasons. Either the passage through the bubbler was not sufficient to reach saturation, or part of the water was lost in the tubes by adsorption. Anyway, the performance of the system was very satisfactory for the level of precision desirable for our experiments.

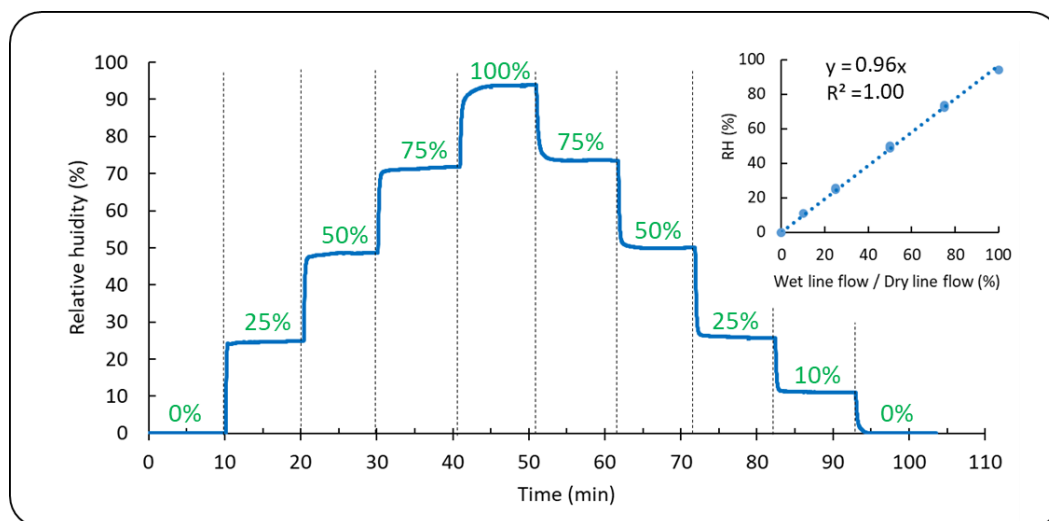


Figure 2-12 Calibration of the humidity stage. The values in green correspond to the wet line flow in comparison with the dry line flow. Insert: Relation between the relative flows and the RH.

However, the actual achievable humidity range depended on the ambient temperature. Indeed, the fluidic circuit was set up outside of the temperature-controlled chamber, for congestion reasons. The observation of a psychrometric chart (Figure 2-13) explains this phenomenon. For a given absolute humidity, the relative humidity will be higher in colder air. Particular attention had to be paid to this when the ambient temperature exceeds the analysis temperature. In this case, for high relative humidity, water could condense in the tubing or even on the prism during cooling.

Besides, the introduction of humidity also brought new difficulties. First, it complicated the evaporation of hydrophobic compounds. This limitation was easily overcome by heating the sample evaporation flask in a water bath. Second, water adsorbed on the entire chip and increased the non-specific signal. Third, this adsorption differed depending on the nature of the sensing materials, and so could modify the signature of a VOC. The effect of the humidity on the performance of our optoelectronic nose is the subject of the ongoing PhD thesis of Jonathan Weerakkody [232].

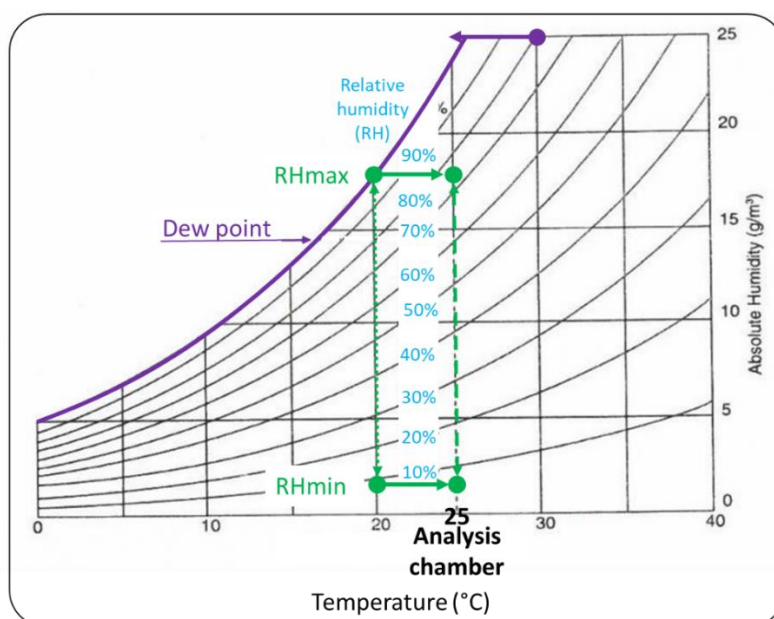


Figure 2-13 Psychrometric chart representing the achievable relative humidity range (blue) at a given ambient temperature. For example (green), at an ambient temperature of 20°C, a range from 8 to 100 % RH corresponds to a reachable range of 6 to 75% RH in the analysis chamber. Note that, if the ambient temperature is above the analysis temperature (purple), condensation can occur (adapted from [233])

## 2.4. TRANSDUCTION SYSTEM: SURFACE PLASMON RESONANCE IMAGING

### 2.4.1. Working principle of SPRi

The device developed by the team is characterized by its transduction method. Indeed, SyMMES laboratory was the first to develop an “optoelectronic” nose taking advantage of surface plasmon resonance imaging (SPRi) in the gas phase [234–237]. This method uses an imaging system to monitor binding events on all the sensing materials deposited on the prism simultaneously. It has been widely applied in the literature, for the development of biosensors and biochips in solution. SPRi monitors binding events in real-time, without labelling and at high-throughput. It benefits from a spatial resolution of 4  $\mu\text{m}$ , a time resolution of about 1 s and a good spot-to-spot reproducibility.

Theoretically, SPRi is based on surface plasmon resonance (SPR), a phenomenon that occurs at the interface of a metal and a dielectric medium. It relies on the excitation and detection of a collective oscillation of free electrons in the metal, known as surface plasmon. This phenomenon is highly located on the surface of the metal and sensitive to the refractive index.

Practically, the setup is presented in Figure 2-14 (a). A polarized light beam serves as the source of optical excitation. It is passed through the prism with a gold-coated surface in a way to achieve total internal reflection at the glass-gold interface. The resulting evanescent wave (in red on the scheme) can then couple with a surface plasmon (in blue). The gold layer is very thin (50

nm), so the penetration depth of this evanescent wave (100 nm) makes it sensitive to its other interface, functionalized with the sensing materials. As a result, the excitation of the surface plasmon, and so its energy depends on the refractive index of these sensing materials. To this extent, one can monitor any change affecting this refractive index, such as the adsorption of molecules. This is done by measuring the energy pumped by the surface plasmon, which causes a change in the intensity of the reflected light.

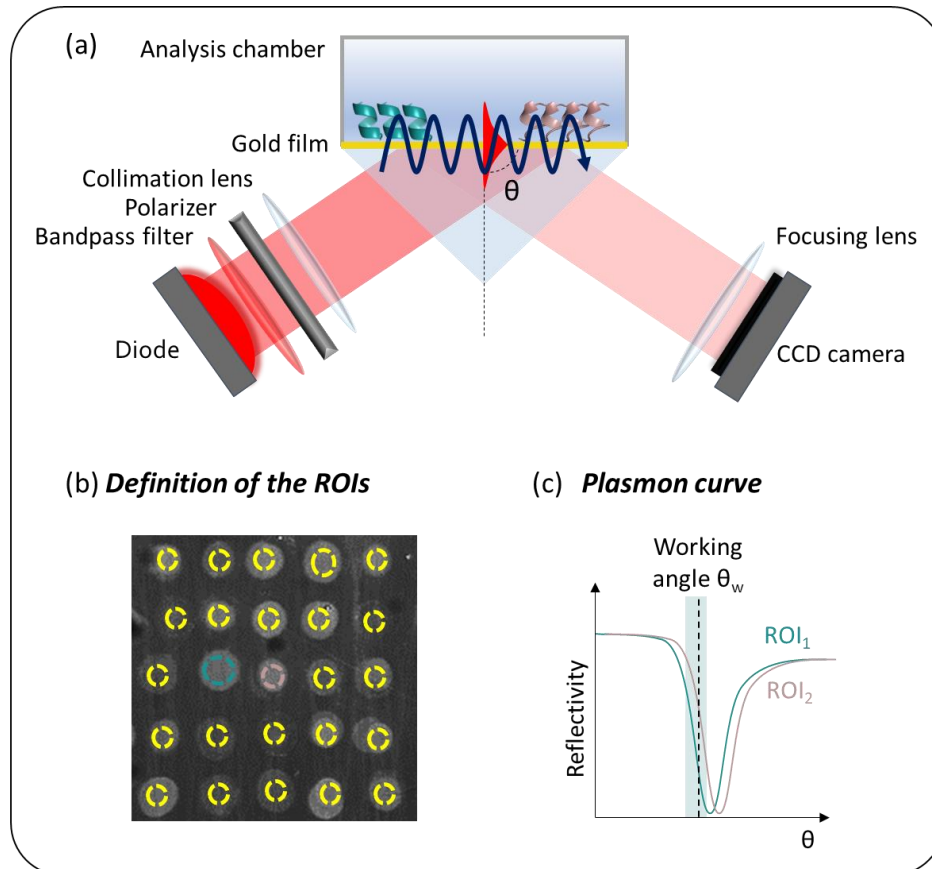


Figure 2-14 (a) Working principle of the SPRi. (b) Definition of the regions of interest. (c) Plasmon curve and choice of a working angle.

SPRi enables to multiplex the SPR principle. To this end, a CCD camera captures an image of the whole surface of the prism. The user defines regions of interest (ROIs), that is to say ranges of pixels whose intensity will then be averaged to get the signal of this sensing area.

In our case, on the CCD image, all the different biosensors were clearly visible, and covered a range of pixels. We defined one ROI for each biosensor, avoiding the border of the spots where the assembly of probes could be imperfect (Figure 2-14 (b)). Whereas some teams preferred to deposit large spots on the chip and to define multiple ROIs in the same sensing area [238], we decided to rather deposit several replicates of the same biosensor on the prism to avoid position effect.

The coupling between light and surface plasmons depends on the wavelength and on the angle of incidence  $\theta$ . In our case, we worked at a fixed wavelength (632 nm) and estimated the best working angle  $\theta_w$  at the beginning of each experiment. For that, we scanned a range of angles  $\theta$  and measured the corresponding reflected intensity for all the ROIs. The resulting calibration curves were called “plasmon curves” (Figure 2-14 (c)). Notably, at the resonance, the maximum of the incident energy is transmitted to the surface plasmon, and the minimum of reflectivity is reached. In the linear region of the plasmon curve (shaded in the figure), the reflected intensity varies linearly with the incident angle  $\theta$ . When the local refractive index changes, the plasmon curve shifts in angle. The working angle was chosen to be in the linear region of the plasmon curves of all ROIs, to make sure that a small variation in refractive index would affect linearly the reflected intensity (Figure 2-15 (c)). In practice, the different sensing materials had slightly different refractive index. As a result, their plasmon curves shifted in relation to each other. Consequently, there was no perfect angle setting. The choice of a fixed working angle promoted the angular sensitivity  $\frac{\partial R}{\partial \theta}$  of some of the sensing materials, to the detriment of others. However, when sensing materials with radically different molecular weight were used, there was no possible working angle to stay in the linear region of all the plasmon curves. For this reason, it was unreasonable to put, for example, both proteins and short peptides on the same chip.

Gas-phase SPRi benefits from two main advantages compared to its liquid-phase analog: the noise is strongly reduced due to the smaller density of gas than liquid and the signal of organic molecules is enhanced due to the greater contrast in refractive index between VOCs and air than between VOCs and water. For this reason, although liquid-phase SPRi is generally considered unsuitable and limited for the analysis of low-weight molecules such as VOCs (molecular weight below 300 g/mol), gas-phase SPR is perfectly adapted to this purpose.

#### **2.4.2. Conduct of a sample analysis**

After the calibration step, which consists in defining the ROIs and choosing the best working angle, the SPRi setup was ready to perform VOC detection. The principle of analysis is depicted in Figure 2-15. The VOC molecules, conveyed by the fluidic circuit described previously, entered the analysis chamber (Figure 2-15 (a)). They bound to the different sensing materials fixed at the gold surface of the prism, with different affinities. This interaction led to a change in refractive index, proportionally to the number of molecules, and so to a shift of the plasmon curve and eventually to a change in reflectivity (Figure 2-15 (b)). The reflectivity of all the spots was simultaneously monitored by a CCD camera, which gave a kinetic information about the binding process (Figure 2-15 (c) and (d)).

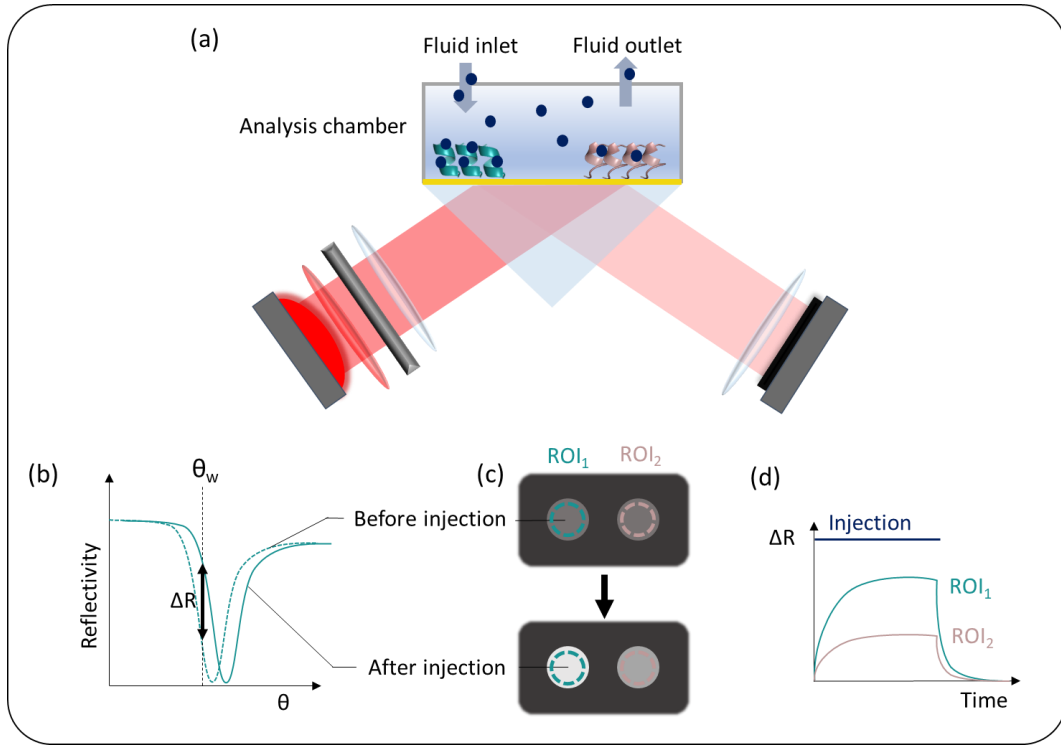


Figure 2-15 Description of the analysis of a sample.

## 2.5. DATA PROCESSING AND ANALYSIS

The surface plasmon is observable when the incident light is in the transverse magnetic polarization mode (TM). Prior to any experiment, a reference “black” image was taken with the diode turned off, and a reference “white” image in the transverse electric (TE) mode. After that, all the experiment was performed in TM mode.

The raw data provided by the LabVIEW program of the SPR imager was the percentage of reflectivity  $R_i(t)$  of every ROI  $i$  at time  $t$ . One measurement was taken every three seconds.  $R_i(t)$  was calculated from the averaged intensity of all the pixels of an ROI, by the following equation.

$$R_i(t) = \frac{I_{TM}(t) - I_0}{I_{TE}(0) - I_0} \times R_{TE} \times 100$$

Where  $I_{TM}$  is the intensity in TM mode,  $I_0$  is the intensity on the “black” reference image,  $I_{TE}$  is the intensity on the “white” reference image, and  $R_{TE}$  is a correction factor taking into account the wavelength and the working angle.

From this, different data processing and analysis could be performed. Every single injection could be analyzed individually, to understand for instance how a given VOC interacted with the different sensing materials. Alternatively, a whole database containing numerous injections could be processed with statistical methods so as to assess the discrimination capabilities of the artificial nose.

### 2.5.1. Analysis of an individual injection

Mainly, two signatures were obtained from the analysis of an individual injection: the kinetic response of every ROI, and the response profile at equilibrium. All the processing steps are depicted in Figure 2-16.

The first step was to subtract the baseline for every ROI, to enable their comparison. For that, the baseline reflectivity  $R_{b,i}$  was calculated as the average reflectivity of an ROI for one minute, just before the injection. Then, the following equation was simply used.

$$\Delta R_i(t) = R_i(t) - R_{b,i}$$

Then, we plotted  $\Delta R$  as a function of time and it gave directly the kinetic response for the sample (Figure 2-16 (b)). Possibly, the signals obtained from the replicates of a sensing material of the same nature could be averaged (Figure 2-16 (c)).

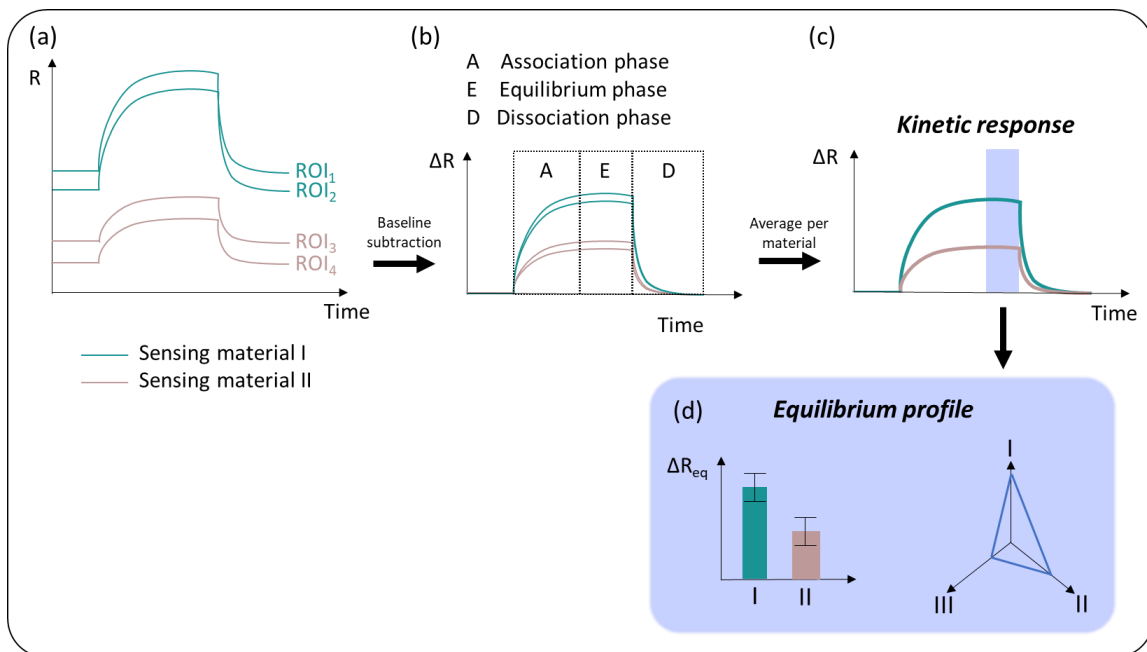


Figure 2-16 Illustration of the data processing steps for a single injection.

This kinetic response could be divided into three phases. First, the association phase, during which the VOC molecules reached the prism surface and bound to the sensing materials. Second, the equilibrium phase, where the signal was stable for all the ROIs. Third, the dissociation phase, during rinsing, where the VOC molecules were flushed from the sensing materials and the biosensor regenerated. It is very important to note that, contrary to what is commonly admitted for liquid SPR measurement, this kinetics did not reflect solely the affinity between the VOC molecules and the sensing materials. Instead, it was the combined result of the evaporation kinetics of the sample, the kinetics of its transport in the tubes, and the kinetics of specific and

non-specific binding (see Figure 3-15) on the sensing materials. This point will be explained in details in 4.3.

The equilibrium profile of an injection, or response profile at equilibrium, was plotted as a diagram representing  $\Delta R$  at equilibrium ( $\Delta R_{eq,k}$ ) for every sensing material  $k$  (Figure 2-16 (d)). It was obtained by calculating the mean  $\Delta R_i$  for one minute in the equilibrium phase for every ROI, and then by averaging the values of the replicates of a same sensing material  $k$ . The standard deviation between replicates, divided by the squared root of the number of replicates gave the error. Alternatively, a radar chart could be used for a visual representation.

Finally, a normalized equilibrium profile could be calculated to get rid of concentration effects. For this purpose, the equilibrium profile was divided by the quadratic average, as follows.

$$\Delta R_{norm,k} = \frac{\Delta R_{eq,k} \times \sqrt{N}}{\sqrt{\sum_{j=1}^N (\Delta R_{eq,j})^2}}$$

With  $N$  the number of sensing materials.

## 2.5.2. Principal component analysis

To assess the discrimination performance of our optoelectronic nose system, it was necessary to analyze numerous samples and to find a classification method able to process a large amount of data. We chose principal component analysis (PCA) as a simple multivariate statistical method, widely used in the domain of artificial noses.

### 2.5.2.1. PCA principle

The equilibrium profile of an injection, which can be considered as the signature of a VOC, can be represented as a vector with  $N$  dimensions,  $N$  being the number of different sensing materials on the chip. For a database with  $M$  injections, the data can then be represented as a matrix with  $M \times N$  dimensions. The columns (sensing materials) are called variables, and the lines (injections) are individuals. This involves a significant amount of data. However, the  $N$  dimensions are not necessarily orthogonal, thus the information is redundant and the data can be compressed.

PCA aims to eliminate this redundancy in the data and to project it into a smaller dimensional space while maintaining most of its variance. The new decorrelated dimensions are named “principal components”. A graphical description of PCA principle is given in Figure 2-17. In practice, this comes down to a problem of searching for eigenvalues and eigenvectors in the correlation matrix. Eventually, the two first principal components, PC1 and PC2 define the most suitable plan to plot the data points (individuals) and maximize the distance between them. It is also possible to project the variables in this plan, as vectors. In our case, this representation can



help to comprehend the contributions of every sensing material to the discrimination capabilities of the optoelectronic nose.

It is interesting to note that PCA is a non-supervised method. As such, the principal components are chosen without knowing the nature of the samples. In this fashion, the data processing is not biased. Nevertheless, some other methods like linear discriminant analysis are supervised, and use a database with labelled samples to choose the principal components that best separate different groups. It can be more interesting than PCA for well-defined applications.

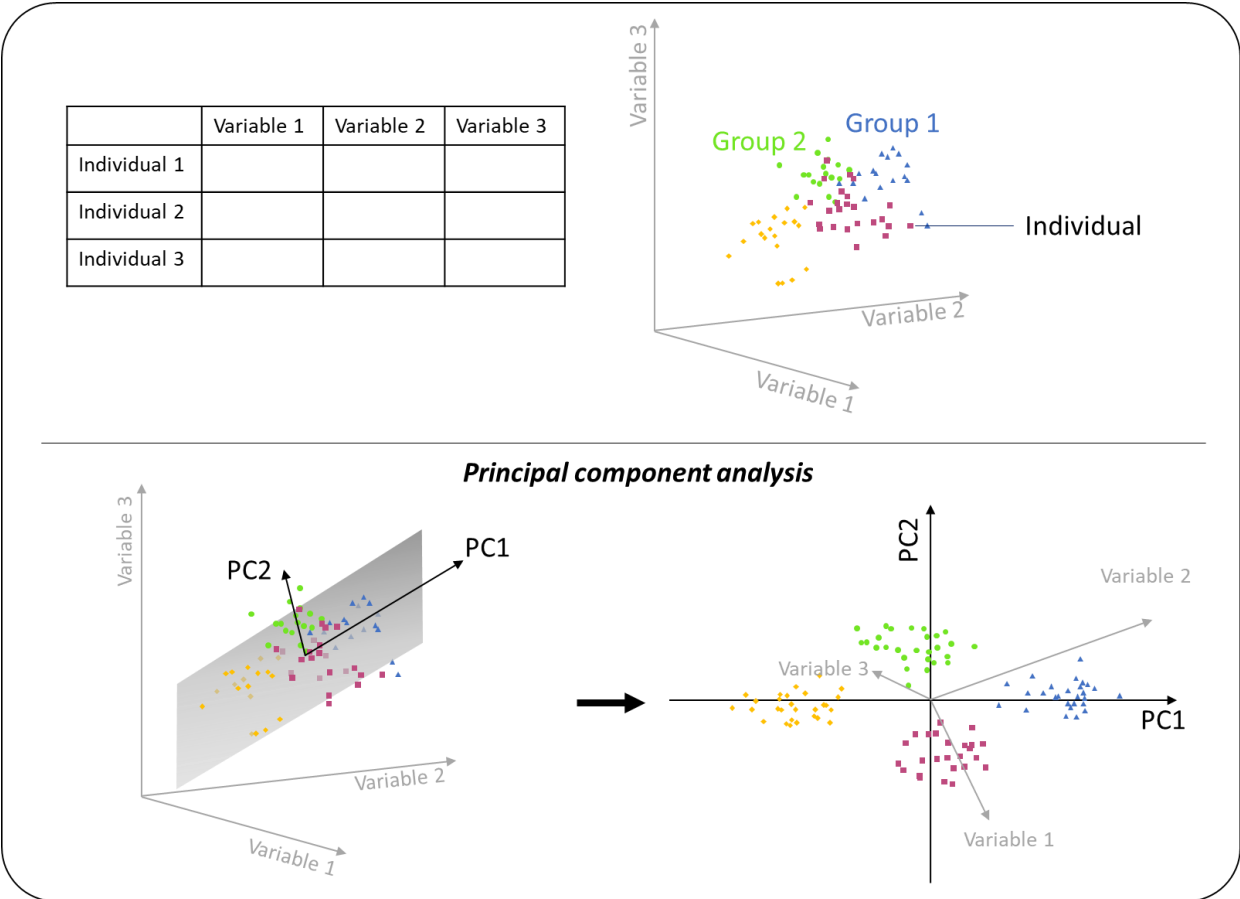


Figure 2-17 : Graphical description of the principle of PCA.

2.5.2.2. Practical application

In some cases, a PCA with the data at equilibrium was not sufficient to distinguish between the different VOCs. In this case, we integrated kinetic data in the PCA. This method is known to facilitate the discrimination of individuals by PCA [175].

In this thesis, we will talk about “static PCA” and “dynamic PCA”. The former refers to a PCA conducted on an equilibrium database. The latter designates a PCA carried out on a kinetic database. Practically, the constitution of these databases is explained in Figure 2-18. The different replicates of a sensing material were treated independently, as virtual injections. For instance, if there were three replicates of each biosensor on the chip, a single injection of VOC would give

three virtual injections in the database.  $\Delta R_{eq}$  was then used to fill the equilibrium database. For the kinetic database, a variable was defined for every sensing material at different times ( $t_1, t_2, \dots$ ). The database was filled with  $\Delta R(t)$ .

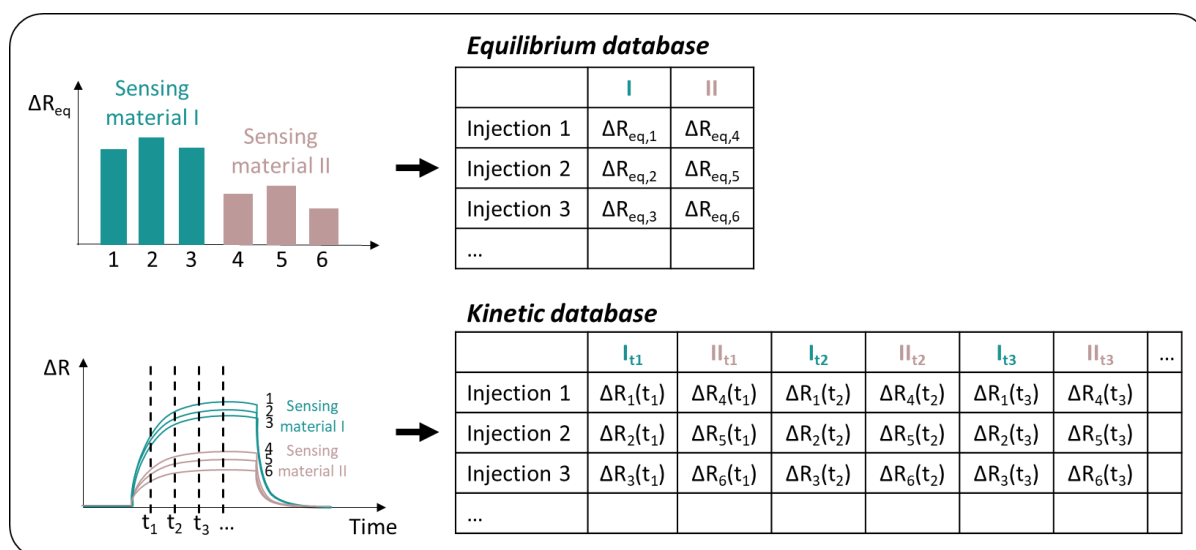


Figure 2-18 Constitution of an equilibrium or a kinetic database.

In any case, the individuals (lines) were normalized by their quadratic average. Theoretically, if the variables are inhomogeneous, it is necessary to standardize them to get a centered and reduced distribution for each, and so to make sure that their weights are equal in the PCA. Here, it was not systematically done, since this step could greatly amplify the noise.

All the PCA analysis presented in this thesis were made using the R package “FactoMineR” [239].



## CHAPTER 3

Characterization and assessment of the  
performance of the device



## Résumé du chapitre 3 - Contrôle et caractérisation des performances du dispositif

L'objectif de cette thèse est de développer de nouveaux matériaux sensibles pour améliorer la sensibilité et la sélectivité du nez optoélectronique développé au laboratoire. Pour cela, comme nous allons le voir dans les chapitres suivants, nous avons sélectionné des sondes en solution pour leur grande affinité pour un COV ou une famille de COV cible. Leur qualification en tant que briques de bases de nouveaux matériaux sensibles s'est faite en plusieurs étapes. Différentes méthodes théoriques et de caractérisations avancées ont été mises en œuvre pour valider les jalons successifs, qui sont présentées dans ce chapitre.

Dans un premier temps, nous avons déterminé l'affinité des sondes libres, en solution, pour leur cible. Pour les peptides, nous avons mené des simulations numériques de structuration et d'amarrage moléculaire. Pour les OBP, nous avons préféré une méthode expérimentale : le titrage calorimétrique isotherme.

Les sondes ont ensuite été déposées sur la surface du capteur. Nous avons mené une étude préliminaire pour déterminer les méthodes de caractérisation adaptées. L'objectif était de connaître l'homogénéité du dépôt, la densité des sondes à la surface, et leur structuration. Un modèle théorique permet d'exploiter les images SPR de la puce. La microscopie à force atomique semble appropriée pour caractériser l'homogénéité des dépôts d'OBP. La spectroscopie de photoélectrons X et la spectroscopie de masse des ions secondaires fournissent quant à elles des informations sur la densité et la nature chimique des dépôts de peptides.

Par la suite, nous avons déterminé si les sondes, une fois immobilisées sur la puce, conservaient leur affinité pour leur COV cible. Pour découpler l'effet de l'immobilisation de celui du passage d'une reconnaissance en milieu liquide à une phase gaz, nous avons commencé par tester la détection de COV en phase liquide sur un dispositif de langue optoélectronique. La SPR étant moins résolue en phase liquide qu'en gaz, il nous a fallu mettre au point des stratégies d'amplification. D'une part, nous avons exploité la propriété naturelle de changement de conformation des OBP lors de la liaison d'un odorant. D'autre part, pour permettre leur détection avec les peptides, les molécules de COV ont été lestées avec des nanoparticules d'or.

Enfin, nous avons caractérisé la sensibilité et la sélectivité de la langue et du nez artificiel obtenus. Les définitions de ces notions ne sont pas consensuelles. La dernière partie de ce chapitre s'attache à expliquer précisément le sens qu'elles prennent dans ce projet, ainsi que les stratégies mises en œuvre pour les évaluer.



## CHAPTER 3 Characterization and assessment of the performance of the device

Once the optoelectronic nose setup ready, characterization was key to assess and improve its performance. As shown in the following chapters, during this PhD project, the selection of all the new probes including OBPs and different peptides was carried out in solution. Schematically, several milestones guided their qualification as probes for the development of new sensing materials. To validate each milestone, it was essential to answer the following questions.

- 1) What is the structure of the new probe? What is its affinity with its target VOC in solution?
- 2) Are the probes properly deposited on the sensor in a dense, reproducible fashion?
- 3) Once immobilized on a surface, do the probes keep their structure and affinity for the VOC? How about the performances of the obtained olfactory biosensors under favorable conditions such as in the liquid phase? Are they sensitive and selective thanks to this new probe?
- 4) Are these performances preserved in dry conditions for the detection of VOCs in the gas phase?

In this chapter, we explain the theoretical models and advanced characterization techniques implemented to answer these questions.

### 3.1. AFFINITY EVALUATION OF A FREE PROBE FOR A TARGET VOC IN SOLUTION

---

Before integrating a new sensing material on the SPRi chip, it was important to know its characteristics, and to check if it was of potential interest for the artificial nose. In our case, the new probes constituting these sensing materials were selected in solution for their relatively high affinity and selectivity for a target VOC. Thus, the first step was to measure this affinity.

We will present here two methods. The first one is based on computer simulations. The second one, isothermal titration microcalorimetry (ITC), is experimental. In both methods, the probes are free, that is to say, not attached to a surface, and in solution.

#### 3.1.1. Computer modelling: determination of the structure and affinity of a peptide for a target VOC

Computer modeling is a powerful tool to perform high-throughput docking simulations. It was of particular interest in our case, where numerous probes and VOCs are studied. During this project, we used different open access software to get a first estimation of the affinity between the different peptides and VOCs.



First, a peptide structure was predicted from its amino acid sequence using PEP-FOLD 3 [240,241]. This tool, developed at Paris Diderot University in France, is based on structural alphabet letters, to describe the conformations of four consecutive residues, coupled to a greedy algorithm and a coarse-grained force field. The simulation reached equilibrium for simple structures ( $\alpha$ -helix), and gave repeatable results in this case. For unstructured peptides, a random conformation was used. However, for peptides with more complex structures, where only some regions folded in a secondary structure, the results of the simulation were not always repeatable. Therefore, the results should be treated with caution. Nevertheless, this structural information was also interesting to visualize the differences between the peptides and to understand the variations in behavior from one to another.

For the affinity prediction, the tridimensional (3D) conformation of the peptide was exported as a PDB file. The 3D structure of the VOC molecules was exported from the PubChem website [242]. The molecular docking simulation, which enabled to calculate the affinity between the peptide and the VOC, was performed using AutoDock Vina. AutoDock Vina is an open-source program, designed and implemented by Dr. Oleg Trott in the Molecular Graphics Lab at The Scripps Research Institute [243]. From the tridimensional structures collected above, it calculated the energy of the peptide-VOC complex at all their possible relative positions in a defined box. In our case, we included the whole peptide in a 20 Å-edge cube. In output, the program gave the nine most plausible binding sites associated with their corresponding binding energy (in kcal/mol). The lower the binding energy, the higher the affinity between the probe and the VOC molecule. A graphical representation of this docking is given in Figure 3-1. Given a peptide structure and a VOC molecule, the results of the docking were very reproducible.

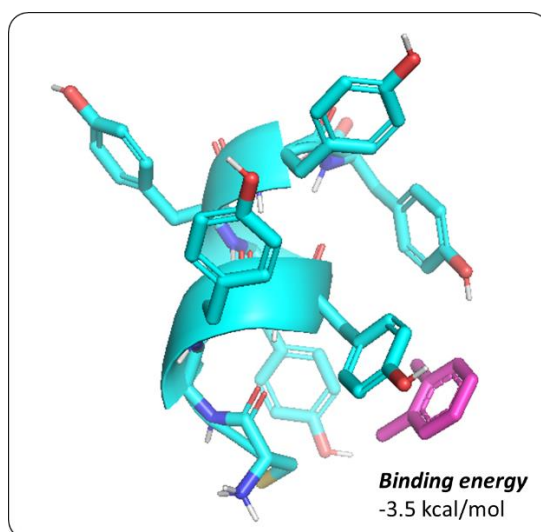


*Figure 3-1 Example of docking simulation with AutoDock Vina for a peptide (blue) and a VOC molecule (pink), with the affinity calculation for one of the most plausible binding sites.*

Nevertheless, the simulations implied several hypotheses that may result in a gap between the computed and experimental results, when the probes will be embedded in a sensing material for artificial nose applications. First, the structures of both the probes and the VOCs were fixed and rigid, thus the entropy and temperature effects were not incorporated. Second, the docking was performed in solution with implicit solvent, thus the hydrogen bonding may not be correctly accounted for. Third, it made a one-to-one approximation thus neglecting the possible multiple binding sites on a given probe as well as potential cooperativity effects between probes when incorporated in sensing materials. Fourth, since the docking was performed in solution, drawing conclusions on the affinity in the gas phase (in presence of humidity or not) may be hazardous.

It is therefore useful to consider various advanced characterization methods to validate or estimate the effects of the above hypothesis on the affinity and bridge the gap between simulations and experiments. This will be the subject of the rest of this chapter.

In the future, it may be interesting to model peptides anchored to a surface, and with a dynamic structure, with the help of molecular dynamics [244,245]. It would be much closer to the real situation. This information could help us to understand how the peptide structure is affected by anchoring on gold surface, and how it changes its affinity for the target VOC. In the long term, similar simulations could also be performed in air with or without humidity. Jonathan Weerakkody will carry out such a study during his PhD.

### **3.1.2. Isothermal titration calorimetry: experimental measurement of the affinity between OBPs and VOCs**

Isothermal titration calorimetry (ITC) is a quantitative characterization method to determine experimentally the thermodynamic parameters of interactions in solution. It is often used to study the binding of small molecules to larger biomolecules (proteins, DNA *etc.*). However, its use is more limited for short peptides such as ours. Anyway, we used it to measure the affinity between our different probes (OBPs or peptides) and VOC molecules.

Still, ITC measures interactions in solution. In addition, although it could account for the multiple binding of VOC molecules onto a peptide or OBP, it will not reproduce the cooperative effects that could occur on the chip, where one VOC molecule could bind to multiple probes. However, contrary to docking simulations, ITC accounts for temperature, entropy and hydrogen bonding. It was therefore a first step to approach the experimental conditions in the artificial nose.

The device is depicted in Figure 3-2 (a). It is composed of two identical cells made of a highly efficient thermally conducting and chemically inert material. There is only buffer in the reference cell. A precise concentration of the molecule to study is put in the sample cell, for example, in our case, the probe (a peptide or an OBP) in aqueous solution. The temperature difference  $\Delta T$  between

the two cells is monitored. The ligand (here the target VOC) is introduced gradually into the sample cell at a precise concentration. When it binds to the probe, this interaction can release or absorb heat. In response, a reference power  $DP$  is applied to the sample cell in order to maintain an equal temperature between the two cells. Observations are plotted as the reference power against time. The raw data consists in a series of spikes of heat flow (power), with every spike corresponding to a ligand injection. It allows measuring the interaction parameters of the binding process: stoichiometry ( $n$ ), dissociation constant at equilibrium ( $K_d$ ), enthalpy ( $\Delta H$ ), etc. The parameter which is usually used to qualify the affinity between the ligand and the probe is the equilibrium dissociation constant  $K_d$ . The lower the  $K_d$ , the higher the affinity. The enthalpy gives information about the interaction force, and so the nature of the binding (hydrogen bond, Van Der Waals, etc.). The stoichiometry assesses the one-to-one character of the interaction or its potential multiple bindings.

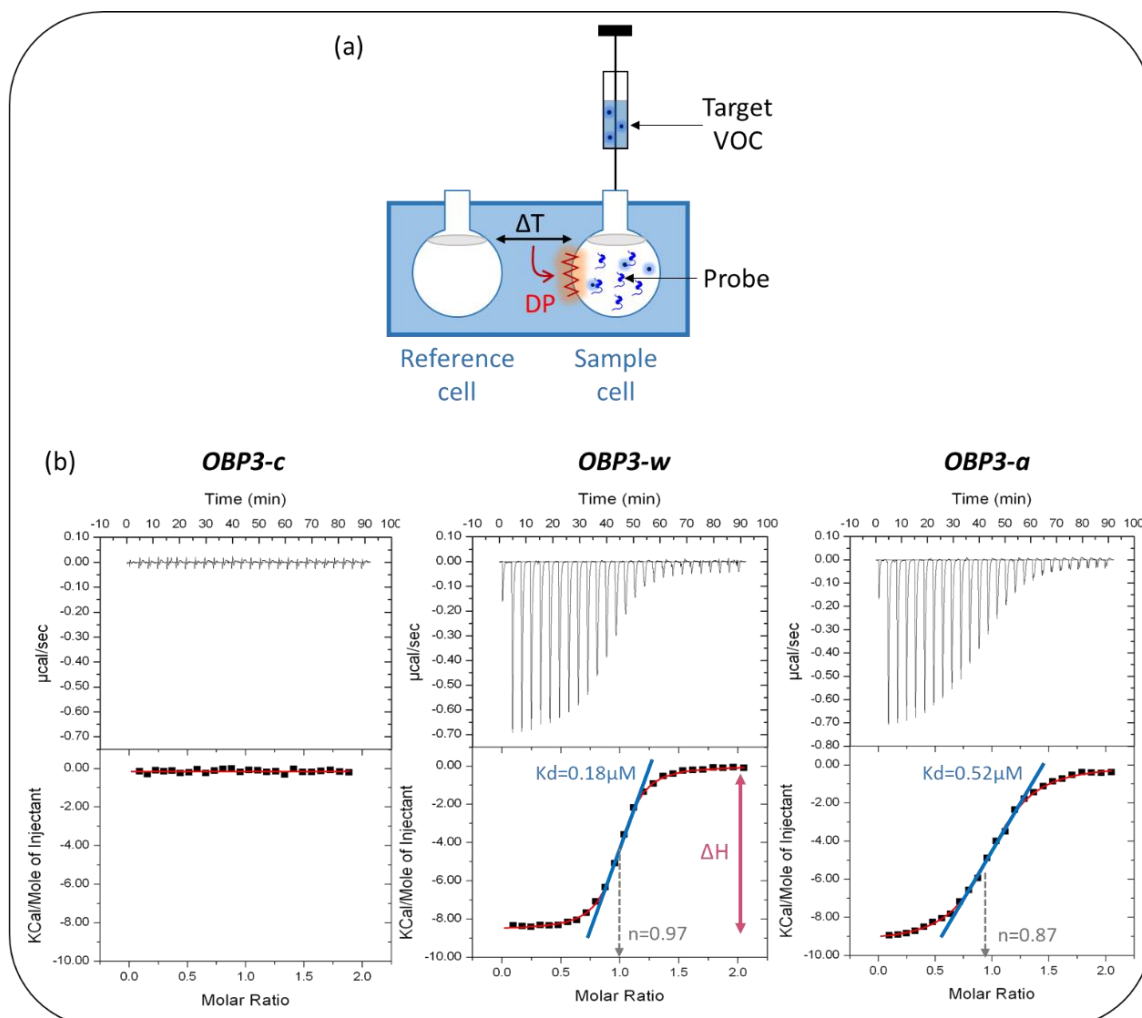


Figure 3-2 (a) Working principle of the isothermal titration calorimetry. (b) Example of results with three different OBPs for binding  $\beta$ -ionone. OBP3-c is a negative control.

Dr. Loïc Briand's team at "Centre des Sciences du Goût et de l'Alimentation", Dijon, France, produced the OBPs used in this project. They performed ITC tests to study the binding properties

of the different OBPs with VOCs. An example is given in Figure 3-2 (b). They concluded that a protein was able to bind only one VOC molecule at a time, and determined  $K_d$  for different VOCs in solution.

With the help of Dr. Anne Imberty of Cermav, Grenoble, France, we performed ITC tests on peptides selected by phage display. This method was used in the literature by Jaworski *et al.* [246]. We chose to work at high concentrations, because the affinity between a peptide and a VOC was expected to be relatively low. The peptides solutions (50  $\mu\text{M}$  in ultrapure water) were put in the sample cell of an ITC200 (Malvern, UK). The VOCs (phenol or toluene, 10 mM in ultrapure water) were put in the syringe.

Unfortunately, the preliminary results showed that there was no clear signal for the different peptides we tested. Perhaps the affinity constant was too low, or the interaction was neither endothermic nor exothermic. Interestingly and as a comparison, Jaworski *et al.* [246] managed to measure a  $K_d$  of 10 nM between a TNT-binding peptide of 15 amino acids and its target. The peptide (10  $\mu\text{M}$ ) and TNT (100  $\mu\text{M}$ ) were diluted in acetonitrile.

In conclusion, ITC is particularly interesting for the determination of the affinity between OBPs and VOCs. It is easier than docking simulations on large molecules, and enable a dynamic structure of the molecules. On top of that, the proteins when free in solution are in their native conformation and so are more likely active. When it comes to peptides however, the characterization is not straightforward. The paper cited above [246] indicates that it may be possible under optimized conditions, or with longer peptides that would have, like it will be explained in the rest of this thesis, higher affinity for their target.

### 3.2. SURFACE CHARACTERIZATION OF THE SENSING MATERIALS ON THE SPRI CHIP

---

The next step was to characterize how the probes were deposited on the SPRI chip. Although the functionalization of the chip was made in a single step procedure, and all the probes were spotted on the prism under the same conditions, the differences between the probes (hydrophobicity, molecular volume, molecular weight...) most probably caused variations in their resulting surface density. That was particularly true when using protocol 1 (see 2.2.1), and thus problematic for the rest of the project.

Indeed, to assess the sensing performances of a new probe, we need to be able to compare its affinity for a VOC, relatively to the other probes. Besides, the probe density in the sensing materials on the surface of the chip affects the intensity of the signal of the resulting biosensor. The higher the probe density, the stronger the signal. As a result, if this density varied, the relative

signals obtained with all the biosensors for a VOC did not reflect directly their relative affinity for this molecule.

We therefore chose to characterize the density of the different probes on the chip surface. In the first instance, this helped us to understand the variability that we could observe, and to develop new functionalization protocols. However, even with an optimized protocol, it is challenging to obtain an equal surface density for all the probes, since they have a great variety of physicochemical properties. Moreover, this would require a new optimization phase for each new probe. That is why in the second instance, the surface characterization could be used to normalize the signals of the different sensing materials depending on the probe density on the chip.

### 3.2.1. Theoretical model based on SPRi images

To do so, the first strategy that we proposed was to use directly the SPRi image. Indeed, the presence of the sensing materials changed the local refractive index of the chip. As explained in chapter 2, this shifted the reflectivity, and made them clearly visible on the SPRi image. Moreover, for a given sensing material, the higher the probe density, the greater the reflectivity variation. As a result, on the SPRi image of the sensor surface after probe spotting, we observed that the contrast of the different sensing materials relative to the background of the chip could vary (Figure 3-3, insert).

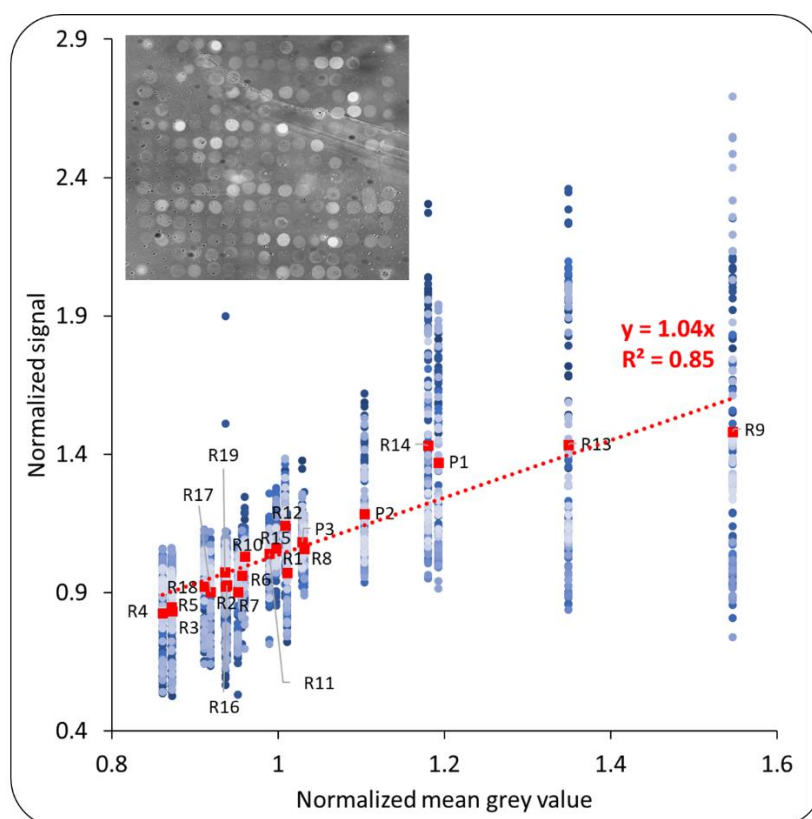


Figure 3-3 Normalized signals at equilibrium obtained for the injection of different VOCs as a function of the normalized grey value of the corresponding ROI. Insert: SPRi image of the prism surface showing the different contrasts of the sensing materials on gold.

The Figure 3-3 gathers the normalized equilibrium responses of 22 biosensors based on different probes, obtained for 110 injections of different VOCs on a same prism. They are presented as a function of the normalized grey level of the corresponding sensing material on the SPRi image of the prism before any VOC injection. Clearly, the sensing materials with a higher contrast on gold gave a higher mean signal at equilibrium (red square). Moreover, the variability of the signals was also higher for these sensing materials. It showed that this contrast was indeed linked with the sensitivity of the sensing materials. It was probably due essentially to a higher surface density of the probes on these ROIs.

Thus, we developed a theoretical model from which we can, extrapolate the surface density of each probe from the grey level on the SPRi image, *inter alia*. All the situations modeled in the next part are schematized in Figure 3-4.

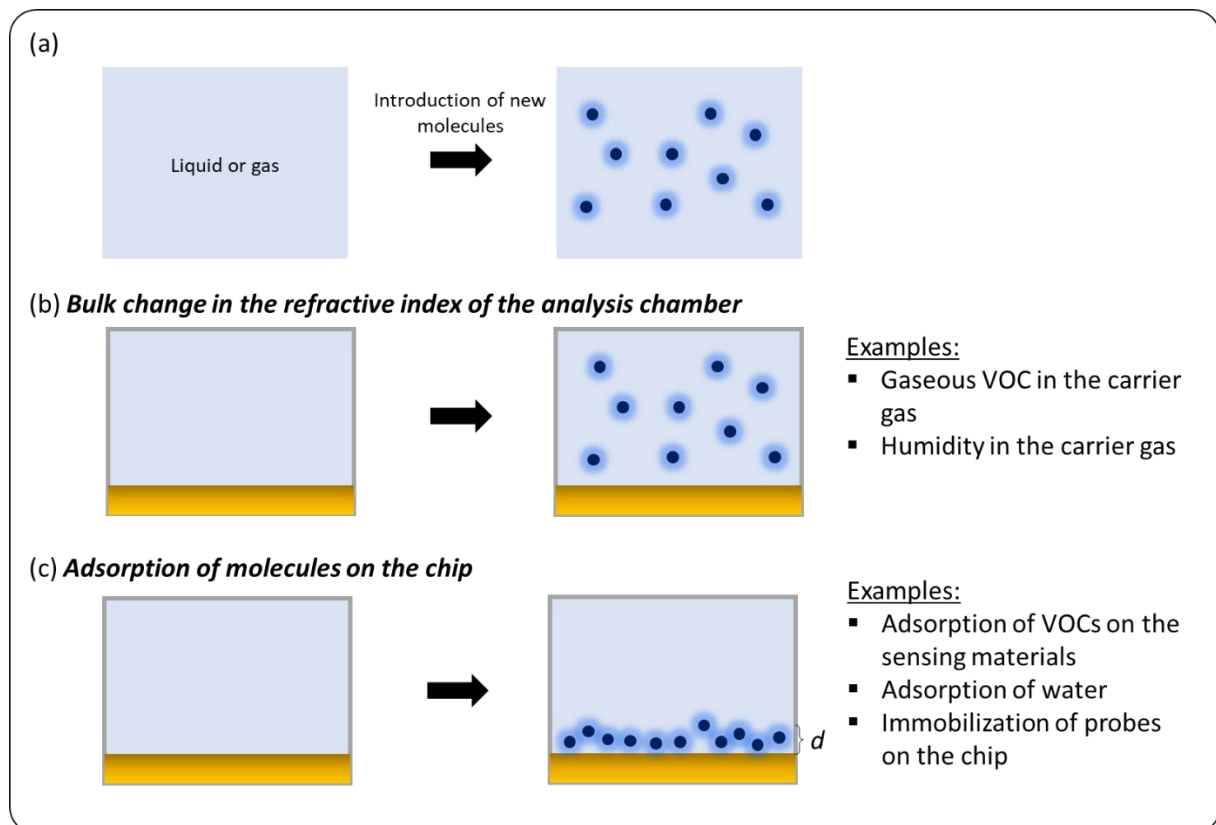


Figure 3-4 Illustration of the different phenomena affecting the refractive index.

### 3.2.1.1. Bulk variation of the refractive index of a gas

The first step towards this theoretical model was to understand how the introduction of a new molecule affects the bulk refractive index of a gas (Figure 3-4(a)). This model could be very easily adapted to the liquid phase.

For a gas of molecular weight  $M$  and refractive index  $n$ , we defined

$$A = (n - 1)/M \times 10^6$$

Gases	Refractive index $n$ in RIU	Molecular mass $M$ in g.mol <sup>-1</sup>	$10^6(n-1)/M$ $A$ in mol.g <sup>-1</sup>
Hydrogen (H <sub>2</sub> )	1.000 132	2	66.0
Helium (He)	1.000 035	4	8.8
Argon (Ar)	1.000 281	40	7.0
Nitrogen (N <sub>2</sub> )	1.000 298	28	10.6
Oxygen (O <sub>2</sub> )	1.000 271	32	8.5
Chlorine (Cl <sub>2</sub> )	1.000 773	70.9	10.9
Bromine (Br <sub>2</sub> )	1.001 132	159.8	7.1
Air (21% O <sub>2</sub> + 78% N <sub>2</sub> )	1.000 292	29.0 (av.)	10.1
<b>Simple gases (except H<sub>2</sub>)</b>			<b>9 (av.)</b>
Water vapour (H <sub>2</sub> O)	1.000 256	18	14.7
Carbon monoxide (CO)	1.000 338	28	12.1
Carbon dioxide (CO <sub>2</sub> )	1.000 449	44	10.2
Nitric oxide (NO)	1.000 297	30	9.9
Nitrous oxide (N <sub>2</sub> O)	1.000 516	44	11.7
Hydrochloric acid (HCl)	1.000 447	36.5	12.2
Chloroform (CHCl <sub>3</sub> )	1.001 450	119.4	12.1
Sulphur dioxide (SO <sub>2</sub> )	1.000 686	64	10.7
<b>Complex gases</b>			<b>11.7 (av.)</b>
Carbon disulphide (CS <sub>2</sub> )	1.001 481	76.1	19.5
Hydrogen sulphide (H <sub>2</sub> S)	1.000 634	34.1	18.6
Ammonia (NH <sub>3</sub> )	1.000 376	17	22.1
<b>Complex gases (others)</b>			<b>20.1 (av.)</b>
Methane (CH <sub>4</sub> )	1.000 444	16	27.75
Methanol (CH <sub>3</sub> OH)	1.000 586	32	18.3
Ethanol (CH <sub>3</sub> CH <sub>2</sub> OH)	1.000 878	46	19.1
Methyl ether (C <sub>2</sub> H <sub>6</sub> O)	1.000 891	46	19.4
Diethyl ether ((C <sub>2</sub> H <sub>5</sub> ) <sub>2</sub> O)	1.001 533	74.1	20.7
Benzene (C <sub>6</sub> H <sub>6</sub> )	1.001 762	78.1	22.6
Pentane (C <sub>5</sub> H <sub>12</sub> )	1.001 711	72.1	23.7
Acetone (C <sub>3</sub> H <sub>6</sub> O)	1.001 090	58	18.8
<b>VOCs</b>			<b>21.3 (av.)</b>

Table 3-1 Refractive index  $n$  (from [247]), molecular weight  $M$  and  $(n-1)/M$  of various gases.

The value of  $A$  was calculated for different gases and listed in Table 3-1. It seems clear that  $A$  is relatively constant for various gases, ranging from around 10 RIU.mol.g<sup>-1</sup> for simple ones (mono or di-atomic ones except hydrogen) up to around 20 RIU.mol.g<sup>-1</sup> for heavier organic molecules. RIU states for “refractive index unit”. Thus, we assumed that the shift in refractive index for an added gas of molecular weight  $M$  and partial pressure  $P$  was

$$\Delta n(P) \simeq (AM - A_i M_i) \frac{P}{P_0} \times 10^{-6}$$

with  $P_0 = 1.0135 \text{ bar} = 1.0135 \times 10^5 \text{ Pa}$  the ambient pressure,  $A \simeq 20 \text{ RIU.mol.g}^{-1}$  for organic molecules. This equation accounts for the reduced partial pressure of the carrier gas  $i$ , through the introduction of  $A_i$  and  $M_i$ . In our case, it will be dry air.

In the model of perfect gases, for  $m$  mol of gas with a concentration  $c$  (in mol/L), a pressure  $P$  (in Pa = J.m<sup>-3</sup>,  $10^5 \text{ Pa} = 1 \text{ bar}$ ), a volume  $V$  (in m<sup>3</sup>), and a temperature  $T$  (in Kelvin), we have

$$c = \frac{m}{V} = \frac{P}{RT}$$

with  $R = 8.314 \text{ J.K}^{-1}.\text{mol}^{-1}$ . From which we deduced that

$$\Delta n(c) = (AM - A_{air}M_{air}) \frac{cRT}{P_0} \times 10^{-6}$$

The equivalent concentration in part-per-million  $c$  ( $ppm$ ) is given by  $c(ppm) = cV_0 \times 10^6$ , with  $V_0 = \frac{RT}{P_0} \approx 24 \text{ L. mol}^{-1}$  the molar volume of air at  $T=20^\circ\text{C}$ . As a result

$$\Delta n = (AM - A_{air}M_{air}) c V_0 \times 10^{-6} = (AM - A_{air}M_{air}) c(ppm) \times 10^{-12}$$

### 3.2.1.2. Volume effect of a refractive index change on the SPRi signal

During our experiments, upon the introduction of gaseous molecules into the carrier dry air, the bulk refractive index of the gas changed homogeneously (Figure 3-4(b)). For a volume addition of a concentration  $c$  ( $ppm$ ) of gas in the analysis chamber, we have roughly

$$\Delta R = \frac{\partial R}{\partial n} \Delta n = \frac{\partial R}{\partial n} (AM - A_{air}M_{air}) c(ppm) \times 10^{-12}$$

With  $\frac{\partial R}{\partial n}$  being the sensitivity to the refractive index of the SPRi apparatus, called physical sensitivity in this thesis. Jonathan Weerakkody measured its value for bare gold experimentally and established that  $\frac{\partial R}{\partial n} \approx 6600 \text{ \%/RUI}$  [248]. To evaluate this sensitivity for the other sensing materials, we measured the variation of reflectivity occurring for a controlled step of refractive index. This was done experimentally by increasing the pressure in dry air (see 3.4.1.2). In any case, the order of magnitude was similar to gold. This first model is useful to describe two experimental situations encountered in this project.

First, during the injection of a VOC, the bulk refractive index in the analysis chamber changed, without considering adsorption on the surface of the chip. Applying the previous equation, we can calculate the impact on the reflectivity of the biosensors. For example, for 500 ppm of butanol in dry air, a concentration well above the ones used in this thesis, we obtain  $\Delta R = 0.04 \text{ \%}$ . This estimation is below the experimental noise ( $\Delta R \sim 0.05\%$ ). Thus, the impact of this bulk change may be neglected in the future. Moreover, the shift in reflectivity that we measure experimentally for this concentration of butanol may be assumed to depend only on the adsorption of VOCs on the surface (see 3.2.1).

Second, when humidity is introduced in the analysis chamber, it also results in a bulk refractive index change. Moreover, the concentration of gaseous water can be quite high. For example, a RH of 100% at  $20^\circ\text{C}$  corresponds to ( $23 \times 10^3 \text{ ppm}$  of water). The impact of humidity on the measurements was also estimated using the previous formula. Interestingly,  $A_{water}M_{water} - A_{air}M_{air}$  is negative. As a result, for humid air (100% RH at  $20^\circ\text{C}$ ) we should observe a negative variation of reflectivity due to the bulk change in refractive index  $\Delta R = -4 \times 10^{-3} \text{ \%}$ . Again, the calculated variation is below the noise level. Experimentally, we always measured a positive variation of reflectivity, due to the adsorption of molecules on the surface, as will be explained in the following.



In conclusion, in both cases, the bulk effect of the introduction of these gas led to a negligible SPRi signal. In practice, this phenomenon coexists with the adsorption of some molecules on the surface. At the first order, we may consider that the measured signals were only due to this second phenomenon. Thus, a model on adsorption was needed.

### 3.2.1.3. Effect of adsorption on the SPRi signal and estimation of the surface density of the probes

To estimate the effect of the adsorption of a molecule layer of thickness  $d$  on the SPRi sensor (Figure 3-4 (c)), the penetration depth  $\lambda$  of the plasmon has to be taken into account. This characteristic length of the evanescent wave corresponds to the maximum sensing distance. At our wavelength,  $\lambda \approx 175$  nm [232]. According to the theory of SPR [249], a change of refractive index  $\Delta n(d)$  at a distance  $d$  from the surface due to an adsorbed gas leads to a refractive index shift. If we make the hypothesis that  $d \ll \lambda$ , we can write

$$\Delta R = \frac{\partial R}{\partial n} \int_0^\infty \Delta n(z) e^{-\frac{z}{\lambda}} \frac{dz}{\lambda} \approx \frac{\partial R}{\partial n} \times \frac{d}{\lambda} \times \Delta n(c)$$

Where  $\Delta n(c)$  is the refractive index change due to a concentration  $c$  of molecule within the adsorption layer. With the previous expression for  $\Delta n(c)$ , we deduce that:

$$\Delta R = \frac{\partial R}{\partial n} \times \frac{d}{\lambda} c A M V_0 \times 10^{-6}$$

At this point, it is important to note that we made the hypothesis that the adsorbed molecules behave like a gas. This hypothesis will be called H1. H1 is roughly valid if they have a very low surface concentration. If it is not the case, another approach is possible, considering the refractive index of the pure liquid molecule. In the case of water, we showed that the two models led to an identical result.

In this thesis, we were interested in calculating the overall number of adsorbed molecules per surface unit rather than the width  $d$ . Thus, we introduced  $\sigma = N_A d c$  (in molecules/m<sup>2</sup>) and wrote the previous equation as

$$\Delta R = \frac{\partial R}{\partial n} \times \frac{\sigma}{N_A \lambda} \times A M V_0 \times 10^{-6}$$

with  $V_0 = 24 \times 10^{-3}$  m<sup>3</sup>.mol<sup>-1</sup> and  $N_A$  the Avogadro number. Reversely,

$$\sigma = \Delta R \times \frac{N_A \lambda}{\frac{\partial R}{\partial n} A M V_0} \times 10^6$$

On the one hand, this equation enabled us to calculate the quantity of VOC (or water) molecules that would adsorb onto the chip during experiments from the experimental  $\Delta R$ . We estimated that  $A$  was similar for all the VOCs and equal to 20. For example, we estimated that a

reflectivity shift of 1% measured for butanol corresponded to  $\sigma = 2.56 \times 10^{17}$  molecules/m<sup>2</sup> = 0.26 molecules/nm<sup>2</sup> adsorbed on the gold surface of the prism. For water, a reflectivity shift of 0.8 % corresponded to an adsorbed quantity of  $\sigma = 10^{18}$  molecules/m<sup>2</sup> = 1 molecule/nm<sup>2</sup>. In both cases, the results seemed plausible, and far from a complete monolayer. Therefore, H1 was relevant in these cases.

This equation could be used on the other hand, to calculate the surface density of probes on the SPRi chip before passivation and any VOC injection. For this, we used the contrast in reflectivity between the sensing materials and gold at the working angle.

$$\chi_R = R_{sensing\ material}(t = 0) - R_{gold}(0)$$

$$\sigma = \chi_R \times \frac{N_A \lambda}{\frac{\partial R}{\partial n} AMV_0} \times 10^6$$

Here, H1 was more debatable since the peptides were expected to be densely deposited on the surface. However, we had no mean to measure the refractive index of a pure liquid peptide. Thus, we worked in this approximation and estimated that  $A$  was similar for all the peptides and equal to 20.

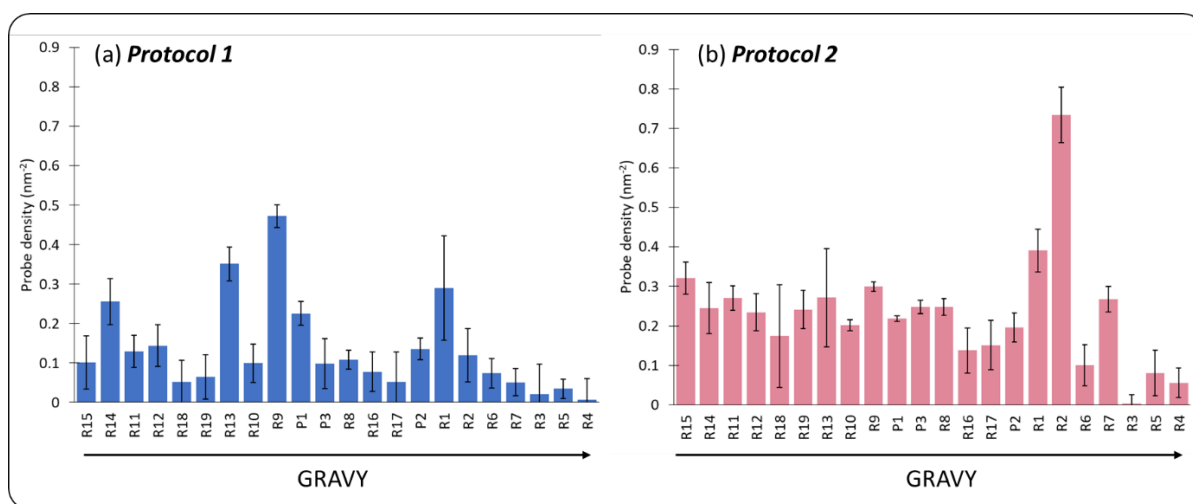


Figure 3-5 (a) Mean surface density of the different probes with protocol 1 (a) or protocol 2 (b). The grand average of hydrophathy (GRAVY) is a scale of hydrophobicity.

The Figure 3-5 presents the surface density of the different probes, spotted on five different chips with the protocol 1 (a) and protocol 2 (b) (see 2.2.1). This density was estimated using the previous equation. With protocol 1, the calculated surface density ranged from 0.04 to 0.4 molecules/nm<sup>2</sup>, with a mean value of 0.13 molecules/nm<sup>2</sup>. The peptide probes typically fit in a 1.5 nm edge box. Thus, the order of magnitude seemed correct for a packed assembly of peptides on the surface. We observed a high variability of the surface density with this protocol. Notably, the peptides with the lowest surface density were the most hydrophobic ones (with the highest

GRAVY), potentially because of their poor solubility in the spotting buffer. Although, it may also result from a stronger probe-probe interaction (attractive vs repulsive). There was no correlation between the molecular weight of the peptides and their observed density on the surface.

To overcome this problem, we established the protocol 2 (Figure 3-5 (b)) with a novel spotting solution, in which all the peptides were highly soluble. With this new protocol, almost all the probes were deposited in a denser fashion (b). The average probe density was 0.23 molecules/nm<sup>2</sup>. The highest improvement was obtained for hydrophobic peptides. In particular, the surface densities of R2, R7 and R4 were multiplied by 6, 5 and 7, respectively. On top of that, the use of Protocol 2 helped to reduce the variability in surface density between probes, even though some hydrophobic probes were still less dense. Finally, it is important to mention that protocol 2 makes the chip fabrication much more reproducible, which is extremely important for industrialization of our optoelectronic nose.

The same calculation performed on an OBP chip, with the same value of A, gave an estimated surface density around 2.6×10<sup>12</sup> molecules/cm<sup>2</sup>. Based on the size of the OBPs, which is typically about 3.5 nm in every dimension, a perfectly dense layer where the proteins would be in contact with each other would have a density of 6×10<sup>12</sup> molecules/cm<sup>2</sup>. Therefore, the calculation seems valid.

In conclusion, this model gave a rough estimation of the density of the probes on the surface of the chip and helped us to improve the functionalization protocol. We can also note that, if we assume that A is the same for all the peptides, independently of their sequence, the density of probes on the sensor surface is proportional to

$$\sigma \propto \frac{\chi_R}{M}$$

This equation provides a quick way to estimate the relative density of the probes and could serve as a normalization method to diminish its influence on the signal. Nevertheless, it rests on the hypothesis that the refractive index of all the probes was proportional to their molecular weight, and that no other optical effect affected the SPR signal. Whereas in reality, polarization for example had an influence on plasmon propagation.

These results must therefore be qualified and compared with an experimental characterization. This will be the subject of the next part.

### 3.2.2. Experimental surface characterization methods

To check the previous theoretical model, and get more precise information on the surface density, we looked for appropriate experimental surface characterization techniques. In addition to the density information, we were interested in knowing the arrangement of the probes on the

surface: structuring, homogeneity, thickness of the layer, *etc.* However, the choice of a method was not straightforward and none of them was perfectly suited since the peptide layers were very thin. Moreover, the gold surface was quite rough and easily contaminated, and the prism was cumbersome. We identified different techniques in the literature to characterize self-assembled monolayers (SAM) of peptides on gold surfaces. They are summarized in Table 3-2. We decided to consider several of them to combine their advantage and overcome their respective limitations.

Characterization technique	Method	Information on the peptide SAM
<b>X-ray photoelectron spectroscopy (XPS)</b>	- Detection of C, N, O, S atoms [250,251] - Attenuation of gold [252]	- Density
	- Angle resolved [250]	- Thickness
	- Position of the S peak [250–252]	- Thiol anchoring
<b>Fourier-transform infrared spectroscopy (FTIR)</b>	- Reflection absorption spectroscopy (RAS) [250,251] or attenuated total reflectance (ATR) [252] - Position of amide I and II bands [250,252]	- Secondary structure of the peptides (helices) - Orientation of the self-assembled monolayer
<b>Atomic force microscopy (AFM)</b>	- Tapping mode [251,253] in ambient air	- Homogeneity [251] - Thickness [253]
<b>Time-of-flight secondary ion mass spectrometry (TOF-SIMS)</b>	- Observation of characteristic ions for the peptides [254,255]	- Relative density (semi-quantitative method) - Orientation and steric arrangement [255]

Table 3-2 Main techniques used in the literature to characterize peptide SAM on gold.

During this thesis project, we have tested X-ray photoelectron spectroscopy (XPS), atomic force microscopy (AFM) and time-of-flight secondary ion mass spectrometry (TOF-SIMS). We benefited from the material and expertise of the nano-characterization platform (PFNC) of CEA Grenoble, France [256]. The results presented below are not conclusive and should be considered as a preliminary study of the interest of these methods for our project.

#### 3.2.2.1. Roughness and homogeneity of the spots with atomic force microscopy

AFM is a very-high resolution scanning probe microscopy [257]. It characterizes the topology of a sample under ambient conditions, with a vertical resolution of less than 1 nm and a lateral resolution around 10 nm. Depending on the tip and the working mode that are used, AFM can also provide information on the properties of the materials on the surface (stiffness, electric potential, magnetization, *etc.*).

The working principle of AFM is quite simple. A sharp tip is mounted on a cantilever, which can optionally be controlled with a piezoelectric actuator. The tip is put in contact, or in very close proximity to the surface, and scans the sample. An optical detector records the deflection of the cantilever as it bends to follow the topology of the surface. In the case of peptide SAM on gold, the Tapping™ mode is preferred in the literature [251,253]. In this mode, the piezoelectric actuator

oscillates the cantilever near its resonant frequency. When the tip approaches the surface of the sample, this oscillation is attenuated, in a way that depends on the nature of the surface [258] .

In our case, AFM was performed directly on the chips used for gas phase SPRi. Previously, Sophie Brenet tried to characterize the peptide chips, in Tapping™ mode. Unfortunately, the high roughness of the gold surface (Figure 3-6 (a)), which approximated 1.5 nm, impeached the visualization of the small peptides on its surface.

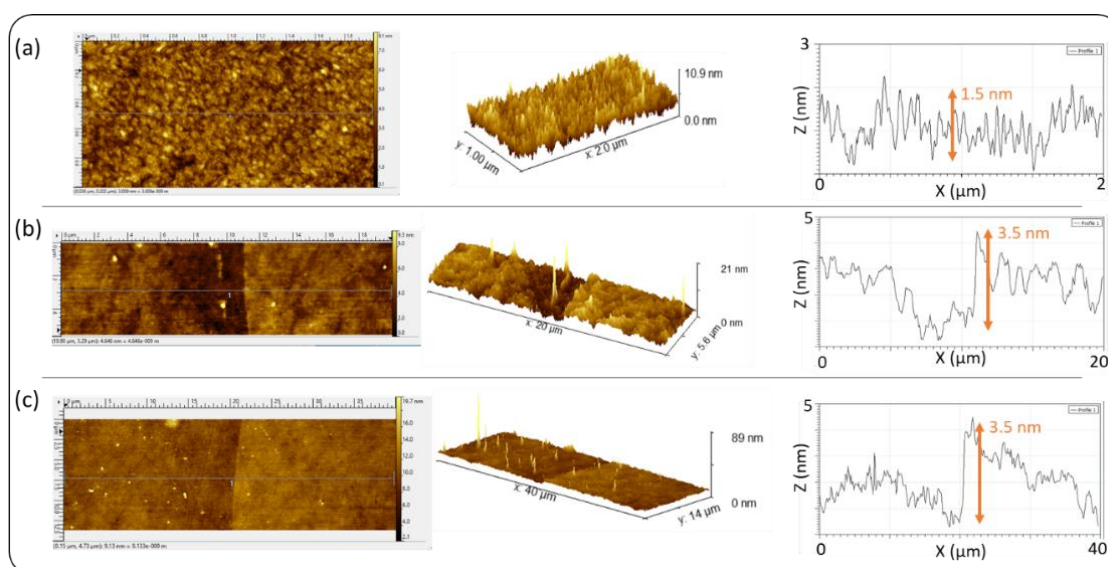


Figure 3-6 AFM images of the topography of (a) the bare gold surface of the prism, (b) a mixed spot of OBP3-a (8  $\mu\text{M}$ ) and PEG (80  $\mu\text{M}$ ) (c) a mixed spot of OBP3-w (8  $\mu\text{M}$ ) and PEG (80  $\mu\text{M}$ ).

During this project, we performed AFM characterization on OBP chips. The proteins are much larger than peptides. In their active conformation, their shape can be approximated by a cube of 3.5 nm edge. The chip that we characterized was prepared with spots of different kind of OBPs (see chapter 4) mixed with poly (ethylene glycol) (PEG, MW  $\approx$  2000 Da). The prism was not passivated. AFM (Dimension ICON, Bruker, USA) images were made at the border of these spots in Tapping™ mode, using a silicon tip (OTESPA-R3, Bruker, USA). They are presented in Figure 3-6 (b) and (c). From what we see, both types of proteins were homogeneously spotted on the prism. The spots had a nice, clear edge, approximately the height of a protein (3.5 nm). The topography inside the spots was similar to that of bare gold, probably revealing a homogeneous layer of proteins. However, based on these preliminary results, it is difficult to determine the shape of the proteins, since no apparent individual protein was observed.

We also made some images in amplitude modulation Kelvin probe force microscopy (KPFM) mode [259,260]. This technique enables to measure the surface electric potential. It is a double-pass mode: the first one allows to record the topography in Tapping™ mode (Figure 3-7 (a)); the second one allows to make the electric potential measurement by reproducing the topography recorded at the first pass while keeping the tip at a height called lift height (typically here 25 nm)

to get rid of the capacitive effects in the potential measurement. We used a silicon tip covered with a metallic layer.

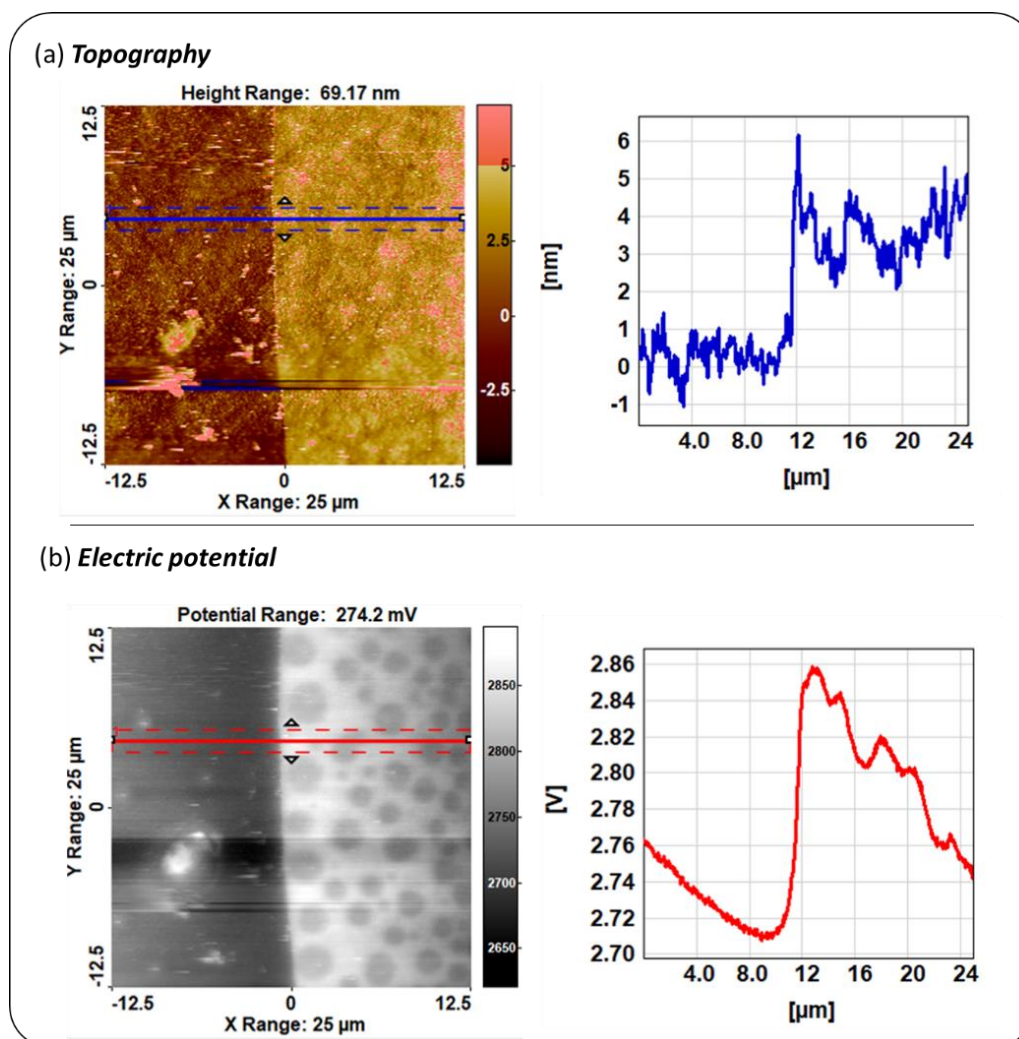


Figure 3-7 KPFM characterization of the border of an OBP spot. (a) First pass: topography. (b) Second pass: electrical potential

On the first images (Figure 3-7 (b)), we can see that this mode was particularly suited to our application. Notably, it highlighted some domains in the OBPs-PEG layers, much larger than the roughness of gold. If this observation was not caused by a surface contamination, it could be explained by two hypotheses. Either the probes were deposited in multi-layers, or there was a phase segregation between PEG and OBPs. However, to go further with this method, an earthed surface should be used to avoid the accumulation of electric charges.

In conclusion, AFM in tapping mode was not efficient enough for the characterization of short peptide surfaces. It would be interesting to repeat these measurements on flatter surfaces such as gold covered mica surface, or in KPFM. For OBP chips, AFM in tapping mode and KPFM already showed interesting results. It could be interesting to dilute OBPs in order to characterize their individual shape on the surface. Moreover, before studying their mixture with PEG, we should

characterize layers of pure OBPs. These studies will be carried out in the near future during the PhD thesis of Marielle El Kazzy.

#### 3.2.2.2. *Density and chemical information on an individual spot by x-ray photoelectron spectroscopy*

X-ray photoelectron spectroscopy (XPS) is a quantitative surface characterization technique [261]. As such, it is the most promising to determine the exact surface density of a peptide on our chip. It measures the elemental composition of a material, and gives information on the chemical neighborhood and electronic state of these elements. Notably, in the literature, it was used to check the anchoring of peptides on gold via thiol chemistry [250–252]. Nevertheless, it usually requires to put the sample in ultra-high vacuum ( $< 10^{-9}$  mbar).

XPS spectra are obtained by irradiating a material with a beam of X-rays of known energy. The photoelectric effect extracts core electrons from the atoms. The ionization energy depends on the element, and so the remaining kinetic energy is a characteristic of this element. In XPS, the number of electrons of a given kinetic energy gives a quantitative information on the number of atoms of one element.

The analysis of a peptide chip by XPS by the PFNC is in progress and we are waiting for the results.

#### 3.2.2.3. *Relative densities and chemical information of several spots by time-of-flight secondary-ion mass spectroscopy*

Time-of-flight secondary-ion mass spectroscopy (ToF-SIMS) is a semi-quantitative surface characterization technique. The images are obtained by bombarding the sample with primary ions in a way to detach secondary ions. These secondary ions are then sent to a mass analyzer, which counts the number of fragments of a given mass over charge ratio. The fragments can be from single atoms to whole proteins. Like for XPS, this requires to work in ultra-high vacuum. ToF-SIMS provides information on the chemical nature of a sample [262].

With the help of the PFNC, we analyzed different peptide spots, and a spot of perfluorothiol (R0). For practical reasons, they were all deposited on the gold surface of a small SPRi prism, adapted for the portable optoelectronic nose developed by Aryballe technologies. The prism was not passivated. The characterization was performed using an ION TOF 5 (ION TOF GmbH, Germany). In our case, ToF-SIMS was quite complementary to the XPS because it allowed a larger field of view to be analyzed. Thus, the direct comparison between the different spots was possible.

The preliminary results are presented in Figure 3-8. The gold surface was almost uniformly covered with elements of hydrogen (b) and oxygen (c), probably resulting from organic contamination. The variations in intensity observed on the first two images (notably the black

stripe in the middle) are instrumental artefacts. Interestingly, there was almost no organic contamination on the spot of perfluorothiol. The fluoride ions were very clearly visible with ToF-SIMS (h). This confirmed that perfluorothiol is a good reference surface (see 2.2.2). There was a small extinction of the gold signal (d) on the R15-peptide spots, but not on the other ones. Thus, it was not a good indicator for the peptide density.

Remarkably,  $\text{NH}^-$  (e) and  $\text{CN}^-$  (f) ions gave a much higher intensity on the peptides than on gold, whatever the nature of the peptides. Therefore, they could be used to characterize the relative surface density. Moreover,  $\text{C}^-$  and  $\text{CH}^-$  (not shown) were also tested, but they did not give as much contrast. Interestingly, we observed a clear peak attributed to a sulfur ion (maybe  $\text{SO}_4\text{H}^-$ ) on the R15-peptide spots (g). Hypothetically, this could correspond to a counter ion that would bind to the peptides during their production or their immobilization on the prism. It has to be verified.

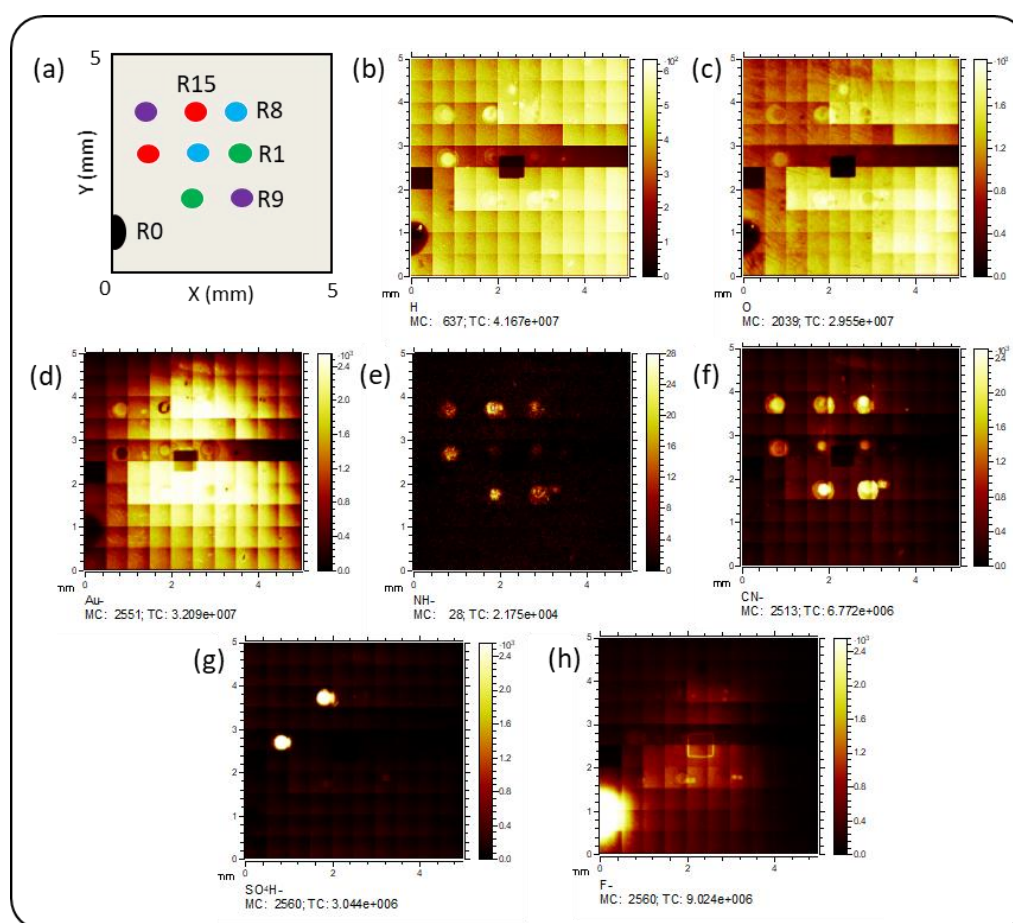


Figure 3-8 (a) Deposition plan. (b) to (h) ToF-SIMS images of the peptide chip for different ions.

In conclusion, these preliminary results show that ToF-SIMS seems to be an interesting method to characterize the relative densities of the peptide spots on the chip surface. Finally, all the characterization methods discussed in this part should be compared and combined to get the most precise information possible. For this, a further study is necessary with optimized conditions.



### 3.3. OPTOELECTRONIC TONGUE FOR VOC DETECTION IN THE LIQUID PHASE WITH IMMOBILIZED PROBES

Thanks to the characterization methods presented above, we had a reasonable idea of the affinity of the probes for their target VOC when they were free in solution. Moreover, we knew these probes were properly deposited on the prism's surface to form the sensing materials. However, their immobilization might modify their structure, and so their affinity with the VOCs. Not to mention the drying of the prisms for the function of the optoelectronic nose in the gas phase, which was a particularly harsh step for peptides and proteins. As a result, in some initial gas-phase VOC detection experiments, the signatures obtained did not match our predictions. To understand the reasons of this deviation, we introduced an intermediary step to characterize the new sensing materials. The goal was to decouple the possible effects of immobilization and drying. For this purpose, we performed SPRi measurements in liquid, and characterized the detection performances of an optoelectronic tongue. This characterization method was particularly interesting, since it used the same kind of chip and the same transduction method.

#### 3.3.1. Working principle of liquid-phase SPRi

Liquid-phase SPRi works exactly like gas-phase SPRi (see 2.4.). A scheme of the setup is given in Figure 3-9 (b). We used a commercial SPRi apparatus (Horiba Scientific, France), placed in an incubator at 25 °C. A collimated, polarized light beam at 647 nm was sent through the prism to illuminate the whole microarray. The analysis of VOCs was achieved at a fixed working angle, determined from the plasmon curves to maximize the sensitivity of all the sensing materials. Upon the injection of a sample, the variations of reflectivity for all the ROIs were simultaneously monitored and recorded with a CCD camera. A measurement was taken every three seconds.

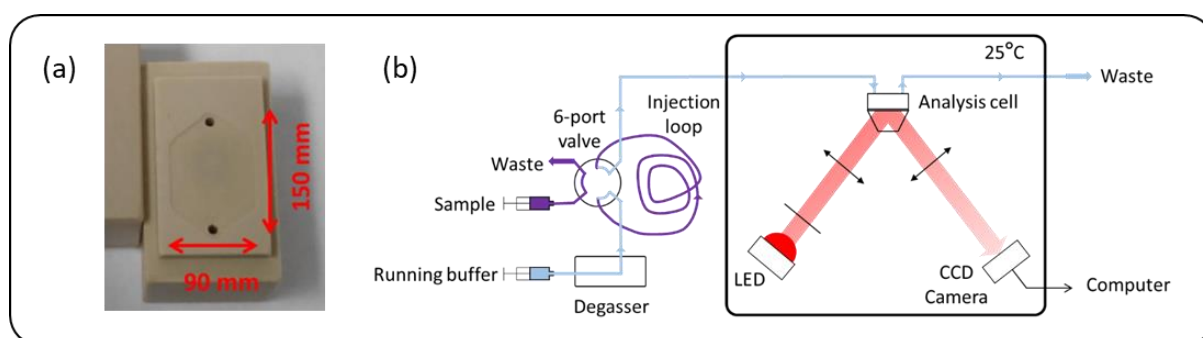


Figure 3-9 (a) Fluidic cell used for liquid-phase SPRi experiments. (b) Schematic setup for liquid-phase SPRi

The prism for the detection in the liquid phase had a slightly different geometry comparing to the one for the detection in the gas phase. However, most importantly, the gold-coated layer on the prism was similar. Thus, it was spotted with the same functionalization protocol as used for the gas-phase prism. Then, the chip was mounted in the polyetheretherketone (PEEK) flow

analysis chamber with hexagonal shape Figure 3-9 (a). This cell was connected to a fluidic system to convey the sample, this time in liquid. A running buffer was pushed in PEEK tubing by a computer-controlled syringe pump (Cavro Scientific Instruments, USA) at a constant flow of 1.56  $\mu\text{L/s}$ . The running buffer was filtered beforehand and passed through a degassing system (Alltech, France) before arrival in the flow cell to avoid dust and air bubbles. Prior to each experiment, all the tubing was rinsed carefully with methanol and water to ensure that no pollutant would remain from previous experiments. Before any sample injection, a blank injection of running buffer was systematically performed to control the cleanliness of the fluidic system. The samples were prepared by diluting pure products in the filtered running buffer. Then, they were manually injected through a six-port injection valve (Upchurch Sci., USA) using a syringe. The volume of the injection loop could be 500  $\mu\text{L}$ , 1 mL or 2 mL.

In the liquid phase, the position effects of the sensing materials on the prism were more significant than in the gas phase. Indeed, the diffusion of VOCs was slower in water than in air. As a result, some regions of the chip, which correspond to the “center” of the flow, received a higher concentration of VOCs. To compensate for this variability, the replicates of a same sensing material were randomly scattered on the chip. The drift was also higher, due to the adsorption of buffer constituents. On top of that, this drift was also higher in the center of the chip. When processing the data, we chose to approximate this drift by a linear regression, which was then subtracted from the signals. Interestingly, and in contrast with gas-phase SPRi, in optimized conditions [263], this relatively lower diffusion makes it possible to use the kinetic profiles to calculate the affinity constants between a probe and a target.

### **3.3.2. Amplification strategies for the detection of small molecules in the liquid phase**

The limit of detection in mass commonly admitted for commercial SPRi apparatus is 200 g/mol. Thus, an amplification was required to achieve a reliable detection of VOCs in the liquid phase.

Interestingly, some previous studies showed that the binding of VOCs might induce local conformational changes in OBPs (Figure 3-10 (a)) [264,265]. As will be detailed in 4.2.2, we hypothesized that this affected the local refractive index, acting as an optical amplification of the liquid-phase SPRi signal [266,267].

However, for the peptides, there was no such phenomenon, or it was too weak to enable VOC detection. We have therefore developed an alternative amplification strategy based on VOC labelling with gold nanoparticles (Figure 3-10 (b)) [268]. The high weight of nanoparticles and their optical properties greatly facilitate SPRi detection, as will be detailed in Chapter 5.

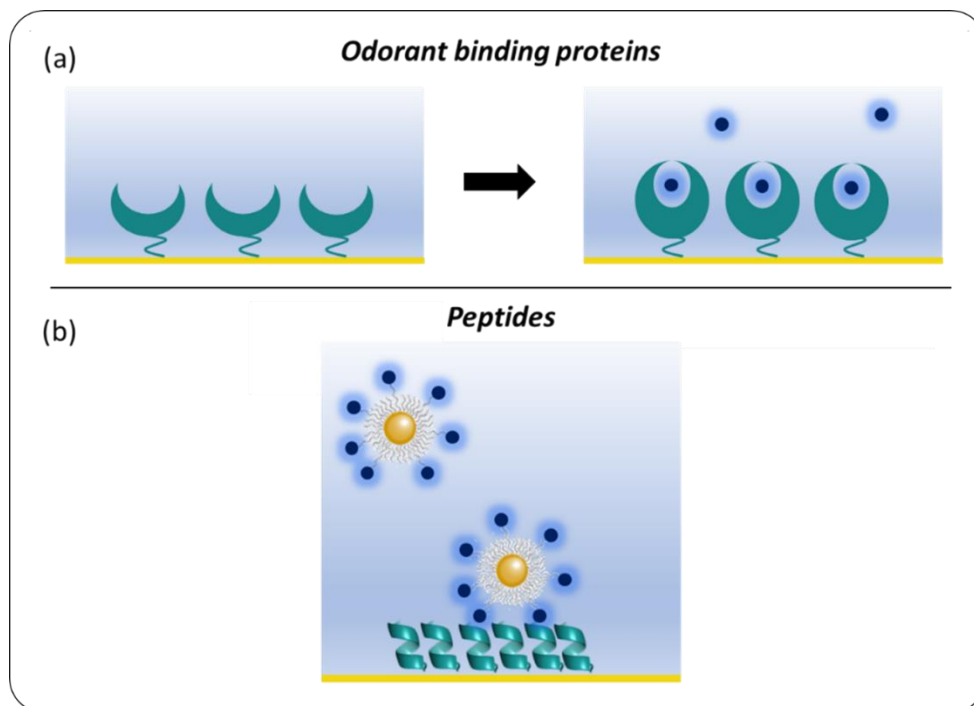


Figure 3-10 Different amplification strategies employed for the optoelectronic tongue. (a) The OBPs may undergo a conformational change when binding a VOC, which amplifies the optical signal. (b) Gold nanoparticles were labeled with VOC molecules; their high mass facilitated the detection in liquid-phase SPRi.

### 3.4. PERFORMANCE ASSESSMENT OF THE OPTOELECTRONIC TONGUE AND NOSE

Eventually, when the probes were successfully characterized and immobilized on the sensor surface, while conserving part of their activity for the binding of VOCs in the liquid phase, the goal of this thesis project was to gauge their interest in improving the performance of the artificial nose. Notably, as explained in the first two chapters, in terms of sensitivity and selectivity. The definition and the estimation of these features are not straightforward, and the establishment of protocols was a work in itself. In our case, this was even truer since we were not only trying to make our artificial nose work, but above all to understand more fundamentally the interactions at stake. In this part, we describe the methods finally implemented to characterize the sensitivity and the selectivity of artificial tongues and noses.

#### 3.4.1. Characterization of the sensitivity

The sensitivity of a sensor qualifies the amplitude of its answer to a given stimulus. It has no consensual definition. It is often confused with the lower limit of detection, *i.e.* the smallest amount of detectable analyte. However, in most cases, it is defined as the derivative of the output signal as a function of the input signal. In our case, the output signal is a variation of reflectivity, and the input signal is a variation of concentration of VOC.

With this definition, each biosensor based on a sensing material  $i$  would have its own sensitivity  $\eta_i$  defined as follow

$$\eta_i = \frac{\partial R(i)}{\partial C}$$

with  $\partial R$  an infinitesimal variation of reflectivity, and  $\partial C$  an infinitesimal variation of VOC concentration.

### 3.4.1.1. Sensitivity to a VOC

Therefore, the most direct method to estimate the sensitivity of the biosensors to a VOC was to perform a set of analyses using a concentration range of this VOC.

Practically, for liquid-phase SP<sub>R</sub>i, the VOC samples were diluted in the running buffer. The achievable range was only limited by the solubility of the hydrophobic VOCs in this buffer. The different dilution methods for gas-phase SP<sub>R</sub>i were explained in part 2.3.1. It could be performed by diluting the evaporated VOC sample in clean air (on the homemade bench or using the computerized calibration system), or by diluting the liquid VOC in mineral oil before evaporation. This characterization had to be performed in the linear region of the artificial nose or tongue, that is to say, in the range of concentration where all the olfactory sensors give a measurable signal to the VOC, and are not saturated by the molecules.

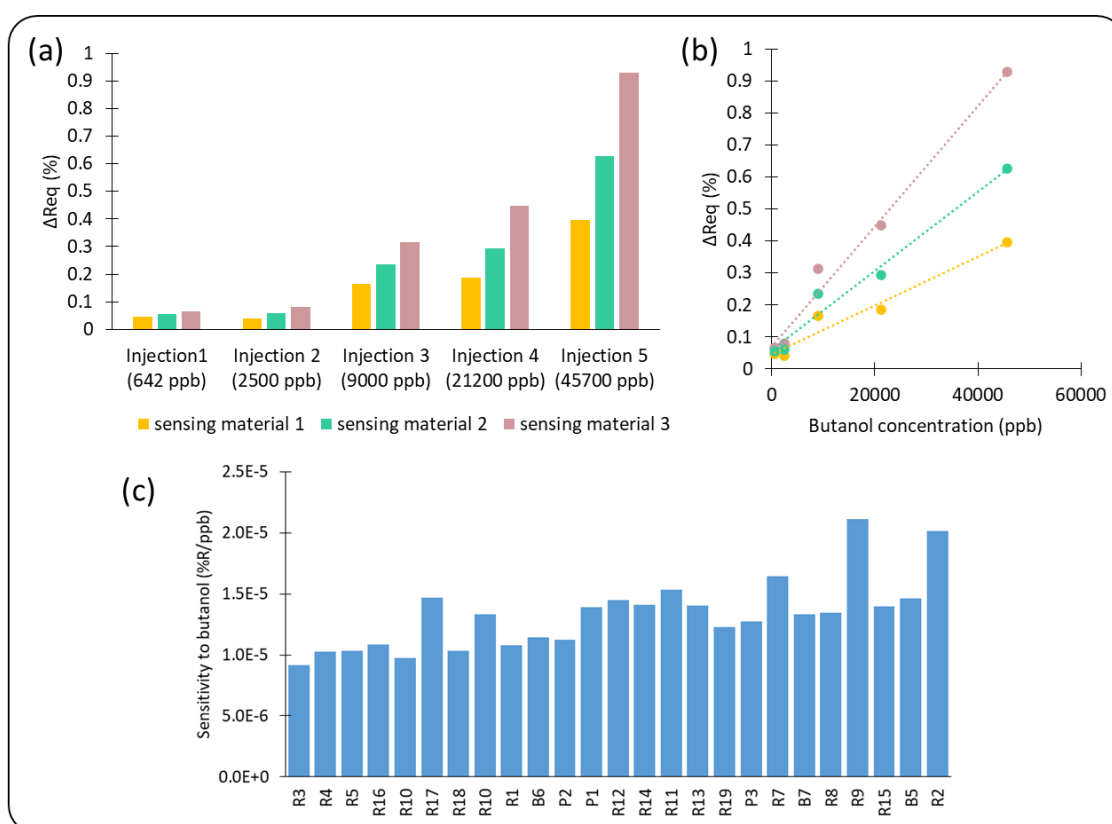


Figure 3-11 (a) Extract of the equilibrium profiles for five injections of butanol at different concentrations. (b) Variation of  $\Delta R_{eq}$  with the concentration of butanol. (c) Sensitivity to butanol of the different sensing materials.

The injections analyzed in Figure 3-11 were performed with the last method. A peptide chip was mounted on the gas-phase SPRi bench to analyze the sensitivities of the different sensing materials to butanol as a reference compound. Indeed, the European Odor Standard recommends the use of butanol (20–80 ppb) as a panelist evaluation and screening tool and for quality criteria for the overall performance of the sensory measurement method. We determined the equilibrium profiles for gaseous butanol injections at different concentrations ranging from 642 ppb to 45700 ppb (Figure 3-11 (a)). The sensitivity to butanol of each sensing material was calculated as the slope of the linear regression of the curve depicting  $\Delta R_{eq}$  as a function of butanol concentration (Figure 3-11 (b)).

In fact, the interaction between a sensing material and VOC molecules is a complex process. The sensitivity that we measured in this part is the reflection of several phenomena, which occur simultaneously. To have a better understanding of what is at stake, we suggested going further in the study of sensitivity in the rest of this part.

Our theoretical model suggests that the measurable variation of reflectivity in SPRi is caused by the adsorption of molecules on the prism surface. When VOC molecules are introduced in the analysis chamber, part of them bind to the sensing materials. It results in a change in the refractive index of this material, which in turn causes the variation of reflectivity through the SPR phenomenon. It is thus interesting to write the sensitivity as the product of three derivatives to reflect the behavior of the system.

$$\eta_i = \frac{\partial R}{\partial C} = \frac{\partial R}{\partial n} \times \frac{\partial n}{\partial \sigma} \times \frac{\partial \sigma}{\partial C}$$

With  $\partial \sigma$  being an infinitesimal variation of the number of VOC molecules adsorbed on the sensing material  $i$  per unit surface and  $\partial n$  being an infinitesimal variation of the refractive index.

- $\frac{\partial R}{\partial n}$  defines the *physical sensitivity*. It is an intrinsic characteristic of the SPRi apparatus that defines how the reflectivity is affected by a bulk change in refractive index. The physical sensitivity depends on the wavelength, the working angle and the prism (gold and adhesive layer). In the ideal case, for a correct adjustment of the optical setup with a correct homogeneous illumination, it should hardly vary between the different sensing materials on a same prism. However, it may slightly vary from prism to prism.
- $\frac{\partial n}{\partial \sigma}$  describes how the addition of molecules on the surface of the sensing material affects the refractive index in the full volume sensed by the SPR. In theory,  $\frac{\partial n}{\partial \sigma}$  depends only on the nature of the VOC and on the penetration depth of the SPR. The theoretical model in 3.2.1.3. accounts for this adsorption phenomenon. Note that VOC binding can

also affect the structure or the polarization of the sensing materials, which would affect the optical signal. We did not determine this factor experimentally.

- $\frac{\partial\sigma}{\partial c}$  depends only on the interaction between the sensing material and the VOC molecules. In the case of a high affinity, the adsorption will be higher, meaning that for a given concentration of the VOC in the analysis chamber, more molecules will adsorb on the sensing material. As a result, the higher the affinity between the sensing material and the VOC, the greater the value of  $\frac{\partial\sigma}{\partial c}$ . As such, it is the most interesting parameter in our study, since it does not depend on the transduction method. This parameter was named *chemical sensitivity*.

In the following, we will explain how the physical sensitivity and the chemical sensitivity were measured or estimated experimentally. To facilitate the visualization, all the figures were made the same day.

#### 3.4.1.2. Physical sensitivity

We explained in the previous chapter (part 2.4.) that a variation of reflectivity in SPRi results from a shift in angle of the plasmon curve. As a result, in the literature, the physical sensitivity is often approximated by the angular sensitivity  $\frac{\partial R}{\partial \theta}$ , through the following equation (see Appendix A-1).

$$\frac{\partial R}{\partial n} = \frac{\partial R}{\partial \theta} \times \frac{\partial \theta}{\partial n}$$

$\frac{\partial \theta}{\partial n}$  quantifies the shift of the plasmon curve due to a bulk phase variation of the refractive index. In making this assumption, it is presumed that this second factor is constant for all sensing materials; whereas in practice, this hypothesis is difficult to verify. It also implies that the variation of reflectivity results only from the translation in angle of the plasmon curve, whilst in reality; the amplitude of this curve could also be crushed or stretched by optical effects.

For all these reasons, we preferred to use a direct method. We showed in part 3.2.1.2 that, theoretically, a bulk change of refractive index  $\Delta n$  in the SPRi analysis chamber resulted in a variation of reflectivity  $\Delta R$ . It provided the experimental method to estimate the physical sensitivity of the different sensing materials: we provoked a controlled  $\Delta n$  in the analysis chamber, and measured the resulting change in reflectivity. To increase the precision, several measurements were averaged.

$$\frac{\partial R}{\partial n} \simeq \frac{\overline{\Delta R}}{\Delta n}$$

Practically, in liquid-phase SPRI, a range of refractive index was performed by mixing glycerol and water in different proportions (Figure 3-12 (a)). The refractive index of the different glycerol solutions was measured thanks to a refractometer (HI 96801, Hanna Instruments, USA). This provided a direct way to measure the physical sensitivity. We presupposed that glycerol did not adsorb on the sensing materials or interact with them. However, the Figure 3-12 (b) shows that it was actually not the case, since the linear regressions do not cross the y-axis at zero. As a result, this calculation was not perfect.

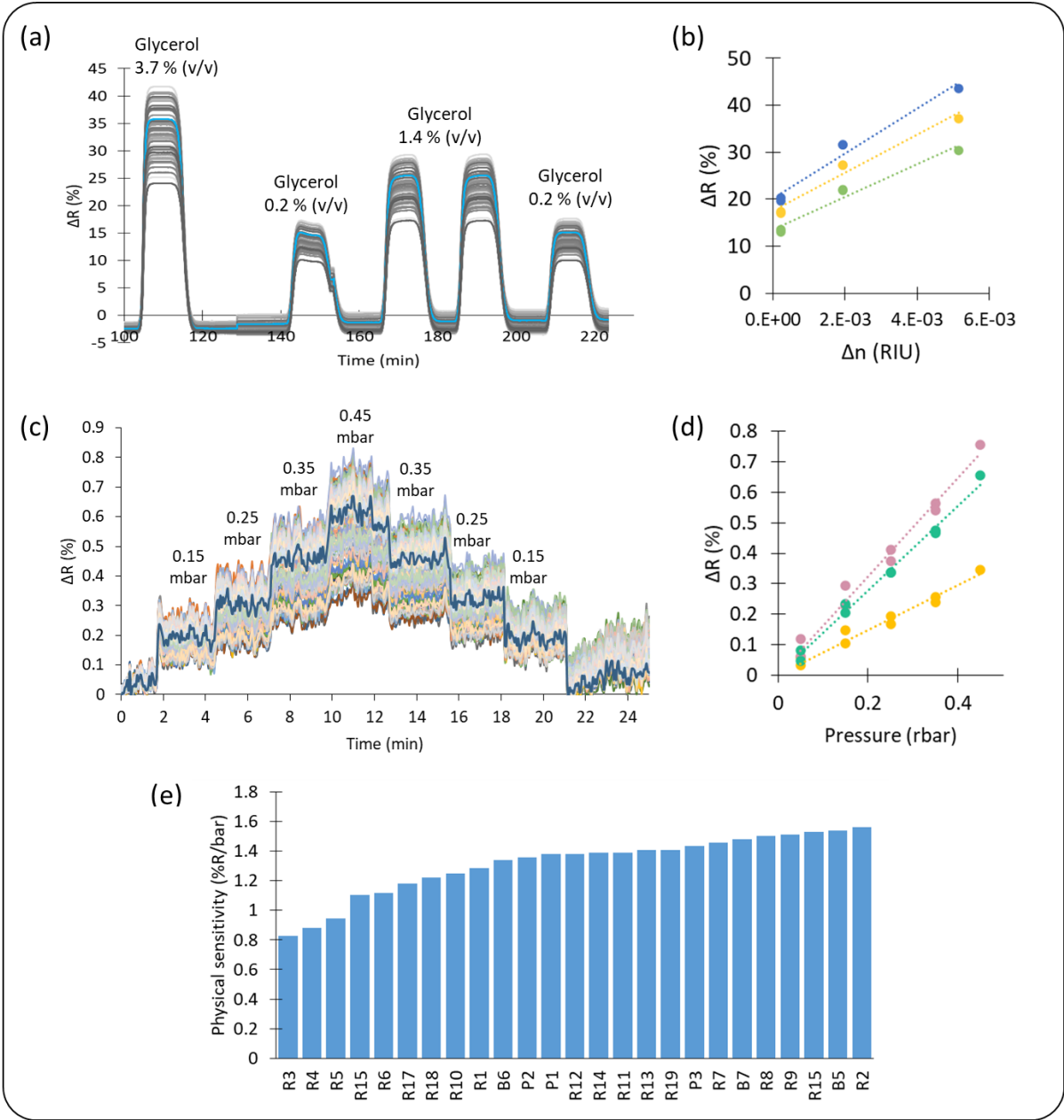


Figure 3-12 (a) Liquid-phase SPRI signal for refractive index jumps. (b) Variation of reflectivity as a function of the relative refractive index for three sensing materials. (c) Gas-phase SPRI signal for pressure jumps. (d) Variation of reflectivity as a function of the relative pressure for three sensing materials. (e) Physical sensitivity for all the sensing materials (in gas).

For gas-phase SPRi, we varied the pressure of the carrier air in the analysis chamber (Figure 3-12 (c)). The Gladstone-Dale relation states that the refractive index of a gas is a linear function of its density [269]. It implies that, in the case of a perfect gas,  $n$  varies linearly with the pressure. In our case, we plotted  $\Delta R$  as a function of the relative pressure (Figure 3-12 (c)) and considered that the slope of the curves gave a good approximation of the relative physical sensitivity of the different sensing materials (Figure 3-12 (d)). To get an absolute value, the observed  $\frac{\Delta R}{\Delta P}$  should be corrected by the known  $\frac{\Delta n}{\Delta P}$  of the carrier gas. For dry air, this last value was calculated by Jonathan Weerakkody as  $2.55 \times 10^{-7}$  RIU/mbar [248]. Satisfyingly, changing the carrier gas from He, dry air, CO<sub>2</sub> or Ar does not affect the measurement of  $\frac{\partial R}{\partial n}$ . Here, we considered air as a perfect gas, and that the effect of pressure on the soft sensing materials was negligible. However, this was apparently not the case, since different physical sensitivities were measured for the different sensing materials.

With this method, we obtained an average sensitivity of  $4.0 \times 10^3$  %/RIU for liquid-phase SPRi and  $5.2 \times 10^3$  %/RIU for gas-phase SPRi, for prisms functionalized under the same conditions. This could be due to a slight difference in the wavelength and in the prisms themselves (glass quality, gold and adhesion layer). In addition to the higher contrast between air and VOCs and the lower noise in the gas phase (see 2.4.1.), the higher sensitivity of gas-phase SPRi contributed to facilitate the detection of VOCs.

This calculation also enabled to check if the setting was right. We aimed to minimize the variations in angular sensitivity between the sensing materials. It also provided a way to determine the chemical sensitivity of the different sensing material, as explained in the next part. It is noteworthy that this method does not take into account the position effect evoked in part 3.3.1. Indeed, a bulk change in refractive index affected homogeneously the whole chip, whereas the adsorption of VOCs on the surface could be locally enhanced by the transport of the molecules, or diminished by a more important pollution. This was particularly true in the liquid phase.

#### 3.4.1.3. Chemical sensitivity

To compare the performance of the different sensing materials, we wanted to make sure that an equal modification of their refractive index would affect equally their reflectivity. Thus, the physical sensitivity was used as a correction factor. This correction was key to assess the real relative chemical sensitivities of the different sensing materials. It was done by dividing the sensitivity to a VOC by the physical sensitivity, since, like explained above,  $\frac{\partial n}{\partial \sigma}$  was independent from the sensing materials.



The Figure 3-13 shows the same data before correction (a) and after correction by the physical sensitivity (b). The chemical sensitivity of a biosensor accounts for the amount of gaseous VOC molecules that adsorb on it, which reflects its affinity for the VOC. It is also impacted by the possible change in the sensing materials (conformation, optical properties, *etc.*) that occurs upon VOC binding. The chemical sensitivity was finally chosen as a performance indicator to characterize a new sensing material.

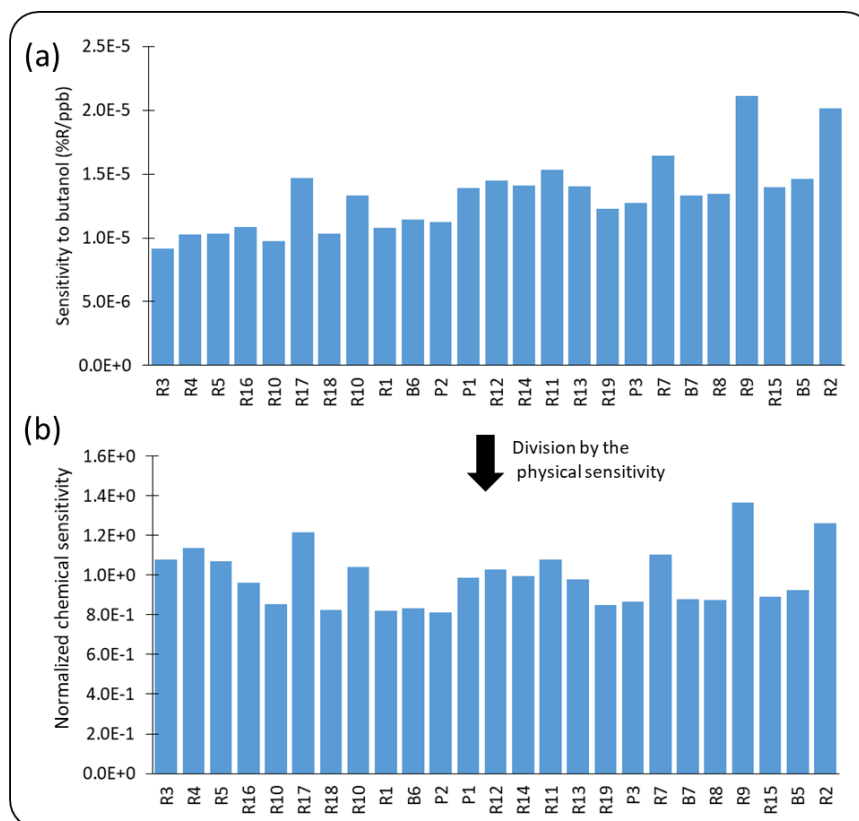


Figure 3-13 Correction made for obtaining the normalized chemical sensitivity of all sensing materials to butanol.

### 3.4.2. Characterization of the selectivity

The second important feature of the new sensing materials that we wanted to characterize was their selectivity. Once again, this notion does not have a perfectly settled definition. It can qualify the ability for the sensor to detect a VOC in a complex sample with certainty. That is to say, without any other admixture interfering with the measurement. In our case, it was rather defined as the quality of a biosensor that has a very different binding affinity with VOC molecules of different families, or even VOCs with very similar structures.

Our approach was then to analyze several molecules with similar structures, one after another, and to show that they had different affinities for the sensing material being tested. For example, to attest the selectivity of peptides screened specifically for a phenyl ring containing VOC target, we would study their interaction with the molecules presented in Figure 3-14. They include

benzene, some other phenyl ring containing VOCs such as monosubstituted molecules with different physicochemical properties and sizes (toluene, phenol, phenylethylalcohol) and disubstituted molecules with the three xylene isomers, and finally methylcyclohexane without phenyl ring but with a cyclohexane ring for negative control.

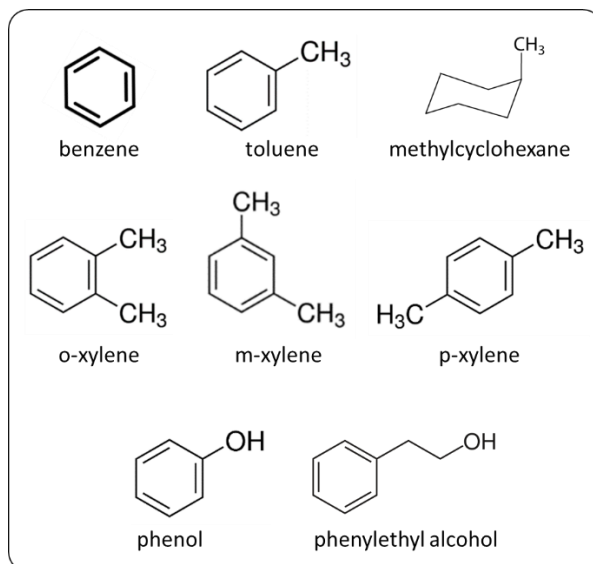


Figure 3-14 Example of a list of molecules studied to assess the selectivity of our sensors to molecules with a phenyl ring.

Experimentally, the main difficulty was that two interaction phenomena occurred between a VOC and a sensing material supposed to be specific for this VOC.

- Specific binding occurs only between a specific probe and its target VOC. The VOC molecules bind to the preferred binding site of the probe, with a relatively high affinity. Since the number of binding sites available in the sensing material are limited, it is characterized by a Langmuir behavior, with a saturation of all the binding sites at high concentration.
- However, the VOC molecules can also bind to the probes outside of their binding site. This non-specific binding with low affinity increases linearly with the concentration of VOCs since the saturation is only approached at very high concentration.

All the different cases are summarized in Figure 3-15 (a) and (b) as a reminder.

The Figure 3-15 (b) illustrates the evolution of the two phenomena with the concentration of a VOC. At low concentration of the target VOC (I), specific binding dominates. Under these conditions, the VOC molecules interact preferentially with the binding site of the probes, for which they have a higher affinity. However, at higher concentration (II), the binding sites saturate. In parallel, VOC molecules adsorb non-specifically on the sensing material thanks to electrostatic interaction, hydrophobic/hydrophobic interaction, hydrogen bond, Van der Waals force, *etc.* In this case, there could most probably be multiple binding on a single probe and the saturation

occurs at much higher concentrations (not shown in the figure). As a result, non-specific binding becomes predominant.

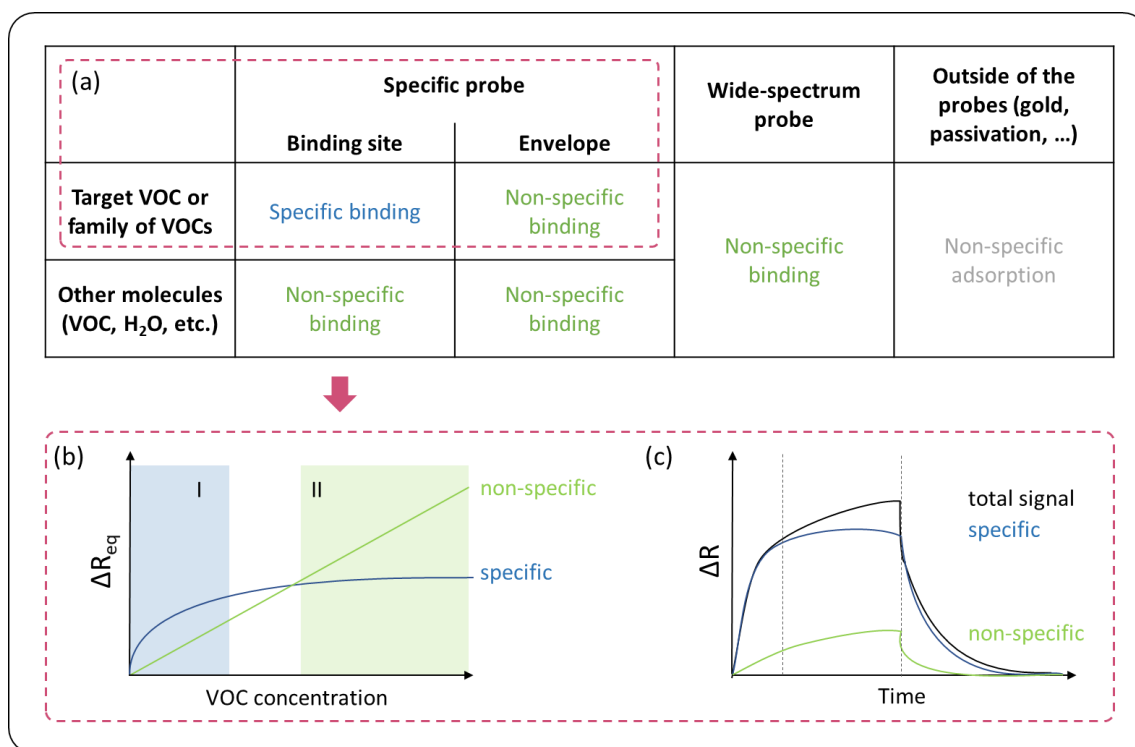


Figure 3-15 (a) Summary of the different terms that will be used in this thesis to describe the interactions between different probes and VOCs. (b) Evolution of specific and non-specific binding with the concentration of VOC. In phase I, specific binding predominates. In phase II, non-specific binding prevails. (c) Kinetic response of a specific biosensor to its target VOC due to combined specific and non-specific binding.

The Figure 3-15 (c) shows how the specific and non-specific binding kinetics cumulated during an injection of the target VOC on its specific biosensor. Since the affinity at stake was usually stronger, it was harder to regenerate a sensing material after specific binding. As a result, the specific component was expected to be predominant in the dissociation phase.

Understanding that, there were several strategies to assess the selectivity of a given olfactory sensor to a VOC. The first one was to use equilibrium profiles at very low concentrations of VOCs (phase I on the Figure 3-15). In this case, the non-specific binding was very low and the specific binding was prevailing. As a result, a specific olfactory sensor would give a measurable signal only for its target VOC, and reversely, the only sensing materials to bind VOC molecules would be the specific ones. Nevertheless, it was not always feasible, either to reach very low concentrations of VOCs, or to get a measurable signal at these concentrations. We could also study the dissociation kinetics. VOCs specifically bound to a probe would dissociate from it at a lower rate.

Nevertheless, the experiments were time-consuming, the lifetime of the chips limited and we needed several injections of the same VOC to perform a statistical analysis of the data. This restrained the range of molecules that we could test on the same biosensors. Thus, docking

simulations with Autodock were particularly interesting to predict the selectivity of the different probes towards a larger range of VOCs and families of VOCs.

The selectivity of an olfactory biosensor must be distinguished from the selectivity of the artificial tongue or nose. In this second case, it was more a question of determining the chemical resolution of the sensor array. Indeed, the purpose of introducing more specific sensing materials was not to restrain the detection spectrum of our array of sensors, but rather to become able to discriminate between similar VOCs. To characterize this chemical resolution, we performed suitable PCA analyses.

As explained in the part 2.5.2., the determination of the principal components PC1 and PC2 is done in such a way as to maximize the variance between individuals (injections). Entering a database with very different VOCs would therefore tend to squash the differences between two very similar VOCs. To assess the chemical resolution of our artificial tongue or nose, we performed PCA on databases containing only VOCs with similar structures. We could then compare the performance of discrimination with or without the new and more specific sensing materials. Analyzing the variable chart was also interesting. Indeed, the projection of variables related to new sensing materials on PC1 and PC2 was a good indicator of their role in this discrimination.

In some cases, we have also carried out PCA on kinetic data, separating the association, equilibrium and dissociation phase to check in which one the separation of similar VOCs was the best. In such a way, we hoped to determinate if specific adsorption improved the performance of our device.



## CHAPTER 4

Protein engineering: using odorant binding proteins  
as sensing materials



## Résumé du chapitre 4 – Ingénierie protéique : utilisation de protéines liant les odorants comme matériaux sensibles

Dans ce chapitre, nous avons cherché à utiliser des protéines liant les odorants (OBP) comme matériaux sensibles pour notre nez optoélectronique. Ces petites protéines solubles du nez biologique lient les COV avec une relativement bonne affinité, de manière réversible. Elles sont robustes aux variations de température et de pH et faciles à produire et à immobiliser sur une puce. De plus, il est possible de modifier leurs propriétés de liaison par mutagenèse dirigée.

Dans ce projet, trois mutants de l'OBP3 du rat avec des propriétés de liaison modifiées nous ont été fournies par le Dr. Loïc Briand (INRAE, Dijon). Nous les avons déposées sur une même puce, et nous avons montré que, dans des conditions optimisées, les protéines conservaient leurs propriétés de liaison après immobilisation. Nous avons ensuite testé les performances de cette puce à OBP pour la détection de COV en solution et en phase gazeuse.

En solution, les différents biocapteurs olfactifs ont permis d'atteindre des limites de détection très basses à la fois en concentration (200 pM de  $\beta$ -ionone) et en masse moléculaire de COV (100 g/mol pour l'hexanal). Une telle performance obtenue par SPRi en phase liquide est particulièrement remarquable. Nous avons émis l'hypothèse que la liaison des COV aux sites actifs des OBP induisait un changement de conformation local dans les protéines. Un tel changement pourrait avoir donné lieu à une variation de l'indice de réfraction, à laquelle la SPRi est extrêmement sensible. En outre, ces biocapteurs olfactifs ont démontré une grande sélectivité, en particulier pour de faibles concentrations de COV. Avec des procédures de régénération optimisées, la répétabilité était très satisfaisante, non seulement d'une mesure à l'autre, mais aussi d'une puce à l'autre avec une durée de vie pouvant atteindre presque deux mois. Ces biocapteurs olfactifs sont donc particulièrement intéressants pour la détection de traces de COV en solution.

Le passage en phase gazeuse représentait un réel défi pour conserver la structure et donc la fonction des OBP. Nous avons démontré que travailler en air humide permettait de faciliter ce passage. L'effet de l'humidité sur les biocapteurs a été caractérisé. Une fois les conditions de travail optimisées, le nez optoélectronique permet une bonne discrimination des COV en phase gazeuse à partir de données SPRi cinétiques. C'est un résultat prometteur, puisque trois matériaux sensibles à base d'OBP, dont deux différant d'un seul acide aminé, suffisent à permettre cette séparation. Une réflexion a été engagée pour comprendre les phénomènes impliqués dans cette bonne résolution chimique. Les premiers résultats tendent à confirmer que les différentes propriétés de liaison des trois mutants étaient nécessaires. Nous avons transféré avec succès cette



puce dans le dispositif industriel NeOse Pro commercialisé par Aryballe, sans altération notable de ses performances.

## CHAPTER 4 Protein engineering: using odorant binding proteins as sensing materials

Thanks to great progress in the fields of biology, genetic engineering and biotechnology, it is now possible to use whole proteins as sensing materials. These bio-receptors are very promising for the analysis of VOCs with a high sensitivity and selectivity [270,271]. As we have shown in the first chapter, in the literature, two families of proteins from the olfactory system of animals have particularly garnered attention for their role in the design of olfactory biosensors: olfactory receptors [272–274] and odorant binding proteins [51,275–278]. However, the stability and function of membrane proteins such as ORs can be easily lost after their immobilization onto a sensor. Moreover, their mass production and purification are still complicated today. In contrast, OBPs are ideal candidates for such applications [279]. First, they are more stable to temperature and pH change, organic solvents and proteolytic digestion. Second, they are soluble and thus easy to produce and purify. Finally, their binding properties can be tailored through site-directed mutagenesis.

Vertebrate OBPs are small soluble proteins of the lipocalin family (~20 kDa), highly secreted in the olfactory mucus covering the olfactory epithelium. They have a calyx structure with eight beta-sheets forming a hydrophobic binding pocket, in which they reversibly bind VOCs with dissociation constants in the micro-molar range. Although the physiological role of OBPs is not completely elucidated, one of their speculated functions is to transport VOCs through the aqueous mucus, release them to ORs, and even facilitate their interaction with ORs [280].

In some species, for instance porcine and bovine, OBPs are broadly tuned and capable of binding numerous odorants. In contrast, in rats, three OBP subtypes have been identified with complementary binding spectra [281]. Rat OBP1 binds with heterocyclic compounds such as pyrazine derivatives, OBP2 is specific for aliphatic aldehydes and carboxylic acids, while OBP3 interacts with VOCs possessing saturated and unsaturated ring structures. Herein, OBP3 was chosen as a base to design three different recombinant proteins. The amino acid residues composing the binding pocket of the rat OBP3 were modified to create synthetic OBPs with various binding properties.

To date, only a very few olfactory biosensors described in the literature used more than one kind of OBP. Di Pietrantonio and colleagues used a combination of two bovine and one porcine OBPs [44], and Kotlowski and collaborators made slight modifications of an insect OBP to improve its orientation and rigidity [276]. To our knowledge, this was the first time that custom-made OBPs with controlled binding properties were used for the development of olfactory biosensors.

	<i>Sensing material (expression sys.)</i>	<i>Transduction</i>	<i>Phase</i>	<i>Odorants</i>	<i>Linear range</i>	<i>Limit of detection</i>	<i>Sensitivity</i>
<b>Hou et al. (2005)</b> [51]	Rat OBP (yeast)	Electrochemical impedance spectroscopy (EIS)	gas	isoamyl acetate			
<b>Cannata et al. (2012)</b> [52]	Bovine OBP ( <i>E. coli</i> )	Solidly Mounted Resonator	gas	Octenol	7-27 ppm	7 ppm	600 Hz/ppm
<b>Zhao et al. (2012)</b> [282]	Mosquito OBP ( <i>E. coli</i> )	Film Bulk Acoustic Resonator	gas	N,N-diethyl-met-atoluamide			
<b>Di Pietrantonio et al. (2013)</b> [44]	Bovine OBP ( <i>E. coli</i> ) Mutant of bovine OBP ( <i>E. Coli</i> ) Porcine OBP	Surface Acoustic Wave (SAW)	gas	Octenol Carvone	13-61 ppm 9-80 ppm	13 ppm 9 ppm	25.9 Hz/ppm 9.2 Hz/ppm
<b>Di Pietrantonio et al. (2013)</b>	Porcine OBP	SAW	gas	Octenol Carvone	9-60 ppm	0.48 ppm 0.72 ppm	20.7 Hz/ppm 13.8 Hz/ppm
<b>Di Pietrantonio et al. (2014)</b>	Bovine OBP ( <i>E. coli</i> )	SAW	gas	Octenol Carvone	5-25 ppm 5-25 ppm	0.2 ppm 0.2 ppm	48.6 Hz/ppm 51.4 Hz/ppm
<b>Lu et al. (2014)</b> [283]	Bee OBP ( <i>E. Coli</i> )	EIS	liquid	methy-p-hydroxyl benzoate isoamyl acetate 4 floral VOCs	1 µM – 1 mM	µM	
<b>Manai et al. (2014)</b> [278]	Porcine OBP	Diamond MEMS	liquid	IBMP 2,4-DNT	6 µM - 1.3 mM	0.1 mM	3 / M
<b>Di Pietrantonio et al. (2015)</b> [55]	Bovine OBP ( <i>E. coli</i> ) Mutant of bovine OBP ( <i>E. Coli</i> ) Porcine OBP	SAW	gas	Octenol Carvone	13-61 ppm 9-43 ppm	2.02 ppm 0.74 ppm	4.95 Hz/ppm 13.5 Hz/ppm
<b>Larisika et al. (2015)</b> [122]	Bee OBP ( <i>E. Coli</i> )	FET	liquid	Floral VOCs	100 nM - 250 µM		
<b>Lu et al. (2015)</b> [284]	Fly OBP ( <i>E. Coli</i> )	EIS	liquid	Fruity and floral VOCs	0.1 µM - 0.1 mM	80 nM	0.01/M
<b>Zhang et al. (2015)</b> [127]	Bee OBP ( <i>E. Coli</i> )	Localized SPR	liquid	β-ionone Butanedione Acetic acid Explosives	10 nM- 1 mM	26.7 pM	
<b>Lu et al. (2016)</b> [285]	Human OBP ( <i>E. Coli</i> )	Impedance measurement in nanopores	liquid	Aldehydes Fatty acids	10 <sup>-8</sup> -10 <sup>-5</sup> mg/mL	10 <sup>-9</sup> mg/mL 10 <sup>-12</sup> mg/mL	1.9% / 1 mg/mL 1.3% / 1 mg/mL
<b>Gao et al. (2017)</b> [182]	Fly OBP ( <i>E. Coli</i> )	CMOS-compatible Silicon Nanowire Array	gas	Nonanoic acid	10-70 ppb	10 ppb	
<b>Lu et al. (2017)</b> [286]	Human OBP ( <i>E. Coli</i> )	Screen-printed electrodes	liquid	Docosahexaenoic acid Linoleic acid Lauric acid	10 <sup>-8</sup> -10 <sup>-4</sup> mg/mL	6x10 <sup>-11</sup> mg/mL 10 <sup>-9</sup> mg/mL	
<b>Kotlowski et al. (2018)</b> [108]	Bee OBP ( <i>E. Coli</i> ) + two mutants	FET	liquid	14 VOCs		10 µM	
<b>Gao et al. (2020)</b> [54]	Three mosquito OBPs ( <i>E.coli</i> )	Silicon nanowire array	gas	Carboxylic acids Geranylacetone Methyl dodecanoate Linalool		2 ppb	

Table 4-1 Description and performances of OBP-based biosensors in the literature.

The different OBP-based olfactory biosensors developed to date are listed in Table 4-1. So far, different transduction techniques have been used, including electrochemical impedance [51,285],

field-effect or capacitance-modulated transistors [276,287,288], localized surface plasmon resonance [289], micro-cantilevers [278], surface acoustic wave (SAW) [55], and solidly mounted resonators [52]. These studies showed that OBPs were stable and active after the immobilization and the obtained biosensors are efficient for VOC analysis both in the gas phase and in the liquid phase. It is noteworthy that in the literature, none of the OBP-based biosensors utilized surface plasmon resonance imaging for the detection of VOCs.

During this thesis project, we challenged the sensing of VOCs by SPRi both in the liquid phase and in the gas phase. In this aim, we used several OBPs with varying binding affinities towards different classes of VOCs. The proteins were immobilized on gold-prism chips in a microarray format. First, we ensured the feasibility of VOC detection and discrimination in solution by SPRi. Then, we used the same design of chip in the gas phase. We finally assessed the sensitivity and selectivity of the fabricated electronic tongue and nose.

The content of this chapter has been the subject of two publications [267,290] and oral presentations in national [291,292] and international conferences [290,293]. Based on results obtained in this work, a collaborative research project was funded by ANR OBP-Optinose (ANR-18-CE42-0012-01).

## 4.1. FABRICATION OF OBP-CHIPS

---

### 4.1.1. General information on the OBPs used in this project

The OBPs used in this project were provided by Dr Loïc Briand (INRAE, Dijon, France).

Three derivatives of the third rat odorant binding protein (OBP3) were used in this work, including a “wild type” protein (named OBP3-w), and two modified proteins named OBP3-a and OBP3-c. The binding properties of these proteins were customized by modifying the amino acid residues of their binding pockets.

- OBP3-w corresponds to the natural OBP3, which binds preferentially aromatic compounds.
- The OBP3-a variant was designed by introducing a lysyl residue in the binding pocket of the wild type protein. This modification was inspired by the human OBP, to which this residue confers a higher affinity for aldehydes through the formation of H-bond with the added amine function [294]. Thus, the affinity of OBP3-a towards aldehydes is improved.
- For the last derivative OBP3-c, two bulky amino acids were introduced in its binding pocket. Consequently, the binding site is cluttered and it is incapable of binding any VOCs. Herein, it was used as a negative control.

In addition, a histidine tag (His-tag) and a cysteine were included at the N-terminal end of the three OBPs. The His-tag enabled their purification using immobilized metal affinity chromatography (IMAC), and the cysteine ensured their immobilization by self-assembly on the gold surface of the prism. Importantly, the N-terminus is located opposite the entrance of the binding pocket, so anchoring the protein at this point should promote its correct orientation on the sensor. A schematic representation of an OBP3 mutant is given in Figure 4-1. These proteins are approximately the size of a 3.5 nm-edge cube.

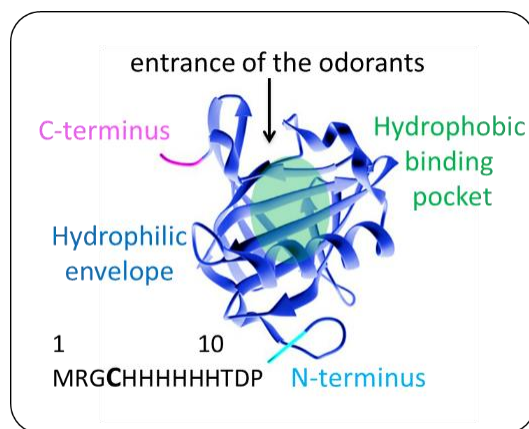


Figure 4-1 Schematic representation of the structure of the OBPs used in this project.

The general method used for the production, purification and characterization of such recombinant proteins was previously described [275,295]. Briefly, the mutants were expressed in the intracellular medium of genetically modified bacterial strains of *Escherichia coli* M15. The bacteria were then separated from the culture medium by centrifugation, and lysed to release proteins. Eventually OBPs were purified by IMAC.

When immobilized on IMAC columns, the OBPs were rinsed in order to make sure that their binding pocket was empty. Indeed, they were likely to bind any small hydrophobic molecule present in the medium. Proteins were usually stocked in a phosphate buffer ( $\text{NaH}_2\text{PO}_4$  50 mM, pH 7.5), that allowed them to be stable and keep their tridimensional structure. The washing principle developed by Loïc Briand's team was to expose OBPs to a more denaturing environment, adding organic solvents to the buffer in order to slightly and reversibly "unfold" them. In such a way, they released the molecules trapped in their binding pocket, whose solubility in buffer was also facilitated. This procedure inspired the regeneration process used during this study.

The affinity of OBPs towards contaminants implied harsh restrictions on the conditions of their manipulation. It was one of the main difficulties of this project. Indeed, OBPs had to be protected from any VOC to avoid their contamination by unwanted compounds. All experimental containers had to be made of glass, as plastic could release trace of organic compounds in the solutions, and washed with great precautions. All buffers had to be prepared with extremely pure

water, with the same quality as for liquid chromatography and mass spectroscopy experiments (LC-MS grade). During experiments, the OBPs were kept on ice or at 4°C whenever it was possible to restrain their activity. More classically as far as proteins are concerned, it was important to keep good pH and saline conditions (OBP3 loses its activity at pH < 6.0).

The protein purity was assessed by SDS-PAGE (sodium dodecyl sulfate–polyacrylamide gel electrophoresis). The binding properties of the three OBPs for different VOCs were measured using ITC at 25°C (see 3.1.2), which revealed a 1:1 stoichiometry for binding. The dissociation constant at equilibrium  $K_d$  obtained for the VOCs used in this chapter with OBP3-w and OBP3-a are summarized in Table 4-2. IBMP stands for 3-Isobutyl-2-methoxypyrazine.

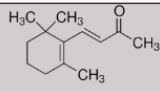
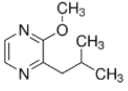
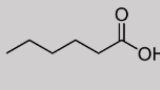
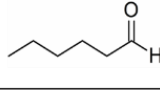
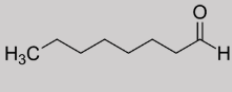
Odorant	Skeletal formula	Molecular weight (g/mol)	$K_d$ with OBP3-w ( $\mu\text{M}$ )	$K_d$ with OBP3-a ( $\mu\text{M}$ )
$\beta$ -ionone		192.3	0.18	0.52
IBMP		166.22	0.27	4.2
Hexanoic acid		116.16	* Negative control	* Negative control
Hexanal		100.16	4.6	0.026
Octanal		128.21	0.86	0.008

Table 4-2 Characteristics of the VOCs used in this study and their respective dissociation constants at equilibrium with OBP3-w and OBP3-a, determined in solution by ITC.

#### 4.1.2. Immobilization of OBPs on the chip

The OBPs have a much higher molecular weight than the peptides historically used in our optoelectronic nose. For this reason, it would have been impossible to find a suitable SPRi working angle for both the peptides and the OBPs. As a result, this preliminary study was led on chips dedicated to OBPs. In the long term, we could either extract high-affinity peptides from the binding pockets of OBPs, or develop more proteins with various binding properties to enable the wide-spectrum detection of VOCs. These strategies will be explored in the framework of the ANR project OBP-Optinose. The objective of this chapter was to provide a proof-of-concept of the value of these probes in the development of new sensing materials for SPRi-based tongues or noses.

Whether for the detection of VOCs in the liquid or gas phase, the OBPs were similarly immobilized in a microarray format onto a prism. The detailed functionalization protocol was given in 2.2.1 (Protocol 3). An important point of this protocol is that, contrary to peptides, the

OBPs were never dried with argon, for fear of denaturing them. In the case of the liquid-phase SPRi chip, the prism was stored in phosphate buffer (50 mM NaH<sub>2</sub>PO<sub>4</sub>, pH 7.5) before use, at 4 °C. The gas-phase SPRi chip was stored in a humid chamber (relative humidity of 30%) at 25 °C.

Preliminary tests were led to optimize spotting conditions. Notably, the density of OBPs grafted on the microarray was a key point. In an ideal case, the proteins would form a well-organized monolayer with their binding pockets pointing upwards to facilitate the access of VOCs. If the density of OBPs was too weak, the adsorbed quantity of VOC would be low. It could be critical for the analysis of small VOCs by SPRi. On top of that, the layer could not be dense enough to ensure steric and electrostatic repulsion between the proteins, resulting in OBPs being badly orientated and binding sites being less accessible. Furthermore, in this case, since the chips were not passivated, the gold surface may not be completely blocked, allowing non-specific adsorption (see 2.2.2). On the contrary, if the concentration of proteins was too high, the formation of additional disordered layers could be favored. In this case, the proteins on the top layer would have random orientation and may block access to the binding sites of the proteins in the underlayer. Moreover, it would be difficult to prepare reproducible biosensors under such conditions.

To optimize the density of OBPs, four concentrations of OBP3-w and OBP3-a (2 μM, 4 μM, 8 μM and 16 μM) were tested in the spotting solution. As shown in the SPRi image (Figure 4-2 (a)), the spots obtained after protein self-assembly at different concentrations were not identical. For the highest concentration at 16 μM, non-homogeneous spots with a halo and even coalescence with other spots nearby were observed. It is likely that at this concentration additional disordered layers were formed. During the rinsing or storage of the prism in phosphate buffer, the proteins from the top layer tend to spread and self-assemble around the spot to form the halo.

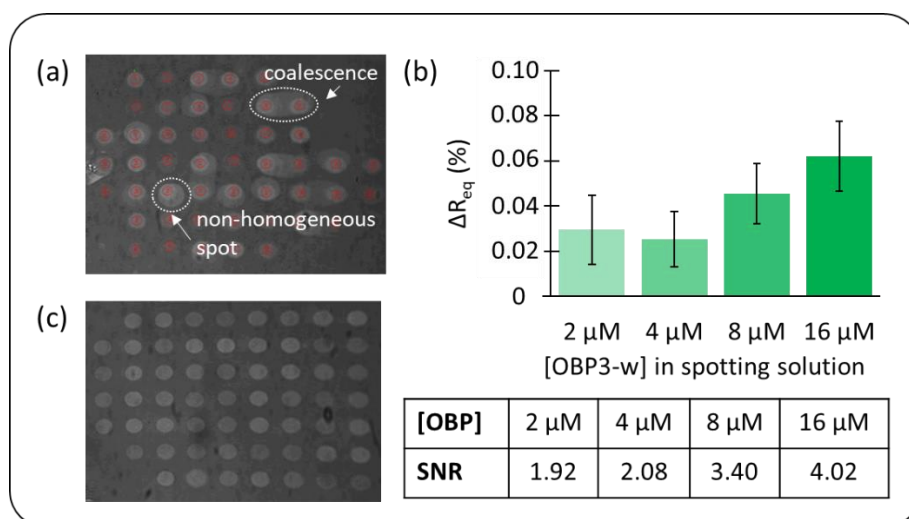


Figure 4-2 (a) SPR image of the microarray after self-assembly of the OBPs at different concentrations (2 μM, 4 μM, 8 μM and 16 μM), showing non-uniform spots. Red circles define the ROIs. (b) Effective signals obtained with OBP3-w immobilized at the four different concentrations and after exposure to β-ionone (200 pM). The corresponding signal-to-noise ratio (SNR) values are presented in the table below. (c) An SPRi image of all the spots obtained after self-assembly of OBPs with the optimized concentration (8 μM).

The signal-to-noise ratio (SNR) was used as an indicator for the VOC detection ability of the sensors. It was defined from the mean signal and the standard error between replicates of the same OBP at the same functionalization concentration (see 4.2.1). When the microarray was put in contact with  $\beta$ -ionone at 200 pM in solution (Figure 4-2(b)) the SNR was below 3 for the spots of OBP3-w deposited at both 2  $\mu$ M and 4  $\mu$ M. Thereby, these signals were considered as unreliable, probably due to a too low density of OBPs on the prism, as mentioned earlier. For all the spots of OBP3-w deposited at 8  $\mu$ M and 16  $\mu$ M, the SNR was above three. Thus, in both cases the signals were valid.

Taking into account these two observations, we assumed that at 8  $\mu$ M, a dense monolayer was formed, since an additional layer would have spread around, as at 16  $\mu$ M, and a monolayer not dense enough would have led to a weaker signal. Thus, the microarray was prepared using spotting solutions at 8  $\mu$ M for all the OBPs for the following study. Six replicates of the same sensing material were randomly disposed on the prism to limit position effect. Satisfyingly, all the obtained spots were dense, homogeneous and uniform (Figure 4-2 (c)). The first AFM measurements that we performed on the OBP chips tended to confirm this observation (see 3.2.2.1). Thanks to the theoretical model described in 3.2.1, we estimated a surface density of  $1.5 \times 10^{12}$  proteins/cm<sup>2</sup>, which is very close to the value that could be reached for 3.5 nm edge proteins packed in contact with each other ( $6 \times 10^{12}$  proteins/cm<sup>2</sup>).

## 4.2. OBP-BASED OPTOELECTRONIC TONGUE

---

As a first step, we wanted to make sure that the three OBP mutants kept their activity once immobilized on the chip. Thus, we evaluated the performance of the obtained olfactory biosensors for the detection of VOCs in the liquid phase. We have determined their sensitivity, selectivity, repeatability and stability.

### 4.2.1. Particularities of the protocol and data processing

All the solvents used in this study were LC-MS grade to avoid any possible contamination by undesired VOCs that may block the binding sites of OBPs.

The prism with immobilized OBPs was mounted into a 10  $\mu$ L PEEK flow cell with hexagonal shape. We used filtered phosphate buffer (50 mM NaH<sub>2</sub>PO<sub>4</sub>, pH 7.5) as running buffer. VOC samples were prepared by diluting pure products in this running buffer. The injection loop volume was 1 mL.  $\beta$ -ionone, selected as a reference compound, was injected systematically at the beginning and the end of any session in order to assess the functionality and stability of the chip with time.

As explained in 3.3.2, the detection was challenging without external amplification. Indeed, the detection limit of commercial liquid-phase SPRi devices is around 200 g/mol, which is larger



than the size of the target VOCs used during this project (Table 4-2). As a result, the signal was very weak, and the drift and the noise tended to overwrite it. To overcome this limitation, the data processing was slightly adapted. Assuming that the drift was linear with time, it was evaluated and subtracted to the signal for each spot. The signals obtained on the six replicated biosensors based on the same OBP mutant were averaged, and a standard error was calculated between them. The average reflectivity given by the spots of OBP3-c, used as negative control, was subtracted to the signals of OBP3-w and OBP3-a at all time. It allowed to get rid of refractive index variation effects. These effective signals were used for the calculation of the SNR. The noise value was calculated using the following equation, with *StdError* the standard error calculated between the N replicates.

$$Noise = \frac{StdError}{\sqrt{N}}$$

In this way, the calculated value gave a direct indication of the repeatability between replicates on the same chip. The SNR was then calculated by dividing the effective signal by the noise. The effective signals obtained with OBP3-w and OBP3-a were considered valid if the SNR was above three.

A one-minute rolling average was performed on the curves presented herein. All the experiments presented thereafter were performed on at least three different chips.

#### 4.2.2. Detection of VOCs in solution

The efficiency of SPRi for VOC sensing in solution was assessed using three VOCs:  $\beta$ -ionone, hexanoic acid and hexanal. Their characteristics are presented in Table 4-2.  $\beta$ -ionone is an aromatic compound found in a variety of essential oils, contributing significantly to the odor of violets and the taste of raspberries. It can bind to both OBP3-w and OBP3-a but with a higher affinity for OBP3-w. It was chosen as the reference VOC during this experimental phase. On the contrary, hexanal whose scent resembles that of freshly cut grass was shown to bind preferentially to OBP3-a in solution. As for hexanoic acid, a carboxylic acid with a fatty and cheesy odor, it did not bind to any of the three recombinant proteins during ITC tests. Therefore, it was used as a negative control.

The three VOCs ( $\beta$ -ionone at 68 nM, hexanal at 2.3  $\mu$ M, hexanoic acid at 680 nM) were successively injected onto the microarray. For being able to compare the obtained signals, we worked with concentrations corresponding approximately to 0.5 times the  $K_d$  measured in solution by ITC (see Table 4-2). However, we have to keep in mind that, obviously, the  $K_d$  may be highly impacted by the immobilization of the proteins on the chip. For hexanoic acid, which is the negative control, it was injected at a concentration ten times higher than the reference,  $\beta$ -ionone. Their interaction with the three OBPs was simultaneously monitored by SPRi. The effective kinetic

responses for the biosensors based on OBP3-w and OBP3-a are presented in Figure 4-3. For example, with  $\beta$ -ionone at 68 nM (Figure 4-3 (a)), nothing happened during the first 4 minutes following the injection. It corresponds to the time needed for the sample to go through the injection valve and reach the microarray. As soon as the sample came into contact with the olfactory biosensors, the reflectivity of the spots of OBP3-w and OBP3-a increased (compared to the reflectivity observed on the control spots of OBP3-c) and reached equilibrium about 10 minutes after the injection. Then, when the injection loop was empty (here, after 10 minutes in the case of  $\beta$ -ionone for a 1 mL loop and 20 minutes in the case of hexanal for a 2 mL loop), the chip was rinsed *in situ* with the running buffer, resulting in the release and desorption of some of the VOC molecules. In this phase, a decreasing signal was observed most of the time, depending on the regeneration efficiency (see 4.2.3).

In order to confirm that these signals resulted from the binding of VOCs to OBPs rather than physical sensitivity differences between the spots of different protein derivatives (see 3.4.1), hexanoic acid (negative control) was injected and analyzed. Indeed, in practice, any injection of VOCs induced a slight shift in bulk refractive index, which, in this case, could result in different variations of reflectivity. Satisfyingly, in Figure 4-3 (b), no increase of signals was observed on OBP3-w and OBP3-a spots compared to OBP3-c spots. OBP3-w and OBP3-a were sensitive to  $\beta$ -ionone and hexanal (Figure 4-3 (c)), but not to hexanoic acid. Therefore, these results demonstrated that the different OBPs conserved their activities and part of their specificity toward a range of VOCs even after the addition of a cysteine residue at their N-terminal end and their immobilization onto the prism.

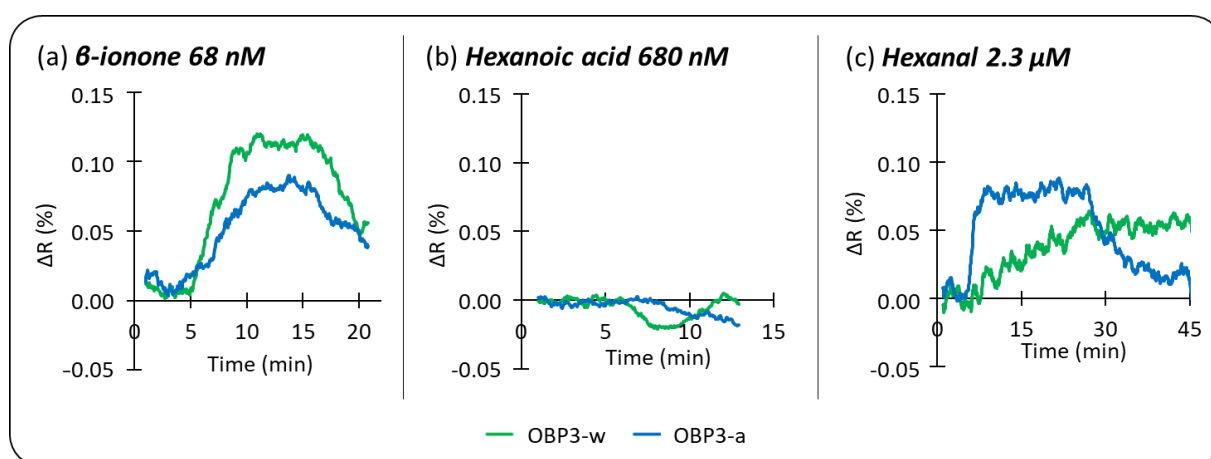


Figure 4-3 Kinetic responses of the two active OBPs after exposure to (a)  $\beta$ -ionone, (b) hexanoic acid and (c) hexanal. The average reflectivity obtained with the biosensors based on OBP3-c was subtracted to the signals of the ones based on OBP3-w and OBP3-a.

Furthermore, in order to check if these signals were valid, the effective signals obtained with the three olfactory biosensors after exposure to  $\beta$ -ionone, hexanal, and hexanoic acid were presented in Figure 4-4, together with their corresponding SNR values. Here, the reference signal

(subtracted to the raw signals) was the average signal given by all the biosensors containing OBP3-c. That is, with different concentrations of OBPs in the spotting solution (Figure 4-2). The signals presented in Figure 4-4 are those of the biosensors based on pure OBPs spotted at 8  $\mu$ M.

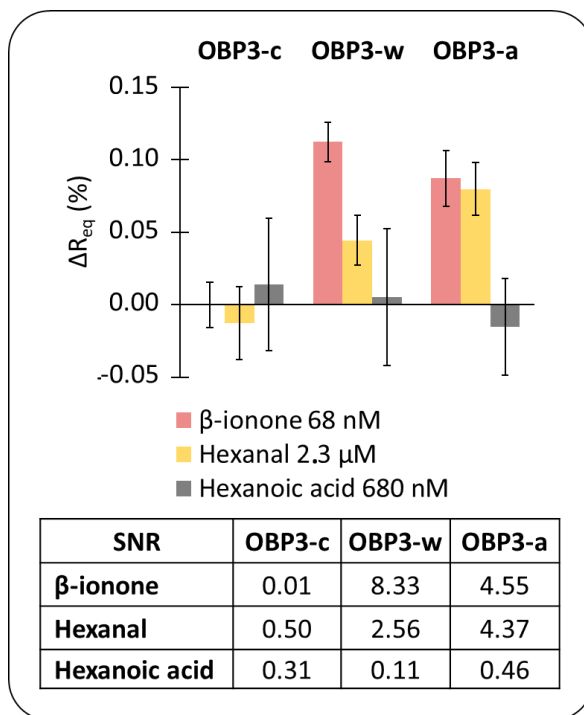


Figure 4-4 Effective signals obtained with the three olfactory biosensors after exposure to  $\beta$ -ionone, hexanal, and hexanoic acid. The corresponding SNR values are presented in the table below.

Interestingly, the signals obtained on OBP3-c based biosensors were almost null. It showed that this signal was independent on the probe density. Therefore, as intended, the negative control proteins did not bind the different VOCs. Moreover, there was almost no non-specific binding on the OBP3-c envelopes, or it did not lead to any measurable signal. This point is a huge advantage in the liquid phase, as we will discuss later.

Satisfyingly, the SNR calculated for the responses of the biosensors based on OBP3-w and OBP3-a to  $\beta$ -ionone and hexanal was greater than three. It confirmed that the OBP chip used in association with SPRi was efficient for the direct detection of VOC.

However, in all the cases, the variation of reflectivity was low (< 0.15%). It was expected that a detection of VOCs using liquid-phase SPRi would give rather low signal. To determine whether it was possible to obtain such a variation simply by virtue of the binding of the VOCs on a monolayer of OBPs, we made a comparison with the typical variation obtained for the detection of biomolecules by SPRi in the literature. For instance, an adsorbed layer of thrombin (37 kDa) gave rise to a variation of reflectivity of 6 to 7% on an aptamer chip [296]. A reflectivity increase of about 1% was found with the ligation of a DNA fragment (6 kDa) [297]. Extrapolating to VOC

detection (200 Da), it was expected to lead to a reflectivity variation around  $[0.03 \pm 0.01]\%$ . In fact, the observed signal intensity was much higher.

In fact, since SPR is very sensitive to the optical properties of the sensing layer on the prism surface, any phenomena having impact on the local refractive index, which are not due to direct mass addition, can be observed [298]. In particular, in the field of biosensors, such phenomena can amplify the SPR signal. For instance, Miyazaki and his collaborators successfully detected uric acid and glucose despite their small size through the variation of polarization of specific enzymes [299]. More interestingly, the conformational change of immobilized proteins after the binding of a ligand may result in a modification of their hydrodynamic radius [266] and, consequently, a variation of the refractive index. It enabled the detection of targets as small as calcium ions (40 g/mol), in a dynamic way [300] by SPR and SPRi [301]. These small molecular weight ligands would not give valid signals with these methods if only based on mass variation on the sensor.

To our knowledge, no study has been led on the conformational change that could occur in the rat OBP3 upon ligand binding. Nespoulous and collaborators showed that ligand binding induces local structural change in the rat OBP-1F [265]. Slight shifts of tyrosine residues are likely to induce a rearrangement of the protein backbone, which modifies its circular dichroism spectrum. This experimental observation was confirmed by molecular dynamics simulations, implying that in the presence of a ligand, a strand pair separation yields to an “open barrel” conformational state [264]. If we cannot assert that the same type of behavior is observed for OBP3-w and OBP3-a solely based on the results presented here, we hypothesized that the binding of VOCs to the active OBPs most likely induced a conformational change of the proteins. Such a change would give rise to a variation of local refractive index detectable by SPRi [302]. Further characterization would be needed to confirm it.

#### **4.2.3. Regeneration procedure**

As mentioned before, in nature, OBPs can reversibly bind VOCs. In this study, after the injection of  $\beta$ -ionone at relatively low concentrations ( $< 800$  pM), keeping the buffer solution running was sufficient to obtain a complete regeneration of the active olfactory biosensors. In this case, the reflectivity went back spontaneously to its original baseline in 25 minutes (Figure 4-5 (a)). The microarray was subsequently re-used to analyze other samples up to 12 consecutive injections of  $\beta$ -ionone in a row, with a SNR above three. However, after an injection at a concentration above 800 pM and a spontaneous regeneration, the signal did not go back exactly to the baseline and a subsequent loss of signal intensity was observed. For instance, at 6.8 nM, the signal decreased to about half of its intensity.

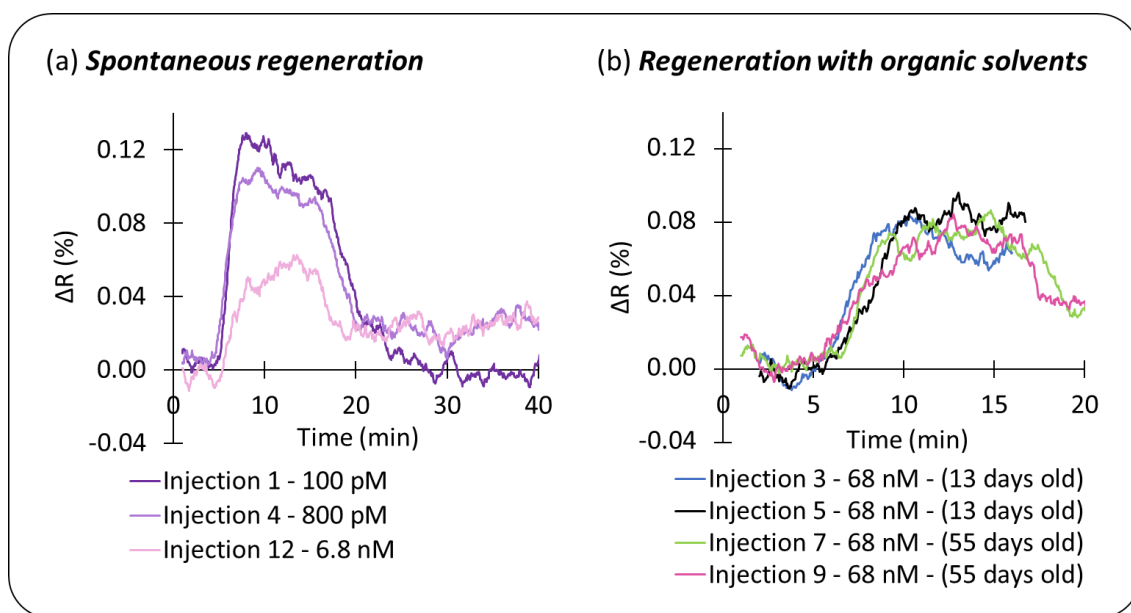


Figure 4-5 Repeatability of the kinetic response of OBP3-w-based biosensors to several injection of the reference compound  $\beta$ -ionone. The regeneration was spontaneous at low concentration (a). At higher concentrations, we used a regeneration procedure based on organic solvents (b). The number of injections, the concentration and the age of the chip are indicated in the caption.

In fact, after an injection of  $\beta$ -ionone at high concentrations or after an injection of hexanal, this process did not allow a complete regeneration of the microarray. Therefore, a new strategy was developed, taking inspiration from the purification method used after the production of OBPs [275] (see 4.1.1). The idea was to put OBPs in contact with organic solvents. It allowed, on the one hand, to slightly and reversibly denature the proteins and thus unfold their binding pocket, on the other hand, to solubilize the VOCs and facilitate their evacuation out of this binding pocket.

All the procedure was performed *in situ* with the chip mounted on the SPRi setup, with an optimal flow rate of 1.04  $\mu\text{L/s}$ . The Figure 4-6 shows the variation of reflectivity measured by SPRi on all the biosensors during a regeneration. Practically, the running buffer was changed to acetate buffer ( $\text{CH}_3\text{CO}_2\text{Na}$  at 50 mM, pH 7.5). Then, three successive injections were performed using 20% ethanol (v/v) in acetate buffer, and then 30% acetonitrile (v/v) in acetate buffer, twice. The changes in reflectivity measured during these different steps were mainly due to a bulk change in refractive index of the milieu. After this procedure, when back in phosphate buffer, the OBPs recovered their original structure and activity. The complete regeneration took 90 min. On the enlargement in Figure 4-6 (b), we can see that the reflectivity was lower at the end of the regeneration than before, due to the release of the ligands from the proteins.

This procedure was very efficient for all the VOCs tested, even at high concentrations. Thanks to it, our olfactory biosensors demonstrated a very good repeatability from measurement to measurement. For instance, we obtained a signal at equilibrium of  $[0.07 \pm 0.01]\%$ , for nine injections of  $\beta$ -ionone in a row at 68 nM (Figure 4-5 (b)). Moreover, the lifespan of the olfactory

biosensors was increased to about two months, which is remarkable, compared to other olfactory biosensors in the literature. The repeatability from chip to chip, assessed by injections of  $\beta$ -ionone, was also good on eight chips (not shown).

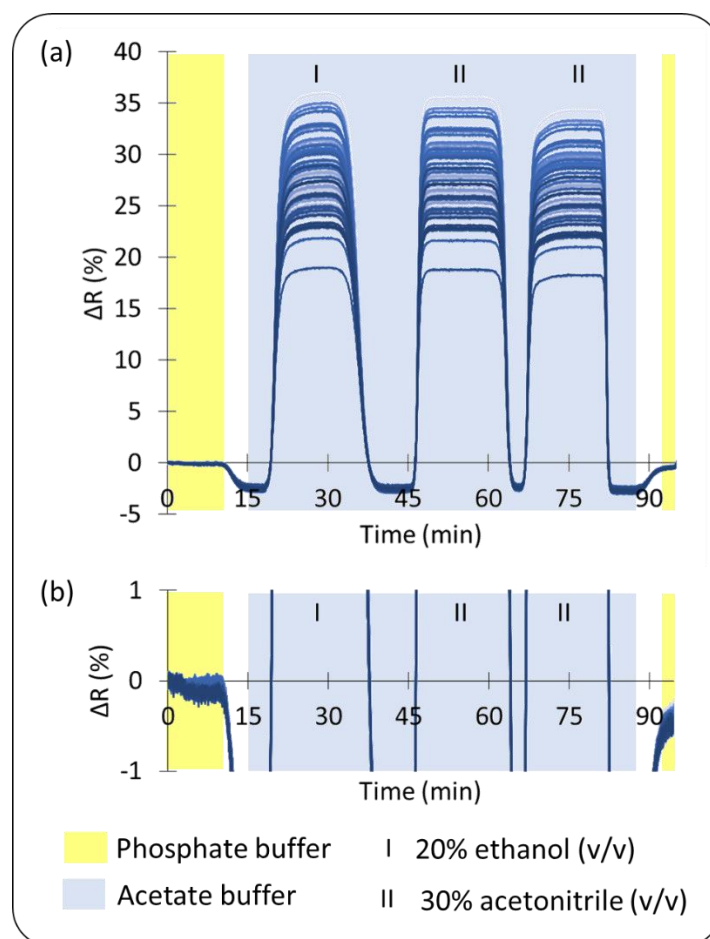


Figure 4-6 Variation of reflectivity measured by SPRi for all the OBP-based biosensors during a complete regeneration based on organic solvents. Figure (b) is an enlargement of (a)

#### 4.2.4. Performances of the optoelectronic tongue

##### 4.2.4.1. Sensitivity to $\beta$ -ionone

In order to evaluate the sensitivity of the olfactory biosensors to  $\beta$ -ionone, a set of measurements was performed using different concentrations ranging from 36 pM to 36 nM. The results presented in Figure 4-7 (a) and (b) were obtained on two different chips. These measurements were made difficult by the noise and the weak signals, as we can see from the large error bars. As a result, the measurable part of the linear range was very narrow: from 40 pM to 300 pM approximately in the case of OBP3-w-based olfactory sensors (Figure 4-7 (a)). For the concentrations above 300 pM, valid signals were obtained but with comparable intensity (Figure 4-7 (b)). It is likely that the saturation was reached.

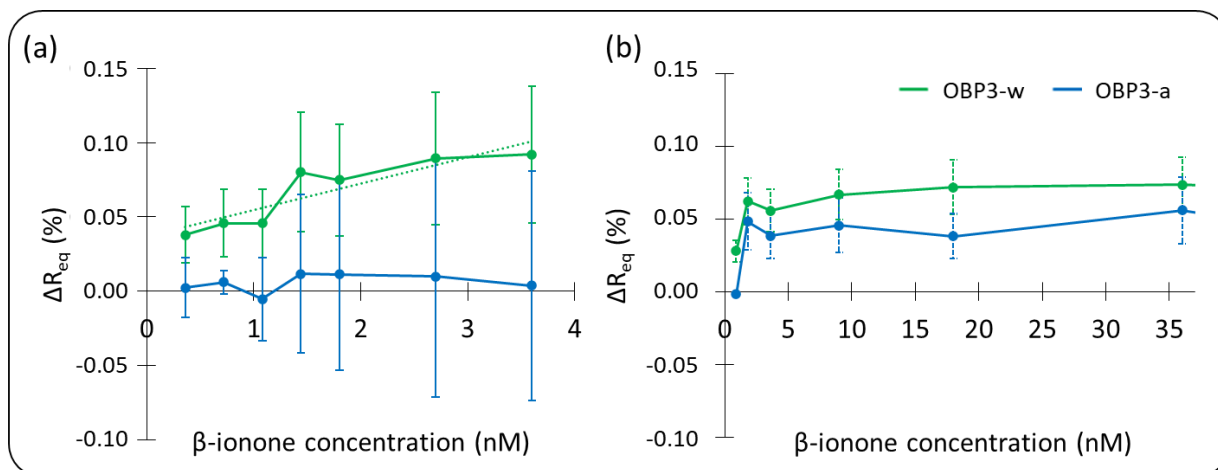


Figure 4-7 Analysis of  $\beta$ -ionone with a concentration range from 36 pM to 36 nM and resulting reflectivity at equilibrium for OBP3-w and OBP3-a biosensors.

An analyte concentration above  $K_d/1000$  is generally required to obtain a reliable signal without signal amplification in SPRi. Yet, here, a valid signal was observed using a concentration at  $K_d/5000$  for the binding of  $\beta$ -ionone to OBP3-w. This is purely indicative since the  $K_d$  on chip probably differs from the  $K_d$  in solution. Nevertheless, these results supported our hypothesis that the reflectivity variation was not simply due to the binding of the VOCs to the OBPs, but rather to the conformational change of the proteins. As a result, the linear range of the sensor was shifted to lower concentrations of VOCs.

These results showed that such optoelectronic tongues were unsuitable for the quantitative detection of VOCs in solution. Improvements to the sensors will be needed to increase the signal-to-noise ratio so as to construct a valid calibration curve. Nevertheless, since we aimed at the detection of VOCs in the gas phase, this was not a real limitation in our case.

#### 4.2.4.2. Limit of detection in concentration and mass

The minimum concentration detected with a valid signal ( $SNR > 3$ ), which was validated on at least three different microarrays, was 200 pM (Figure 4-2 (b)). In the literature, most of the OBP-based biosensors used for the detection of VOCs in solution have a limit of detection in the micro-molar range. Therefore, the limit of detection obtained with our olfactory biosensors was among the lowest ones. Zhang and his colleagues [289] obtained a limit of detection of 26.7 pM for  $\beta$ -ionone using insect OBPs and localized surface plasmon resonance as a transduction method. However, this value was extrapolated from the calibration curve as the concentration corresponding to 3 times the noise of detection and the lowest concentration tested was 10 nM. More recently, Lu and collaborators [285] developed an olfactory biosensor using human OBPs based on electrochemical cyclic voltammetry for the detection of aldehydes and fatty acids. The concentrations tested ranged from 5 pM to 500 nM. They estimated a limit of detection, once again by calculation, around 0.5 pM.

Furthermore, the limit of detection in mass commonly admitted for commercial SPRi apparatus is 200 g/mol, without any amplification [249]. Herein, we obtained a valid signal with hexanal, which has a molecular weight of 100 g/mol.

#### 4.2.4.3. Selectivity

Concerning the selectivity, as shown in Figure 4-3, at relatively high concentration,  $\beta$ -ionone bound to the two olfactory biosensors with a higher affinity for the OBP3-w-based olfactory biosensor. In contrast, hexanal bound preferentially to the biosensor based on OBP3-a. This is consistent with the results obtained in solution by ITC measurements. The binding of hexanal to OBP3-a was also much quicker than its binding to OBP3-w. These results confirmed that the modification of the binding pocket of OBP3-a yielded new binding properties, which were preserved after immobilization of the proteins onto the prism. Moreover, these kinetic features could be useful for the discrimination between different VOC families, for instance using kinetic PCA.

Most importantly, it was observed that at much lower VOC concentrations, the biosensors exhibited an extremely high selectivity (Figure 4-8). Indeed, at 360 pM,  $\beta$ -ionone bound only to the olfactory biosensors based on OBP3-w. Similarly, at 460 nM, hexanal bound only to the OBP3-a-based biosensor. All these results demonstrate that our olfactory biosensors are relevant for the trace detection with a high selectivity, rather than for quantitative analysis of VOCs.

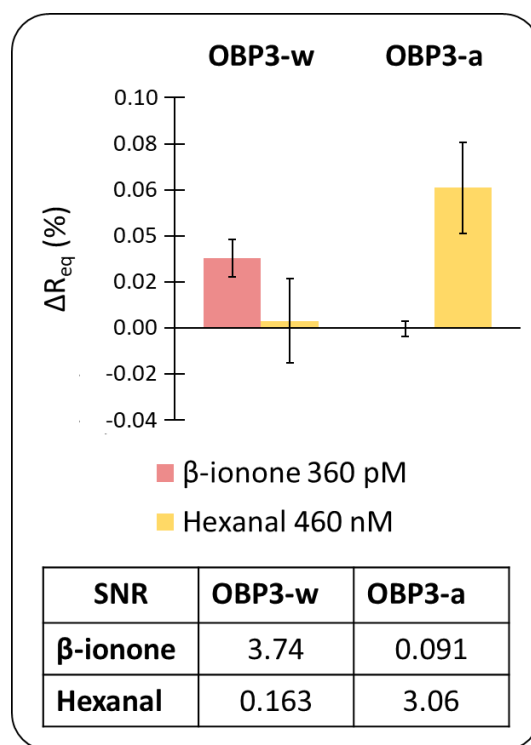


Figure 4-8 Effective signals obtained with OBP3-w and OBP3-a biosensors upon exposure to  $\beta$ -ionone and hexanal at low concentrations, showing their high selectivity. The corresponding SNR values are presented in the table below.



To conclude on this first part, under optimized deposition conditions, we showed that OBPs directly immobilized on the chip retained their activity. These biosensors were promising for highly sensitive and selective analysis of VOCs in solution. First of all, the detection limits both in concentration (200 pM of  $\beta$ -ionone) and in molecular weight of VOCs (100 g/mol for hexanal) were among the lowest in the literature. The intensity of the signals was relatively high compared to what we were expecting. It could not be explained solely by the mass increase after adsorption of VOCs on the protein layer. We therefore hypothesized that the binding of VOCs to OBPs induced a conformational change, which led to a variation in the local refractive index and amplified the SPRi signals. Moreover, the distinct binding properties of the OBP derivatives enabled very high selectivity at low concentrations of VOCs. Finally, different regeneration strategies were established. With appropriate regeneration procedures, these biosensors showed good repeatability for both measurement-to-measurement and chip-to-chip, as well as good stability with a lifespan of up to nearly two months.

Besides, the narrow observable part of the linear range (from 40 pM to 300 pM for  $\beta$ -ionone) was not appropriate for the quantitative analysis of VOCs. Future work could be done on the passivation of the chip surface to limit non-specific adsorption so as to reduce the noise. A rational surface chemistry could also be developed to stabilize the protein layer and so increase the lifespan of the biosensors.

### 4.3. OBP-BASED OPTOELECTRONIC NOSE: TOWARD THE DETECTION OF VOCS IN THE GAS PHASE

---

We showed that the design of new OBPs tailored to target specific VOCs was promising to design new sensing materials for optoelectronic tongues. The next step was to evaluate the possibility of a transfer to the gaseous phase.

#### 4.3.1. Detection of VOCs in dry air

At first, we simply dried an OBP chip under a stream of argon before using it in the gas-phase SPRi bench. We performed injections of  $\beta$ -ionone and hexanal, using dry air (0% RH) as carrier gas, to assess the performance of this optoelectronic nose, before further optimization. We sought to compare the sensitivity and selectivity of the system to that of the related artificial tongue.

As expected from a theoretical point of view, there was an important increase in the signal-to-noise ratio for the optoelectronic nose, as compared with the optoelectronic tongue. For instance, the Figure 4-9 gives the compared kinetic response obtained for an injection of hexanal in the liquid phase (a) and in the gas phase (b). The variation of reflectivity was one order of magnitude higher in the second case. This may be explained by the difference between organic molecules or proteins refractive index generally estimated around 1.4 and the refractive index of the respective

buffers (1.33 for water and 1 for gas). Those differences also differ by nearly one order of magnitude (0.07 and 0.4 respectively). As a result, we could expect to have a wider observable range of the linear region of the OBP-biosensors, and so, maybe to achieve quantitative analysis of VOCs.

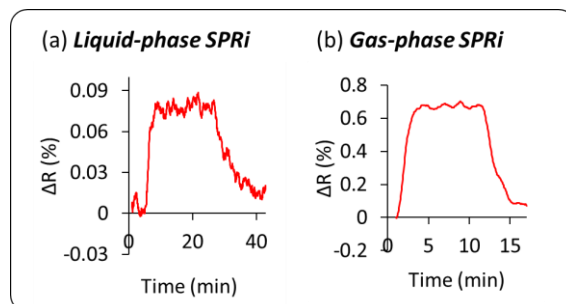


Figure 4-9 Kinetic response of OBP3-a-based biosensors after exposure to hexanal (a) in solution ( $2.3 \mu\text{M}$ ), (b) in the gas phase (75 ppm).

However, the equilibrium profiles obtained under these conditions were radically different than the one expected from the previous part. Indeed, in Figure 4-10 for example, we can see that, in dry air, the OBP3-c based biosensors gave the highest signal for both  $\beta$ -ionone and hexanal. Yet, this protein was supposed to be the negative control and gave systematically the minimum signal in the liquid-phase. We gave two possible explanations to this observation. First, the structure and activity of the proteins could have been lost when they were dried. Second, even if it was not the case, there could be much more non-specific binding in the gas phase. Actually, in the liquid phase, the hydrophilic envelope was unlikely to bind hydrophobic VOCs, in competition with water molecules. Whereas in the gas phase, and especially in dry air, very few or no water molecules were present to block access of the VOCs to the envelope of the OBPs. Moreover, under these conditions, the chemical equilibrium shifted. As a result, VOCs may bind not only specifically, in the binding pocket of OBPs, but also non-specifically on their envelope by electrostatic interaction, hydrophobic/hydrophobic interaction, hydrogen bond, Van der Waals force, *etc.*

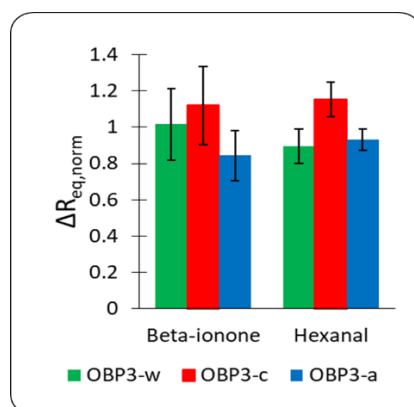


Figure 4-10 Equilibrium response of the three OBP-based biosensors to  $\beta$ -ionone and hexanal in dry air.

On top of that, a PCA was performed on a database gathering the equilibrium profile of several injections of  $\beta$ -ionone and hexanal in dry air. The result, presented in Figure 4-11 shows that under these conditions, there was no discrimination between the aromatic compound and the aldehyde.

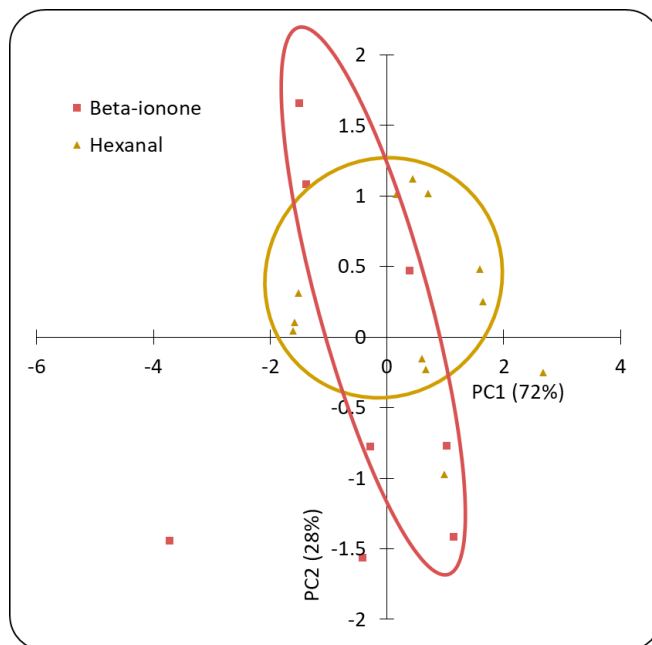


Figure 4-11 PCA of several injections of  $\beta$ -ionone and hexanal in dry air on an OBP-chip.

These preliminary results showed that the application of the protein chip for the analysis of VOCs in the gas phase, though promising, represented a real technical challenge.

#### 4.3.2. Strategies to increase the specific binding over non-specific binding ratio

A glance at the literature allowed us to identify three axes of work, on one side to preserve the structure and activity of OBPs in the gas-phase, and on the other side to increase the specific binding over non-specific binding ratio (see Figure 3-15 for the definition of these terms). They will be developed in this part.

To achieve this goal, hydration was key. As a matter of fact, the activity and the specificity of a protein depends on its 3D structure. This structure is maintained in solution by different interactions: covalent binding (via disulphide bridges), electrostatic (ions and hydrogen bonds), hydrophobic/hydrophobic, and van der Waals [303]. The rat OBP3, used in this project, does not have any disulphide bridge. Its folding rests mostly on the fact that non-polar amino acids will tend to avoid water. Conversely, polar residues will try to stay close to the aqueous milieu. Thus, a hydrophobic core is formed in the center of the tertiary structure of the protein, while the polar groups tend to remain on the surface [279]. As a result, in the total absence of water, this protein could be denatured. On top of that, the binding of the VOCs is likely to involve hydrogen bonds.

To tackle this problem, the first option was to work on the surface chemistry of the chip. The second was to use humid air instead of dry air as carrier gas. We tested these two first solutions on our device, as discussed below. The third possibility would have been to stabilize the structure of the proteins through site-directed mutagenesis. Illustratively, Kotlowski *et al.* [276] added a disulphide bond between two helices of an insect OBP. In such a way, the dynamics of the protein was reduced, and its specificity improved. We did not test this solution during this project.

#### 4.3.2.1. Surface chemistry

We drew inspiration from nature and tried to add an “artificial mucus” on the sensor surface. We thought this hygroscopic layer could retain moisture around the proteins. It could even work in dry air, by providing a scaffold to the proteins to preserve their structure. The literature on artificial mucus used for this purpose was very scarce, as we explained in chapter 1. Notably in the literature, Jaworski *et al.* [246] used short PEG as a linker to immobilize peptides on a sensor surface. They considered that it provided a moisturized environment, necessary to achieve sensitive and selective detection of explosives in the gas phase. Interestingly, PEG could also form hydrogen bonds with the hydrophilic envelope of OBPs to prevent the non-specific binding of VOCs on it.

Therefore, we decided to experiment with PEG. Different sensing materials with both OBPs and PEG were tested. For this, we mixed OBPs and thiolated PEG in the spotting buffer. We varied the PEG length: the shorter PEG molecules (PEG 350, Prochimia, 350 g/mol) were less likely to block access to the binding pocket of the OBPs, whereas the longer PEG molecules (PEG 2000, Prochimia, 2000 g/mol) could better act as a scaffold to support the protein structure. Different relative concentrations of the two molecules in the spotting buffer were also used (OBP-PEG 1:1 and 1:10). All these conditions were tested on the same chip, together with pure-OBP biosensors.

#### 4.3.2.2. Working conditions: humidity

The second option was to add humidity in the carrier gas, by the mean of the new optimized fluidic bench (see 2.3.2). The chip described in the previous paragraph was tested at different RH (0%, 8%, and 25%). Moreover, we decided never to dry the chip with argon, as this treatment could probably be too harsh for the proteins.

To determine whether these two methods were efficient, we measured the SNR obtained for each of the sensing materials for the detection of  $\beta$ -ionone in the gas phase. It was defined as the average signal of all the biosensors made of this sensing material, divided by the noise between them (see the equation in 4.2.1). We assumed that this indicator was linked with the specific binding to non-specific binding ratio. The results are presented in Table 4-3.

The last line gives the average signal to noise ratio of the different biosensors, with various PEG length and proportion. Adding PEG to the OBP-based sensing materials did not globally improve their detection performance in a significant way. If we go into details, it seems that PEG of both lengths helped the detection in dry air, resulting in a two-fold improvement of the SNR, from six to eleven. In contrary, at 8% RH, the PEGs were rather detrimental to specific sensing, but the difference was not significant. At 25% RH, surprisingly, OBPs mixed with PEG 2000 gave a higher SNR than pure OBPs, but this increase was again, not significant. If the PEG effectively had a support function for the OBPs, it is likely that it also increased the non-specific adsorption (on PEG). Overall, the two phenomena offset each other. Overall, we decided to stick with pure-OBP sensing materials.

		Pure OBP	OBP-PEG 350		OBP-PEG 2000		
[OBP]:[PEG]			1:1	1:10	1:1	1:10	Average
0% RH	OBP3-w	4	7		10		7
	OBP3-c	8	18		16		14
	OBP3-a	5	7		6		6
	Average	6	11		11		9
8% RH	OBP3-w	43	27	47	35	29	36
	OBP3-c	32	40	30	32	29	33
	OBP3-a	54	53	36	40	24	41
	Average	43	40	38	36	27	37
25% RH	OBP3-w	36	47	48	39	55	45
	OBP3-c	60	44	42	52	41	48
	OBP3-a	20	38	31	49	78	43
	Average	39	43	40	47	58	45
Average (8% and 25% RH)		41	41	39	41	42	

Table 4-3 Signal to noise ratio obtained upon the injection of  $\beta$ -ionone in the gas-phase in different conditions of surface chemistry and relative humidity.

The last column gives the average signal to noise ratio of all the biosensors at different RH. Clearly, it increased with the RH, from 9 in dry air, to 45 at 25% RH. The use of humid air as a carrier gas therefore seemed promising to improve the performance of our sensor. Nevertheless, we had to understand how humidity affected the response profile of the VOCs detected with the OBP-based optoelectronic nose.

#### 4.3.3. Detection of VOCs in humid air

Introducing moisture into our optoelectronic nose was not without consequence. In effect, water itself gave an SPRi signal on all the biosensors, since it adsorbed on the proteins. To illustrate this, the Figure 4-12 shows a typical kinetic response obtained upon the injection of water on our OBP-based optoelectronic nose. It was performed just like for a classical VOC

injection, by introducing 50  $\mu\text{L}$  of liquid water on perfumery paper in the evaporation flask. The carrier gas was dry air (0% RH).

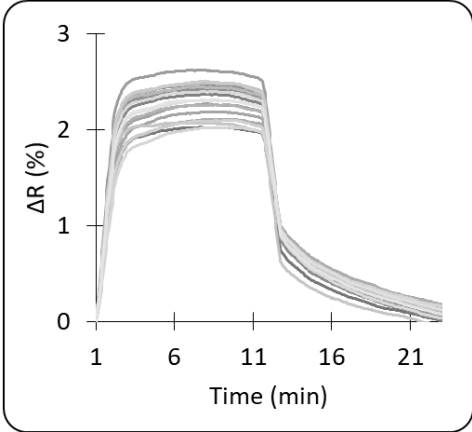


Figure 4-12 Kinetic response obtained for water injected in dry air on an OBP chip.

As explained in 2.3.2, we modified the bench so as to use humid air as carrier gas. It was made in such a way that the humidity reaching the prism had a controlled RH, highly stable in time. In this way, the baseline was already impacted by humidity, and any change in reflectivity measured during VOC injections was only due to its interaction with the biosensors.

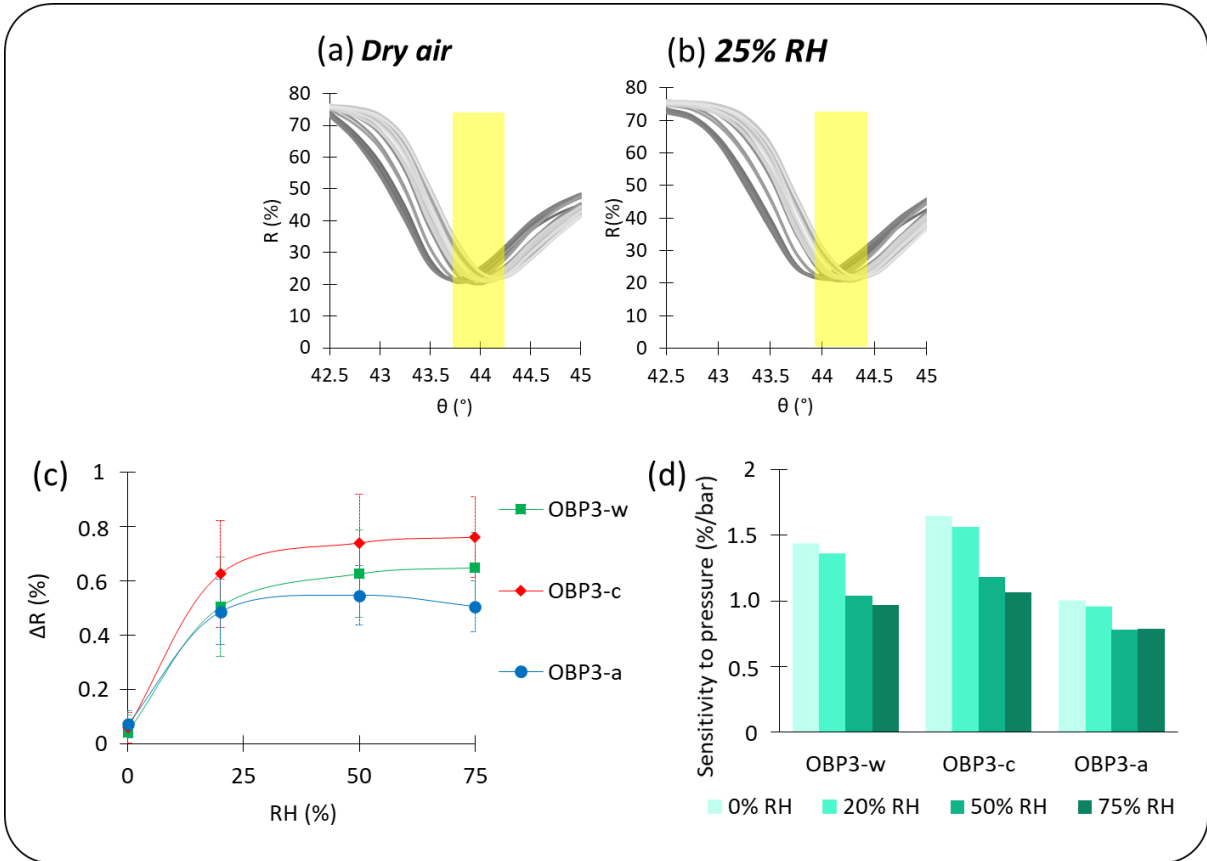


Figure 4-13 (a) Plasmon curves of the different OBP-based biosensors in dry air. (b) Plasmon curves for the same prism in humid air (25% RH). (c) Baseline drift due to the adsorption of water on the different OBP biosensors. (d) Sensitivity to pressure jumps of the different biosensors at different relative humidity.

The Figure 4-13 explains how the OBP-based optoelectronic nose reacted to this change in working conditions. By introducing humidity, the baseline reflectivity increased (Figure 4-13 (c)). According to simulations led by Jonathan Weerakkody, this was caused by the adsorption of water molecules on the biosensors. The figure seems to indicate that a saturation in water occurred above 25% RH. The adsorption of water also led to a shift in angle of the plasmon curves of the biosensors (Figure 4-13 (a and b)). As a result, at fixed working angle, there was a small loss in sensitivity to pressure, and so of physical sensitivity, on all the biosensors when increasing humidity (Figure 4-13 (d)). For this reason, we decided to adjust the working angle every time the relative humidity of the carrier air was changed.

The Figure 4-14 presents the response profiles at equilibrium of  $\beta$ -ionone and hexanoic acid, using humid air at 8% RH and 25% RH as carrier gas. The working angle was optimized successively for each RH, so that the differences that we measured were mainly due to chemical considerations.

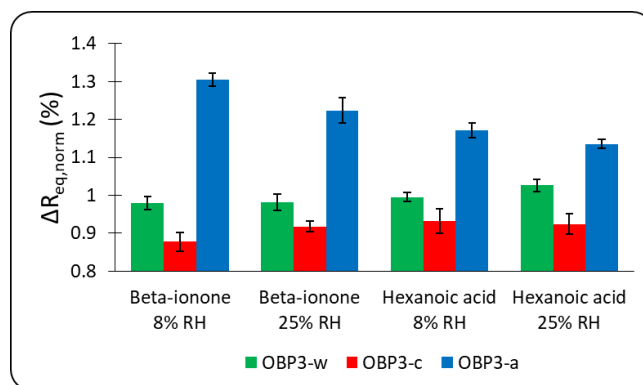


Figure 4-14 Normalized equilibrium profiles of  $\beta$ -ionone ( $\sim 2500$  ppb) and hexanoic acid ( $\sim 750$  ppb) at 8% RH and 25% RH.

First, we can notice that the OBP3-c gave the lowest signal in humid air. It seems to confirm that the specific binding to non-specific binding ratio was improved. However, there was no clear specificity of the OBP3-a and OBP3-w for the two VOCs. Notably, hexanoic acid, which did not give any response in liquid-phase SPRI, gave a signal on the two active proteins in gas-phase SPRI. This point will be discussed in details in the next part.

Second, the augmentation of relative humidity from 8% to 25% reduced slightly the contrast in the equilibrium response of the two VOCs, but did not change drastically their signature. To further illustrate this point, we performed a static PCA on several injections of  $\beta$ -ionone and hexanoic acid (Figure 4-15). It showed that, for a given VOC, the individuals recorded at 8% RH were plotted in the same region as individuals recorded at 25% RH. Again, we can note that this static PCA did not separate well the clusters of the two VOCs, which had radically different

signatures in the liquid phase. However, the classification success rate was much better than in dry air (see Figure 4-11 for comparison).

Moreover, the discrimination between the two VOCs was mostly inferable to PC2. Interestingly, the variable plot (Figure 4-15 (c)) shows that PC2 correlated with the two active OBPs (OBP3-a and OBP3-w) but not to the negative control protein OBP3-c. In fact, with our unsupervised classification method, PC1 essentially reflected noise, which accounted for most of the variability between individual injections.

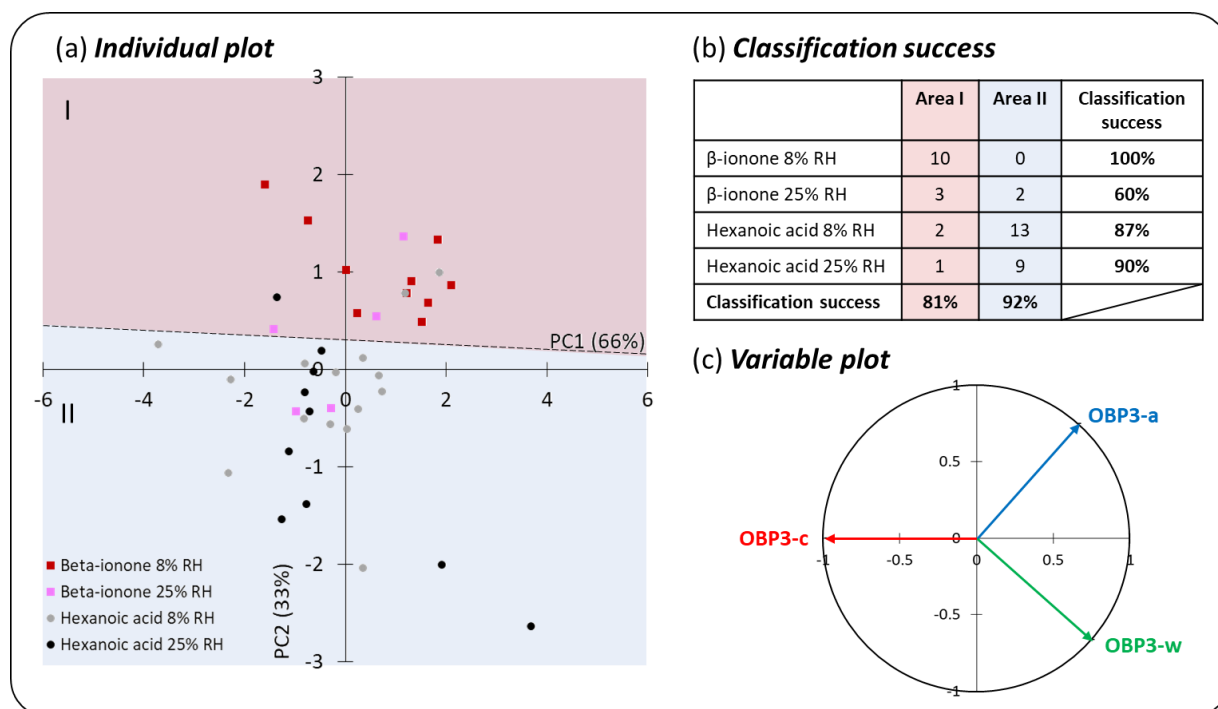


Figure 4-15 (a) Individual plot of a static PCA on a database of injections of  $\beta$ -ionone and hexanoic acid at different RH. (b) Classification success of this PCA. (c) Associated variable plot.

In the light of all these observations, we decided to work with carrier air with 30% relative humidity. This combined the advantages of being close to the ambient humidity, while not affecting too much the VOC signatures.

## 4.4. PERFORMANCE OF THE OBP-BASED OPTOELECTRONIC NOSE

### 4.4.1. Selectivity

As we showed in the previous part, in the gas phase, the selectivity of the different OBP mutants was not clearly observable. Indeed, in Figure 4-14, we can see that the signatures obtained for  $\beta$ -ionone and hexanoic acid were not radically different. Yet, in solution, OBP3-w and OBP3-a were binding  $\beta$ -ionone with a good affinity, but not hexanoic acid. On top of that, for



$\beta$ -ionone, the highest signal was obtained with OBP3-a, which was not consistent with the results in the liquid phase.

To determine the chemical resolution of the OBP-based optoelectronic nose, we analyzed several VOCs, with different affinity for the three OBP mutants (see Table 4-2). A static PCA was then performed on the equilibrium profiles of these injections (see 2.5.2). It is presented in Figure 4-16 (a). As we can see, it was not efficient to discriminate between the different VOCs. The clusters are due to position effect between the different biosensors on the SPRi chip, which causes a loss of reproducibility.

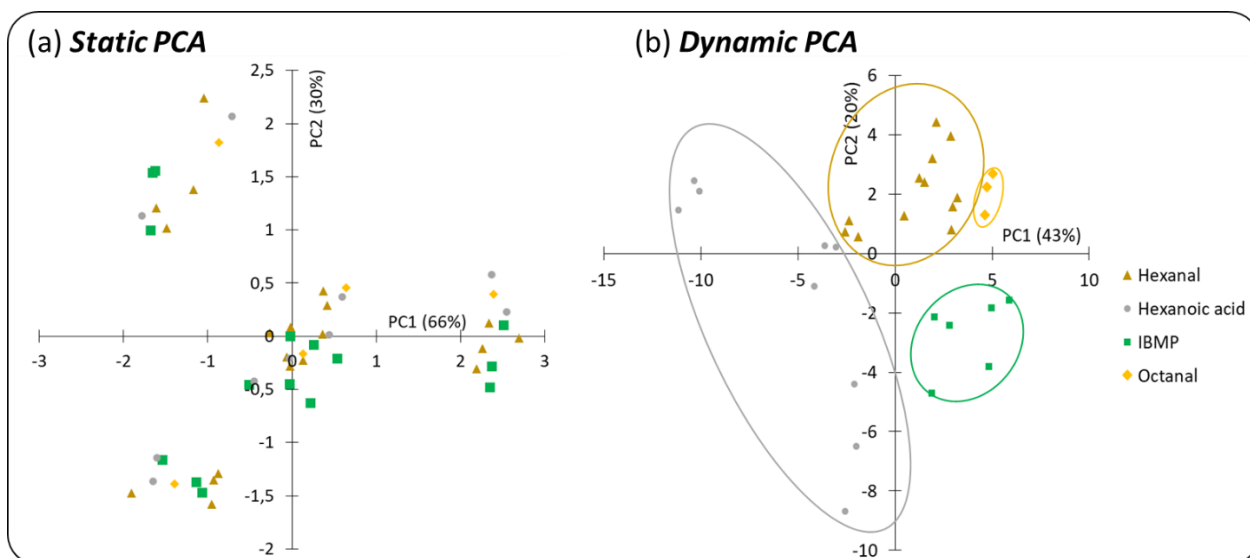


Figure 4-16 Study on the chemical resolution of the OBP-based optoelectronic tongue. (a) Static PCA on a database of 10 injections of different VOCs. One variable was defined for each kind of VOC at equilibrium. (b) Dynamic PCA on the same data. One variable was defined for each kind of OBP and every minute.

We then decided to process the same data using dynamic PCA. One variable was defined for each kind of OBP every minute. The correlation matrix was filled with the mean reflectivity of the biosensors constituted from this mutant for one minute. In Figure 4-16 (b), we can see that, with this data processing method, we obtained a good discrimination of the different VOCs. The position effect was eliminated and the repeatability from injection to injection was highly improved. On top of that, with only three different sensing materials, we could distinguish between the molecules, and the chemical families. Indeed, the two aldehydes were sorted in the same area of the PCA.

This was a very impressive and promising result, since the three OBPs used in this project only differ by one amino acid from each other. It showed that the use of OBPs could be appropriate for the design of optoelectronic noses. In the future, it could be interesting to check whether a similar discrimination would be achievable with any kind of proteins, as a control.

#### 4.4.2. Analysis of the discrimination mechanisms

To understand the physicochemical mechanisms enabling this discrimination, we also studied the variable plot of this dynamic PCA. In the Figure 4-17 (a), every arrow represents a variable of the PCA presented in Figure 4-16 (b). They are labeled as follow: x8\_t, with x the type of OBP (for example a for OBP3-a), 8 representing the concentration of OBPs in the spotting solution in  $\mu\text{M}$ , and t the time in minutes following the beginning of the injections. To facilitate the reading, c8\_2, a8\_2 and w8\_2 (association phase) were squared in blue, c8\_8, a8\_8 and w8\_8 (equilibrium) were squared in pink, c8\_12, a8\_12 and w8\_12 (dissociation phase) were squared in green. An example of injection with a typical duration is provided in Figure 4-17 (b). Interestingly, at a given time, the vectors representing the three mutants were further apart during equilibrium and dissociation phase, than during the association phase. It seems to indicate that these phases were more important for the discrimination of VOCs. In comparison, during the association phase, the three mutants did not help the separation of the individuals. This was encouraging, since mostly non-specific binding usually influences the kinetics of the association phase, whereas the kinetics of the dissociation phase has more to do with the specific binding of VOCs on the different probes. For this reason, we think that there is an effect of the specificity of the different mutants on the ability of discrimination.

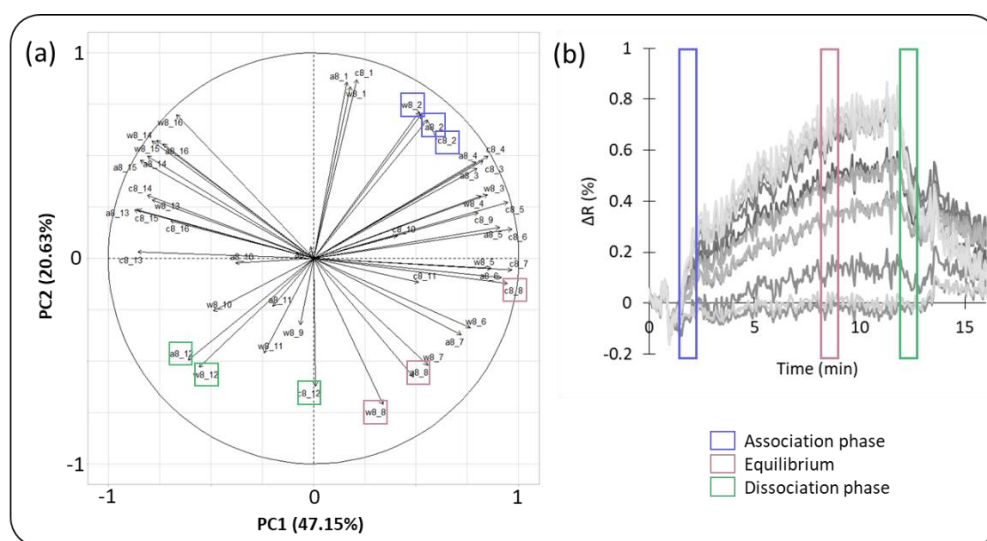


Figure 4-17 (a) Variable plot associated with the dynamic PCA presented in Figure 4-16. (b) Example of injection: hexanoic acid on an OBP-based chip.

However, as evoked in 2.5, the kinetics that we observed in gas-phase SPRi was not only due to the interaction between the VOC molecules and the probes, but also to fluidic considerations. Indeed, the VOCs used in this study had different molecular weight and volatility. As a result, their concentration in time varied differently. The Figure 4-18 schematically illustrates the different phenomena at stake. An ideal analysis by SPRi is usually carried out on an injection of analyte at constant concentration. To limit the effects of the volatility of the VOCs on the concentration

profile at the output of the evaporation chamber, we waited for the steady state for 30s after the introduction of the sample and before its analysis. Thus, the difficulty to obtain constant VOC concentration for sampling was partially due to the valve, which was manually triggered and subject to pressure effects, and partially to the VOC transport in the fluidic circuit (tubing, analysis chamber, *etc.*). During the latter, diffusion, convection and adsorption might hinder the conservation of an ideal injection profile in a way that depends on the molecular weight of VOCs, their volatility, their likeliness to adsorb on the tubes, *etc.*

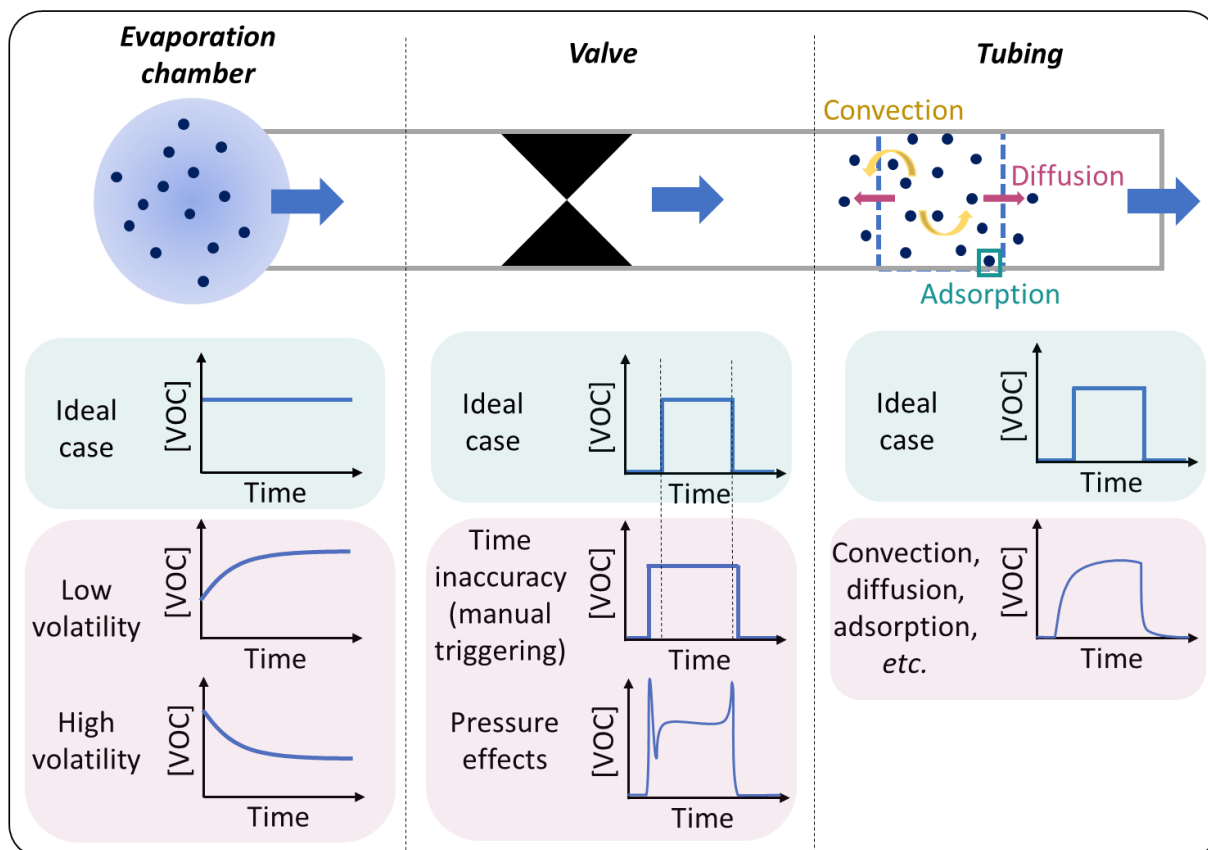


Figure 4-18 Different phenomena affect the fluidic and the profile of concentration of a VOC over time.

To visualize the magnitude of these different mechanisms on our artificial nose, we monitored continuously the concentration of VOCs at the close output of the analysis chamber using the PID measurements. The concentration profiles over time of the injections studied in this part are presented in Figure 4-19 (a). First, despite the 30s delay, the concentration in time did not reach a steady state in some cases, which can be due to evaporation and/or transport effects. Moreover, the various volatility of the VOCs caused important variations in the concentrations at equilibrium. We can also see clearly that there were pressure effects in the valve, resulting for example in a peak of concentration at the beginning of hexanal injections.

These profiles were used to perform a dynamic PCA, using the exact same protocol as for SPRi signals. A variable was defined every minute for 16 minutes. The concentration in ppb measured

for a VOC at this time was used to fill the correlation matrix. We then normalized the lines of the matrix by their quadratic average, as it was usually done on profiles at equilibrium to get rid of concentration effects (see 2.5.1). To illustrate this step, the Figure 4-19 (b) shows the normalized time response of the PID for the different injections studied here. As we can see in Figure 4-19 (c), this dynamic PCA performed only on the PID data was sufficient to discriminate between the different VOCs. This explains partly the effectiveness of kinetic data processing for the discrimination of VOCs. However, it is difficult to de-correlate these concentration effects from the real interaction between the biosensors and the VOCs. In the current configuration of our laboratory setup, it was therefore very difficult to determine whether the different OBP mutants actually played a role in the discrimination of the VOCs.

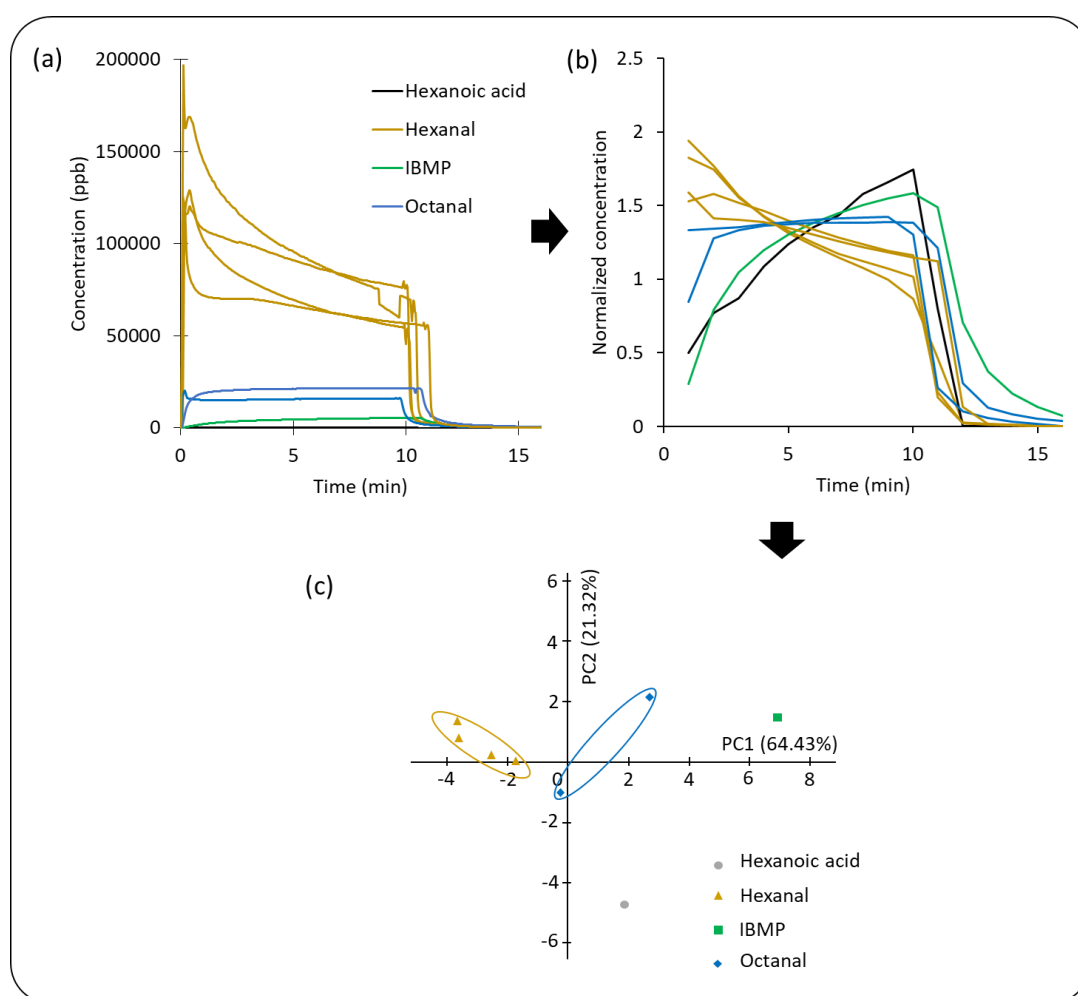


Figure 4-19 (a) Concentration profiles in time of the different VOC injections, obtained with the PID. (b) Normalized profiles of concentration. (c) Dynamic PCA performed from these profiles.

We considered different solutions to tackle this limitation. First, the dissociation kinetics is less affected than the association kinetics and thus could be the most interesting to study. Second, we could have used gas bottles of VOCs instead of our evaporating chamber. However, after checking, the VOCs that we used were not commercially available. Third, we transferred the chip

in a portable optoelectronic nose device equipped with an automatic valve for reproducible VOC sampling and a much shorter fluidic circuit. This will be detailed in 4.5. Fourth, we could potentially use the PID data to normalize the SPRi ones. We did not have the time to test this method during this thesis project.

#### **4.4.3. Other performances**

We also aimed to measure the limit of detection for the different VOCs, by diluting them in air. However, we were prevented from getting a quantitative result by the lack of PID calibration data. In fact, the concentration value indicated by the PID was given based on a calibration gas (isobutylene) and had to be multiplied by a correction factor to find the real concentration for the injected VOC. This correction factor depends on the nature of the VOC and lacked for octanal, IBMP and  $\beta$ -ionone. We obtained a valid signal for hexanal at 6 ppm and hexanoic acid at 150 ppb. For the lowest measurable signal, the PID indicated 4 ppm (equivalent isobutylene) for octanal and for IBMP, and 200 ppb (equivalent isobutylene) for  $\beta$ -ionone.

In the gas phase, the regeneration of the chip was simply performed with a flow of clean carrier air. With this method, the same prism could give a valid and reproducible signal for up to 25 injections. At most, the same chip could be successfully used for one month.

### **4.5. TRANSFER TO THE NEOSE PRO**

---

#### **4.5.1. Performance of the OBP chips integrated in the NeOse Pro**

In the framework of ANR project OBP-Optinose, in close collaboration with Aryballe Technologies, we performed the same experiment on the Aryballe's "NeOse Pro". The fluidic circuit of the device differed from ours. Indeed, a pump collected the ambient air via a very short tube. Therefore, we were expecting less concentration effects due to VOC transport. Moreover, an automatic valve ensured a repeatable injection, which made possible for a more detailed kinetic study, as explained below. On top of that, in this fashion, it took only a few seconds to perform a VOC injection and its analysis. Thus, it became possible to perform much more analyses in a same day, which facilitated the statistical analysis of the results. Nevertheless, the working conditions were less reproducible than in our circuit, since the temperature, humidity and composition of the carrier (ambient) air were not controlled. Besides, the prisms used in this miniaturized device had a lower optical quality than ours.

First, we tested the fluidic circuit of the NeOse Pro by replacing the chip with a PID. We measured the concentration profiles of injections of pure hexanal, octanal, hexanoic acid, IBMP and  $\beta$ -ionone, with a total duration of 10 s. The Figure 4-20 (a) shows these profiles, normalized. From these, we performed a dynamic PCA with one point taken every second (which was the time resolution of the PID). The results in Figure 4-20 (b) showed that it enabled the discrimination

between the different VOCs, but the distance between the clusters of hexanal, octanal and IBMP was much smaller than on our device.

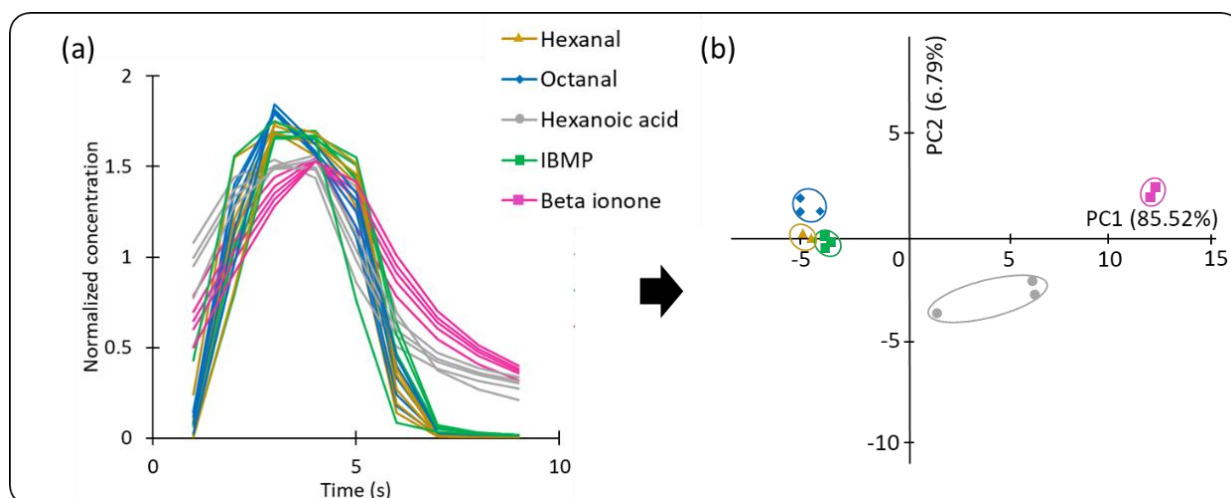


Figure 4-20 (a) Normalized profiles of concentration measured with a PID and the NeOse Pro fluidic system for injections of pure VOCs. (b) Associated dynamic PCA.

We then integrated an OBP-chip in the NeOse Pro. It was functionalized with the three mutants at different concentrations in the spotting buffer ( $4\ \mu\text{M}$ ,  $8\ \mu\text{M}$ ,  $16\ \mu\text{M}$  and  $32\ \mu\text{M}$ ), and so, different densities on the sensor surface. Again, multiple injections of pure hexanal, octanal, hexanoic acid, IBMP and  $\beta$ -ionone were performed, with a duration of 10 s.

A static PCA at equilibrium was not sufficient to discriminate between the different VOCs. However, thanks to the computer-controlled automatic valve, we could then process the data in a more precise fashion. Databases for kinetic PCAs were built up from two different time slots: the association phase and the dissociation phase. That is to say, we have defined a variable per type of OBP3 (a, c or w), per spotting concentration and per 0.33 second, from the start of injection to equilibrium, or from the equilibrium to the end of the desorption, respectively. The results are presented in Figure 4-21 (a) and (b).

First, we can note that a dynamic PCA performed on the database from the dissociation phase enabled to separate the different VOCs. This proved that the OBP chip was transferrable to the industrial device, with a similar chemical resolution, in spite of the less controlled experimental conditions. Moreover, the discrimination was much better than the one obtained only with the PID, which comforted the fact that the OBPs' affinity for the VOCs played a role in the kinetics measured by SPRi. We will confront this hypothesis in the following section.

We also roughly measured the limit of detection for the different VOCs by diluting them in mineral oil. We obtained a valid signal for all OBPs when diluted ten times in mineral oil. It gave a limit of detection of the same order of magnitude as on the experimental bench for all the VOCs.

#### 4.5.2. Analysis of the discrimination mechanisms

As intuited from the study of the variable plot in our experimental bench (Figure 4-17 (a)), the discrimination was much better using the dissociation phase than the association phase. Notably, the different injections of hexanoic acid were not clustered with data from the association phase, and the distance between the clusters was smaller. This observation again seemed to indicate that mutant specificity was important for the chemical resolution of the artificial nose.

To back this hypothesis, and to determine the impact of concentration effects on this chemical resolution, we performed a dynamic PCA in the dissociation phase on two different biosensor sets. On the one hand, we considered the three mutants OBP3-a, OBP3-w and OBP3-c at 8  $\mu\text{M}$  (Figure 4-21 (c)). On the other hand, we considered only the mutants OBP3-w, at all the spotting concentrations: 4  $\mu\text{M}$ , 8  $\mu\text{M}$ , 16  $\mu\text{M}$  and 32  $\mu\text{M}$  (Figure 4-21 (d)).

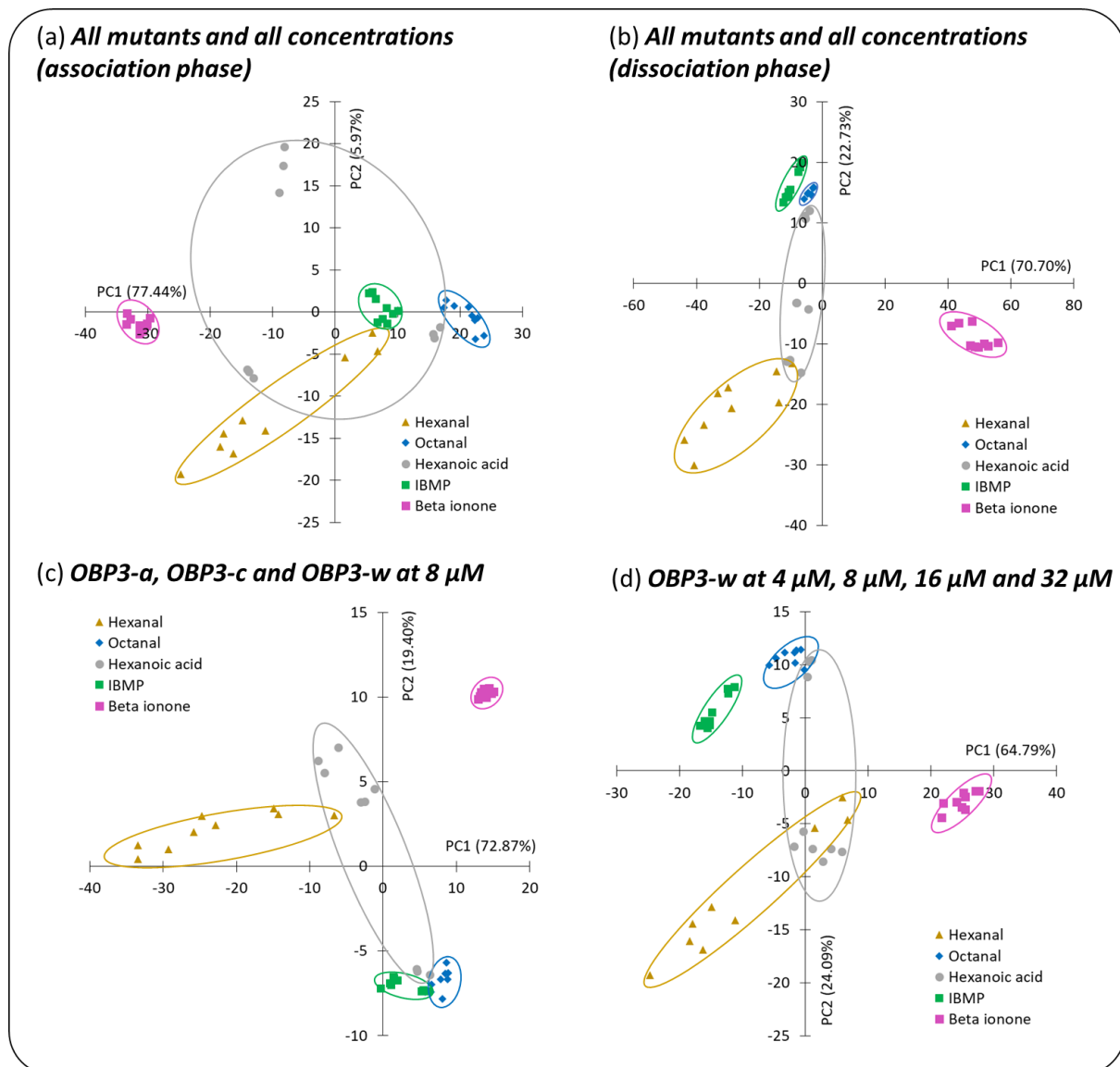


Figure 4-21 Dynamic PCA performed on injections of VOCs on an OBP-based chip integrated to the NeOse Pro.

The separation of the different clusters was better using the three different mutants, than only one mutant at different concentrations. However, the number of biosensors considered was greater in the latter case. This result was very encouraging and further supported the role of the different mutants in the chemical resolution of the artificial nose based on OBPs. It is interesting to note that the clusters corresponding to hexanal and octanal were not in the same region of the PCA. Their separation could be related primarily to their properties of mass and volatility, rather than to their chemical family.

In conclusion, the transition to the gas phase was a challenge to maintain the structure and therefore the function of the OBPs. We have shown that working in humid air can facilitate this transition. The effect of humidity on the biosensors was characterized. Once the working conditions optimized, the optoelectronic nose allows a good discrimination of the gas phase VOCs from kinetic SPRi data. This is a promising result, since three OBP-based sensing materials, differing from a single amino acid, are sufficient to enable this separation. A reflection has been initiated to understand the phenomena involved in this good chemical resolution. Initial results tend to confirm that the different binding properties of the three mutants were necessary. We have successfully transferred this chip into the NeOse Pro industrial device commercialized by Aryballe, without any noticeable change in its performance. However, the lifespan of these biosensors, as well as the manipulation conditions remained intrinsically limited by the use of proteins. This preliminary study may pave the way for the design and use of new custom-made olfactory proteins to target specifically a wider range of VOCs with high societal impact, or to extract high-affinity peptides from the binding pocket of OBPs.





## CHAPTER 5

# Phage display: in vitro screening of high-affinity peptides



## Résumé du chapitre 5 – *Phage display* : criblage *in vitro* de peptides à haute affinité

Dans ce chapitre, nous avons étudié la faisabilité et l'intérêt du *phage display* pour sélectionner des peptides ayant une forte affinité pour un COV cible ou une famille de COV. Le *phage display* est une technique de laboratoire qui utilise des bactériophages comme outils pour le criblage à haut débit de protéines et de peptides. Ce processus est aussi appelé sélection *in vitro*, par analogie avec la sélection naturelle.

Le *phage display* consiste à exposer une bibliothèque de phages portant chacun un peptide aléatoire à une surface sur laquelle la molécule cible est immobilisée. Les phages présentant des peptides ayant une haute affinité pour cette cible se fixent à la surface. Après rinçage pour éliminer les autres, ils sont récupérés et amplifiés par l'infection de bactéries. La nouvelle bibliothèque de phage est utilisée pour le tour suivant. Après 3 à 4 tours, on isole et on récupère les phages sélectionnés. Le séquençage de leur ADN permet de remonter à la séquence peptidique. Il y a plusieurs points d'attention pour chacune des étapes décrites ci-dessus. Ils font l'objet de la première partie de ce chapitre. Dans notre cas, la mise en œuvre du protocole de *phage display* représentait un défi, car les molécules de COV sont beaucoup plus petites que les cibles classiquement utilisées. Trois sessions d'expériences ont abouti à l'identification de trois peptides avec une haute affinité pour le cycle phényle.

Leur structure, leur affinité pour différents COV, et leur sélectivité pour ceux possédant un cycle phényle ont été simulés numériquement. Ils présentent des caractéristiques communes, telles qu'une structure courbée et des résidus aromatiques. Ces derniers sont très probablement les sites de liaison préférentiels des composés phényles, par empilage  $\pi$ - $\pi$ . En conséquence, les trois peptides ont une bonne sélectivité prédite pour ces COV, meilleure que des peptides sélectionnés précédemment dans la littérature. Cependant, certains des peptides historiques, avec davantage de résidus aromatiques, ont obtenu de meilleurs résultats.

Les trois peptides ont été synthétisés et immobilisés sur un prisme pour la détection de COV en solution, puis en phase gazeuse. En phase liquide, l'utilisation de nanoparticules exposant des groupes phényle ou non a permis de montrer que les nouveaux peptides sélectionnés par *phage display* présentaient bien une sélectivité pour les composés phényles. Les résultats, conformes aux simulations, ont cependant confirmé que certains peptides historiques étaient encore plus sélectifs. A cause de leur petite taille, nous n'avons pas détecté directement des COV phényle libres, mais un test en compétition a permis de confirmer que ceux-ci se fixaient très probablement sur les nouvelles sondes. En revanche, il a été impossible de qualifier la sensibilité et la sélectivité précises des biocapteurs, ainsi que la résolution chimique de la langue artificielle.

Dans des conditions de dépôt et de travail optimisées, les peptides sélectionnés par *phage display* ont conservé leur sélectivité pour les composés phényles en phase gazeuse. Nous avons observé une légère amélioration de la résolution chimique du nouveau nez optoélectronique. Cependant, sa limite de détection et sa sensibilité aux composés phényles n'ont pas été améliorées. Toutefois, les sondes peptidiques sont beaucoup plus robustes que les protéines entières, ce qui les rend plus faciles à mettre en œuvre dans un biocapteur et prolonge la durée de vie du dispositif.

La découverte de nouveaux peptides ayant une forte affinité pour un COV, par *phage display*, semble prometteuse. Les trois peptides courts identifiés ici ne permettent pas d'améliorer radicalement les performances de notre nez optoélectronique. Cependant, le protocole peut être adapté à différentes cibles et à différentes bibliothèques de peptides et de protéines. En particulier, les peptides longs ou cycliques pourraient avoir des affinités beaucoup plus élevées pour leur cible que les peptides courts que nous avons conçus ici. Cette étude préliminaire nous a permis de valider l'intérêt de cette voie de développement pour améliorer la sélectivité et la résolution chimique du nez optoélectronique dans le futur.

Enfin, le protocole classique de *phage display* présentait plusieurs limites, notamment les expériences sont longues et réalisées en aveugle. Nous proposons à la fin de ce chapitre deux protocoles alternatifs pour y remédier. Il s'agit encore d'un travail préliminaire. Cependant, nous pensons que ces nouvelles méthodes pourraient s'avérer avantageuses pour le suivi du bon déroulement de la sélection de sondes et son optimisation.

## CHAPTER 5 Phage display: *in vitro* screening of high-affinity peptides

In the previous chapter, we showed that the integration of proteins from the biological olfactory system to our optoelectronic tongue or nose could help to improve their sensitivity and selectivity. However, this method is limited by the fragility of these probes and requires very delicate manipulation conditions that could be difficult to conciliate with an industrial device. Moreover, when a specific application is targeted, there is not always a known natural receptor with a good affinity to the VOC of interest. It is possible to tune the binding properties of OBPs or ORs by site-directed mutagenesis, as we have shown formerly, but this approach remains very limited by the structural requirements for the proteins' activity. Finally, the large size of the proteins prevents their use in combination with our historical probes with an SPRi transduction. In this context, we decided to consider another strategy that would allow discovering novel peptides with a high-affinity for a target VOC experimentally.

Phage display is an *in vitro* technique that uses bacteriophages as a tool for the high throughput screening of proteins and peptides with a high affinity for a target. This process is called *in vitro* selection for its analogy to natural selection. G. P. Smith began the development of this technique in 1985 [304]. He was awarded the Nobel prize in chemistry for his discovery, together with his colleague G. Winter, in 2018 [305].

In this chapter, we have studied the feasibility and the interest of the phage display technique to select peptides with a high affinity for a target VOC or family of VOCs. This represented a challenge, since the VOC molecules are much smaller than the typical targets used traditionally in phage display. Furthermore, the selection is made in solution while we expect to use the selected peptides in the gas phase. We mostly drew inspiration from Ju *et al.* [1], who selected peptides with a high affinity for phenyl compounds.

This study was carried out in close collaboration with Dr. Natale Scaramozzino at the laboratory LiPhy (UMR 5588, CNRS-UGA) at Grenoble. In this thesis, phage display experiments were done at LiPhy.

### 5.1. PHAGE DISPLAY WORKING PRINCIPLE

---

Bacteriophages, or phages, are viruses that infect bacteria. They are naturally found everywhere in our environment, and are widely used as tools for molecular genetics study. Bacteriophages simply consist of a capsid that encloses their genetic material. They are not able to reproduce themselves. To multiply, they inject their genetic material into a bacterium. Therefore, the cellular mechanism of the host is redirected towards viral genome replication and

translation. In such a way, the bacterium produces many copies of the virus that are, in most cases, released by its lysis. There is a very wide variety of bacteriophages in our environment, each with its own target bacteria.

The phage display technique rests on the link that naturally exists between the genotype and the phenotype of a phage. Concisely, one generates a library of random genes *via* an error-prone PCR. Each gene codes for a random peptide or a protein with a random variable part. All the genes of the library are inserted into phage DNA. In this way, one can obtain a library of phages that "display" random peptides on one of their coat proteins.

The principle is outlined in Figure 5-1. The phage library is screened against a target immobilized on a solid surface. This target can be anything, from a protein in the most common case, to metal [306] or semiconductor surfaces [307]. During the selection phase, the phages displaying peptides with a high affinity for the target attach to the solid surface. The other ones can be easily rinsed off. The phages of interest are then eluted from the surface, and put in contact with bacteria. The infection of their host enables the amplification of these phages, to obtain an enriched library that will be used for the next round of selection. Classically, one carries out 3 to 4 selection rounds. After that, the selected phages are isolated, and their DNA is sequenced. One thus finds the corresponding peptide sequences. Subsequently, these sequences can be synthesized for use.

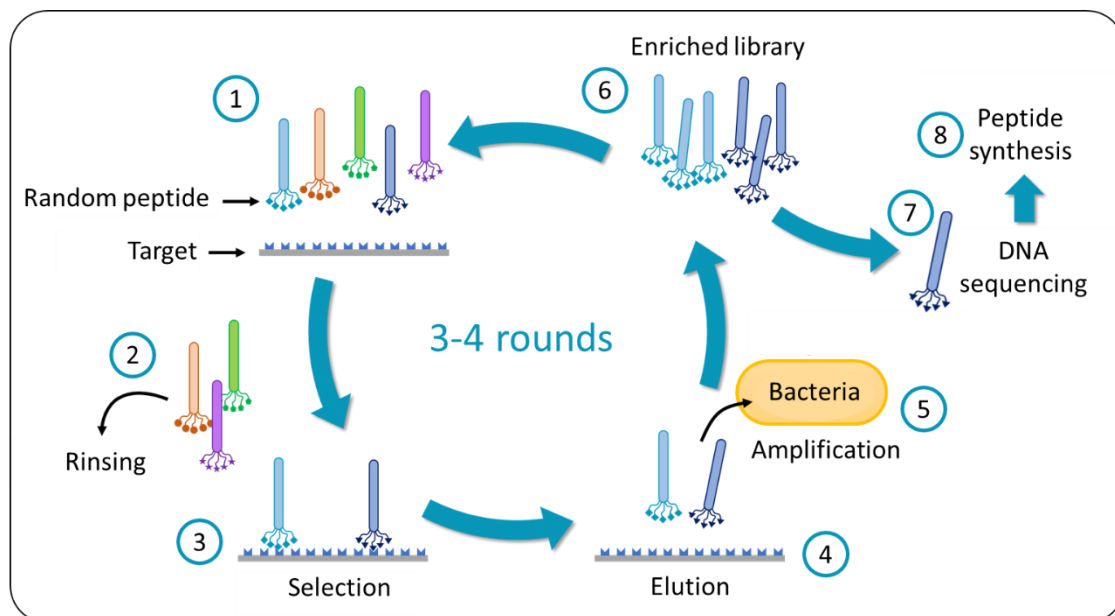


Figure 5-1 Schematic representation of the phage display principle.

In practice, there are several critical points to pay attention to when setting up this protocol. This includes the choice of a phage library, the immobilization of the target on a solid surface, the selection procedure with the choice of an appropriate solvent used for rinsing and elution, and

the monitoring of the selection and choice of final candidates. All these points will be discussed in the first part of this chapter.

### 5.1.1. Phage library

When choosing a phage library, one may think about the type of phage, the choice of a coat protein to modify, the length and type of peptide or protein to be displayed, and the variety of the library, *etc.* We worked with a commercial library of M13 phages (New England Biolabs, Australia), displaying peptides with seven variable amino acids on their p3 protein.

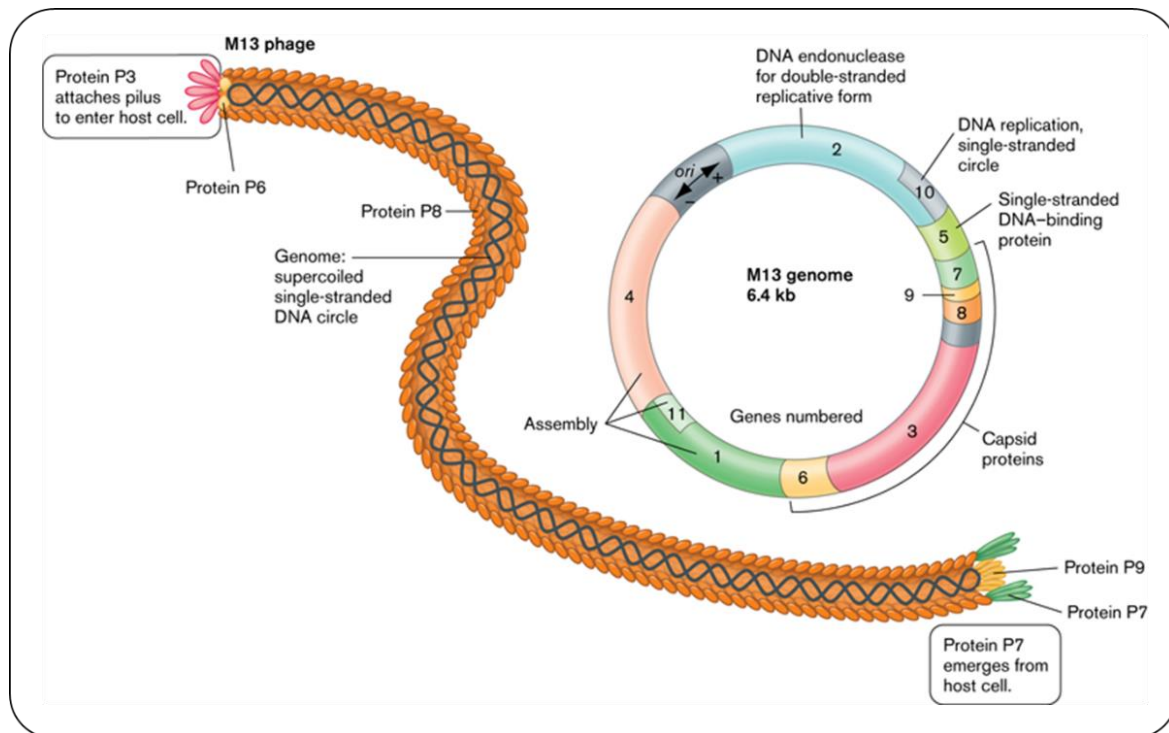


Figure 5-2 The M13 phage structure and genome. The actual phage is about 150 times as long as it is wide. [308]

The structure of the M13 phage is schematized in Figure 5-2. It is a filamentous phage, with a cylindrical shape. It has a length of approximately 1  $\mu\text{m}$  and a diameter of 6 nm. Its DNA is single-stranded [309]. The M13 phage is commonly used for the phage display protocol, since the species presents several features of particular interest for this application.

First, the M13 phage is a chronic phage, with a non-lytic replication cycle. It buds at the bacterial membrane, without breaking it. The infected cell then becomes a factory to produce phage continuously. This feature facilitates the amplification of the viruses during phage display. Moreover, the bacteria automatically produce the complementary strand to the phage DNA. As a result, it increases the quantity of viral double-stranded DNA available for sequencing.

Second, the capsid of the M13 phage is made up of only five different proteins, present in multiple replicates. The link between the genome and the proteome of this virus is well known. As a result, it is relatively simple to modify it selectively by genetic engineering.



Third, it is possible to display the peptide on different coat proteins [310,311]. Notably, one can modify the major coat protein p8, present in 2700 copies on the whole length of the phage capsid. This strategy with increased valency of the peptide is particularly adapted when its affinity with the target is expected to be relatively low. It was adopted by *Ju et al.* [1]. However, to our knowledge, there is no commercial p8 library. Another option is to modify the p3 minor coat protein, present in only five copies at the tip of the filament, which modulates the phage infectivity by binding to the F-pilus of the host bacterial cell. The reduced valency of p3 libraries compared to p8 libraries makes them suitable for the discovery of higher affinity ligands ( $K_d < 10 \mu\text{M}$ ).

For screening peptides with high affinity to VOCs of interest, the phages used in this study displayed a random peptide as N-terminal fusion on the five copies of their p3 protein (Figure 5-3). The same library was used by Tanaka *et al* [312] to screen peptide against benzaldehyde. The random peptides were 11 amino acid long, with a serine and three glycine used as a linker to the p3 protein, and 7 variable residues. As such, their size was comparable to that of the peptides historically used by the laboratory. There were approximately  $10^9$  unique sequences in the library, and thus almost all the possible random sequences were represented.

Several modifications were made to the genome of the M13 phage. First, since the displayed peptide was short, the infectivity of the phage was not affected, even if all the five copies of p3 carried it. As a result, the modified genome contained only a single copy of gene III. This is in contrast to phagemid systems, which provide both modified and unmodified copies.

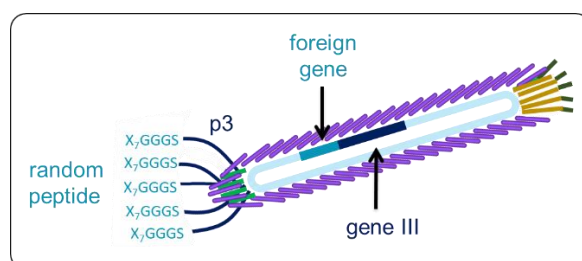


Figure 5-3 Schematic representation of the M13 phages used in this study.

Second, the library was provided with its bacteria host, a non-pathogen strain of *Escherichia coli* (*E. coli*), unable to digest lactose and with a resistance to tetracycline. The addition of this antibiotic to the various bacterial cultures prevented their contamination by environmental bacteria, even though we were working under sterile conditions. A *lacZ $\alpha$*  gene was inserted in the genome of the phage. As a result, infected bacteria acquired the ability to digest lactose through the production of the  $\beta$ -galactosidase enzyme. Phage plaques appeared blue when plated on a medium containing IPTG (isopropyl  $\beta$ -D-1-thiogalactopyranoside, inducer of the lactose operon) and Xgal (5-bromo-4-chloro-3-indolyl-beta-D-galactopyranoside, a dye coupled to lactose).

It is interesting to note that other commercial libraries are available, displaying more structured peptides, with either a longer amino acid sequence, or a cycle-containing structure formed under voluntary constraint. For example, Jaworski *et al.* mixed two commercial libraries: one with random peptides of 12 amino acids, and the other with cyclic peptides to select the strongest binders for explosives [246]. In the future, it may be interesting for us to try some of these libraries. However, we have to keep in mind that it would complicate the integration of the new peptides to the historical system. Indeed, there would be a higher mismatch in molecular weight, and so of SPRi plasmon curve. Moreover, in the case of cyclic peptide, if a disulphide bridge is engaged, the surface chemistry for the immobilization of peptides on the chip covered with a gold layer would have to be modified. Otherwise, the disulfide bridge could break, resulting in the loss of the interesting structure of the selected peptides.

### 5.1.2. Immobilization of the target on a solid surface

The phage display protocol requires the target VOC to be immobilized on a solid surface. The choice of a molecule of interest, its immobilization on the surface, the practicality of the experiments, *etc.* are all important points to consider.

For this preliminary study, we aimed at the detection of compounds containing a phenyl group from the BTX family (benzene, toluene, and the three xylene isomers). The BTX are mono-aromatic VOCs that are very toxic and ecotoxic. They are often released by the petrochemical and fine chemical industry. Their chemical structures are represented in Figure 5-4 (a). For phage display, we immobilized phenylethylamine on the surface. This molecule presents both a phenyl group and a primary amine function for its immobilization on the solid surface (Figure 5-4 (b)).

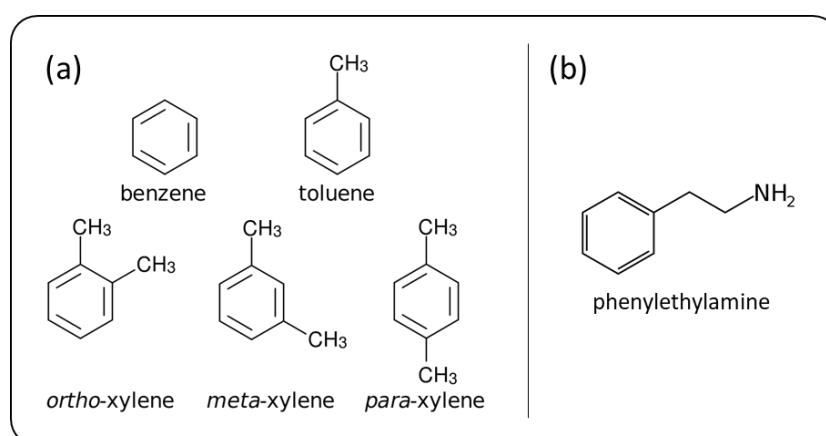


Figure 5-4 (a) Chemical structures of the BTX. (b) Chemical structure of the phenylethylamine, used as a target for phage display experiments.

In our study, phenylethylamine was covalently immobilized on gold-coated glass slides. We used amine-reactive crosslinking chemistry between the surface, functionalized with NHS-ester, and aminated VOC molecules [313]. This method allows for a robust binding of the

VOCs to the surface. Moreover, it can be adapted to different types of surfaces and different VOCs. This is particularly interesting in our case, since the method that we developed here must be generalizable to meet different applicative needs. The precise protocol was established and previously described by Sophie Brenet [228]. The surface of the gold-covered glass slide was calculated to make sure that there would be enough space for all the phages to interact with the target. That way, we were sure not to miss any hits. It is important to mention that, for easier manipulation, magnetic beads can also be used as solid support. Their use can facilitate transferring steps for the different rinse steps and increase the accessibility of the phages to the target thanks to 3D surface.

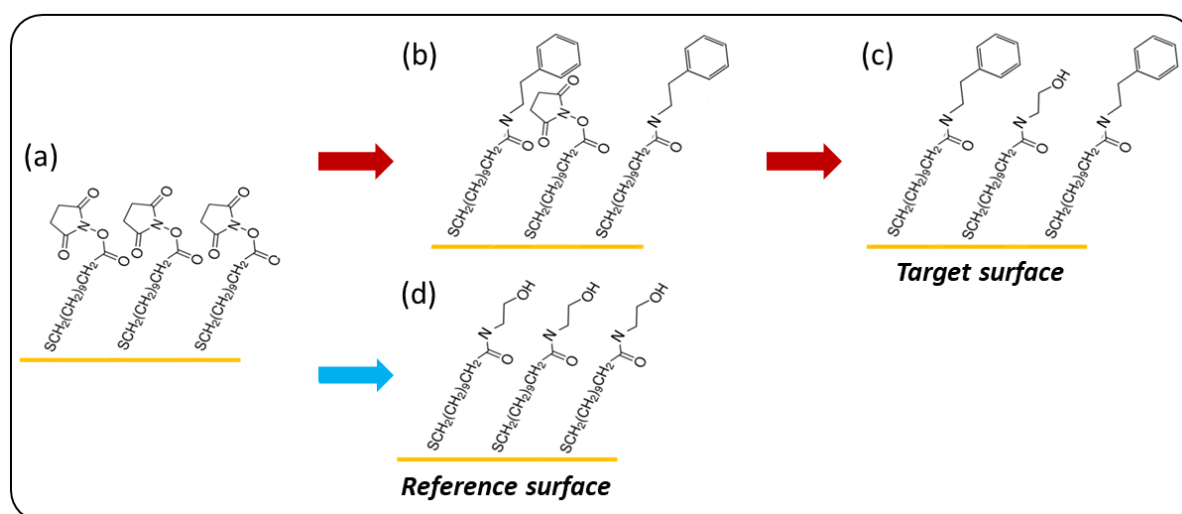


Figure 5-5 Immobilization of amine-VOC molecules on a gold surface (adapted from [228]).

In detail, the gold-covered glass slides were priority plasma cleaned (25% O<sub>2</sub>, 75% Ar, 0.6 mbar, 40W, 3 minutes). Then, they were put in successive bath for functionalization. First, the slides were put in a bath containing 12-mercaptododecanoic acid NHS ester (Sigma-Aldrich) at 2 mM in DMSO overnight, at 25°C. Consequently, a SAM ended with NHS-ester formed on the gold surface (Figure 5-5 (a)). The unbound thiol molecules were washed out. Then, the functionalized slides were immersed in a bath containing phenylethylamine at 4 mM and triethylamine at 4 mM in DMSO overnight at 30°C. In this way, phenylethylamine was coupled to the solid surface via amide bonds (Figure 5-5 (b)). Again, the unbound molecules were rinsed out. Finally, the unreacted NHS-ester groups on the surface were “blocked” with ethanolamine at 1 mM in DMSO for 1h (Figure 5-5 (c)). In parallel, gold-covered glass slides with a reference surface were also fabricated, functionalized with the SAM and ethanolamine alone Figure 5-5 (d)). Each step has been verified by contact angle measurement by Sophie Brenet. Eventually, prior to a phage display selection, the glass side of the slides that was not functionalized was blocked with BSA.

### 5.1.3. Selection procedure

To perform a round of selection, the phage library was diluted in tris-buffered saline (TBS) with 0.1% of Tween 20 (v/v). This surfactant enabled to limit the non-specific attachment of phages on the surface. The selection was performed in Protein LoBind tubes. We used  $2 \times 10^{11}$  phages in 1 mL of buffer for a round of selection. In such a way, there was approximately 200 phages displaying the same random peptide in the initial solution. For the following rounds, the concentration of the enriched library was systematically adjusted to the same value.

Despite all the care taken to block the surfaces other than the target, some of the phages were still prone to stick on the plastic surface of the tubes, on ethanolamine, or on BSA, *etc.* To make sure that these phages would not be selected, we performed a “negative selection” first. To this aim, the library was put in contact with the reference surface for one hour. During this phase, these unwanted phages bound to the interfering surfaces [246,314]. After that, only the supernatant was put in contact with the target surface, again for one hour of incubation. At the end of the incubation, the supernatant was discarded, and the surface was rinsed to eliminate the phages that were less strongly bound. The rinsing protocol is important. If it is too harsh, the phages may be damaged and lose their infectivity, which is necessary for their subsequent elution and amplification. On the contrary, if it is too soft, the selection will be less efficient. In our case, the target surface was rinsed ten times with TBS with 0.5% of Tween 20 (v/v). Tween 20 is a mild nonionic surfactant, which disrupts hydrophobic interactions. After that, we used an acidic Glycine-HCl buffer (pH 2.2) to break hydrogen bonds. With this protocol, after the first round of selection, the number of phages drop from  $2 \times 10^{11}$  pfu/mL to approximately  $10^7$  pfu/mL. We explored new strategies to optimize this phase, which are still under development (see 5.5). Other detergents such as sodium dodecyl sulfate (SDS) or Triton X100 could also be considered [315].

To retrieve the selected phages, we chose to perform a bacterial elution. Briefly, the target surface was put in a culture of *E. coli* for 30 minutes at 37°C. During this step, the phages that were still attached to the target surface infected the bacteria, which integrated their genetic material. The infected cell culture is called eluate. Since the phages recognize and infect the bacteria through their pilus, it was important to make sure that the bacteria were in exponential growth (when they express this pilus) to perform the infection. The optical density at 600 nm (OD<sub>600</sub>) monitored the growth of the culture. We started the elution when the OD<sub>600</sub> reached a value of approximately 0.42. In the end, 5 µL of the eluate was kept for titering (see 5.1.4).

Again, other options exist for this step that could be envisaged to improve the efficiency of the protocol further. Notably, the target molecules, free in solution, could be used for a competitive elution. This would enable a selective elution of the phages that bound to the target. Proteases can

also be used to cut the p3 protein and release the phages. In such a way, only the phages that bound to the surface *via* the peptide displayed on p3 would be eluted.

The rest of the eluate was diluted again in a fresh culture medium with new bacteria ( $OD_{600} = 0.05$ ), and kept at  $37^{\circ}\text{C}$  for 4.5h for amplification. In the end,  $5\ \mu\text{L}$  of this enriched library was kept for titering. We generally obtained a phage titer of  $10^{12}$  pfu/mL. The rest was centrifuged to lyse the bacteria and release the phages, and used for the next round of selection. We typically performed four rounds of selection. Overall, it took one week to perform a phage display experiment.

#### 5.1.4. Phage titering and clone isolation

The phage titering intends to quantify phages. It is very useful to monitor the selection efficiency along the different steps and rounds.

A dilution cascade was performed on the solution containing phages to titter. The objective was to get a countable number of phages in  $10\ \mu\text{L}$  of TBS. For example, if the titer of the solution is expected to be around  $10^7$  pfu/mL ( $10^5$  pfu/ $10\ \mu\text{L}$ ) after selection, we would be able to count phages in  $10\ \mu\text{L}$  for a  $10^5$  to  $10^3$ -fold dilution (Figure 5-6). These  $10\ \mu\text{L}$  solutions were added to  $200\ \mu\text{L}$  of bacterial culture ( $OD_{600} = 0.5$ ) for infection. The infected bacteria were immediately poured in top agar and spread on a petri dish. The petri dish contained a rich culture medium with IPTG and Xgal (see 5.1.1). After one night of incubation at  $37^{\circ}\text{C}$ , the individual phages formed blue lysis plaques on the dishes. Then, we just had to count these plaques to obtain the titer in “plaque forming unit” (pfu) / $10\ \mu\text{L}$ .

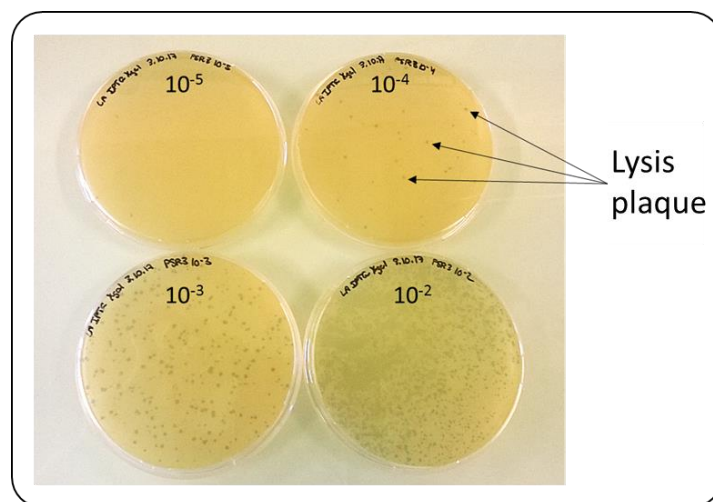


Figure 5-6 Picture of Petri dishes used for phage titering.

These Petri dishes were also used at the end of the phage display experiment to isolate phages displaying a single kind of peptide before DNA sequencing. For this, isolated blue plaques were stabbed using a pipette, and transferred to separated tube containing bacterial culture. After this,

all the different phages were amplified, using the same protocol as for the eluate. Sequencing and peptide synthesis were subcontracted to private companies.

## 5.2. SELECTION OF THREE PEPTIDES FOR THE DETECTION OF PHENYL COMPOUNDS

### 5.2.1. First results of the phage display experiment

Three whole runs of experiments were performed with the classical protocol described in the previous part. The titering results for one run of experiments are presented in Figure 5-7. The phage titer after selection is a good indicator of the efficiency of the protocol. As we can see here, it dropped during the first two rounds, from  $2 \times 10^{11}$  pfu/mL to  $7 \times 10^4$  pfu/mL, as the phages that did not bind to the target were progressively eliminated from the library. From the round three, the titer after selection started to rise again. It was a good sign that the library was enriching with strong binders. The titer after amplification was always higher than  $2 \times 10^{11}$  pfu/mL, which ensured the proper conduct of the next round.

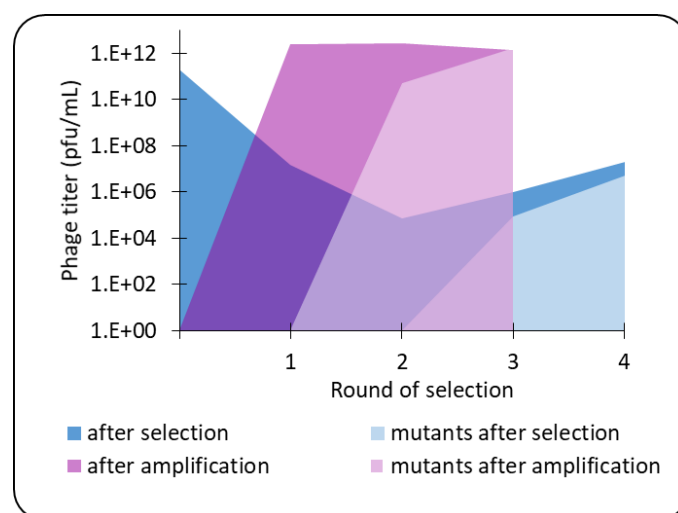


Figure 5-7 Evolution of the phage titer after selection and after amplification during the different rounds of a phage display experiment.

However, there was an increasing number of lysis plaques that were not blue on the Petri dishes used for titering. It could correspond either to mutated phages, that lost the *lacZ $\alpha$*  gene, or to environmental contamination. In our case, we sent some of them for DNA sequencing, which revealed that they were mutants. After three rounds of selection and amplification, there were almost as many mutated phages as phages of interest.

At the end of each experiment run, twelve blue plaques were chosen randomly, amplified and sent for DNA sequencing. This step was not optimal. Indeed, we did not have the equipment capacity to isolate and prepare more phages, though there were many more. Moreover, we did not perform any affinity test on the phages beforehand. As a result, there is no certainty that we have

selected the best binders. Yet, some techniques exist to compare the relative affinities of the selected phages for the target before sequencing. The most commonly used is phage-ELISA (enzyme-linked immunosorbent assay) [316]. This method could be used in the future.

The results are presented in Table 5-1. Unfortunately, for some of the selected phages, the quantity of DNA was too low to enable sequencing. During the three phage display experiments, we finally obtained nine, eight and six peptide candidates, respectively. For each experiment, one of the sequences was found several times (squared in the table). It indicated that the selection was efficient, and that there was an enrichment of the library with stronger binders. However, in phage display experiments, one usually considers that 50% of identical probes are necessary to have a good consensus. Thus, the protocol could probably be further optimized. Besides, we did not double find the same peptide sequence from two different experiments. However, there were some similarities in the physicochemical properties of their constituting residues, represented as colors in Table 5-1. Notably, a basic residue (lysine K or arginine R) was often found next to the C-terminal end of the peptide. Serine was also widely represented. All the sequences included aromatic residues (phenylalanine F, tyrosine T or tryptophan W). This was expectable, since these amino acids are likely to interact with phenyl group through  $\pi$ - $\pi$  stacking.

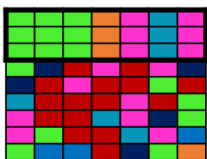
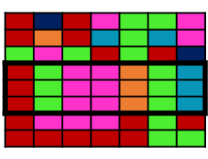

	Experiment 1	Experiment 2	Experiment 3
<b>Readable sequences</b>	9/12	8/12	6/12
<b>Identical sequences</b>	3 (33.3%)	3 (37.5%)	5 (83.3%)
<b>Schematic selected sequences</b> <span style="color: red;">■</span> aliphatic <span style="color: green;">■</span> aromatic <span style="color: orange;">■</span> acidic <span style="color: blue;">■</span> basic <span style="color: pink;">■</span> hydroxylic <span style="color: darkblue;">■</span> amidic			

Table 5-1 Sequencing results of the three phage display experiments led on phenylethylamine targets.

The three selected consensual peptides were synthesized to subsequently test their performance for the detection of BTX when integrated to our optoelectronic tongue and nose. A cysteine was added at their C-terminus, and a linker. They will be referred to as P1, P2, and P3.

## 5.2.2. Characterization of the affinity of the free peptides in solution for phenyl compounds

### 5.2.2.1. ITC measurement

As explained in chapter 3, our attempt to characterize the affinity of the selected peptides by ITC was mostly unsuccessful. This could be for several reasons. The affinity constant may have been too low, or the interaction was neither endothermic nor exothermic.

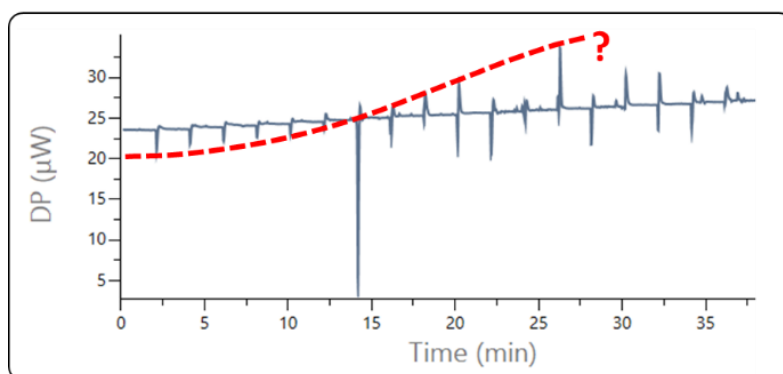


Figure 5-8 ITC measurement for P2 peptide and phenol.

However, an interesting observation was made for the P2 peptide and phenol (Figure 5-8). The signal was quite noisy. Nevertheless, an affinity curve seemed to appear (in red). Moreover, we noticed aggregation in the sample cell, which did not occur without VOC and could reveal an interaction between the probes and the target. Further investigation is necessary to confirm the observation.

### 5.2.2.2. Docking simulations for individual peptides

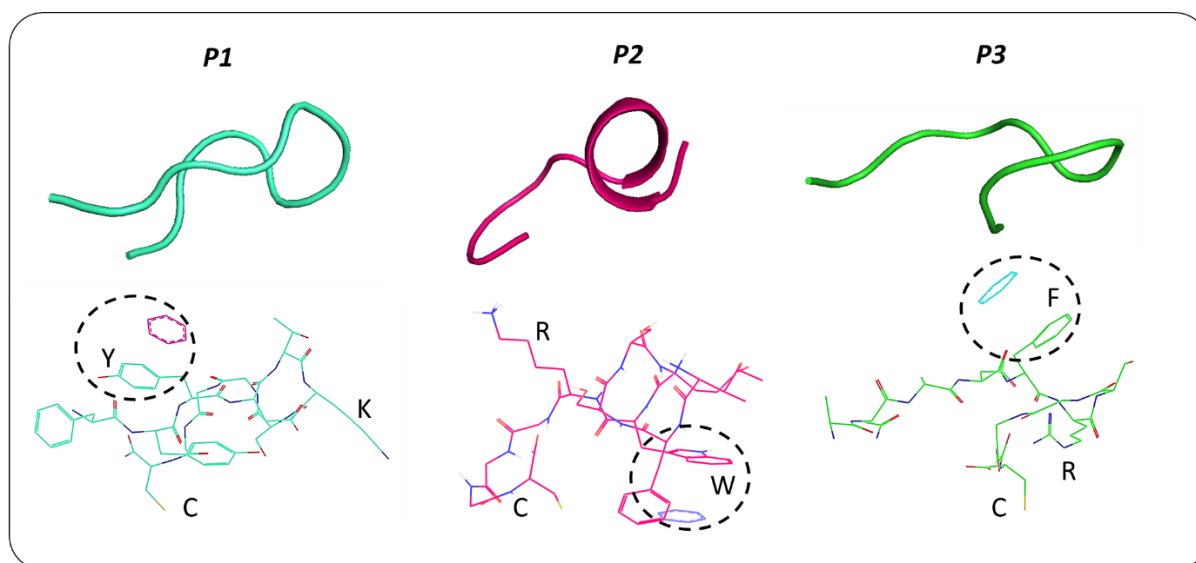


Figure 5-9 Structure of the three selected peptides, and illustration of the preferred binding site for benzene.



We performed computer simulations to determine the structure of P1, P2 and P3 (free in solution) and their affinity for different VOCs (see 3.1.1 for the protocol).

According to simulation, the three peptides have a bent conformation. This is partly due to a lysine or arginine residue with a long and cumbersome side chains present in all sequences just after the linker. As a result, P1 and P3 expose aromatic residues at the opposite of the cysteine (C). P2 is the only selected peptide with an  $\alpha$ -helix (Figure 5-9). As expected, the docking simulation showed that these aromatic cycles are privileged binding sites for phenyl compounds such as benzene, *via*  $\pi$ - $\pi$  stacking for all the selected peptides.

	P1	P2	P3	B5	B6	B7	R1	R2	R3	R4	R5	R6	R7	R8	R9	R10	R11	R12	R13	R14	R15	R16	R17	R18	R19
ethane	-3.4	-3.3	-3.0	-2.9	-3.0	-2.9	-2.1	-2.3	-2.6	-3.4	-2.7	-2.5	-3.5	-3.5	-3.6	-3.0	-2.9	-2.7	-2.5	-3.0	-3.1	-2.2	-2.3	-2.7	-2.9
propane	-3.2	-3.3	-3.3	-3.2	-3.0	-2.6	-2.2	-2.4	-2.8	-3.1	-2.7	-2.4	-3.4	-3.5	-3.5	-2.7	-2.9	-2.9	-2.5	-2.9	-3.5	-2.4	-2.8	-2.4	-2.9
pentane	-1.9	-2.0	-2.3	-1.8	-1.9	-2.0	-1.7	-1.5	-1.9	-1.8	-1.6	-1.6	-2.1	-1.9	-1.9	-1.8	-1.8	-1.6	-1.7	-1.8	-1.9	-1.6	-1.8	-1.7	-1.9
heptane	-2.7	-2.6	-2.5	-2.4	-2.3	-2.1	-1.3	-1.8	-2.2	-2.2	-1.9	-1.7	-3.1	-2.8	-3.0	-2.3	-2.0	-2.1	-1.9	-2.4	-2.6	-1.4	0.0	-1.8	-2.1
methylcyclohexane	-3.1	-3.0	-3.9	-2.7	-2.7	-2.4	-1.5	-2.1	-2.4	-2.6	-2.2	-1.8	-3.4	-3.3	-3.3	-2.6	-2.2	-2.3	-2.1	-2.7	-2.9	-1.6	-1.8	-2.0	-2.4
benzene*	-2.7	-2.6	-2.5	-2.4	-2.3	-2.1	-1.3	-1.8	-2.2	-2.2	-1.9	-1.7	-3.1	-2.8	-3.0	-2.3	-2.0	-2.1	-1.9	-2.4	-2.6	-1.4	-1.6	-1.8	-2.1
m-xylene*	-2.9	-2.8	-2.8	-2.5	-2.3	-2.5	-2.1	-2.0	-2.8	-2.7	-2.2	-2.1	-3.3	-2.7	-2.8	-2.3	-2.6	-2.1	-2.3	-2.6	-3.0	-2.2	-2.6	-2.3	-2.7
o-xylene*	-3.4	-3.5	-3.2	-2.8	-2.8	-2.7	-1.7	-2.2	-2.6	-2.8	-2.4	-2.0	-3.5	-3.6	-3.6	-2.8	-2.4	-2.5	-2.2	-2.9	-3.1	-1.7	-2.0	-2.1	-2.6
p-xylene*	-3.1	-2.5	-2.9	-2.5	-2.5	-2.6	-2.0	-2.0	-2.5	-2.7	-2.3	-2.1	-3.0	-3.0	-3.1	-2.7	-2.6	-2.3	-2.1	-2.6	-2.9	-2.0	-2.3	-2.1	-2.7
toluene*	-3.4	-3.2	-3.2	-3.0	-2.8	-2.5	-1.6	-2.2	-2.6	-3.0	-2.4	-2.0	-3.6	-3.6	-3.6	-2.7	-2.4	-2.5	-2.3	-3.0	-3.1	-1.7	-2.0	-2.1	-2.6
indole*	-2.3	-2.1	-2.5	-2.0	-1.9	-2.1	-1.8	-1.6	-2.1	-2.0	-1.9	-1.7	-2.4	-2.1	-2.3	-2.0	-2.0	-1.8	-1.8	-2.0	-2.2	-1.7	-1.9	-1.8	-2.0
ethanol	-1.2	-1.2	-1.0	-1.1	-1.2	-1.0	-0.6	-0.8	-1.1	-1.0	-0.9	-0.8	-1.5	-1.3	-1.4	-1.1	-0.9	-1.0	-0.9	-1.2	-1.2	-0.7	-0.8	-0.9	-0.9
propanol	-1.6	-1.7	-1.5	-1.5	-1.6	-1.3	-0.8	-1.1	-1.5	-1.4	-1.3	-1.1	-2.0	-1.7	-2.0	-1.4	-1.3	-1.4	-1.3	-1.6	-1.7	-0.9	-1.1	-1.2	-1.3
butanol	-3.5	-3.2	-3.2	-3.1	-2.8	-2.8	-2.4	-2.4	-2.9	-3.3	-2.7	-2.2	-3.6	-3.5	-3.4	-3.0	-2.7	-2.7	-2.4	-3.0	-3.2	-2.2	-2.7	-2.4	-3.1
pentanol	-2.1	-2.3	-2.0	-2.0	-1.9	-1.7	-1.1	-1.5	-2.0	-1.9	-1.8	-1.3	-2.6	-2.2	-2.5	-1.9	-1.7	-1.8	-1.5	-2.1	-2.3	-1.2	-1.3	-1.5	-1.9
heptanol	-2.5	-2.7	-2.4	-2.1	-2.2	-2.2	-1.4	-1.8	-2.2	-2.3	-2.1	-1.5	-2.9	-2.4	-2.7	-2.0	-1.9	-2.0	-1.6	-2.4	-2.5	-1.4	-1.4	-1.7	-2.0
phenol*	-3.4	-3.3	-3.2	-2.9	-2.9	-2.5	-1.7	-2.2	-2.6	-2.8	-2.4	-2.0	-3.5	-3.6	-3.7	-2.7	-2.4	-2.5	-2.2	-2.9	-3.1	-1.7	-2.0	-2.2	-2.6
phenylethanol*	-2.8	-2.7	-2.6	-2.6	-2.5	-2.3	-1.4	-1.9	-2.3	-2.5	-2.0	-1.8	-3.1	-3.0	-3.1	-2.4	-2.2	-2.2	-1.9	-2.7	-2.8	-1.5	-1.8	-2.0	-2.3
ethanal	-2.5	-2.3	-2.6	-2.2	-2.2	-2.2	-2.0	-1.8	-2.3	-2.3	-2.1	-1.8	-2.8	-2.3	-2.5	-2.2	-2.2	-1.9	-1.8	-2.2	-2.3	-1.8	-2.0	-1.9	-2.3
propanal	-1.4	-1.9	-1.8	-1.6	-1.4	-1.7	-1.4	-1.3	-1.7	-1.6	-1.2	-1.5	-1.8	-1.4	-1.6	-1.2	-1.4	-1.2	-1.6	-1.5	-1.6	-1.5	-1.7	-1.4	-1.3
pentanal	-1.8	-2.1	-2.2	-1.8	-1.6	-1.8	-1.5	-1.5	-2.0	-1.9	-1.4	-1.7	-2.0	-1.9	-2.0	-1.6	-1.7	-1.5	-1.7	-1.7	-1.9	-1.6	-1.8	-1.5	-1.6
heptanal	-1.6	-1.8	-2.0	-1.6	-1.7	-1.9	-1.6	-1.3	-1.6	-1.6	-1.4	-1.5	-1.8	-1.5	-1.5	-1.6	-1.6	-1.4	-1.5	-1.5	-1.6	-1.5	-1.7	-1.5	-1.8
benzaldehyde*	-2.3	-2.4	-2.4	-2.2	-2.0	-2.0	-1.7	-1.7	-2.4	-2.3	-1.8	-1.8	-2.7	-2.3	-2.5	-1.9	-2.1	-1.7	-1.9	-2.1	-2.4	-1.7	-2.1	-1.8	-2.0
hexylester	-2.5	-2.6	-2.6	-2.5	-2.3	-2.1	-1.8	-2.0	-2.7	-2.5	-2.1	-1.9	-3.0	-2.6	-2.8	-2.0	-2.1	-2.1	-2.1	-2.5	-2.8	-1.7	-2.2	-2.0	-2.2
methyl acetate	-3.7	-3.3	-3.3	-3.2	-2.9	-3.1	-2.6	-2.6	-3.3	-3.5	-2.9	-2.7	-4.0	-3.6	-3.5	-3.1	-3.0	-2.9	-2.9	-3.4	-3.6	-2.7	-3.1	-2.7	-3.3
methyl propanoate	-2.0	-2.2	-2.4	-1.9	-1.7	-2.1	-1.8	-1.7	-2.0	-2.0	-1.5	-2.0	-2.4	-1.9	-1.9	-1.7	-2.0	-1.6	-2.1	-2.0	-2.2	-2.2	-1.9	-1.9	-1.7
methyl valerate	-2.3	-2.4	-2.5	-2.0	-1.8	-2.2	-1.8	-1.7	-2.2	-2.2	-1.7	-2.0	-2.6	-2.1	-2.3	-1.9	-2.1	-1.8	-2.2	-2.2	-2.4	-2.2	-2.1	-2.1	-1.8
methyl heptanoate	-2.8	-2.6	-2.6	-2.4	-2.2	-2.4	-2.1	-1.9	-2.5	-2.5	-2.0	-2.1	-3.2	-2.7	-2.7	-2.2	-2.2	-2.1	-2.3	-2.3	-2.7	-2.2	-2.2	-2.2	-2.2
phenylbutyrate*	-2.8	-3.3	-2.5	-2.7	-2.2	-2.3	-1.9	-1.8	-2.8	-2.5	-2.4	-2.1	-3.1	-3.1	-2.8	-2.3	-2.1	-2.7	-2.2	-3.0	-3.1	-2.1	-2.4	-2.1	-2.3
acetic acid	-3.3	-3.0	-2.9	-2.8	-2.6	-2.6	-2.1	-2.0	-2.7	-2.7	-2.2	-2.2	-3.3	-3.4	-3.4	-2.6	-2.4	-2.3	-2.4	-2.8	-3.1	-2.2	-2.4	-2.2	-2.5
propanoic acid	-2.0	-2.2	-2.3	-1.8	-1.9	-2.2	-2.0	-1.6	-2.0	-1.9	-1.7	-1.9	-2.4	-1.7	-1.8	-1.9	-1.9	-1.6	-1.9	-1.9	-1.9	-2.1	-2.2	-1.9	-2.3
valeric acid	-2.3	-2.4	-2.6	-2.0	-2.1	-2.4	-2.0	-1.6	-2.3	-2.2	-2.0	-2.0	-2.5	-2.0	-2.2	-2.1	-2.2	-1.8	-2.0	-2.0	-2.3	-2.1	-2.3	-2.1	-2.4
hexanoic acid	-2.6	-2.7	-2.7	-2.6	-2.4	-2.4	-2.0	-2.0	-2.5	-2.6	-2.3	-1.8	-3.0	-2.7	-2.7	-2.3	-2.3	-2.3	-2.1	-2.5	-2.7	-2.0	-2.2	-1.9	-2.5
heptanoic acid	-2.8	-2.6	-2.8	-2.3	-2.3	-2.4	-2.2	-1.9	-2.7	-2.6	-2.2	-2.1	-3.2	-2.5	-2.6	-2.3	-2.5	-2.0	-2.2	-2.4	-2.8	-2.1	-2.5	-2.2	-2.6
phenylacetic acid*	-3.0	-2.9	-2.9	-2.6	-2.5	-2.7	-2.1	-2.1	-2.7	-2.5	-2.5	-2.1	-3.4	-2.7	-2.9	-2.4	-2.7	-2.4	-2.2	-2.8	-3.1	-2.0	-2.5	-2.2	-2.7

Table 5-2 Binding energies obtained by molecular docking for the binding of the different peptides to a range of VOCs from different chemical families with (\*) or without phenyl groups.

Furthermore, we performed docking simulations with AutoDock to compare the affinity of P1, P2 and P3 for 35 different VOCs of various chemical families and molecular weight. It is important to remind that those docking simulations were led on rigid peptides, in solution, for a one-to-one interaction with a VOC molecule. For comparison, the same simulations were also led on all the historical peptides, as well as on the specific peptide sequences selected by Ju et al. [3] targeted to the detection of benzene, named B5 (DSWAADIPGC), B6 (DNPIQAVPGC) and B7 (DRNESSVPGC) here. All the results are compiled in Table 5-2.

We defined an indicator of the simulated selectivity for phenyl compounds “Simulated  $S_{phenyl}$ ” as follows:

$$\text{Simulated } S_{phenyl} = \frac{E_{bind}(phenyl) - E_{bind}(other)}{\overline{E_{bind}}} \times 100$$

With  $E_{bind}(phenyl)$ ,  $E_{bind}(other)$  and  $\overline{E_{bind}}$  the average simulated binding energy of the peptide with phenyl compounds, other compounds, or all compounds, respectively. In the rest of this chapter, a similar indicator will be calculated from the SPRi signals. In this case, “Experimental  $S_{phenyl}$ ” designates:

$$\text{Experimental } S_{phenyl} = \frac{\Delta R_{eq}(phenyl) - \Delta R_{eq}(other)}{\overline{\Delta R_{eq}}} \times 100$$

With  $\Delta R_{eq}(phenyl)$ ,  $\Delta R_{eq}(other)$  and  $\overline{\Delta R_{eq}}$  the average variation of reflectivity at equilibrium of the biosensors based on the peptide upon exposure to phenyl compounds, other compounds, or all compounds, respectively.

The results are presented in Figure 5-10.

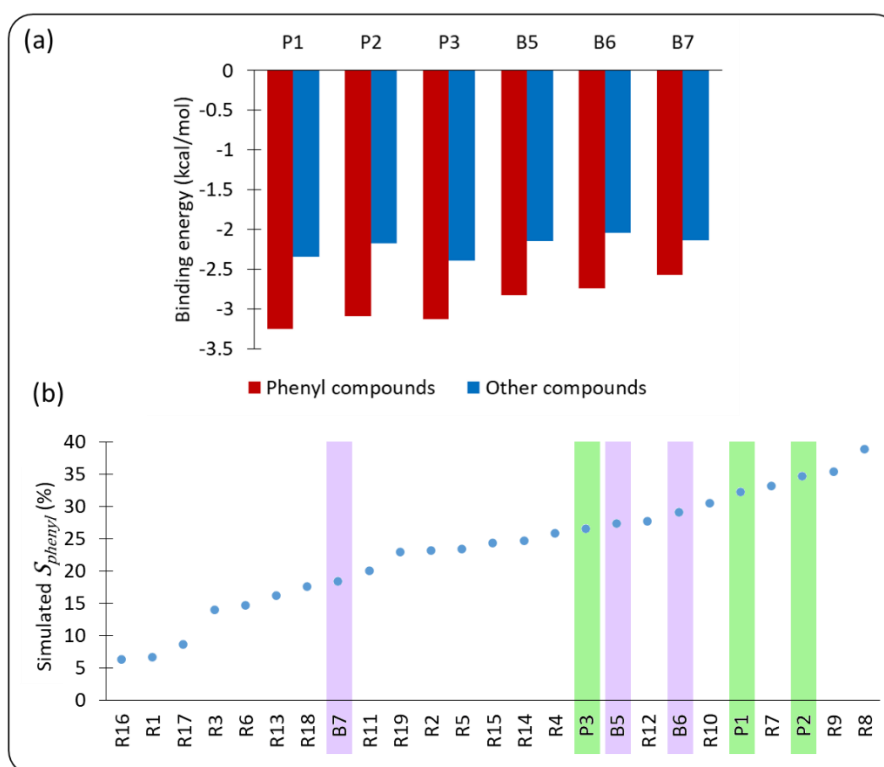


Figure 5-10 (a) Binding energies calculated by molecular docking for the three peptides selected here (P1, P2 and P3), and in the literature (B5, B6 and B7). (b) Selectivity for phenyl compounds of all the peptides used in this project. The peptides squared in purple were directly adapted from Ju et al. [91]. The peptides squared in green were selected in this project. The other peptides were historically used in the laboratory.

As a general tendency observed in Table 5-2, the binding energy between the three peptides selected by phage display and phenyl compounds was lower than the average one between the historical peptides and phenyl compounds. The lower the binding energy, the higher the affinity.

Thus, this result was encouraging. More interestingly, P1, P2 and P3 had also a higher affinity for phenyl compounds than the three peptides B5, B6 and B7 selected by Ju *et al.* [91] (Figure 5-10 (a)). However, generally speaking, the affinity was quite low, with a minimum binding energy of -3.9 kcal/mol obtained between P3 and toluene. For comparison, the energy of thermal agitation is  $RT = 0.593$  kcal/mol at 25°C. This value gives an evaluation of the uncertainty related to thermal noise, which is not taken into account in the simulations performed on rigid “frozen” structures.

Another satisfying result is that P1, P2 and P3 had a good simulated selectivity for phenyl compounds (Figure 5-10 (b)). On top of that, the selectivity of P1 and P2 was better than the selectivity of B5, B6 and B7. Nevertheless, some of the historical peptides had even a higher simulated  $S_{phenyl}$  value such as R8 and R9. This was not surprising, since these peptides possess several repetitive amino acids containing aromatic residues and a helical structure.

In fact, for unconstrained peptides as short as the ones we use, and small VOCs with a simple structure like benzene, we could not expect a very high affinity and selectivity. Indeed, the possible structures that they could adopt were very simple, with no possibility of forming a folded “binding site” involving several amino acid residues, like in proteins. Thus, a VOC interacted with only one of the amino acids of the peptide. Under these conditions, rationalizing the sequences made less sense than with longer or more constrained peptides.

However, the results may be different when the peptides will be attached to the gold surface, with a dense assembly, and with the possibility to bind several VOCs on each peptide.

### 5.2.2.3. Simulated chemical resolution of an artificial tongue

Even if the individual performance simulated *in silico* for P1, P2 and P3 was not particularly remarkable, their association with the historical peptides in an artificial tongue or artificial nose system may improve their chemical resolution, especially for the phenyl compounds. To verify this assumption, we performed a PCA using the calculated binding energies from the docking simulations.

Each point in Figure 5-11 corresponds to a different VOC. The PCA was not radically changed by the addition of P1, P2 and P3. The new peptides selected by phage display did not affect the ability of the device to classify chemical families (colors).

The mean distance between individuals increased with P1, P2 and P3. This result must be qualified, because the addition of supplementary dimensions mathematically causes this effect. In this case, the increase is not significant to prove that the binding properties of the peptides selected by phage display are responsible for this better separation. However, based on these simulations, the addition of these peptides is expected to improve slightly the discrimination capability of the artificial tongue or nose. Notably, in the simulations, the VOCs with a phenyl ring

were spaced further apart from the other individuals. It particularly helped to separate phenyl butyrate from heptanol and heptanoic acid, or phenol from phenyl ethanol and indole.

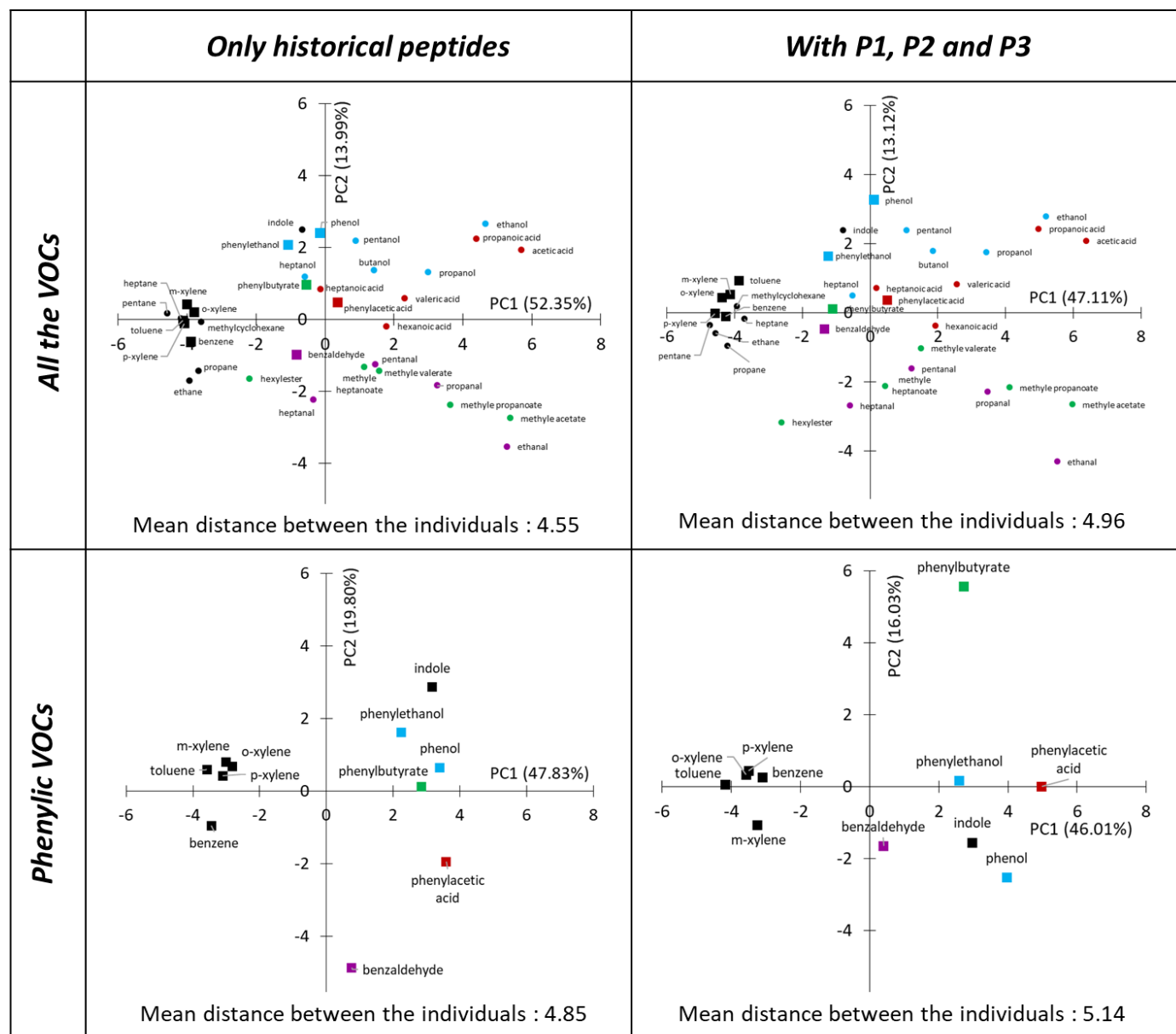


Figure 5-11 PCA performed on docking simulations results.

The Figure 5-12 (a) and (b) are projections of the former PCA in the plan (PC1:PC3), with a zoom around alkanes. It shows that the addition of P1, P2 and P3 helped to separate the phenyl VOCs from others along PC3. Interestingly, P3 strongly correlated with PC3 (Figure 5-12 (c)), which showed that it played an important role in this discrimination.

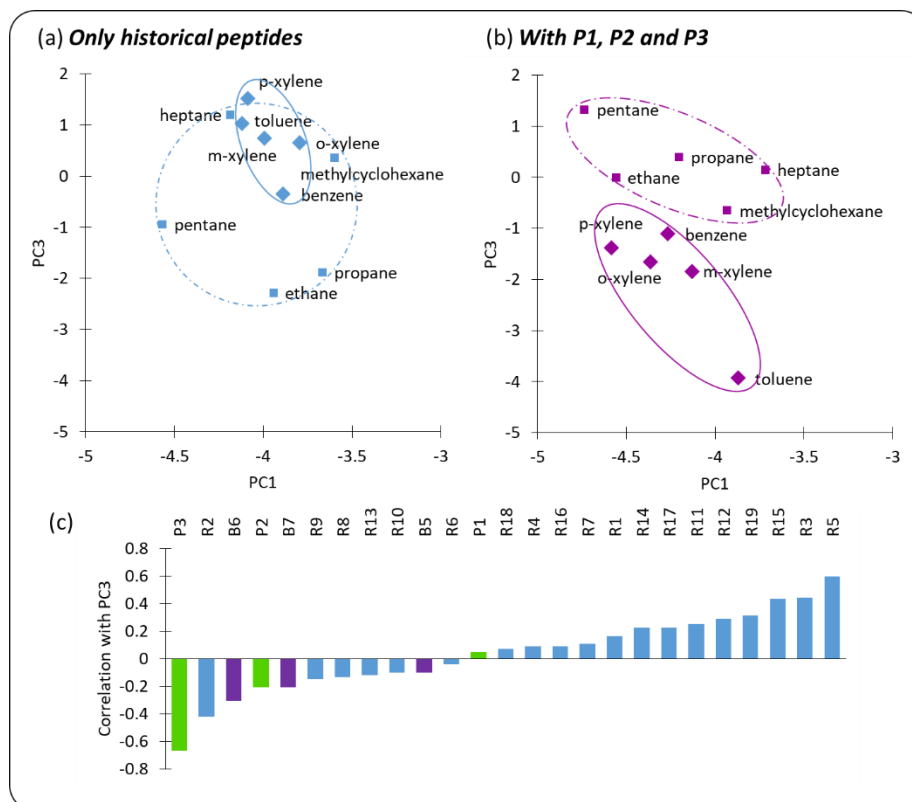


Figure 5-12 Extract of the PCA performed on docking simulations results (Figure 5-11 top), projected in the plan (PC1:PC3). (a) With only the historical peptides. (b) When adding P1, P2 and P3. (c) Correlation of the different variables with PC3.

In conclusion, three consensual peptide sequences were identified by phage display, named P1, P2 and P3. They exhibit similar features such as a bent structure and aromatic residues. Docking simulations showed that these residues are most likely preferred binding sites for phenyl compounds, through  $\pi$ - $\pi$  stacking. As a result, the three peptides have a good predicted selectivity for these VOCs, better than the peptides selected previously in the literature. However, some of the historical peptides, with more aromatic residues, performed even better. In fact, with peptides as short as the ones we used, we cannot expect extremely high affinities. Nevertheless, adding P1, P2 and P3 to our peptide chip is expected to improve slightly the chemical resolution of the optoelectronic tongue or nose, notably to separate phenyl compounds from others. Nevertheless, the simulations are rough estimations of what may occur in the liquid phase. Indeed, they consider the different peptides as free, in solution, with a rigid structure and a one-to-one interaction.

### 5.3. PEPTIDE-BASED OPTOELECTRONIC TONGUE: DETECTION OF VOCs IN THE LIQUID PHASE

---

Before their use in our optoelectronic nose, the peptides selected by phage display have to be attached to the surface of the prism, and dried. Both may affect their structure and binding affinity for the target VOCs. To decouple the effects of immobilization and drying, we deposited the new peptides on a prism, together with some of the historical ones, and we first evaluated the performance of P1, P2 and P3 for VOC detection in solution. The liquid-SPRi chips being smaller than the gas-phase SPRi ones, we could not spot all the historical peptides. Only some of them were chosen for comparison.

In the phage display experiments, the possibility of cooperation between peptides was low. Only five peptides that could bind to the target were located at the end of phage, which helped to reduce steric hindrance. To reproduce this situation on our chip, we also deposited spots with a lower peptide density on the surface of the prism. To this end, the peptides were mixed with perfluorothiol molecules in the spotting buffer in a one-to-ten proportion.

The free gold surface on the prism was passivated with PEG OH (100  $\mu$ M in H<sub>2</sub>O) to limit non-specific adsorption on the unprotected gold. After all the functionalization steps, it was rinsed and dried with argon.

The peptide chip was mounted in a PEEK analysis chamber. We used filtered phosphate buffer (NaH<sub>2</sub>PO<sub>4</sub> 50 mM, pH 7.5) as running buffer. The samples were diluted in the running buffer. The injection loop volume was 1 mL. Once the chip had been in contact with the phosphate buffer, we had to be very cautious not to dry it. Indeed, the salt present in the solution would crystallize on the prism surface, making impossible further SPRi analysis. As a result, the prism was never moved away from the liquid-phase SPRi bench between experiments. A same prism was only used up to five days and twenty injections.

#### 5.3.1. Signal amplification by the detection of nanoparticles functionalized with VOCs

As explained in chapter 3, the small size of the VOCs made impossible their direct detection in liquid-phase SPRi. We therefore used gold nanoparticles (AuNPs) to carry VOC substitutes for signal amplification. For this, we functionalized nanoparticles with phenylethylamine, called P-AuNPs. Besides, we prepared nanoparticles functionalized with PEG OH (OH-AuNPs) for negative control. They were both used to estimate the selectivity of the new peptide probes. Indeed, there were phenyl rings on the P-AuNPs but not on the OH-AuNPs.

In practice, to prepare P-AuNPs, in the first step, AuNPs (20 nm, BBI solutions, UK) were functionalized with a mixture of a thiolated PEG OH (HS-(CH<sub>2</sub>)<sub>11</sub>(EG)<sub>3</sub>-OH, Prochimia, Poland), and

a longer thiolated PEG COOH (HS-(CH<sub>2</sub>)<sub>11</sub>(EG)<sub>6</sub>-COOH, Prochimia, Poland) in a 10:1 proportion (v/v). PEG-thiols were chosen to ensure a good dispersion and stability of P-AuNPs in aqueous solutions. Besides, the PEG OH was used as a diluent. In the second step, the carboxyl function on the PEG COOH was activated to form stable amine-reactive ester by EDC/NHS (1-ethyl-3-(3-dimethylaminopropyl) carbodiimide hydrochloride and N-hydroxy-sulfosuccinimide, Thermofisher, France). Finally, phenylethylamine was introduced and covalently immobilized on AuNPs via amide bond. The functionalization of the nanoparticles was assessed by dynamic light scattering (DLS, LiteSizer 500, Anton Paar, Austria), as shown in Figure 5-13, which confirmed that their size increased after each step.

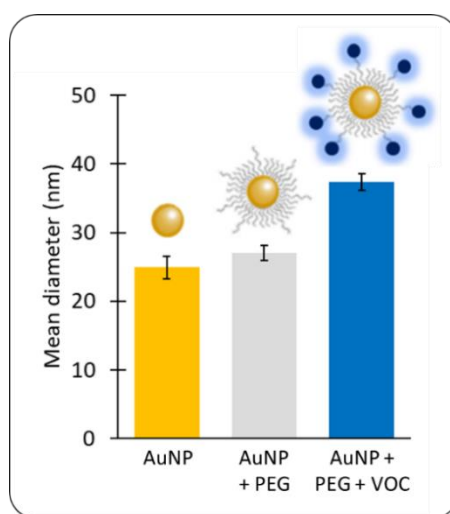


Figure 5-13 Characterization of the different intermediates of P-AuNP by DLS

The Figure 5-14 (a) shows the kinetic response obtained on a peptide chip in liquid-phase SPRi for toluene without amplification. Clearly, there was no valid signal (with a SNR>3) in this case. In comparison, for the injections of the decorated nanoparticles (b) and (c), the variation of reflectivity was approximately twenty times higher.

The regeneration of the biosensors was not spontaneous in this case. We used SDS (0.5% v/v in phosphate buffer) to this end. SDS is an anionic surfactant. A test experiment showed that it was efficient to recover the baseline after injection of nanoparticles on all the biosensors, as far as a low-enough concentration was used. In our case, all the injections were made with 100 pM of nanoparticles. Their concentration was assessed by their absorption at 520 nm ( $\epsilon = 8 \times 10^8 \text{ M}^{-1} \text{ cm}^{-1}$  [317]) with the use of a NanoDrop™ (2000c, Thermo Scientific, USA).

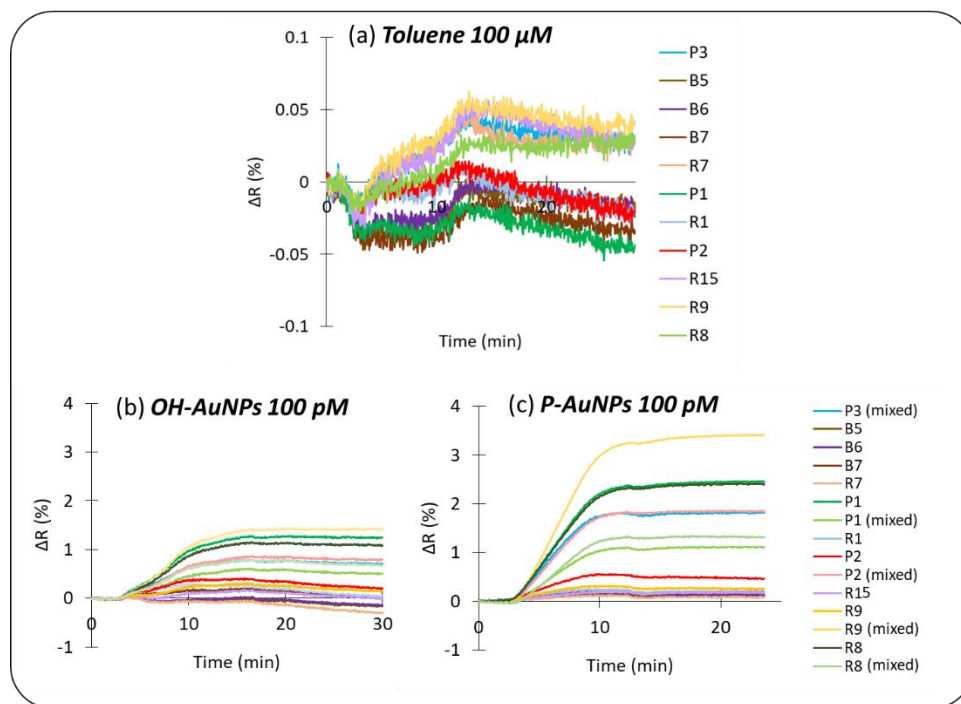


Figure 5-14 Kinetic response obtained in liquid-phase SPRi upon the injection of: (a) toluene (100  $\mu\text{M}$ ), (b) OH-AuNPs at 100 pM and (c) P-AuNPs at 100 pM. B5, B6 and B7 were selected by phage display in a reported work; R1, R7, R8, R9, and R15 are historical peptide. They were all used for comparison.

Examples of equilibrium profiles obtained for the injection of OH-AuNP and P-AuNP are presented in Figure 5-15 (a). The chip was regenerated between each injection. The signal obtained on the background of the chip (passivated with PEG OH) was subtracted to the response profile. For pure P1 and P2 and P3 mixed with perfluorothiols, there was a significant contrast between the signals obtained for the two types of nanoparticles. Thus, the peptides that we selected by phage display seem to have a certain selectivity for compounds containing a phenyl group. As expected, similar results were obtained with R8 and R9 high in aromatic residues. Satisfyingly, P1, P2 and P3 have much higher affinity to P-AuNPs than most of the historical peptides and also than the three other peptides selected by phage display for a phenyl target in the literature: B5, B6, and B7.

This was consistent with the simulation results. The Figure 5-15 (b) makes a comparison between the simulated selectivity for phenyl compounds (see 5.2.2.2) and the contrast between the SPRi signals measured experimentally with P-AuNP and OH-AuNP. There was a good correlation between them. It seemed to indicate that the immobilization of the peptides on the surface of the prism did not radically affect their affinity for the different VOCs. Besides, it demonstrated that the results of the simulations were reasonably correct, despite all the approximations involved.

Furthermore, we defined a regeneration efficiency, as the ratio between the variation of reflectivity during regeneration and the variation of reflectivity during the preceding injection



(Figure 5-15 (c), insert). Interestingly, the Figure 5-15 (c) shows that, for P1 and P2, the regeneration efficiency was much higher after an injection of OH-AuNP than after an injection of P-AuNP (red area). It could result from a higher affinity for the phenyl group. However, surprisingly, the opposite phenomenon was observed for P3.

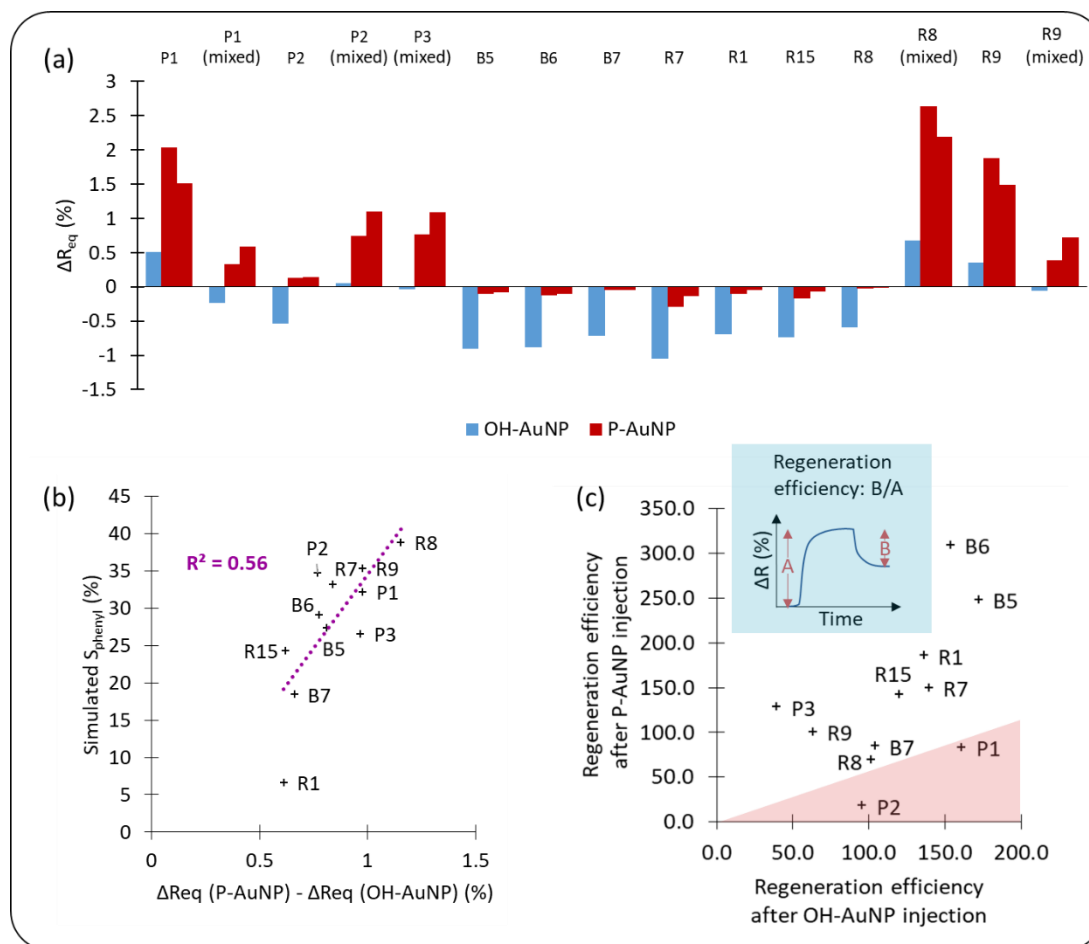


Figure 5-15 (a) Equilibrium profiles obtained for OH-AuNP and P-AuNP injections in liquid-phase SPRI. The signal obtained on the background of the chip (passivated with PEG OH) was subtracted to the response profile. (b) Comparison between the simulated selectivity for phenyl compounds of the different probes and the contrast in the SPRI signals of the corresponding biosensors upon the injection of P-AuNP and OH-AuNP. (c) Regeneration efficiency after P-AuNP or OH-AuNP injections on the different probes.

### 5.3.2. Competitive assay

With these two kinds of nanoparticles, we were only able to get an idea of the specificity of the peptides P1, P2 and P3 for VOCs with a phenyl ring. On top of that, it was not possible to characterize the sensitivity of the biosensors, or the chemical resolution of the optoelectronic tongue. We considered using competitive assays for a more precise characterization.

The first idea (Figure 5-16 (a)) was to first inject P-AuNP on the chip, then in a second time, to inject different VOCs with a phenyl group like toluene, phenol, *etc.* Had the affinity of these free VOCs for the peptides been significantly higher, they could have competed and replaced the nanoparticles. As a result, a SPRI signal decrease would have been observed. Unfortunately, this

strategy was unsuccessful. The AuNP were potentially too heavy to be detached from the biosensors, or the contrast in affinity was not high enough, possibly due to multiple interactions between one AuNP and the peptides.

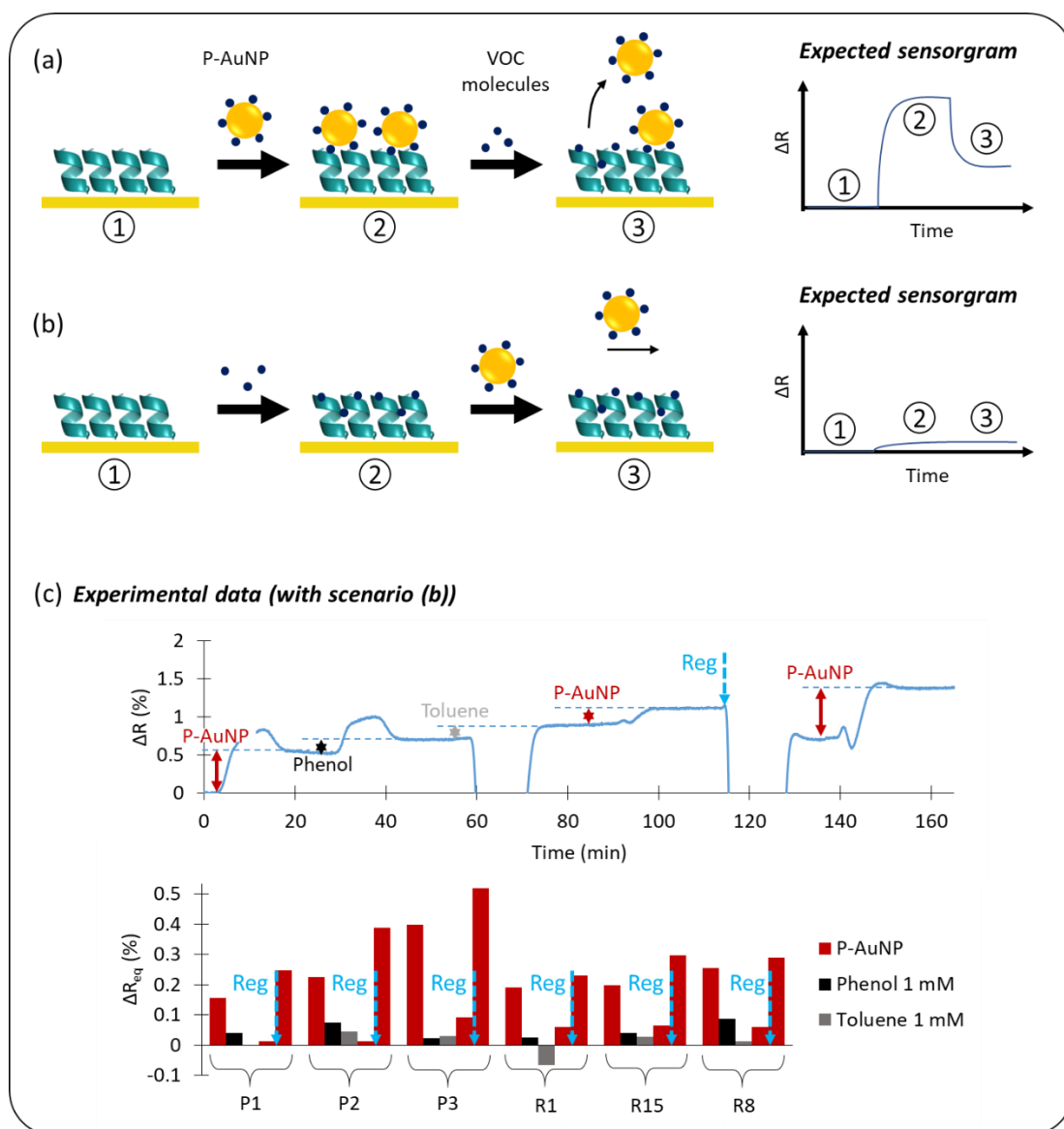


Figure 5-16 (a) and (b): Alternative strategies proposed for competitive assays of the selectivity of the peptides to different VOCs. (c) Kinetic and equilibrium profiles of a series of injections performed in liquid-phase SPRI on a peptide chip with protocol (b). The blue arrow indicates the regeneration of the chip (SDS 0.05%).

Alternatively, the second idea (Figure 5-16 (b)) was to inject the free VOCs first, at a high concentration to ensure the saturation of the binding sites on peptides. Then, in a second time, P-AuNP were injected for competitive assays. Some preliminary experiments were performed using this protocol. The results are presented in (Figure 5-16 (c)). An injection of P-AuNP was made on the same chip beforehand, for comparison. In a second time, we performed injections of the free VOCs (phenol 1 mM, then toluene at 1 mM), which did not give any measurable signal. Then without regeneration, P-AuNP were further injected. This time, there was no measurable signal at

all on the different peptides. It is most likely that the injection of phenol and toluene saturated the biosensors. This result was encouraging, since it indirectly demonstrated that phenol and/or toluene bound to most binding sites of the peptides selected by phage display. Consequently, P-AuNP could not bind to the blocked peptides, or much less free binding sites were accessible. As a supplementary proof, after regeneration, which enabled to release part of the VOCs attached to the probes, we obtained, again, a higher signal for the injection of P-AuNP, especially for P2 and P3. However, similar phenomenon occurred on other peptides (like R1 and R15) that had a poor predicted selectivity for phenyl compounds.

As a first conclusion, in the liquid phase, the direct detection of VOCs such as phenol and toluene by the optoelectronic tongue is not possible. Satisfyingly, our amplification strategy using P-AuNPs demonstrated that the peptides selected by phage display and immobilized on a prism showed a good selectivity for phenyl compounds. At equal concentration, a significantly higher signal was obtained on the biosensors based on P1, P2 and P3 with nanoparticles displaying this functional group, comparing to the reference nanoparticles displaying OH functions. Therefore, the three peptides selected by phage display were more suitable for the selective and sensitive detection of phenyl compounds than three other peptides selected for this purpose in the literature and many other historical peptides. However, R8 and R9, high in aromatic residues, showed an even better selectivity to phenyl VOCs. The results were consistent with the computer simulations. Interestingly, the biosensors based on P1 and P2 were harder to regenerate after an injection of P-AuNPs.

However, we were unable to get a finer estimation of the performances of the new sensing materials for an optoelectronic tongue. For their sensitivity, the presence of gold nanoparticles biased the results. Besides, the incapacity to perform direct detection of VOCs and effective competitive assays prevented us from determining their selectivity among the phenyl compounds. The higher sensitivity of gas-phase SPRi could thus be of particular interest, as we will explain in the next part.

#### 5.4. PEPTIDE-BASED OPTOELECTRONIC NOSE: DETECTION OF VOCs IN THE GAS PHASE

---

Subsequently, we sought to verify the interest of the three peptides selected by phage display for the detection of VOCs in the gas phase. Following the protocol described in 2.2, P1, P2 and P3 were deposited on a gas-phase SPRi chip, together with all the historical peptide probes. We also added spots with peptides mixed with a perfluorothiol molecule, since it improved the selectivity of some of the biosensors in the liquid phase. After functionalization and passivation with a

perfluorothiol, the prism was dried with argon and mounted in the analysis chamber of the gas-phase SPRi bench.

Here again, the high contrast in refractive index between the VOCs and air made it possible to detect VOC binding directly, without amplification. As a consequence, we were able to assess the selectivity of the individual biosensors to different VOCs, their sensitivity, as well as the chemical resolution of the peptide-based optoelectronic nose much more precisely than in the liquid phase.

#### 5.4.1. Influence of humidity on the optoelectronic nose

The first essential question is whether the affinity of the peptides for the different VOCs has been conserved after drying. Even if the peptides are much smaller than OBPs and have more simple structures, their interaction with VOCs is mediated by their structure and by hydrophobic/hydrophobic interactions, electrostatic interaction, hydrogen bonds, *etc.* All these notions have no longer the same meaning in the gas phase. We then decided to test the influence of humidity on the optoelectronic nose to determine the optimal working conditions.

First, we performed a ramp in humidity and calculated the sensitivity to water of the different biosensors. That is to say, the slope of the calibration curve. The results are presented in Figure 5-17. In humid air, water molecules adsorbed on all the biosensors. The thickness of the water layer seemed to increase linearly with the relative humidity, and, contrary to what we observed with the OBP chips, there was no saturation (Figure 5-17 (a)). Logically, the sensitivity to water was higher for hydrophilic peptides (with a negative GRAVY) (Figure 5-17 (b)). This could result in a distortion of the response profile of a VOC with humidity. Indeed, at high RH, there would be more water molecules on the biosensors based on hydrophilic peptides, which could affect their response.

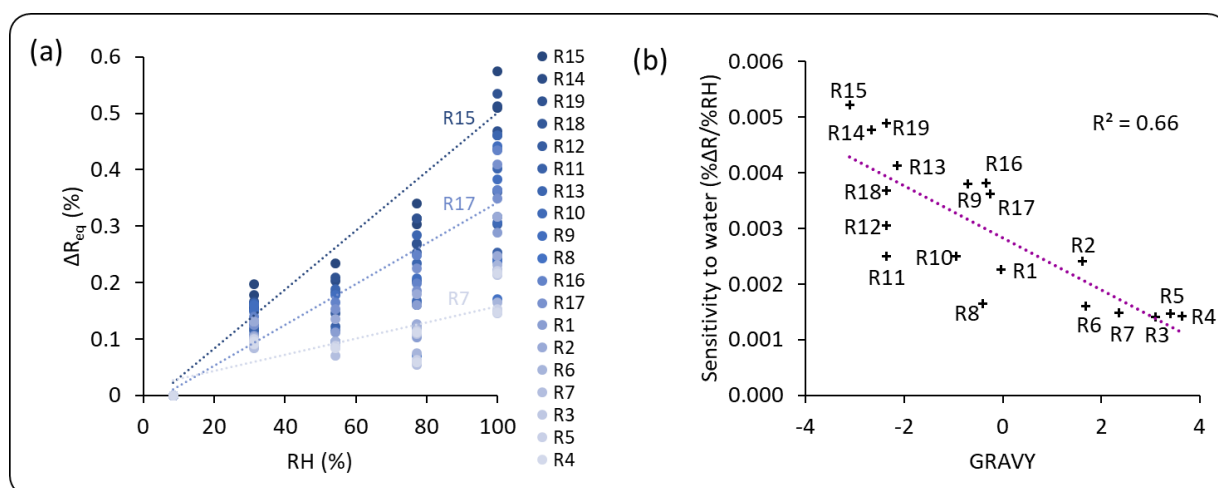


Figure 5-17 (a) Variation of reflectivity of the different biosensors with the relative humidity. The darkest points represent hydrophilic peptides, and the clearest are hydrophobic ones. The reference for the reflectivity ( $\Delta R = 0$ ) is arbitrarily set for the carrier air from the zero air generator (RH=8%). (b) Sensitivity to water of the different biosensors versus hydrophobicity of their constituent peptides.

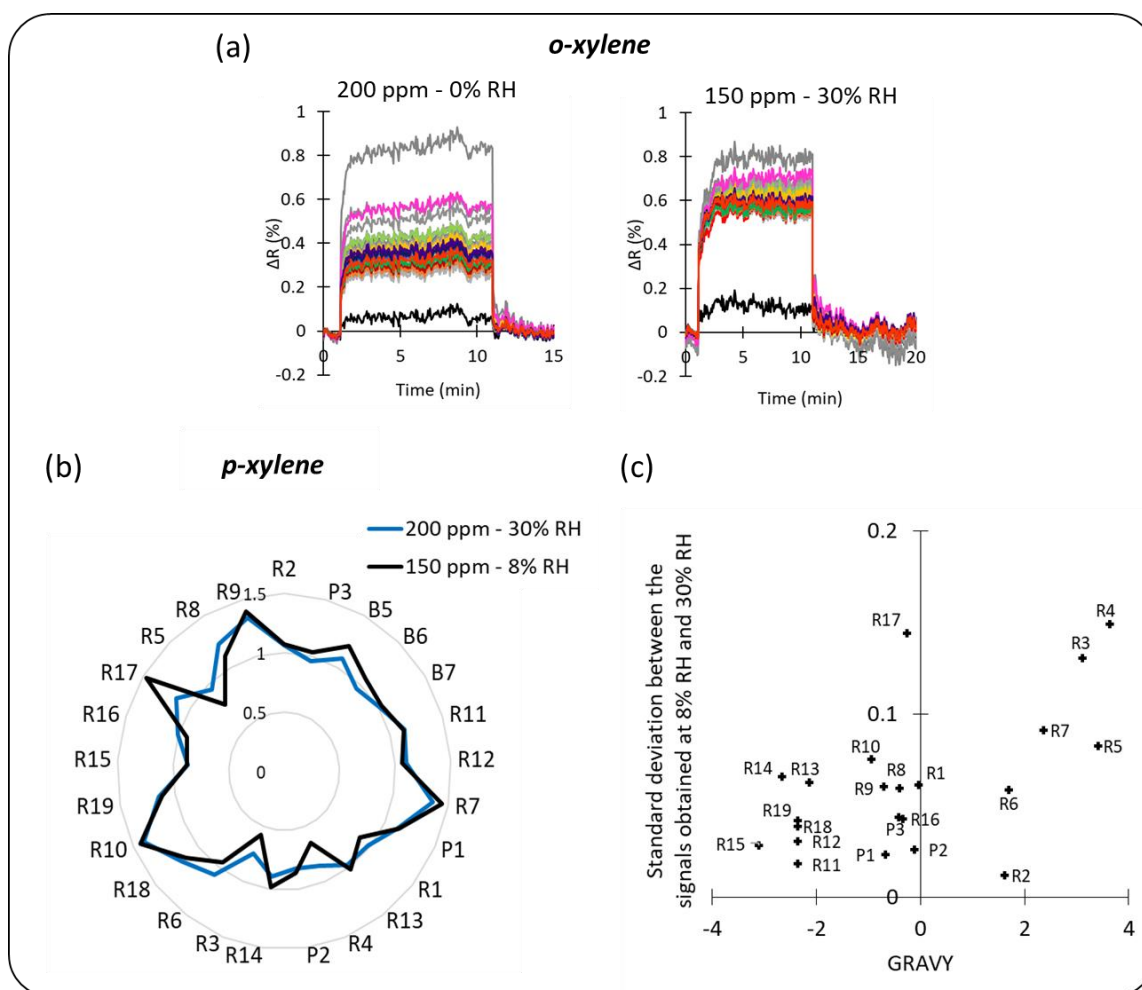


Figure 5-18 (a) Compared kinetic response of the different biosensors to *o*-xylene in dry air or humid air. The black line corresponds to the reference biosensor. (b) Normalized equilibrium profiles of *p*-xylene in air with 8% RH or 30% RH. (c) Variability of a biosensor signal with humidity as a function of the hydrophobicity of its constituent peptide.

In a second time, we analyzed VOC samples with different humidity rates in the carrier gas thanks to the new experimental setup described in part 2.3.2. The Figure 5-18 (a) compares the kinetic responses of the different biosensors to *o*-xylene in dry air (0% RH) and in humid air (30% RH). For a similar VOC concentration, there was a higher contrast between the signals obtained with the different biosensors in dry air. For the most of biosensors, the signal intensity was higher in humid air. These observations were the same for all the tested VOCs, and are consistent with the results obtained on OBP-based chips. The loss of contrast was probably caused by the non-specific binding of water on all the biosensors. However, the normalized equilibrium profile of a VOC was not radically changed by a change in humidity, like illustrated in the Figure 5-18 (b) for *p*-xylene. Surprisingly, the most hydrophobic biosensors (with a positive GRAVY, such as R3, R4 and R5) tended to show more variability in their response to a VOC than the hydrophilic ones. This is shown in Figure 5-18 (c) that represents the standard deviation between the signals obtained with a given biosensor at 8% RH and 30% RH, as a function of its GRAVY. This result

must be qualified, because these peptides also gave the weakest signal for all the VOCs tested. Moreover, there is no clear correlation between the two parameters.

As a result and as previously intuited, the classification ability of the optoelectronic nose may be impacted by humidity. In the Figure 5-19, we made a static PCA from several injections of VOCs at 8% RH or 30% RH. First, at a given humidity, the different individuals corresponding to a same VOC clustered (except for toluene at 30% RH). At 8% RH, these clusters separated quite well. However, at 30% RH, it was harder to distinguish between toluene and p-xylene. Second, when combining the data from the two levels of relative humidity, the individuals corresponding to a given VOC were still in the same region of the PCA plot. However, there was a slight offset due to the addition of water. As a result, the cluster of toluene at 30% RH overlapped with p-xylene at 8% RH. Therefore, the classification performance of the optoelectronic nose was better at low relative humidity. This difficulty represents a challenge since it can limit the on-site use of the optoelectronic nose.

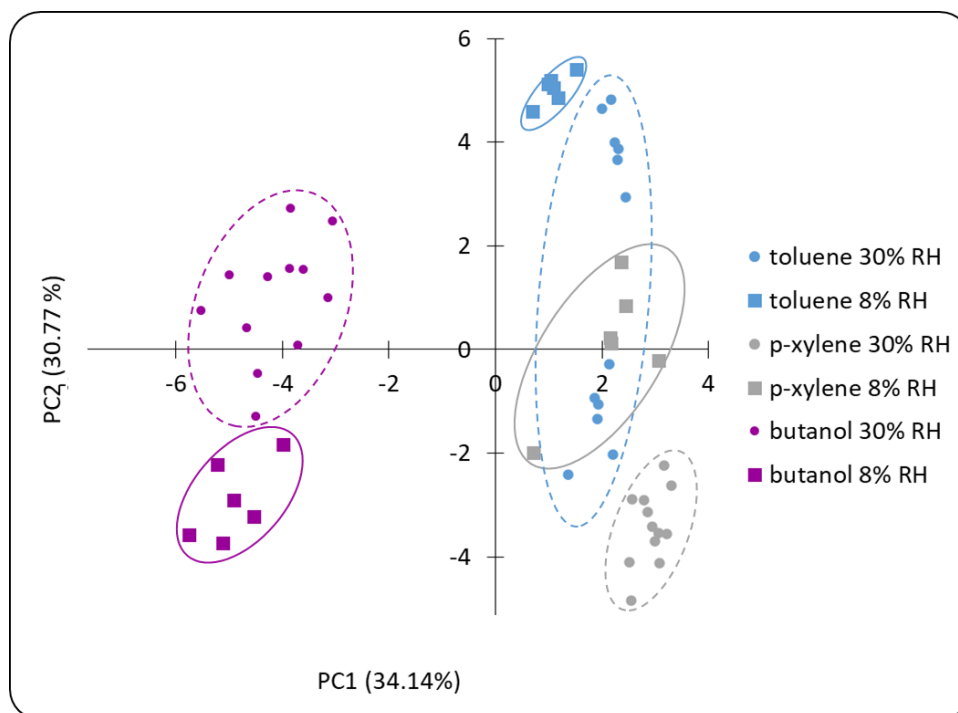


Figure 5-19 Static PCA of gas-phase SPRi analysis of toluene, p-xylene and butanol with a peptide chip. The relative humidity in the carrier air was set at 8% or 30%.

In conclusion, contrary to what was observed with the OBP-based optoelectronic nose, humidity appeared to be rather detrimental to the performance of the peptide-based optoelectronic nose. Thus, we decided to work with a minimum relative humidity of 8%. This was the relative humidity at the output of the zero-air generator.

### 5.4.2. Performance of the peptide-based optoelectronic nose

As explained previously, in the gas phase, the non-specific binding was much higher than in the liquid phase. As a result, the study of the individual properties of the biosensors based on the peptides selected by phage display required us to work at very low concentration of VOCs. To this end, we used the computerized calibration system (see 2.3.1.) in addition with three span gas bottles: p-xylene at 50 ppm in dry air, butanol at 5 ppm in dry air, and toluene at 50 ppm in dry air (Air products, USA). We increased the VOC concentration gradually, until we measured a valid signal. It enabled the direct measurement of the limit of detection of the optoelectronic nose for the three VOCs. It was established at 550 ppb for p-xylene, 5 ppm for toluene, and 4 ppm for butanol. We already obtained similar limit of detection without P1, P2 and P3 [318]. Thus, adding these new peptides selected by phage display to our device did not decrease the limit of detection.

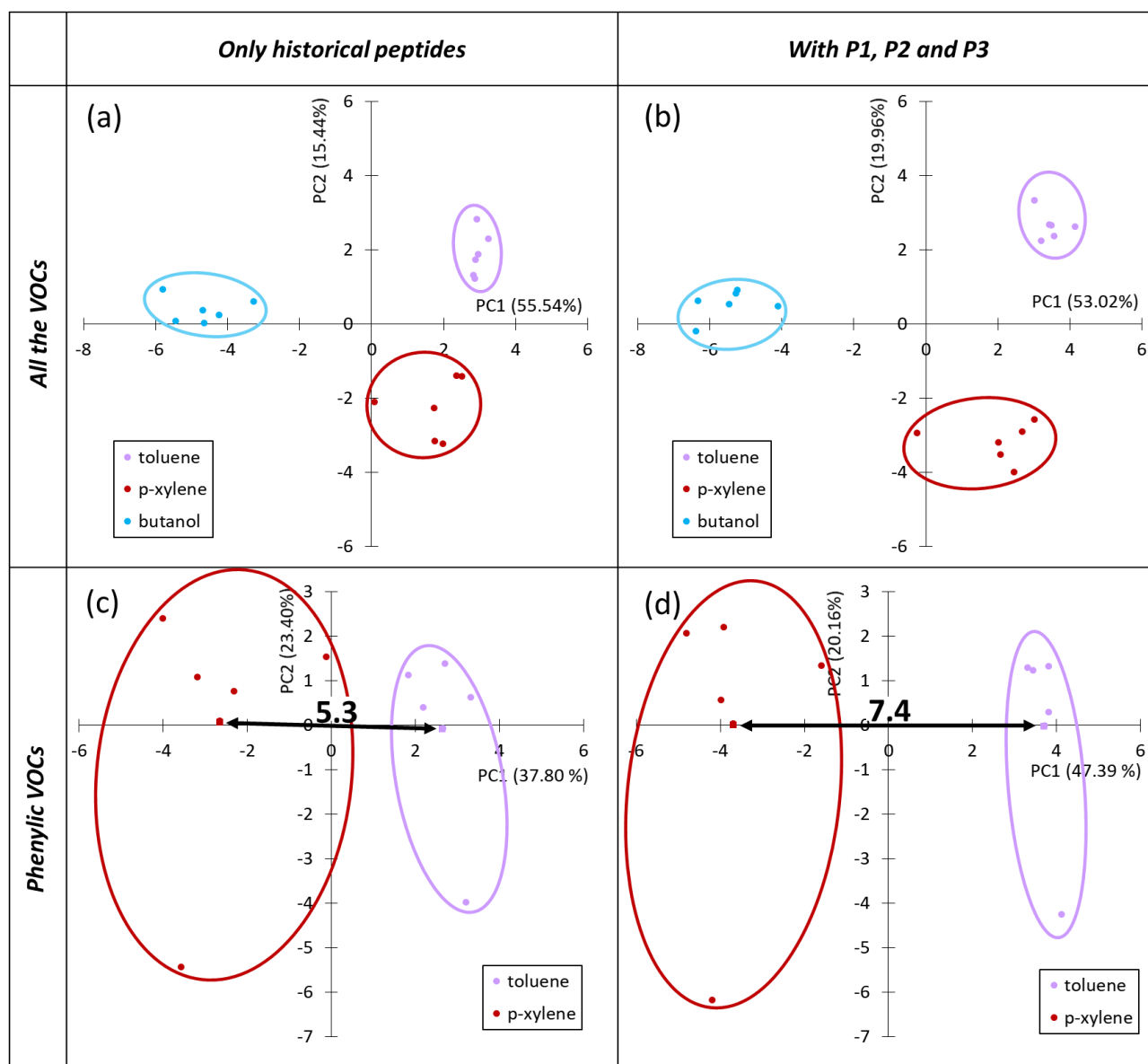


Figure 5-20 Comparison of the discrimination capacity of the optoelectronic nose for three VOCs before and after the integration of P1, P2, and P3 based on static PCA.

Furthermore, we compared the chemical resolution of the optoelectronic nose for these VOCs before and after the integration of P1, P2, and P3 based on a PCA. As shown Figure 5-20 (a) and (b), in both cases, a very good discrimination was obtained between the three VOCs. With the addition of the peptides selected by phage display, the discrimination capability of the optoelectronic nose improved slightly. Notably, the distance between the clusters of the two compounds with a phenyl group (toluene and p-xylene) increased significantly. Indeed, this increase was higher than the mathematical contribution of adding supplementary dimensions to the data space. A variable analysis revealed that the peptides selected by phage display contributed greatly to this performance. Indeed, in the PCA (Figure 5-20 (d)), PC1 was strongly correlated to the variables associated to mixed P1 (85.0%), mixed P2 (96.3%), and mixed P3 (85.3%).

The regeneration of the sensor was spontaneous for all the VOC tested. After each analysis, flowing clean air over the chip was enough to restore all the biosensors (Figure 5-18). Therefore, the same chip could be used to perform more than 25 different injections without any loss in their performance. On top of that, the peptide primers were robust. They could be stored dry at 4°C before use for more than one month.

#### 5.4.3. Individual selectivity of the different peptide biosensors

The previous experiment also enabled to determine the selectivity of the individual biosensors. For this, we performed several injections of p-xylene and butanol just above the limit of detection. Then, we calculated an experimental  $S_{phenyl}$  on the normalized profiles for the different peptide-based biosensors, using the equation written in 5.2.2.2. The results are presented in Figure 5-21.

At very low concentration of VOCs (Figure 5-21 (a)), the biosensors based on peptides selected by phage display were very selective to phenyl compounds. Interestingly, this was particularly true for mixed spots, where P1, P2 and P3 were immobilized combined with perfluorothiol on the chip surface (in green on the figure). Notably, the biosensors based on mixed P2 showed a 180% higher signal to p-xylene than to butanol. It is most likely that, thanks to the presence of perfluorothiol, non-specific binding of VOC on these biosensors was greatly decreased. As described in Chap 2, perfluorothiol can block free gold surface in the spot with extremely low binding to VOC. Another observation supports this hypothesis. Indeed, the contrasted response of these biosensors to the two VOCs was mostly due to their very weak response to butanol, rather than to a high response to xylene. At higher concentrations of VOCs (Figure 5-21 (b)), the response profiles at equilibrium were different. This was potentially because the non-specific binding dominated the specific signature of the VOC.



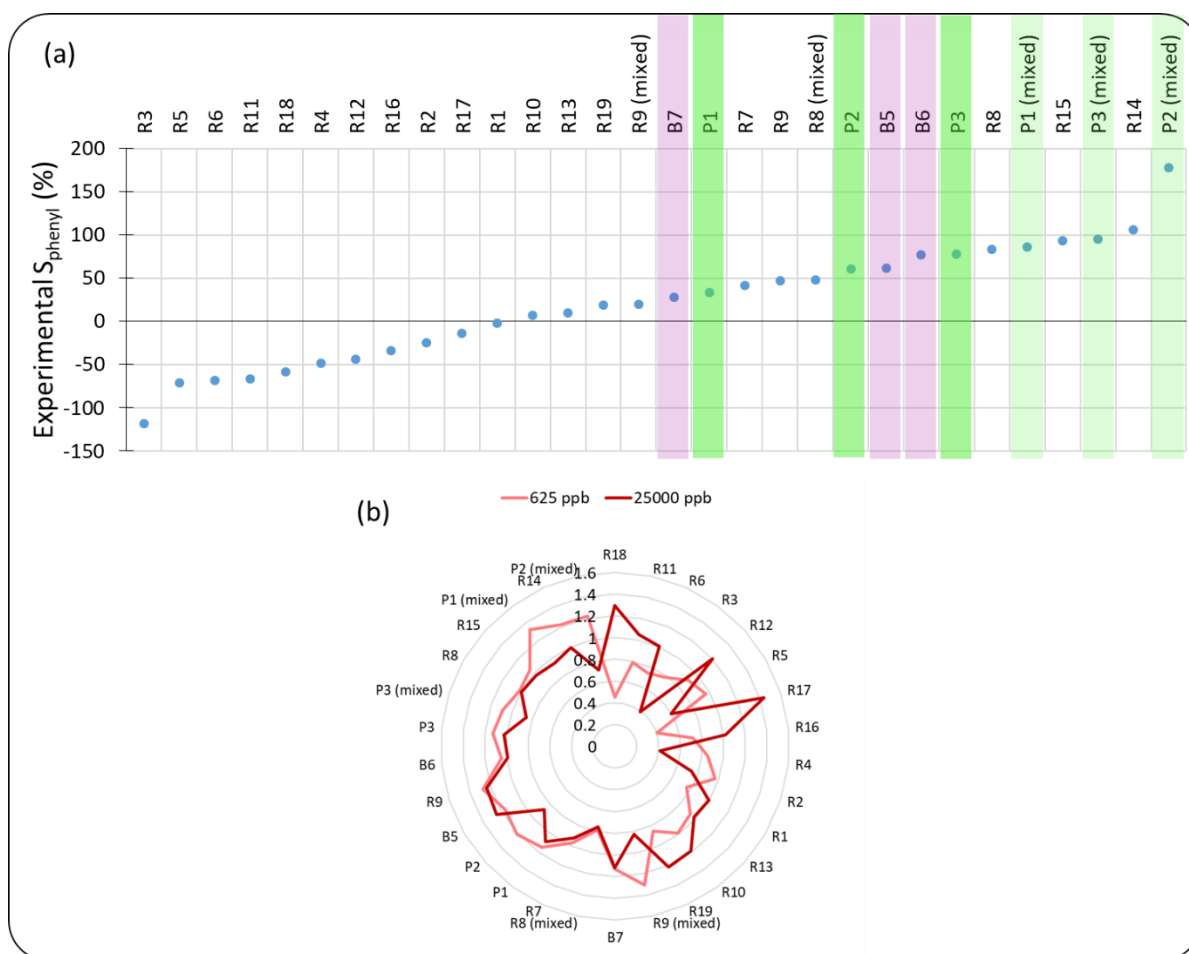


Figure 5-21(a) Experimental selectivity for phenyl compounds of the different peptide-based biosensors. It was calculated from four injections of p-xylene and butanol at very low concentration. (b) Equilibrium profiles for two injections of p-xylene at 625 ppb and 25000 ppb.

In Figure 5-22 (a), we made a comparison between the experimental  $S_{\text{phenyl}}$  in Figure 5-21 (a) and the simulated  $S_{\text{phenyl}}$  results obtained in 5.2.2.2. There is a correlation between them, which comforts us in the fact that part of the binding properties of the peptides was conserved after deposition and under the working conditions in the gas phase. However, we obtained a  $R^2$  of only 0.30, which reflects the limitations of the computer model and experimental implementation. When we compared the results obtained in the liquid phase with the results obtained in the gas phase (Figure 5-22 (b)), the fit to a linear regression was even worse ( $R^2=0.02$ ). This results probably from the accumulation of different parasitic phenomena that exist in the liquid phase or in the gaseous phase and interfere with the specific signal.

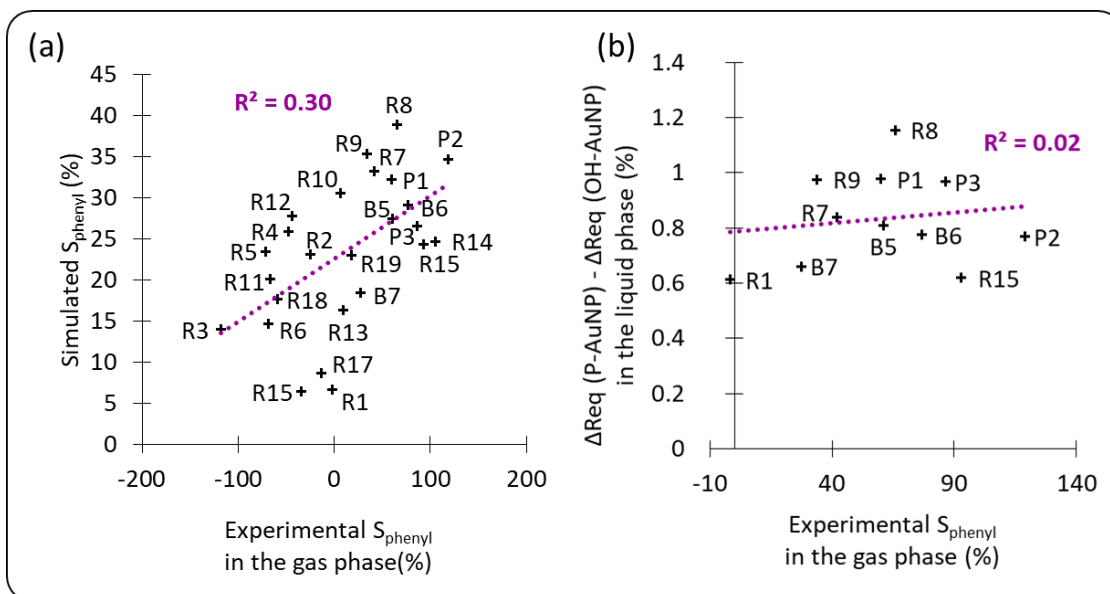


Figure 5-22 (a) Comparison between the experimental (gas-phase) and simulated selectivity for phenyl compounds of the different probes. (b) Comparison between the liquid-phase and gas-phase results.

In conclusion, it seems that the peptides selected by phage display retained part of their selectivity for phenyl compounds when dried on a gas-phase SPRi chip. The way they were immobilized on the prism was important to derive maximum benefit from this feature. Notably, the presence of perfluorothiol helped to improve the specific binding to non-specific binding ratio. Moreover, the working conditions were also optimized. First, contrary to what was observed with the optoelectronic nose based on odorant binding proteins, humidity was detrimental to the performance of the peptide-based optoelectronic nose. Second, the response profile at equilibrium was highly impacted by the VOC concentration. We observed a slight improvement of the chemical resolution of the new optoelectronic nose with the addition of P1, P2 and P3. However, the limit of detection and sensitivity to phenyl compounds was not improved.

## 5.5. PERSPECTIVES FOR THE OPTIMIZATION OF THE SELECTION PROTOCOL

As explained in the first part of this chapter, there were several limitations to the classical protocol of phage display. Notably, the experiments are long, and carried out blindly. That is to say, the effectiveness of the selection, rinsing or elution cannot be immediately verified. We proposed two alternative protocols to tackle this. We made some preliminary tests but did not have enough time to optimize these protocols during this PhD project. However, we think they can provide interesting clues to improve the phage display protocol.

### 5.5.1. Phage-HRP display

The first alternative phage display protocol was inspired by the work of Gordiichuk *et al.* [319]. It consisted in using fluorescence to detect and quantify the phages. For this, we fixed horseradish peroxidase (HRP) on the p8 major coat protein of the M13 phages of our library (Figure 5-23 (a)). This enzyme is extensively used in chemistry, for example in ELISA tests. It catalyzes the oxidation of various substrates. Notably, in our case, a colorless substrate gave a fluorescent product (QuantaBlu, Thermofisher Scientific). As a result, when phages functionalized with HRP were put in the presence of the substrate, the solution became fluorescent. The intensity of the fluorescence provided information on the phage concentration. To facilitate fluorescence reading, the experiments could be led in well plates. Commercial well plates carrying NHS-ester functions are available. As a result, we could conserve the same surface chemistry strategy to immobilize target VOCs or to create reference surface.

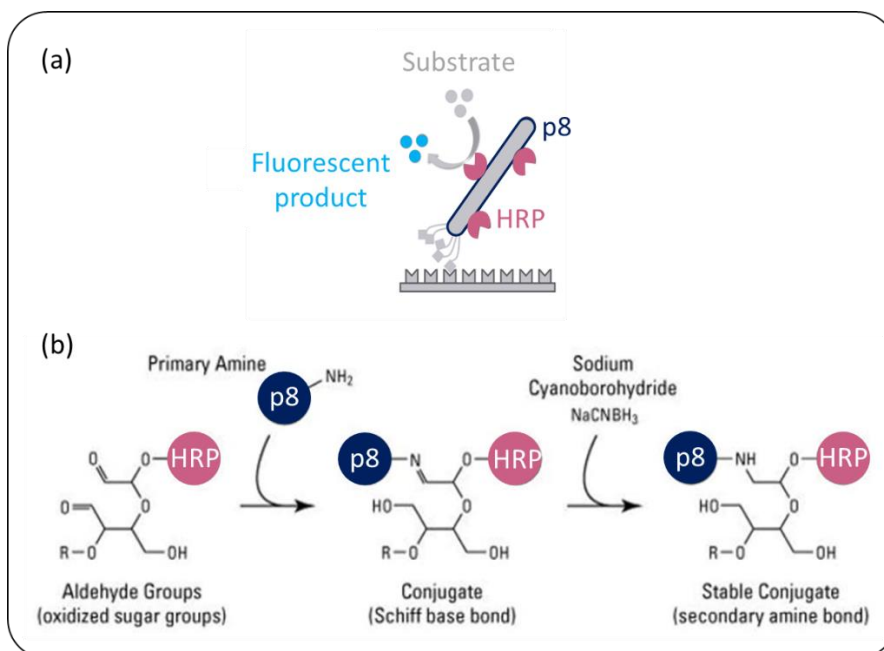


Figure 5-23 Functionalization of the M13 phages with HRP.

Tagging the phages with HRP was very simple (Figure 5-23 (b)). We followed the protocol of a commercial kit that is commonly used to bind HRP to the free amine groups of proteins covalently (EZ-Link Plus Activated Peroxidase Kit, Thermofisher Scientific). Namely, the p8 protein exhibit this functional group. The whole phage library was incubated with the peroxidase overnight. After that, the unbound enzymes were eliminated by centrifugal filtration. Several tests were led on the library after HRP functionalization. The enzyme remained active. The infectivity of the phages was not affected. We do not know how many of the 2700 replicates of the p8 proteins on one phage were carrying the HRP enzyme. However, we performed a range of dilutions of the

marked library and showed that 200 phages in one well of the plate gave a measurable fluorescence after 30 minutes.

The use of this tagged library could simplify the optimization of the different steps of the phage display protocol (Figure 5-24). During this thesis, we led preliminary tests that were not conclusive yet. However, we remain optimistic about the interest of this protocol once optimized.

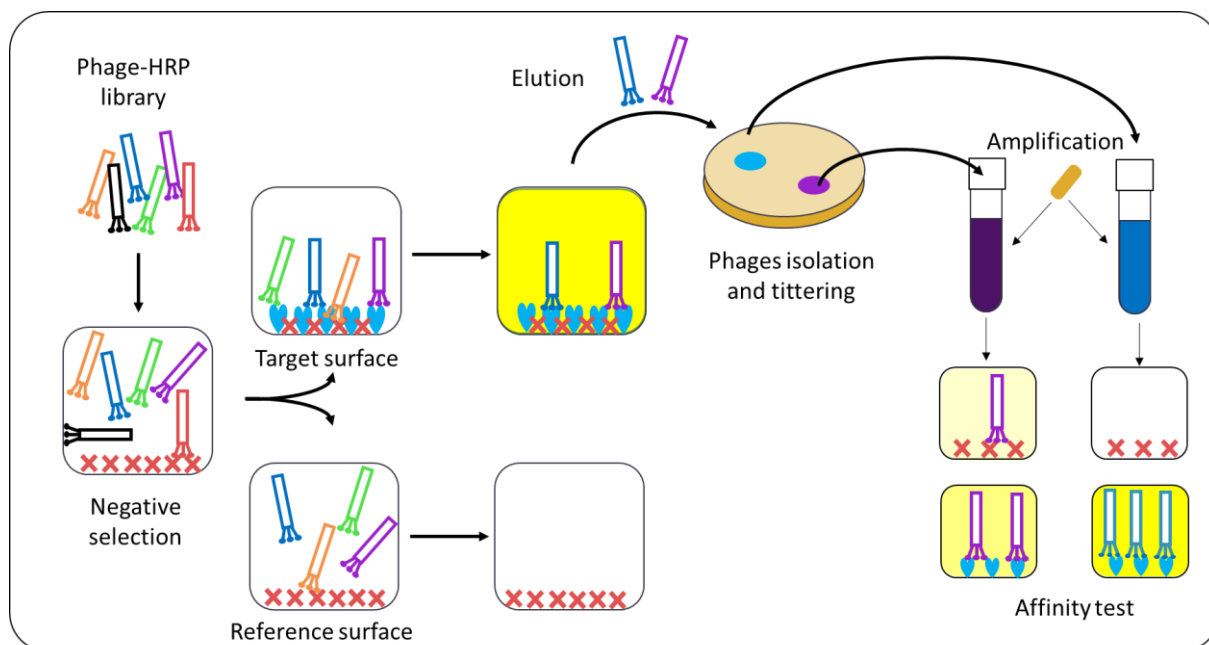


Figure 5-24 Schematic principle of the selection protocol for phage-HRP display.

First, we could check whether the negative selection is efficient. Like in the classical protocol, the phages that were likely to bind to the wells are eliminated during this phase. Practically, the library has first to be incubated in a reference well. Then, the supernatant has to be divided in two. Half of it will be transferred in another reference well, whereas the second half will be put in contact with the target surface. We can then rinse both wells to remove unbound phages and add the HRP substrate. If the negative selection is successful, there should be much more fluorescence in the target well than in the reference one (Figure 5-24 (left)).

Different rinsing procedures could also be quickly compared thanks to this tagged library. For this, it would be sufficient to divide the library into several target wells. A rinsing method can then be tested in each well to remove unbound phages before introducing the substrate. Fluorescence will be lower in the well that has been rinsed most effectively. A fluorescence measurement carried out after the elution would also enable to check if we retrieved most of the bound phages during this step. The results of a preliminary experiment are presented in Figure 5-25. We used our historical rinsing and elution solutions for the classical phage display protocol. On the one hand, they confirm the feasibility of a titring by fluorescence: the evolution of phage quantity

upon rinsing and elution step is clearly visible. On the other hand, they tend to confirm that the classical solutions are efficient.

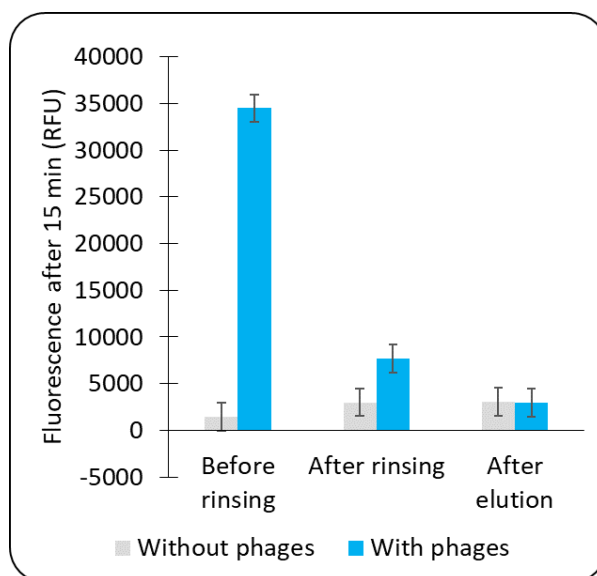


Figure 5-25 Fluorescence measurements in a target well with and without phage library during the different steps of a round of phage display.

It is important to note that, after amplification, the new phages produced by the bacteria will not display the HRP protein. However, in the end of the selection, the isolated clones could be functionalized separately with HRP, to perform affinity tests prior to sequencing (Figure 5-24 (right)). The principle would be similar to ELISA, but would not require antibodies. For this, individual HRP-tagged clones would be incubated in wells containing the target or the reference surface. After rinsing, the substrate would be introduced in the different wells. Only the phages for which the maximum contrast in fluorescence between target and reference surface is reached would be sent for DNA sequencing.

### 5.5.2. Phage display monitored by SPRI

The second alternative protocol for phage display uses SPRI to monitor the different steps. It is schematically illustrated in Figure 5-26.

To verify the efficiency of the negative selection, prisms can be functionalized with both the reference surface, and a target surface in different areas. The negative selection is performed beforehand against the reference surface. The supernatant phages are then injected on the prism, and their interaction with the two surfaces (target or reference) are monitored simultaneously by SPRI. If the negative selection is successful, the variation of reflectivity should be higher for the target area. Our preliminary experiments with this protocol have so far been inconclusive.

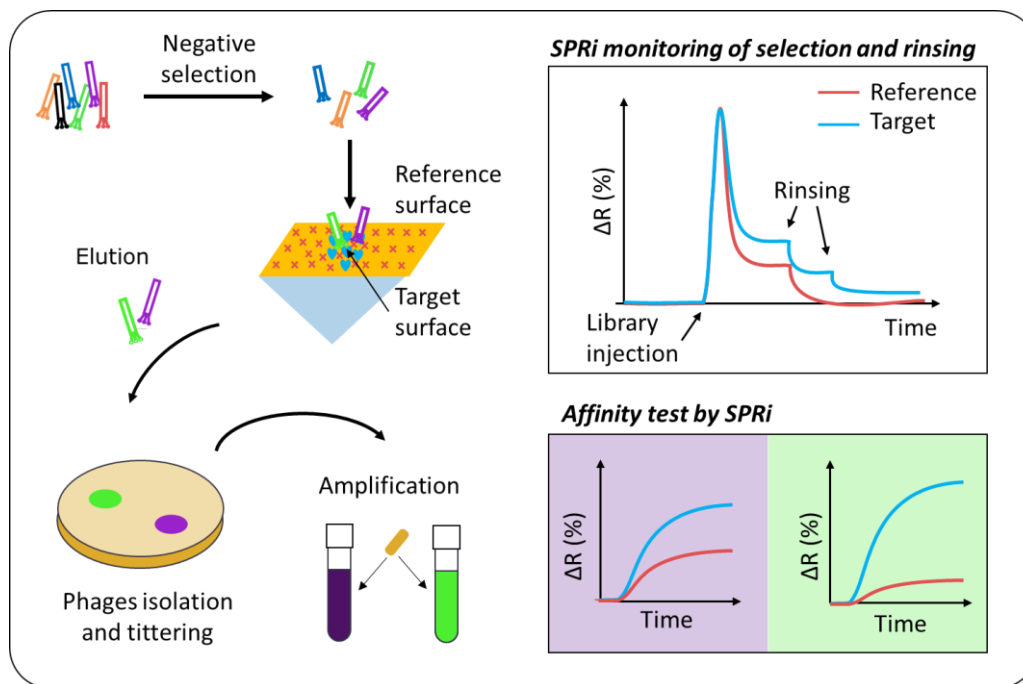


Figure 5-26 Schematic principle of the protocol for phage display monitored by SPRi.

After that, different rinsing solutions can be tested and evaluated *in situ*. The reflectivity drop in SPRi signal upon the injection of a rinsing solution reflects its efficiency. SPRi is particularly interesting for this point, since it also shows how the different rinsing steps can affect the target surface itself. Some preliminary results are presented in Figure 5-27. A library of phages was injected on a prism functionalized like the targets used for phage display, with phenylethylamine (see 5.1.2). Upon the injection of the phages, an increase in reflectivity assessed their binding to the surface. Notably, when switching back to the running buffer, the reflectivity did not come back to its initial baseline. After that, different rinsing solutions were injected and tested. Their efficiency was determined by the resulting  $\Delta R$ . For comparison, the same sequence of rinsing solutions was injected on an identical prism without prior injection of a phage library. This experiment demonstrated that the SAM itself could be affected by some of the rinsing solutions.

A similar protocol could be used to optimize the elution step. However, once optimized, it is better to perform the elution outside the SPRi setup to make sure to retrieve all the phages.

Eventually, SPRi can also be used to perform affinity tests on the individual clones after isolation and amplification. To this end, clones of an individual phages can be injected on the same prism as the one used for negative selection characterization. The phages for which there is a greater contrast in  $\Delta R$  between the reference and the target area will be sent preferentially for sequencing.

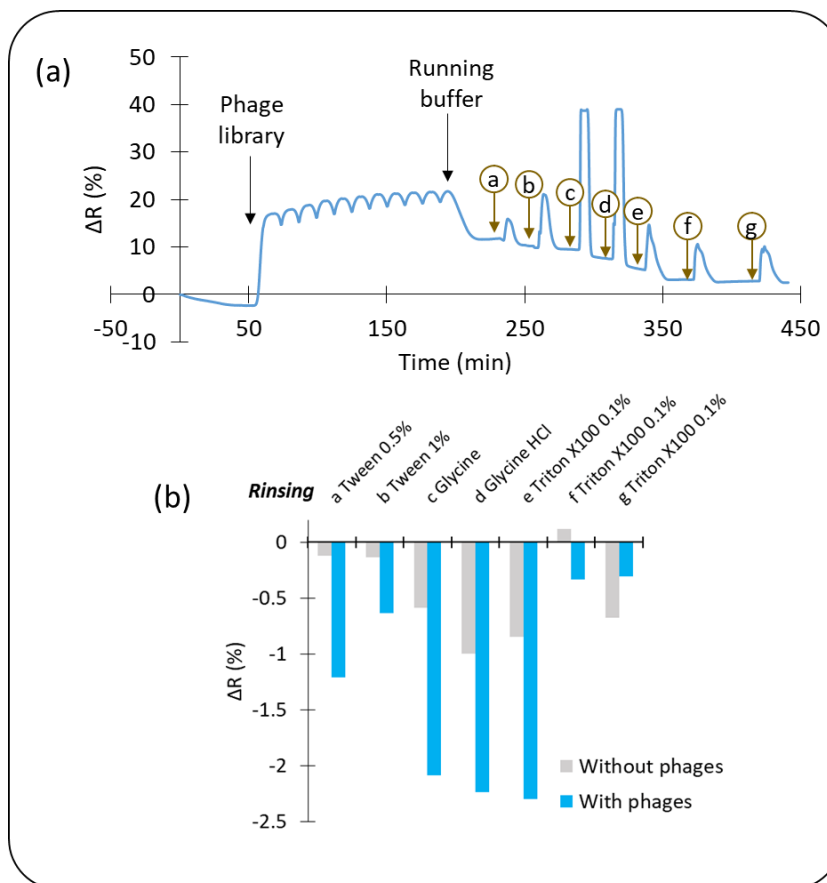


Figure 5-27 (a) Variation of reflectivity obtained on a prism functionalized with phenylethylamine upon the injection of a library of phage and subsequent rinsing steps. (b) Reflectivity drops measured with different rinsing solutions on a prism without or with preliminary injection of phage library.

To summarize this chapter, the discovery of new peptides with a high affinity for a VOC, by phage display, seems promising. It was shown here that peptides identified in solution retained their selectivity for their target after immobilization and drying on a chip for artificial nose applications. Peptide probes do not approach the exceptional sensitivity levels shown by OBPs in liquid. However, they are much more robust than whole proteins, making them much easier to use in a biosensor and extending the lifespan of the device. P1, P2 and P3 do not radically improve the performance of our optoelectronic nose. However, the phage display protocol can be adapted to different targets, and to different peptide and protein libraries. In particular, longer, or cyclic peptides could have much higher affinities for their target than the short peptides we have designed here. This preliminary study has allowed us to validate the interest of this development path to improve the selectivity and chemical resolution of the optoelectronic nose in the future. We proposed two alternative protocols to tackle the limitation of the classical one.

## CHAPTER 6

Prospective work: potential input of  
computational simulations





## Résumé du chapitre 6 – Travaux prospectifs : apports potentiels des simulations numériques

Nous avons montré dans les chapitres précédents que des simulations numériques d'amarrage pouvaient être utilisées pour prédire et comprendre l'interaction entre une molécule de COV et une biomolécule. L'amarrage moléculaire consiste à positionner chaque molécule cible par rapport à la sonde, de manière à minimiser l'énergie du système. Cela permet de déterminer le site de liaison préférentiel, ainsi que l'affinité entre les deux molécules. L'automatisation de ces simulations à haut débit peut permettre d'effectuer un criblage virtuel. C'est-à-dire de classer *in silico* les meilleures sondes pour une molécule cible, parmi une bibliothèque de biomolécules. Ces informations sont ensuite utilisées pour sélectionner et tester expérimentalement un petit sous-ensemble de sondes potentielles. Dans la première partie de ce chapitre, nous détaillons plusieurs applications que cette méthode pourrait avoir pour améliorer les performances de notre nez optoélectronique.

Dans un premier temps, nous présentons une étude préliminaire menée en collaboration avec l'Université de Teramo, en Italie. Nous avons intégré à notre puce six pentapeptides issus d'un criblage virtuel, pour la détection de différents COV en phase gazeuse. L'affinité simulée des pentapeptides pour les COV était assez faible, en raison de leur petite taille. Cependant, grâce à leur réactivité croisée, le nez optoélectronique à base de pentapeptides a été capable de distinguer partiellement les COV de différentes familles chimiques. Le bruit de mesure était élevé, potentiellement en raison de la faible spécificité de ces courtes sondes pour leur cible. En conséquence, la classification n'était pas robuste et dépendait fortement du traitement des données. Par ailleurs, les propriétés de liaison expérimentales des peptides étaient différentes de celles calculées.

Cette étude nous a permis de confirmer que le criblage virtuel était prometteur pour augmenter la diversité des sondes. Cependant, la longueur des peptides semble être une caractéristique essentielle pour leur sélectivité vis-à-vis des COV. Nous avons donc simulé deux groupes de peptides ne différant que par leur longueur, mais avec les mêmes groupes fonctionnels et la même structure. Nous avons calculé leur affinité pour 36 COV de cinq familles différentes par amarrage moléculaire. Nous avons ainsi confirmé qu'un nez optoélectronique basé sur des peptides courts permet une bonne classification des COV par famille chimique, ce qui est cohérent avec nos observations expérimentales. D'autre part, quel que soit le type de peptide, le plus long présentait une meilleure affinité pour tous les COV testés. Les résultats de simulation montrent qu'une langue ou un nez optoélectronique basés sur ces peptides plus longs, de structure très

simple, faciliterait la différenciation de deux COV ayant des caractéristiques chimiques similaires, mais une masse moléculaire différente.

Les simulations d'amarrage peuvent également assister la sélection *in vitro*. D'une part, l'ensemble des sondes sélectionnées pour le COV cible pourraient être testée *in silico* sur une grande variété de COV pour mieux choisir celles à synthétiser. A titre d'illustration, nous avons effectué des simulations sur les douze séquences sélectionnées par *phage display* dans le chapitre 5. Cela nous a permis d'identifier deux peptides non consensus qui présentaient pourtant une sélectivité simulée pour les composés aromatiques plus élevée que tous les peptides intégrés à notre puce. D'autre part, le criblage virtuel peut permettre d'améliorer les peptides sélectionnés par des tests de substitution. Il s'agit de remplacer un ou plusieurs acides aminés par d'autres résidus, puis d'effectuer un criblage virtuel sur ces nouveaux peptides. Les résultats permettent, d'une part, de comprendre quels acides aminés de la séquence peptidique sont essentiels à son affinité pour la cible. D'autre part, cela pourrait permettre d'identifier de meilleurs liants pour la cible.

## CHAPTER 6      Prospective work: potential input of computational simulations

We showed in the previous chapters that docking simulations could be used to predict and understand the binding affinity between a VOC molecule and a biomolecule. Molecular docking involves positioning each target molecule into the binding site of a probe, to minimize the energy of the system. This provides information on the preferred binding site and affinity.

Molecular docking can also be used to perform virtual screening to rank the best binders for a target molecule *in silico* among a library of biomolecules. This information is helpful to select and then experimentally test a small subset of hits. In our case, virtual screening could enable high-throughput testing of VOC - biomolecule binding in a fast and low-cost way [320]. In the first part of this chapter, we will detail several applications that this method could have for improving the performance of our optoelectronic nose. Moreover, virtual screening offers considerable assistance for the understanding of molecular interaction, which can be useful to anticipate if a probe will keep its specificity in the gas phase. Indeed, all the commercial virtual screening tools to date work in the liquid phase.

### 6.1. VIRTUAL SCREENING OF PENTAPEPTIDES FOR OPTOELECTRONIC NOSE DEVELOPMENT

---

We led this preliminary study in collaboration with the team of Prof. Dario Compagnone from the University of Teramo, Italy. In their previous work, they have selected two kinds of probes by computational virtual screening. On the one hand, an optoelectronic nose based on penta-peptides (5 amino acids) was proven efficient for the selective detection of VOCs in food samples [321–324]. On the other hand, for the first time, they have designed and selected several hairpin DNA (hpDNA) for gas sensing [325].

Their peptide-based and hpDNA-based gas sensors were constructed separately using quartz crystal microbalances. However, this transduction method was not sensitive enough. To tackle this limitation, the probes were immobilized onto gold nanoparticles before deposition onto QCM crystals for amplification. Moreover, the multiplexing of these transducers to obtain a large sensor array was limited. They could use only six sensors in parallel.

Thus, we decided to test the performance of all these probes at the same time using gas-phase SPRi as a transduction method. Here, six penta-peptides and nine hpDNA were directly deposited on the same SPRi chip. We evaluated the performance of this novel optoelectronic nose for the analysis of VOCs in the gas phase. The results presented in this chapter were published in *Sensors and Actuators B* [326]. In this thesis project, we concentrate on the sensors based on peptides and

proteins. Thus, we will deal here only with the penta-peptide probes. The results for hpDNA probes are available in Appendix A-2.

### 6.1.1. Selection of the probes used in this project

The procedure followed to select the penta-peptides used in this study was detailed in a previous paper [327]. Mascini *et al.* selected peptides with complementary binding properties towards five different chemical classes (alcohols, aldehydes, esters, hydrocarbons and ketones) thanks to commercially available virtual screening tools (OpenEye Scientific). The set of tested VOCs included various carbon chain length. Molecules are sorted in long or short chains depending on their molecular weight (< 100 g/mol or > 100 g/mol, respectively). Like with AutoDock, the peptides structures and VOC molecules were considered rigid. The affinity energy was calculated in liquid, for the best binding site in a one-to-one interaction.

There are  $20^N$  different possible sequences of  $N$  naturally occurring amino acids. As a result, the time needed to perform the docking simulations on a whole library of peptides increases exponentially with their length. To tackle this, a semi-combinatorial virtual approach was used. Molecular docking simulations were conducted on the complete tripeptide library (8000 elements) versus 58 VOCs. Then, 120 of them were chosen for their cross reactivity toward the five chemical classes. A random supplementary amino acid was then inserted in each possible position to generate a library of 7912 unique tetra-peptides. This library was processed in an analogous way to the former. Six tetra-peptides were finally selected. A terminal cysteine was added to each sequence to enable the immobilization of these probes on the sensor surface. Eventually, the selected peptides were TGKFC, KSDSC, WHVSC, IHRIC, LGFDC, and LAWHC.

The virtual binding properties of five of the six penta-peptides are presented in Figure 6-1 [324,327]. The data are not available for LAWHC.

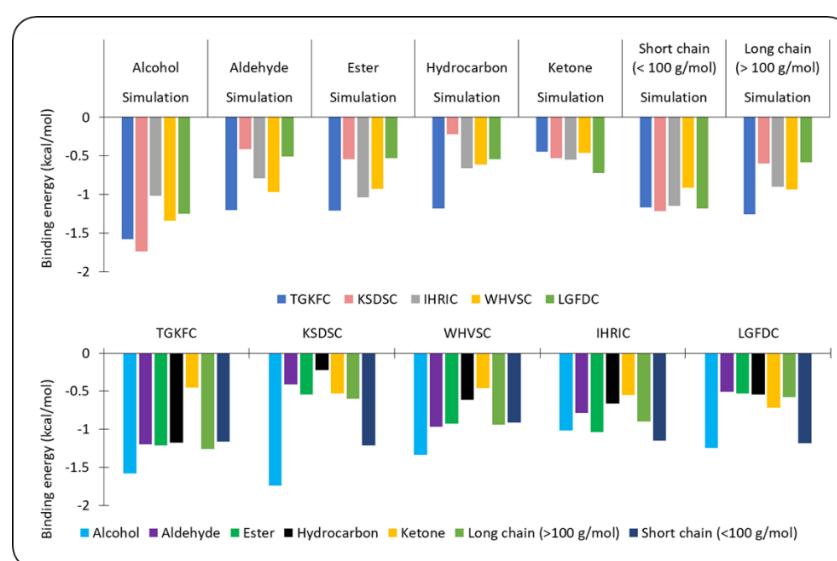


Figure 6-1 Results of the docking simulations for five of the penta-peptides used in this study.

The binding affinities were quite low in every case. As a reference, we remind the value of the energy of thermal agitation  $RT = 0.593$  kcal/mol at  $25^{\circ}\text{C}$ , which quantifies the thermal noise. As a result, the contrast in affinity between the different chemical classes was hardly significant. This is due to several factors. First, the small size of the peptides results in very simple structures and a small surface of interaction. Second, the team did not pick the best binders, but the most selective ones.

The data showed a tendency for KSDSC and LGFDC to bind preferentially VOCs with a shorter carbon chain ( $< 100$  g/mol) and in particular with an alcohol function. TKGFC had good affinity for all the tested VOC families except ketones. Besides, it could probably be useful for the sensitive detection of aldehydes, notably thanks to the amine group provided by the lysine (K) and hydrocarbons. WHVSC and IHRIC were more wide-spectrum.

### 6.1.2. Preparation of the chip

The six sequences of penta-peptides were purchased from Espikem (Italy, purity  $> 85\%$ ). They were immobilized by self-assembly onto a gas-phase SPRi prism to form a microarray. The protocol will not be detailed, for confidentiality issues. Each solution was spotted in quadruplicates on the prism at random positions. After functionalization, the chip was dried under a flow of argon and stored at  $4^{\circ}\text{C}$  before use for the detection of VOCs in the gas phase.

We used a spotting volume of  $1.2$  nL, for which we had a good compromise between the number of bioreceptors that could be spotted on the same chip and the reproducibility of the functionalization. Indeed, there were no observable drop size reduction due to evaporation and all obtained spots on the chip were homogeneous.

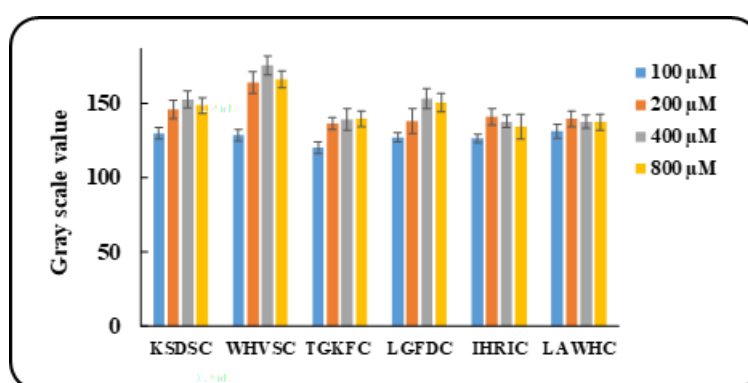


Figure 6-2 Gray scale values on the SPRi image of the spots of the different penta-peptides at different concentrations in the spotting buffer [326].

We have also optimized the probe concentration for a good surface density. For this, solutions with different concentrations of probes were spotted on the same prism ( $100$   $\mu\text{M}$ ,  $200$   $\mu\text{M}$ ,  $400$   $\mu\text{M}$  and  $800$   $\mu\text{M}$ ). The gray level of the spots is presented in Figure 6-2. For all the penta-

peptides, increasing the concentration from 100  $\mu\text{M}$  to 200  $\mu\text{M}$  led to a significant increase of gay scale value, and so, reflectivity. However, in most of the cases, a plateau was reached above 200  $\mu\text{M}$ , probably indicating that the surface was saturated with probes. Therefore, this concentration was chosen for the chip preparation.

### 6.1.3. VOC analysis by the optoelectronic nose

The chip was mounted in the fluidic chamber of the gas-phase SPRi setup for the analysis of VOCs. We used air at 8% RH as carrier gas, similarly to what was done in the previous chapter with the peptides selected by phage display. Six different VOCs (butanol and pentanol for alcohols, hexanal, nonanal and trans-2-nonanal for aldehydes, and hexanoic acid) were selected in order to evaluate their affinity with the peptides.

Figure 6-3 (a) shows an example of the variations of reflectivity obtained on the different penta-peptide-based biosensors for nonanal. Primarily, all penta-peptides gave valid signals for this VOC, as well as for the other ones tested, without needing nanoparticles for signal amplification. Each penta-peptide gave different responses to a given VOC. To illustrate this point, the equilibrium response of each analyzed VOC is given in Figure 6-3 (b).

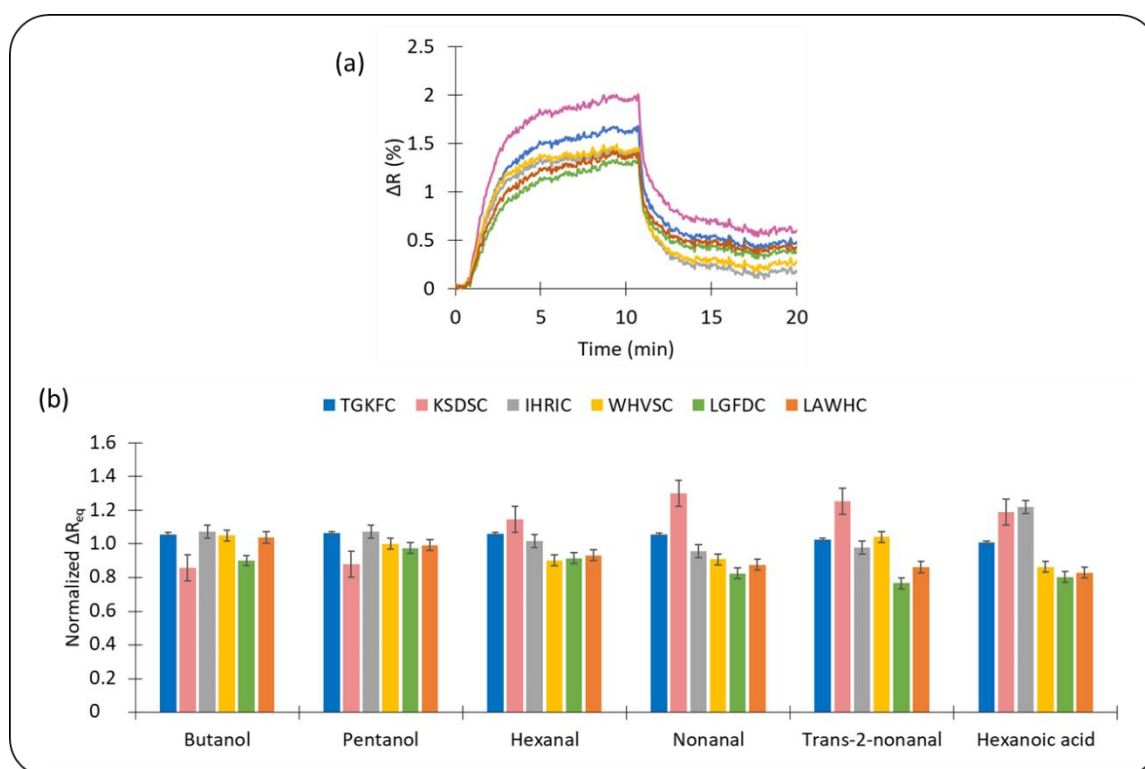


Figure 6-3 (a) Example of biosensor responses after exposure to nonanal (3.6 ppm). (b) Normalized response profiles at equilibrium for butanol, pentanol, hexanal, nonanal and trans-2-nonanal.

From these histograms, KSDSC appears particularly interesting to differentiate aldehydes for which it gave the highest signal, from the other compounds, notably alcohols. IHRIC gave the highest signal for hexanoic acid. When it comes to alcohols, profiles with very low contrast

between signals of different penta-peptides were obtained. As expected, these experimental results were not really consistent with the simulations that were based on interactions between free peptides and VOCs in liquid. Obviously, the difference can be attributed to many factors such as the immobilization of the peptides, the detection in the gas phase, *etc.*

We performed a static PCA analysis to assess the discrimination abilities of the penta-peptide-based optoelectronic nose. The results are reported in Figure 6-4. The correlation matrix was filled only with the variation of reflectivity at equilibrium of the penta-peptide-based biosensors.

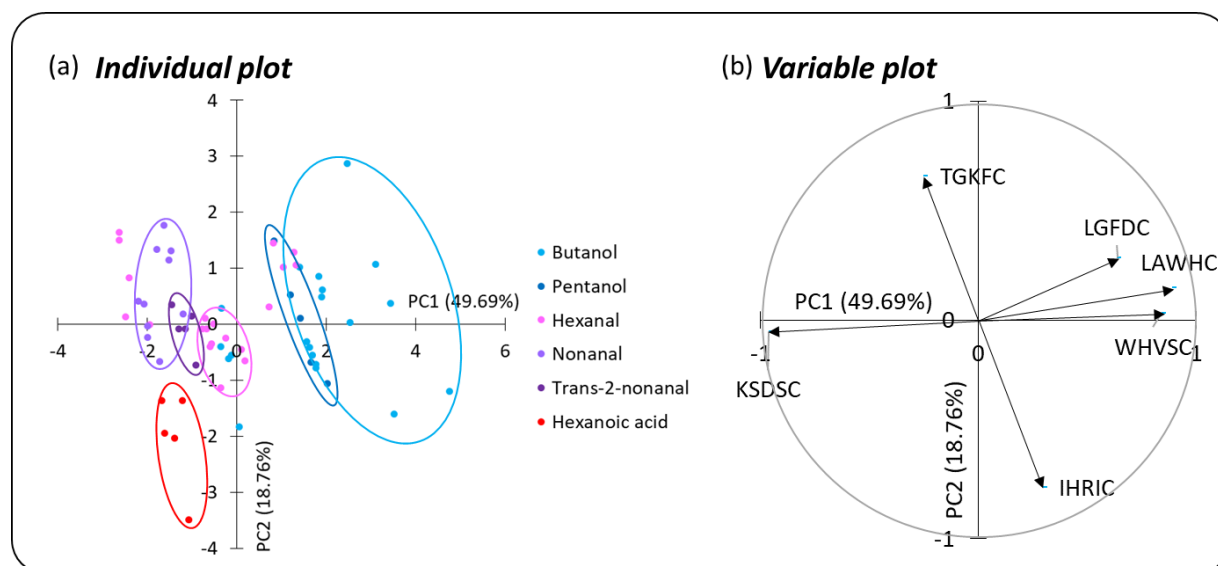


Figure 6-4 Static PCA for the discrimination of different VOCs with the penta-peptide-based optoelectronic nose. (a) Individual plot reporting analyzed VOCs. (b) Variable plot reporting the contribution of the penta-peptides.

As we can see on Figure 6-4 (a), satisfyingly, some VOC classification trends are emerging in the PCA. Spots of alcohols tend to be on the right side of the chart and those of aldehydes on the left. The cluster corresponding to hexanoic acid is separated from those of the other VOCs thanks to PC2. Moreover, discrimination can be made according to the weight of VOCs. The lighter VOCs are clustered on the right side and the heavier ones on the left. A comparison with the variable plot in Figure 6-4 (b) shows that the classification was consistent with the observation on the histograms in Figure 6-3 (b). Indeed, IHRIC was particularly useful for the discrimination of hexanoic acid. KSDSC was highly correlated with PC1, which was crucial for the separation of aldehydes from alcohols.

Nevertheless, generally speaking, there is not sufficient separation between the clusters of the different VOCs to enable their correct discrimination. Notably, the spots corresponding to butanol and hexanal were quite scattered, which highlighted a lack of reproducibility. This could be due to a high level of non-specific binding, which depended on the VOC concentration and affected the normalized profile at equilibrium. This was expectable, since the simulations showed that the peptides had a low predicted affinity and a poor selectivity for all VOCs. To facilitate the



data visualization, individuals far away from the cluster's barycenter were excluded from the ellipses. However, again, the SPR results were not really consistent with the docking simulations. The only verified trend is that LGFDC bound preferentially VOCs with a shorter carbon chain (> 100 g/mol) and an alcohol function.

It is noteworthy that Dario Compagnone's team processed the same data with XLSTAT software (Addinsoft, New York, NY). The results were different. It could be due to the different normalization method used. Here, the data has been auto scaled (zero mean and unitary variance). Moreover, a robust statistical classification method requires a high number of individuals, which was not the case here.

#### 6.1.4. Conclusion

As a conclusion to this part, in this work, we used virtually screened peptides with improved selectivity as sensing materials for our optoelectronic nose system.

Because the size of a peptide library increases exponentially with the length of the amino acid sequence, a semi-combinatorial approach was used. It led to the selection of six tetra-peptides, to which a cysteine was added for their immobilization on gold. The simulated penta-peptides' affinity for VOCs of different chemical classes were quite low, due to the small size of the peptides. However, their cross reactivity enabled the differentiation between the chemical classes.

Thanks to this complementarity of binding properties, the penta-peptide based optoelectronic nose was able to discriminate roughly between VOCs of different chemical families. However, the measurement noise was high, potentially because of the low specificity of these short probes for their target. Consequently, the classification performance was not efficient enough for the discrimination between those VOCs. Moreover, the experimental binding properties of the peptides were different from the computed ones.

Through this study, we confirmed that computational virtual screening was promising for the selection of probes with a good diversity. However, the length of the peptides appeared to be a critical feature for both the screening capabilities and the selectivity toward VOCs. We then decided to perform simulations on longer peptides to test this hypothesis.

## 6.2. EXPLORATORY WORK ON LONGER PEPTIDES

---

In this part, we led an *in silico* study on the influence of the length of the peptides on their affinity and selectivity for various families of VOCs. To this aim, we elaborated a library of peptides with 6 or 12 repetitive amino acids. This made it possible to work on a limited number of peptides, with simple structure and known physicochemical properties, and to decouple the influence of the length of the peptide from that of the amino acid side chains. We then studied their affinity for

36 VOCs from five different families (hydrocarbons, aldehydes, alcohols, carboxylic acid, and esters) by molecular docking.

### 6.2.1. Description of the protocol

G6	L6	I6	G12	L12	I12
A6	V6	M6	A12	V12	M12
F6	Y6	W6	F12	Y12	W12
D6	H6	K6	D12	H12	K12
P6	T6	S6	P12	T12	S12
N6	Q6	R6	N12	Q12	R12
E6			E12	Y12(2)	Y12(3)

Table 6-1 3D structure of the peptides used for the study of the influence of peptide length on the discrimination capacity of an optoelectronic nose.

The library of 3D-structures of peptides was generated using PEP-FOLD 3. It is presented in Table 6-1. The peptides were named X6 and X12, with X being the repeated amino acid. In addition, at their N-terminus a cysteine was added for immobilization and a short spacer for flexibility. For example, herein, L6 sequence represents for C-spacer-LLLLLL, and L12 for C-spacer-LLLLLLLLLLLLLL. C6 and C12 were excluded, because of their particular ability to form disulphide bridges. The table shows that the vast majority of these peptides adopted either no particular secondary structure (linear peptides), or they folded in an  $\alpha$ -helix. Besides, this structure was the same for the hexa-peptide and the dodeca-peptide of a given repeated amino acid. The  $\alpha$ -helices were stable; as a result, the simulation reached equilibrium for the helical peptides, and gave repeatable results. However, there were a few exceptions. G12 formed a  $\beta$ -sheet, which was not the case of G6, potentially because the latter was too short to enable  $\beta$ -sheet formation. V12 had a very elongated structure. N6 and N12 seemed to adopt a large helical structure. The only peptide with a “complex” structure, that is to say a mixture of linear and helical parts was Y12. This structure seems to be dynamical. As a result, the simulation for Y12 did not reach equilibrium. To study the influence of folding, we kept in the database three versions of Y12

structure, named Y12, Y12 (2) and Y12 (3). All these rigid structures were used for docking. A box of 26 Å edge was defined around all the peptides to perform AutoDock simulations.

	A6	D6	E6	F6	G6	H6	I6	K6	L6	M6	N6	P6	Q6	R6	S6	T6	V6	W6	Y6
ethane	-2.3	-2.9	-2.7	-3.5	-2.1	-2.5	-3.4	-3.0	-2.6	-2.5	-2.7	-3.0	-2.9	-3.1	-2.2	-2.3	-2.7	-3.5	-3.6
propane	-2.4	-2.9	-2.9	-3.4	-2.2	-2.5	-3.1	-2.9	-2.8	-2.4	-2.4	-2.7	-2.9	-3.5	-2.4	-2.8	-2.7	-3.5	-3.5
pentane	-1.5	-1.8	-1.6	-2.1	-1.7	-1.7	-1.8	-1.8	-1.9	-1.6	-1.7	-1.8	-1.9	-1.9	-1.6	-1.8	-1.6	-1.9	-1.9
heptane	-1.8	-2.0	-2.1	-3.1	-1.3	-1.9	-2.2	-2.4	-2.2	-1.7	-1.8	-2.3	-2.1	-2.6	-1.4	0.0	-1.9	-2.8	-3.0
methylcyclohexane	-2.1	-2.2	-2.3	-3.4	-1.5	-2.1	-2.6	-2.7	-2.4	-1.8	-2.0	-2.6	-2.4	-2.9	-1.6	-1.8	-2.2	-3.3	-3.3
benzene	-1.8	-2.0	-2.1	-3.1	-1.3	-1.9	-2.2	-2.4	-2.2	-1.7	-1.8	-2.3	-2.1	-2.6	-1.4	-1.6	-1.9	-2.8	-3.0
m-xylene	-2.0	-2.6	-2.1	-3.3	-2.1	-2.3	-2.7	-2.6	-2.8	-2.1	-2.3	-2.3	-2.7	-3.0	-2.2	-2.6	-2.2	-2.7	-2.8
o-xylene	-2.2	-2.4	-2.5	-3.5	-1.7	-2.2	-2.8	-2.9	-2.6	-2.0	-2.1	-2.8	-2.6	-3.1	-1.7	-2.0	-2.4	-3.6	-3.6
p-xylene	-2.0	-2.6	-2.3	-3.0	-2.0	-2.1	-2.7	-2.6	-2.5	-2.1	-2.3	-2.7	-2.7	-2.9	-2.0	-2.3	-2.3	-3.0	-3.1
toluene	-2.2	-2.4	-2.5	-3.6	-1.6	-2.3	-3.0	-3.0	-2.6	-2.0	-2.1	-2.7	-2.6	-3.1	-1.7	-2.0	-2.4	-3.6	-3.6
indole	-1.6	-2.0	-1.8	-2.4	-1.8	-1.8	-2.0	-2.0	-2.1	-1.7	-1.8	-2.0	-2.0	-2.2	-1.7	-1.9	-1.9	-2.1	-2.3
ethanol	-0.8	-0.9	-1.0	-1.5	-0.6	-0.9	-1.0	-1.2	-1.1	-0.8	-0.9	-1.1	-0.9	-1.2	-0.7	-0.8	-0.9	-1.3	-1.4
propanol	-1.1	-1.3	-1.4	-2.0	-0.8	-1.3	-1.4	-1.6	-1.5	-1.1	-1.2	-1.4	-1.3	-1.7	-0.9	-1.1	-1.3	-1.7	-2.0
butanol	-2.4	-2.7	-2.7	-3.6	-2.4	-2.4	-3.3	-3.0	-2.9	-2.2	-2.4	-3.0	-3.1	-3.2	-2.2	-2.7	-2.7	-3.5	-3.4
pentanol	-1.5	-1.7	-1.8	-2.6	-1.1	-1.5	-1.9	-2.1	-2.0	-1.3	-1.5	-1.9	-1.9	-2.3	-1.2	-1.3	-1.8	-2.2	-2.5
heptanol	-1.8	-1.9	-2.0	-2.9	-1.4	-1.6	-2.3	-2.4	-2.2	-1.5	-1.7	-2.0	-2.0	-2.5	-1.4	-1.4	-2.1	-2.4	-2.7
phenol	-2.2	-2.4	-2.5	-3.5	-1.7	-2.2	-2.8	-2.9	-2.6	-2.0	-2.2	-2.7	-2.6	-3.1	-1.7	-2.0	-2.4	-3.6	-3.7
phenylethanol	-1.9	-2.2	-2.2	-3.1	-1.4	-1.9	-2.5	-2.7	-2.3	-1.8	-2.0	-2.4	-2.3	-2.8	-1.5	-1.8	-2.0	-3.0	-3.1
ethanal	-1.8	-2.2	-1.9	-2.8	-2.0	-1.8	-2.3	-2.2	-2.3	-1.8	-1.9	-2.2	-2.3	-2.3	-1.8	-2.0	-2.1	-2.3	-2.5
propanal	-1.3	-1.4	-1.2	-1.8	-1.4	-1.6	-1.6	-1.5	-1.7	-1.5	-1.4	-1.2	-1.3	-1.6	-1.5	-1.7	-1.2	-1.4	-1.6
pentanal	-1.5	-1.7	-1.5	-2.0	-1.5	-1.7	-1.9	-1.7	-2.0	-1.7	-1.5	-1.6	-1.6	-1.9	-1.6	-1.8	-1.4	-1.9	-2.0
heptanal	-1.3	-1.6	-1.4	-1.8	-1.6	-1.5	-1.6	-1.5	-1.6	-1.5	-1.5	-1.6	-1.6	-1.6	-1.5	-1.7	-1.4	-1.5	-1.5
benzaldehyde	-1.7	-2.1	-1.7	-2.7	-1.7	-1.9	-2.3	-2.1	-2.4	-1.8	-1.8	-1.9	-2.0	-2.4	-1.7	-2.1	-1.8	-2.3	-2.5
methyl acetate	-2.6	-3.0	-2.9	-4.0	-2.6	-2.9	-3.5	-3.4	-3.3	-2.7	-2.7	-3.1	-3.3	-3.6	-2.7	-3.1	-2.9	-3.6	-3.5
methyl propanoate	-1.7	-2.0	-1.6	-2.4	-1.8	-2.1	-2.0	-2.0	-2.0	-2.0	-1.9	-1.7	-1.7	-2.2	-2.2	-2.1	-1.5	-1.9	-1.9
methyl valerate	-1.7	-2.1	-1.8	-2.6	-1.8	-2.2	-2.2	-2.2	-2.2	-2.0	-2.1	-1.9	-1.8	-2.4	-2.2	-2.1	-1.7	-2.1	-2.3
methyl heptanoate	-1.9	-2.2	-2.1	-3.2	-2.1	-2.3	-2.5	-2.3	-2.5	-2.1	-2.2	-2.2	-2.2	-2.7	-2.2	-2.2	-2.0	-2.7	-2.7
hexylester	-2.0	-2.1	-2.1	-3.0	-1.8	-2.1	-2.5	-2.5	-2.7	-1.9	-2.0	-2.0	-2.2	-2.8	-1.7	-2.2	-2.1	-2.6	-2.8
phenylbutyrate	-1.8	-2.1	-2.7	-3.1	-1.9	-2.2	-2.5	-3.0	-2.8	-2.1	-2.1	-2.3	-2.3	-3.1	-2.1	-2.4	-2.4	-3.1	-2.8
acetic acid	-2.0	-2.4	-2.3	-3.3	-2.1	-2.4	-2.7	-2.8	-2.7	-2.2	-2.2	-2.6	-2.5	-3.1	-2.2	-2.4	-2.2	-3.4	-3.4
propanoic acid	-1.6	-1.9	-1.6	-2.4	-2.0	-1.9	-1.9	-1.9	-2.0	-1.9	-1.9	-1.9	-2.3	-1.9	-2.1	-2.2	-1.7	-1.7	-1.8
valeric acid	-1.6	-2.2	-1.8	-2.5	-2.0	-2.0	-2.2	-2.0	-2.3	-2.0	-2.1	-2.1	-2.4	-2.3	-2.1	-2.3	-2.0	-2.0	-2.2
hexanoic acid	-2.0	-2.3	-2.3	-3.0	-2.0	-2.1	-2.6	-2.5	-2.5	-1.8	-1.9	-2.3	-2.5	-2.7	-2.0	-2.2	-2.3	-2.7	-2.7
heptanoic acid	-1.9	-2.5	-2.0	-3.2	-2.2	-2.2	-2.6	-2.4	-2.7	-2.1	-2.2	-2.3	-2.6	-2.8	-2.1	-2.5	-2.2	-2.5	-2.6
phenylacetic acid	-2.1	-2.7	-2.4	-3.4	-2.1	-2.2	-2.5	-2.8	-2.7	-2.1	-2.2	-2.4	-2.7	-3.1	-2.0	-2.5	-2.5	-2.7	-2.9

	A12	D12	E12	F12	G12	H12	I12	K12	L12	M12	N12	P12	Q12	R12	S12	T12	V12	W12	Y12	Y12(2)	Y12(3)
ethane	-2.4	-2.8	-3.4	-4.1	-2.2	-2.9	-3.3	-3.8	-2.8	-2.5	-2.4	-3.1	-3.4	-3.3	-2.2	-2.7	-2.5	-3.8	-5.2	-4.3	-4.1
propane	-2.2	-2.5	-3.1	-3.7	-2.0	-2.7	-3.0	-3.4	-2.7	-2.3	-2.2	-2.9	-3.1	-3.0	-2.1	-2.5	-2.2	-3.5	-4.8	-3.9	-4.1
pentane	-2.1	-2.5	-3.0	-3.6	-1.9	-2.7	-2.9	-3.3	-2.5	-2.1	-2.1	-2.8	-3.0	-3.1	-2.0	-2.4	-2.1	-3.1	-4.6	-4.0	-3.7
heptane	-1.8	-2.3	-2.7	-3.3	-1.8	-2.4	-2.5	-2.9	-2.4	-2.1	-2.0	-2.6	-2.6	-2.7	-1.9	0.0	-2.0	-3.0	-4.3	-3.4	-3.5
methylcyclohexane	-2.3	-2.6	-3.4	-4.0	-2.1	-3.9	-3.4	-3.8	-2.8	-2.5	-2.4	-3.2	-3.2	-3.2	-2.3	-2.8	-2.5	-3.7	-5.2	-4.3	-4.4
benzene	-1.8	-2.3	-2.7	-3.3	-1.8	-2.4	-2.5	-2.9	-2.4	-2.1	-2.0	-2.6	-2.6	-2.7	-1.9	-2.2	-2.0	-3.0	-4.3	-3.4	-3.5
m-xylene	-1.8	-2.1	-2.5	-3.4	-1.6	-2.4	-2.7	-3.0	-2.5	-2.1	-2.1	-2.5	-2.8	-2.7	-1.7	-2.1	-1.7	-2.7	-3.9	-3.5	-3.3
o-xylene	-2.2	-2.3	-2.8	-3.5	-1.9	-2.7	-2.8	-3.1	-2.5	-2.4	-2.3	-2.4	-3.2	-3.2	-2.1	-2.8	-2.2	-2.9	-4.1	-3.8	-3.4
p-xylene	-2.1	-2.9	-2.9	-3.5	-2.4	-2.9	-2.9	-3.2	-2.7	-2.4	-2.6	-2.6	-3.1	-3.3	-2.6	-3.2	-2.2	-3.0	-4.2	-3.9	-3.6
toluene	-2.5	-2.6	-3.3	-4.0	-2.1	-3.0	-3.3	-3.7	-2.9	-2.5	-2.6	-3.2	-3.4	-3.2	-2.2	-2.7	-2.5	-3.6	-5.3	-4.5	-4.4
indole	-2.1	-2.9	-3.1	-3.5	-2.6	-2.8	-2.9	-3.1	-2.5	-2.3	-2.5	-3.1	-2.9	-3.2	-2.8	-3.0	-2.4	-3.2	-4.8	-4.0	-3.5
ethanol	-1.4	-1.9	-1.7	-2.1	-1.6	-1.8	-1.7	-1.8	-1.6	-1.5	-1.7	-1.8	-1.9	-1.9	-1.9	-1.9	-1.6	-1.7	-2.6	-2.3	-2.0
propanol	-2.0	-2.4	-2.7	-3.3	-1.7	-2.7	-2.7	-3.0	-2.6	-2.3	-2.1	-2.5	-3.0	-3.0	-2.1	-2.6	-2.0	-2.9	-3.9	-3.7	-3.4
butanol	-0.8	-1.1	-1.2	-1.6	-0.8	-1.2	-1.2	-1.3	-1.2	-1.0	-1.0	-1.2	-1.3	-1.2	-1.0	-0.9	-0.8	-1.4	-1.8	-1.7	-1.5
pentanol	-2.1	-3.0	-3.4	-3.9	-2.0	-3.2	-3.1	-3.8	-2.8	-2.7	-2.1	-2.9	-3.4	-3.6	-2.7	-2.8	-2.1	-3.6	-4.6	-4.1	-3.9
heptanol	-2.6	-2.8	-3.5	-3.7	-2.5	-3.3	-3.5	-3.6	-2.9	-2.8	-3.1	-3.5	-3.5	-2.8	-3.3	-2.7	-3.5	-4.9	-4.2	-4.3	-4.3
phenol	-1.7	-2.2	-2.3	-2.6	-1.9	-2.4	-2.4	-2.5	-2.1	-1.9	-2.1	-2.2	-2.3	-2.4	-2.1	-2.4	-1.8	-3.3	-4.4	-2.8	-2.7
phenylethanol	-2.5	-3.2	-3.5	-3.9	-2.5	-3.1	-3.6	-3.9	-2.7	-2.7	-3.4	-3.4	-3.4	-2.8	-3.2	-2.7	-3.8	-5.2	-4.2	-4.3	-4.3
ethanal	-1.2	-1.5	-1.6	-2.2	-1.1	-1.7	-1.7	-1.9	-1.6	-1.2	-1.3	-1.7	-1.8	-1.7	-1.3	-1.2	-1.2	-1.9	-2.6	-2.3	-2.0
propanal	-1.6	-2.2	-2.0	-2.5	-1.8	-2.1	-2.0	-2.2	-1.9	-1.7	-1.9	-2.0	-2.1	-2.1	-2.0	-2.2	-1.7	-2.1	-3.0	-2.7	-2.3
pentanal	-1.6	-2.0	-2.2	-3.0	-1.5	-2.1	-2.4	-2.6	-2.2	-1.7	-1.7	-2.2	-2.4	-2.3	-1.6	-1.7	-1.6	-2.4	-3.3	-3.0	-2.9
heptanal	-2.6	-3.0	-3.6	-4.3	-2.7	-3.4	-3.5	-3.9	-2.8	-2.8	-3.0	-3.3	-3.7	-3.8	-2.8	-3.5	-2.6	-3.7	-5.2	-4.4	-4.1
benzaldehyde	-1.9	-2.3	-2.5	-2.9	-1.9	-2.5	-2.5	-2.7	-2.2	-2.1	-2.1	-2.3	-2.6	-2.8	-2.1	-2.6	-2.0	-2.5	-3.6	-3.3	-3.0
methyl acetate	-1.8	-2.3	-2.4	-2.8	-1.8	-2.6	-2.4	-2.6	-2.4	-1.9	-2.1	-2.3	-2.6	-2.6	-2.2	-2.5	-1.9	-2.6	-3.4	-3.1	-3.0
methyl propanoate	-2.2	-2.8	-3.1	-3.6	-2.3	-3.1	-3.2	-3.3	-2.7	-2.3	-2.6	-2.9	-3.1	-3.3	-2.7	-3.0	-2.7	-3.5	-4.8	-3.9	-3.9
methyl valerate	-1.6	-2.6	-2.0	-2.3	-2.1	-2.3	-2.0	-2.1	-2.0	-1.9	-2.3	-2.1	-2.1	-2.5	-2.5	-2.6	-1.9	-2.1	-2.9	-2.6	-2.5
methyl heptanoate	-1.7	-2.5	-2.3	-2.7	-2.2	-2.5	-2.5	-2.4	-2.3	-1.9	-2.4	-2.3	-2.5	-2.8	-2.7	-2.8	-2.0	-2.4	-3.6	-2.9	-2.9
hexylester	-1.3	-1.9	-1.6	-1.8	-1.3	-1.8	-1.6	-1.7	-1.7	-1.5	-1.5	-1.4	-1.8	-1.8	-1.9	-1.9	-1.4	-1.7	-2.3	-1.9	-1.9
phenylbutyrate	-1.5	-2.2	-1.9	-2.1	-1.6	-2.2	-2.0	-2.1	-2.0	-1.6	-1.7	-1.8	-2.1	-2.2	-2.1	-2.1	-1.6	-2.2	-2.9	-2.4	-2.2
acetic acid	-2.2	-2.9	-3.1	-3.7	-2.3	-2.9	-3.0	-3.2	-2.9	-2.4	-2.6	-2.7	-3.2	-3.7	-2.6	-3.1	-2.3	-3.3	-4.4	-4.1	-3.8
propanoic acid	-2.8	-3.4	-3.5	-4.0	-2.8	-3.6	-3.7	-3.8	-3.2	-3.0	-3.2	-3.4	-3.7	-4.0	-3.2	-3.7	-2.9	-3.6	-5.1	-4.5	-4.5
valeric acid	-1.7	-2.3	-2.1	-2.4	-2.0	-2.5	-2.0	-2.2	-2.0	-2.0	-1.9	-2.3	-2.4	-2.5	-2.4	-1.7	-2.2	-2.9	-2.6	-2.4	-2.4
hexanoic acid	-2.0	-2.9	-2.7	-3.1	-2.3	-2.7	-2.8	-2.9	-2.7	-2.3	-2.6	-2.6	-2.9	-3.3	-2.7	-3.1	-2.2	-2.8	-4.1	-3.7	-3.4
heptanoic acid	-1.7	-2.5	-2.3	-2.5	-2.0	-2.6	-2.5	-2.4	-2.2	-2.0	-2.2	-2.2	-2.5	-2.7	-2.7	-2.4</					

which was perfect, proving that equilibrium was reached in the simulations. The complete results are presented in Table 6-2.

### 6.2.2. Influence of the peptide properties on their binding affinity

The average binding energy of the different peptides to all the tested VOCs, sorted according to the molecular weight of their repeated amino acid, are represented in Figure 6-5 (a). Peptides were classified by colors according to their physicochemical properties. The lower the binding energy, the higher the affinity. It was noted that the simulated binding properties of some peptides composed of aliphatic amino acids (G, A, V, L) were not improved with longer chain. In contrast, for all other peptides and all the tested VOCs, the longer one had a higher average affinity compared to its short counterpart. However, the amplitude of this affinity increase was neither clearly correlated with the physicochemical properties of the repeated amino acid, nor with their molecular weight. Besides, there was a slight tendency for the average affinity of the peptides to increase when the molecular weight of the repeated residue increases, regardless of their length.

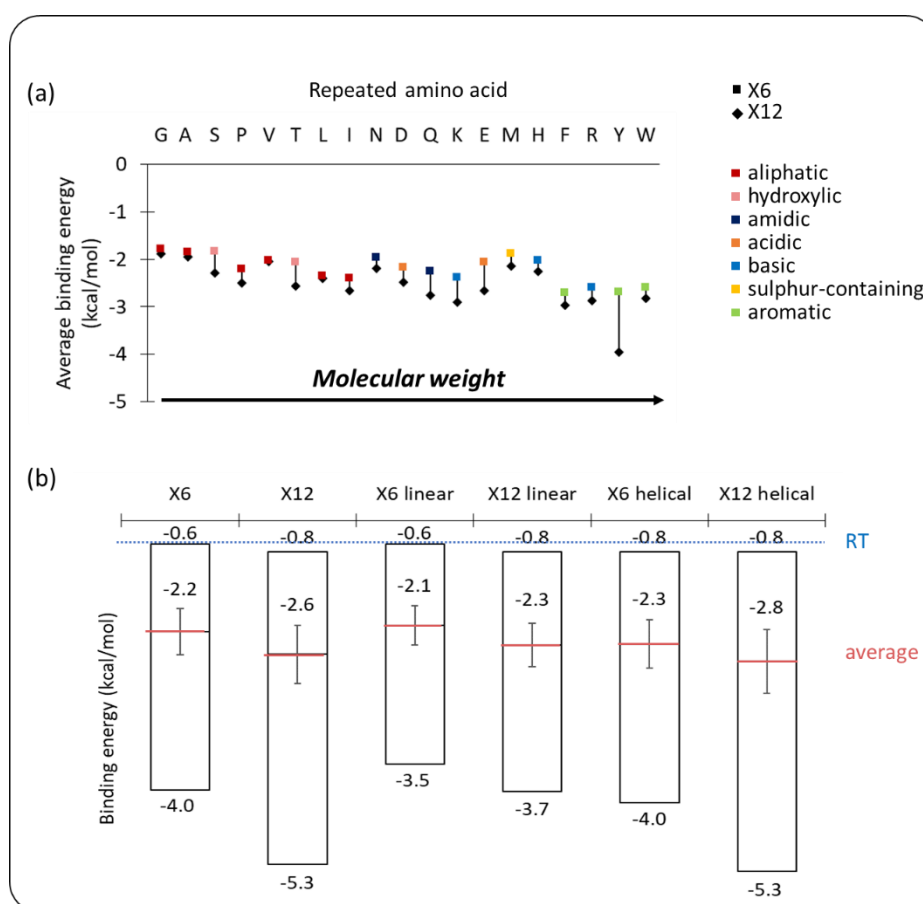


Figure 6-5 (a) Average affinity of the different peptides to all the tested VOCs, depending on their repeated amino acid. The amino acids are sorted by increasing molecular weight. (b) Distribution of the binding energies for different groups of peptides with all the tested VOCs.

The Figure 6-5 (b) represents the distribution of the binding energies of all the peptides of different structures with the ensemble of tested VOCs. The red line is the average value, and the

error bar represents the standard error between all the values. The blue line represents the energy of thermal agitation  $RT$  that serves as a reference.

By elongating the peptides, the average binding energy for all the peptide-VOC assemblies decreased slightly. More satisfyingly, the best binding affinity changed from  $-4$  kcal/mol to  $-5.3$  kcal/mol. Besides, in both X6 and X12 groups, some peptides showed almost no affinity for some of the VOCs, with a binding energy equivalent to  $RT$ . This result was particularly positive since it showed that the variability of binding energies toward the different VOCs increased with the length of the peptides. Thus, most probably, the chemical resolution of an artificial tongue or nose based on longer probes would be improved.

To better understand this observation, we studied separately linear peptides (with repeated G, I, V, D, P, T, S or N) and helical ones (others). Clearly, the affinity distribution of the linear peptides for all the VOCs did not significantly change with their length, which is opposite for the helical ones. It therefore seems that the secondary structure of peptides plays an important role. We suggest two hypothesis to explain this observation. From a first point of view, the amino acids that are more likely to bind VOCs have the ability to form hydrogen bond and to undergo hydrophobic/hydrophobic interactions. Consequently, they are also more likely to form helices. From another point of view, secondary structures may favor the cooperative binding of several amino acids to a VOC. This hypothesis was supported by the fact that the highest variation in average binding energy was obtained for Y (Figure 6-5 (a)). Y6 is helical, but Y12 has both helical and linear parts.

### 6.2.3. Influence of the VOC properties on the binding affinity

From another point of view, we studied the influence of the VOC physicochemical properties on their affinity with the peptides of different length. For this, we defined the “variation of affinity” of a VOC as its absolute average binding energy with all the peptides X12 minus the same value with the peptides X6. The results are presented in the Figure 6-6.

In Figure 6-6 (a), this parameter was plotted against the molecular weight of the VOCs. Clearly, the variation of affinity tend to be higher for larger VOCs. This seems reasonable, since a larger molecule is more likely to bind to a peptide in multiple points, which is made possible by the elongation of the peptide.

In Figure 6-6 (b), the variation of affinity was plotted against the physicochemical properties of the VOCs. It was hardly significant for hydrocarbons, aldehydes and alcohols that have small functional groups. In contrast, VOCs with cumbersome functional groups like carboxylic acids, esters and above all, aromatic compounds showed higher variations of affinity. Therefore, they bind preferentially to longer peptides. Again, large functional groups could promote multiple interactions with the peptides. We also noticed that there was a link between this variation of

affinity and the polarity of the VOCs. Nevertheless, the correlation was much lower than with the molecular weight of the VOCs.

In conclusion, the addition of longer peptides would probably increase the chemical resolution by repelling VOCs with different molecular weight, rather than VOCs with different chemical functions.

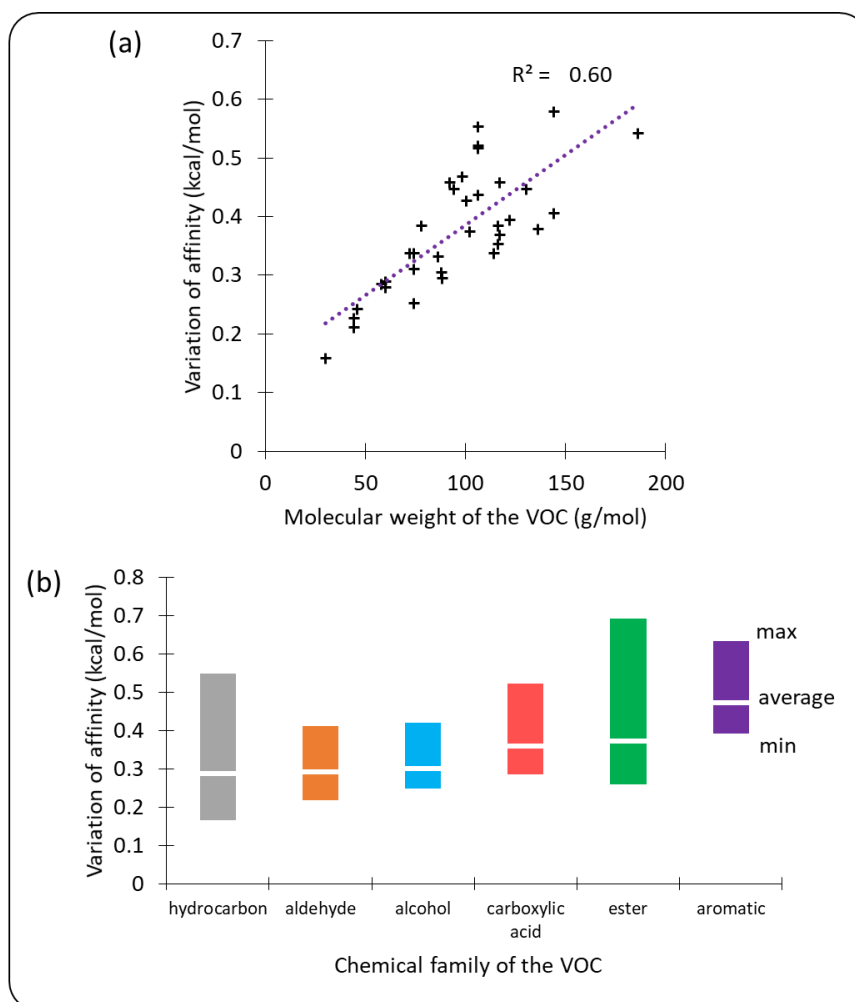


Figure 6-6 (a) Average variation of affinity of all the peptides for a given VOC molecule, as a function of its molecular weight. (b) Distribution of the variations of affinity of all the peptides for different chemical families of VOCs.

#### 6.2.4. Chemical resolution

To verify our hypotheses on the chemical resolution of an artificial tongue or nose based on longer peptides, we presented PCAs on the simulation results with X6 or X12 peptides in Figure 6-7.

With X6 peptides (Figure 6-7 (a)), VOCs from the same chemical family were quite well clustered. Notably, hydrocarbons (black) that are hydrophobic with low polarity were separated from other hydrophobic VOCs such as aldehydes (orange) and esters (green) with higher polarity along PC1. Hydrophilic compounds like alcohols (blue) and carboxylic acids (red) were separated apart thanks to PC2. In general, the simulated artificial tongue or nose made efficient

discrimination between all individual VOCs except in few cases. For instance, methyl heptanoate and methyl valerate were very close to each other, whereas they have different molecular weight. The different hydrocarbons were also close to each other. Based on all these results, the discrimination capacity between VOCs of an artificial tongue or nose based on X6 peptides is dominated by physicochemical parameters. This is also clearly the case for our historical optoelectronic nose based on short peptides (<10 amino acids).

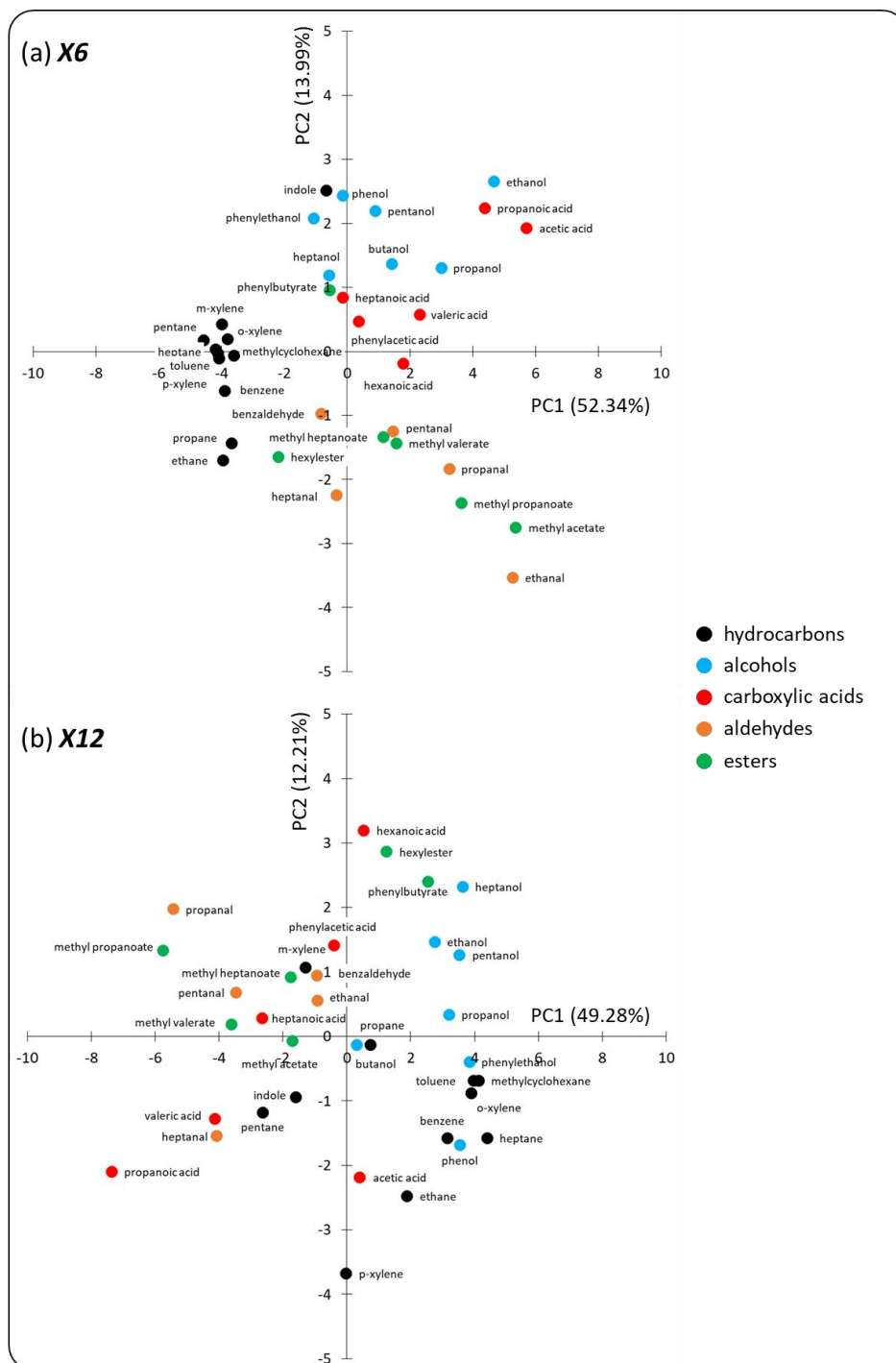


Figure 6-7 PCAs on the docking simulation results for all tested VOCs with X6 or X12 peptides. The correlation matrix was filled with the absolute binding energy between the peptides (variables) and the VOCs (individuals).

In contrast, the classification was very different with X12 peptides (Figure 6-7 (b)). In this case, VOCs from the same chemical family were badly clustered. Interestingly, in general, there was more distance between the VOC individuals. Indeed, the minimum distance between two points, in the sense of the Euclidean distance in the plane (PC1; PC2) was 1.75, compared to 0.75 for X6 peptides. This result is interesting since the number of variable was the same in both cases. Based on these results, it seems that some other parameters rather than physicochemical ones influence significantly the discrimination capacity of an artificial tongue or nose with only X12 peptides. For example, as demonstrated in Figure 6-6 (a), the molecular weight of the VOCs may be an important parameter.

Eventually, we performed a PCA on a correlation matrix containing the absolute binding energy of all peptides (X6 and X12, variables) with all the tested VOCs (individuals). The results are plotted in Figure 6-8.

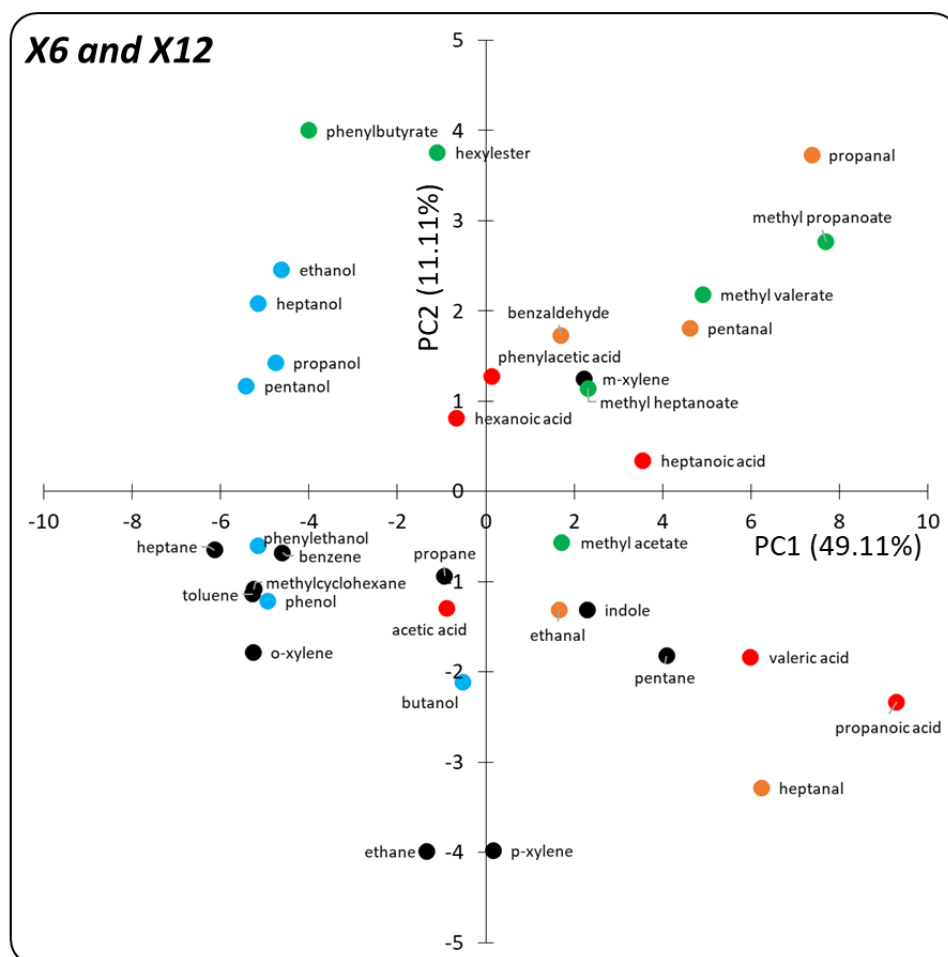


Figure 6-8 PCA on a correlation matrix containing the absolute binding energy of all peptides (X6 and X12, variables) with all tested VOCs (individuals).

By combining X6 and X12 peptides, the minimum distance between two individuals on the PCA was 2.18, which was logically the best discrimination score. However, like for X12 peptides, the chemical families were not well clustered.



### 6.2.5. Conclusion

In conclusion to this part, we computationally studied two groups of peptides differing only in length, but had the same functional groups and structure. Regardless of the peptide kind, the longer one showed a better affinity for the VOCs tested. A greater variation was obtained with helical peptides, or peptides composed of heavier amino acids on the one hand. On the other hand, it was achieved for heavier VOC molecules, regardless of their chemical families. As a result, an optoelectronic tongue or nose based on longer peptides would show a better chemical resolution, but the VOCs of a same chemical group would not be classified as similar.

Thus, the choice of probes should be done according to the application aimed. For example, to determine the chemical family of an unknown VOC or to classify VOCs of different chemical families, a chip based on X6 peptides would be more suitable. In contrast, an X12-based chip would facilitate the differentiation of two VOCs with similar chemical features, but different molecular weight. Finally, by combining X6 and X12 peptides, even better chemical resolution for discrimination between individual VOCs could be reached.

Longer and more structured probes seem to be of particular interest for a high affinity and selectivity. However, the preservation of this structure is key for practical application, and may be difficult to achieve, especially in the gas phase. Besides and importantly, combining peptides of different length on the same chip would bring practical issues. Indeed, using probes of different molecular weight makes it harder to find an appropriate working angle in the linear region of all the biosensors (see 2.4).

This preliminary study was limited for time-constraint reasons to peptides with very simple sequences, and thus, very simple structures. However, the variety of possible structures also increases with the peptide length. The results could be very different with peptides with more complex structures. Plus, the simulations were performed on rigid structures, for free probes in solution, and in the hypothesis of a one-to-one interaction; whereas in a real case experiment, a longer peptide bearing more binding sites could be more sensitive to VOCs than a shorter one.

### 6.3. SUPPORT TO *IN VITRO* SELECTION

---

In the two previous parts, the size of the peptide library that could be screened *in silico* was limited by the computation time. We could either work on very short peptides that could be then elongated through semi-combinatorial approach (6.1), or focus on simple sequences for longer peptides (6.2). In both cases, there was a very weak probability that the sequence with the highest affinity for a target was present in the library and selected.

In comparison, *in vitro* methods like phage display enabled us to select the best binders in a library of  $10^9$  heptamers in a reasonable time, and even wider libraries with longer peptides are available. Nonetheless, at the end of the procedure, we had to choose randomly which sequence

would be synthesized to be integrated on the chip. Besides, the best binder for a target is not necessarily the most selective one. In addition, apart for the molecule used for the negative selection, we had no mean to check if the selected probes had a weak cross-reactivity with other VOCs.

This is where the docking simulations could come into play. On the one hand, after sequencing, the affinity of all the selected sequences for the target VOC and other compounds could be tested *in silico*. This would help to decide which peptide to synthesize. As an illustration, we performed docking simulations on the twelve sequences that were selected by phage display (PhD1 to PhD12), but not synthesized (see Table 5-1), with 35 different VOCs. The results are presented in Table 6-3.

	PhD1	PhD2	PhD3	PhD4	PhD5	PhD6	PhD7	PhD8	PhD9	PhD10	PhD11	PhD12
<i>ethane</i>	-1	-1	-1.1	-1.1	-1	-1.1	-1.3	-1.2	-1.1	-1.1	-1.1	-1.2
<i>propane</i>	-1.3	-1.4	-1.5	-1.5	-1.3	-1.5	-1.8	-1.7	-1.6	-1.5	-1.6	-1.5
<i>pentane</i>	-1.9	-1.8	-2	-2	-1.8	-2	-2.4	-2.4	-2.2	-2	-2.1	-2.1
<i>heptane</i>	-2.3	-2	-2.2	-2.4	-2.1	-2.4	-2.8	-2.6	-2.6	-2.3	-2.5	-2.4
<i>methylcyclohexane</i>	-2.4	-2.4	-2.5	-2.8	-2.3	-2.7	-3.3	-3.1	-3.1	-2.6	-2.7	-2.6
<i>benzene*</i>	-2.4	-2.4	-2.4	-2.5	-2.3	-2.5	-3.1	-3	-2.9	-2.4	-2.6	-2.6
<i>m-xylene*</i>	-3	-3	-2.8	-3.2	-2.8	-3.2	-3.8	-3.8	-3.7	-2.9	-3.3	-3.2
<i>o-xylene*</i>	-3	-3	-2.8	-3.1	-2.8	-3.2	-3.8	-3.7	-3.7	-2.8	-3.3	-3.2
<i>p-xylene*</i>	-3	-2.9	-2.8	-3	-2.8	-3.2	-3.8	-3.7	-3.7	-2.7	-3.2	-3.1
<i>toluene*</i>	-2.7	-2.7	-2.6	-2.8	-2.6	-3	-3.5	-3.5	-3.3	-2.7	-3	-2.9
<i>indole*</i>	-3	-2.8	-3.1	-3	-3	-3.5	-3.6	-3.7	-3.5	-3	-3.1	-3.1
<i>ethanol</i>	-1.8	-1.9	-1.7	-2	-1.4	-1.8	-1.6	-1.6	-1.9	-1.9	-1.6	-1.6
<i>propanol</i>	-2	-2.1	-2	-2.3	-1.7	-2	-1.9	-2	-2.1	-2.2	-1.8	-1.9
<i>butanol</i>	-2.1	-2.4	-2.2	-2.5	-2	-2.2	-2.3	-2.2	-2.3	-2.3	-1.9	-2.1
<i>pentanol</i>	-2.3	-2.5	-2.4	-2.7	-2.1	-2.3	-2.6	-2.4	-2.5	-2.5	-2.2	-2.3
<i>heptanol</i>	-2.6	-2.7	-2.6	-3	-2.4	-2.6	-3	-2.7	-3	-2.6	-2.6	-2.5
<i>phenol*</i>	-2.7	-2.6	-2.7	-3.1	-2.6	-2.9	-3.1	-3.2	-2.8	-3	-2.5	-2.7
<i>phenyl ethanol*</i>	-3.2	-3.2	-3.3	-3.6	-2.8	-3.3	-3.6	-3.6	-3.7	-3.2	-3.1	-3.2
<i>ethanal</i>	-1.8	-1.6	-1.7	-1.7	-1.5	-1.6	-1.6	-1.5	-1.7	-2	-1.5	-1.7
<i>propanal</i>	-1.9	-1.7	-2.1	-2	-1.8	-1.8	-1.9	-1.9	-1.9	-2.2	-1.8	-1.9
<i>pentanal</i>	-2.1	-2.1	-2.5	-2.4	-2.2	-2.2	-2.7	-2.4	-2.3	-2.6	-2.1	-2.2
<i>heptanal</i>	-2.4	-2.2	-2.7	-2.7	-2.3	-2.4	-3	-2.5	-2.8	-2.8	-2.5	-2.5
<i>benzaldehyde*</i>	-2.9	-2.6	-2.9	-3.1	-2.7	-2.8	-3.4	-3.3	-3.2	-3.2	-2.9	-3
<i>hexylester</i>	-2.8	-2.6	-2.6	-3.2	-2.6	-2.8	-3.6	-3	-3.1	-3	-2.6	-2.7
<i>methyl acetate</i>	-2.2	-2.1	-2	-2.3	-2	-2.1	-2	-2	-2.2	-2.6	-2	-2.1
<i>methyl propanoate</i>	-2.3	-2.2	-2.3	-2.5	-2.2	-2.3	-2.2	-2.3	-2.3	-2.7	-2.1	-2.2
<i>methyl valerate</i>	-2.5	-2.4	-2.6	-2.8	-2.5	-2.5	-2.9	-2.6	-2.6	-3.1	-2.3	-2.5
<i>methyl heptanoate</i>	-2.7	-2.6	-2.8	-3	-2.7	-2.8	-3.1	-2.9	-3	-3.1	-2.6	-2.7
<i>phenyl butyrate*</i>	-3	-2.9	-3.3	-3.5	-3	-3.3	-3.8	-3.1	-3.6	-3	-3.2	-3.3
<i>acetic acid</i>	-2.2	-2.3	-1.9	-2.5	-1.8	-2.3	-2	-2.1	-2.1	-2.5	-2	-2
<i>propanoic acid</i>	-2.3	-2.4	-2.2	-2.8	-2	-2.6	-2.1	-2.4	-2.3	-2.7	-2.2	-2.2
<i>valeric acid</i>	-2.4	-2.8	-2.5	-3.1	-2.4	-2.9	-2.7	-2.7	-2.8	-3	-2.4	-2.5
<i>hexanoic acid</i>	-2.6	-3	-2.7	-3.2	-2.6	-2.9	-3	-2.8	-3	-3	-2.6	-2.6
<i>heptanoic acid</i>	-2.8	-2.9	-2.8	-3.2	-2.7	-3.1	-3.1	-3.1	-3.1	-3.2	-2.7	-2.8
<i>phenylacetic acid*</i>	-3.3	-3.4	-3.5	-3.8	-2.9	-3.5	-3.7	-3.6	-3.9	-3.5	-3.2	-3.3

Table 6-3 Free binding energies (kcal/mol) obtained by molecular docking for the binding of the peptides PhD1 to PhD12 to a range of VOCs from different chemical families.

Then, we calculated their simulated selectivity for phenyl compounds like in Chapter 5.

$$\text{Simulated } S_{\text{phenyl}} = \frac{E_{\text{bind}}(\text{phenyl}) - E_{\text{bind}}(\text{other})}{\bar{E}_{\text{bind}}} \times 100$$

With  $E_{bind}(phenyl)$ ,  $E_{bind}(other)$  and  $\overline{E_{bind}}$  the average simulated binding energy of the peptide with phenyl compounds, other compounds, or all compounds (respectively). Figure 6-9 shows that the three selected and synthesized peptides (P1, P2 and P3 in yellow) were the most consensual ones but not the ones with the best selectivity for the target family of VOCs. In fact, the lysis plaques that we choose to collect (random) and the infectivity of the different hits bias the frequency of each peptide. Furthermore, PhD7 and PhD8 had a higher simulated  $S_{phenyl}$  than all the historical peptides, despite their relatively short size. On top of that, the absolute affinity of PhD7 and PhD8 for some of the phenyl compounds was higher than those of the historical and synthesized peptides. As a result, we would have made a better choice by combining phage display and docking simulations; thus, this strategy is very promising.

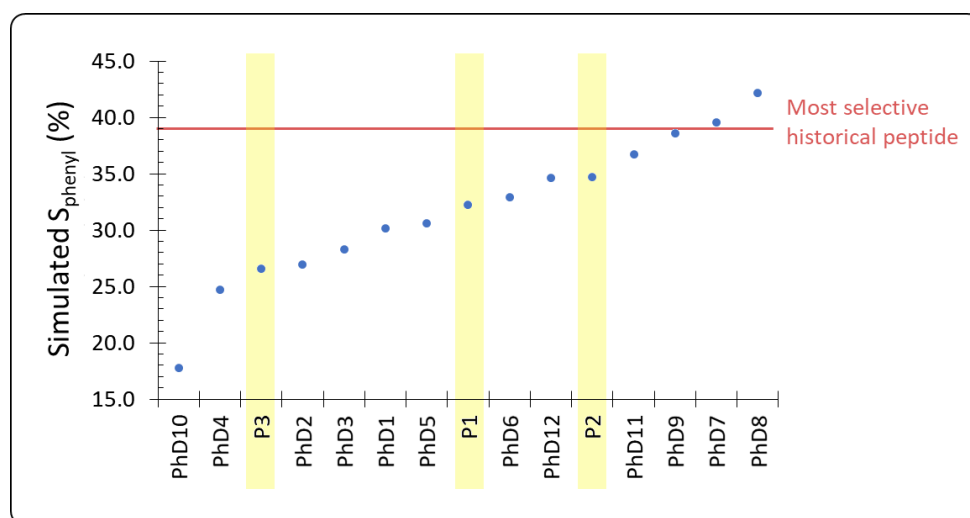


Figure 6-9 Simulated selectivity for phenyl compounds of all the peptides selected by phage display.

Moreover, we could go further and use virtual screening tools to mature the selected sequences. In the literature, substitution assays are commonly used for this purpose. In this strategy, one or several amino acids in a selected peptide are substituted with other residues. Then, a virtual screening assay is performed on all these new peptides. The results enable to understand which amino acid in the peptide sequence are essential to its affinity for a target. Notably, it helped Jaworski *et al.* [246] to identify the key elements in TNT-binding peptides.

As an example, we studied the peptide PhD8 by replacing alternatively all its seven amino acids (excluding the spacer and the cysteine) by a neutral and simple glycine. We chose glycine because this amino acid has no side chain for introducing other physicochemical properties. The affinity of these seven peptides for the 35 VOCs previously used was then calculated using AutoDock, and their selectivity to phenyl compounds was calculated as previously. The results are presented in Figure 6-10. All the peptides with a substituted amino acid had a significantly lower selectivity for phenyl compounds than PhD8. As a result, we can conclude that all the amino acids of PhD8 contribute to its high performance. The lowest score was achieved by replacing the fifth

tyrosine by a glycine. This was most probably because tyrosine is an aromatic residue, which could bind phenyl groups by  $\pi$ - $\pi$  stacking. Moreover, the helical structure of PhD8 was lost in this case, just like when the third alanine was substituted. The fact that the two peptides had the lowest scores seems to indicate that the helical structure of the peptide is key for the good selectivity of PhD8 for phenyl compounds.

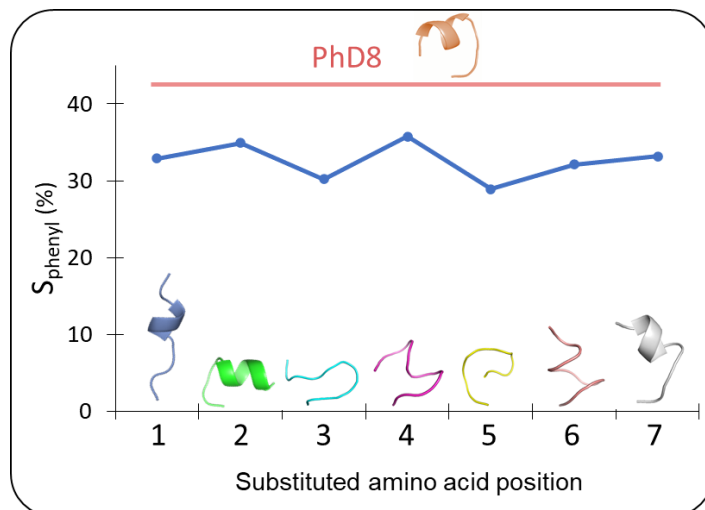


Figure 6-10 Comparison on the selectivity for phenyl compounds between PhD8 and its seven substituted peptides based on simulation results.

Furthermore, the best binders for the target can be identified thanks to substitution assays. For example, Okochi *et al.* [328] used a substitution assay to optimize a peptide derived from an antibody to bind TNT. By substituting an isoleucine to an arginine, they obtained a 1.8-fold increase in sensitivity. Again, a quick test was performed on the peptide PhD8. The first amino acid of the sequence, an alanine, was replaced by one of the five amino acids that were the most frequent in all the peptides identified by phage display. Then, using AutoDock, we performed docking simulations on the five sequences with the 35 VOCs to calculate  $S_{\text{phenyl}}$ . However, none of these peptides showed a higher selectivity to phenyl compounds than PhD8. It could mean that the selection by phage display was successful. However, we cannot conclude based on this limited study, since we did not have the computational abilities to perform high-throughput screening to substitute other amino acids.



# Conclusions and perspectives: thinking tool for improving the performance of the artificial nose

## Description of the tool

The reflection led during this thesis enabled me to identify the principal levers of action to improve the performance of an artificial nose or artificial tongue system. These levers are highly intertwined: acting on one of them has consequences for the others. To illustrate the relationships between them, I propose a graphical representation of my conclusions in Figure C-1. This diagram can also be a very useful tool for identifying optimization potentials in the future.

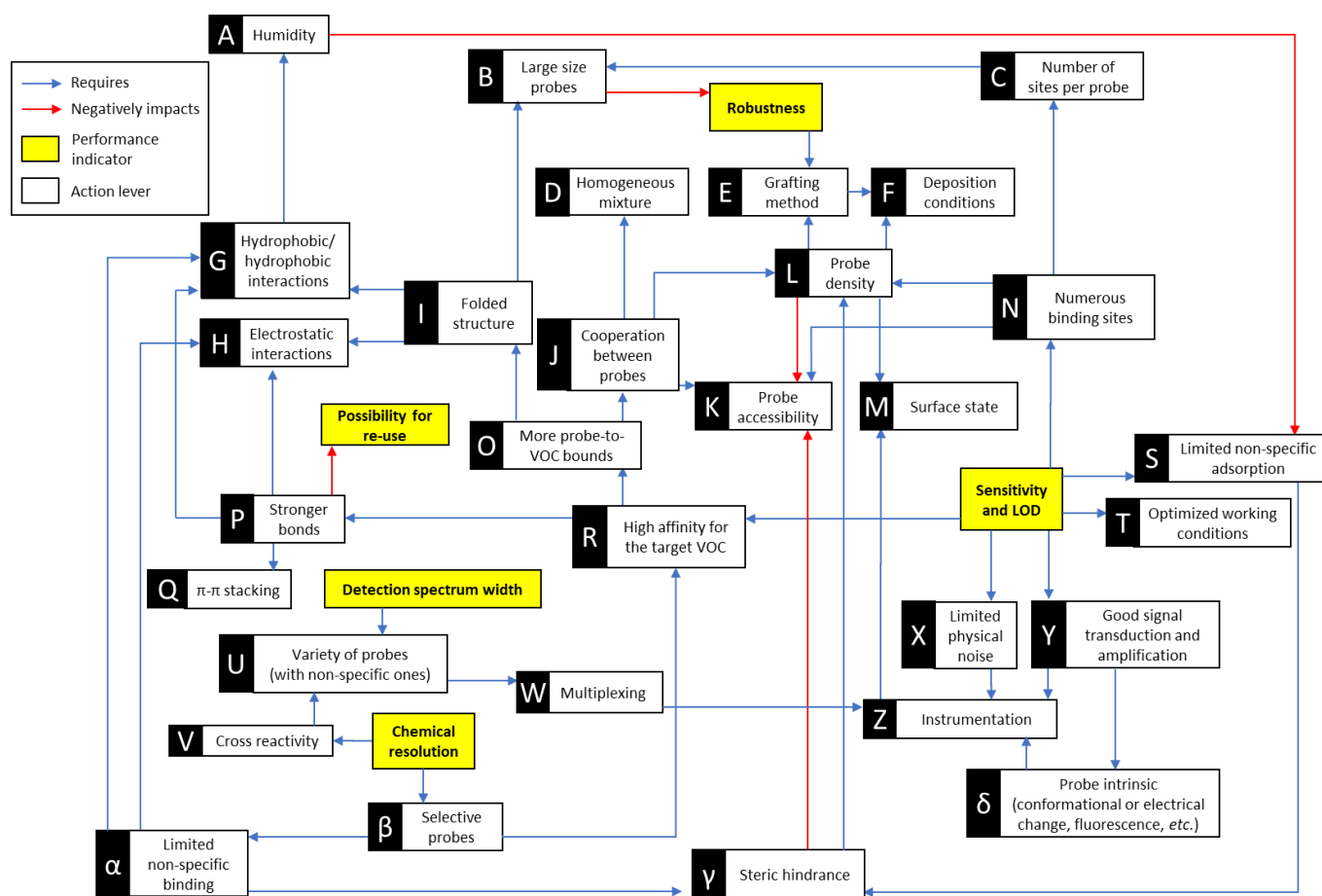


Figure C-1 Histogram summarizing the action levers to improve the performance of the artificial nose system.

The key performance criteria of artificial noses and tongues are represented by yellow rectangles in this diagram: sensitivity and limit of detection, robustness, possibility for reuse, width of the detection spectrum and chemical resolution. To advance these points, several technical action levers are available. They are listed as white boxes. For example, if we want to widen the detection spectrum of the device, we can increase the variety of probes, including non-specific ones (U). A blue arrow represents this relationship. Acting on a lever will influence other ones. If we continue with the same example, increasing the variety of probes will, on the one hand,

require multiplexing. On the other hand, it will enable cross-reactivity, and so participate in a better chemical resolution. Operating a lever can also have a detrimental effect on another one, or on a performance feature. In this case, a red arrow connects the two corresponding boxes. For instance, a high level of humidity (A) is hardly compatible with a limited non-specific adsorption and binding (S). Therefore, it affects the sensitivity and limit of detection of the system.

### **Overview of the actions carried out during this thesis**

In this thesis project, we have been working mostly on improving the sensitivity and the chemical resolution of our optoelectronic nose. This device, developed at the lab since 2012, relies on an array of sensing materials constituted by peptide probes and uses gas-phase SPRi as a transduction method. The interaction of a VOC with the various sensing materials influences their local refractive index, and these variations are recorded. The resulting “signature” of the VOC enables its identification by a multivariate statistical method.

Referring to the Figure C-1, there are two main ways to improve the discrimination capability of the device. We can either rely on cross-reactivity (V), by increasing the variety of probes (U), or integrate more selective probes on the chip ( $\beta$ ). Our laboratory historically chose the former solution, since it also contributed to the wide detection spectrum of the optoelectronic nose. Besides, SPRi enabled to put several hundreds of sensing materials on the same chip (W). This enabled a good identification of VOCs, with up to a single-carbon resolution for some chemical families [329]. Nevertheless, it could be limited by the cost of the probes, and the number of possible probes is limited by the size of the chip, especially if we tend towards miniaturization. A high number of sensing materials also increases the complexity of the data processing.

Moreover, if a precise application is aimed, it is more effective to develop directly a sensing material suited to the detection of the target VOC or family of VOCs. Therefore, designing probes with a high-affinity for a target (R) and a limited non-specific binding ( $\alpha$ ) was at the core of this thesis. This was all the more relevant since such probes also contribute to increasing the sensitivity of the device and lowering its detection limit. To reach this goal, three main strategies were explored herein, each of which has been the subject of a chapter. First, we considered integrating OBPs, proteins naturally involved in the function of the biological nose, on our chips. The binding properties of these soluble proteins can be modified through site-directed mutagenesis to meet the needs of an application. Second, we used phage display to screen specific peptides against a target VOC *in vitro*. Third, we explored the potential input of virtual screening. Interestingly, with the three methods, the cross-reactivity of the selected probes for non-targeted VOCs was limited ( $\alpha$ ). It was naturally the case for OBPs, because of their barrel structure with a binding pocket, whereas for phage display and virtual screening, it was possible thanks to negative selection.

In the light of the results obtained with these three approaches, it appeared that the high affinity of a probe for a target could rely, on the one hand, on stronger bonds between them (P). For example, we showed in the fifth chapter that VOC molecules with a phenyl group would stack on amino acids with similar structures on their side chain (Q). This solution is interesting because it does not require large probes (B) that are commonly less robust. However, this is not implementable for any target and it could make it impossible to re-use the sensor. We also faced difficulties to preserve the strong bounds observed or simulated in the liquid phase when transferring the probes to the gas phase.

On the other hand, a high affinity could be achieved by increasing the number of weaker probe-to-VOC bounds (O). This is the preferred solution in nature, used for DNA strands pairing or protein interactions. In the case of OBPs and longer peptides, that were both envisaged in this thesis, this goes through the folding of the biomolecule to form a binding pocket (I). In most cases, the integrity of this structure relies on hydrogen bonds or hydrophobic/hydrophobic interactions (G) that require humidity (A). Thus, we had to modify our setup to introduce water while limiting the negative impact it could have on the biosensors. Even under these conditions, biosensors developed on this model have a limited lifespan. Indeed, a folded structure is only possible for relatively large probes (for peptides, above 10 amino acids).

During this thesis project, we also worked on improving the sensitivity of our device. Apart for using high-affinity probes, there are several points concerning the preparation of the chip related to this performance point. First, we observed that a signal amplification was profitable. Notably, it was indispensable for the detection of VOCs in the liquid phase. Interestingly, the conformational change of OBPs upon VOC binding acted as a probe-intrinsic amplifier ( $\delta$ ). Second, it is important to limit the non-specific adsorption of VOCs or water on the background of the chip. For our system, Sophie Brenet developed a passivation process to block the gold surface in between probes ( $\gamma$ ). Third, we have to maximize the number of binding sites available on a sensing material (N). To do so, we focused on probe density and developed a new deposition protocol (F) for peptides, named Protocol 2. Our grafting method (E), based on cysteine anchors and flexible linkers contributed to this density, while ensuring a correct orientation, and so accessibility, of the probes.

The thesis of Jonathan Weerakkody was complementary to this study, as he worked on the optimization of the instrumental part (Z), that is, the wavelength of the SPRi apparatus, the conception and fabrication of the prisms (M), *etc.* In the meantime, he assessed the influence of temperature and humidity on the performance of the optoelectronic nose to determine the optimal working conditions (T).

This thesis project should be approached as a preliminary and exploratory work. Although, at the end, none of the new sensing materials tested resulted in a significant improvement in the



performance of the optoelectronic nose, this work provided an insight into different strategies and identified their related issues. We now have a much better understanding of the key points that influence the sensitivity and selectivity of artificial noses. In the future, we will be able to adapt the protocols proposed here to more relevant probes for the greatest benefit to the device. The initial objective was to make the system customizable, based on the needs that an industrial customer might have. It will therefore be particularly important later on to involve these potential users to make sure to work on the detection of relevant molecules, with defined specifications. Some additional approaches were not addressed in this thesis, so I propose some technical perspectives afterwards.

### **Perspectives**

The graphical representation in Figure C-1 can also be a support to identify potential perspectives to improve the performance of our optoelectronic nose further.

We identified that the structure of the probes was key to have a high affinity with a VOC target (I). However, this structure can be fragile, especially if it relies on hydrophobic/hydrophobic or electrostatic interactions and for use in the gas phase. Thus, as far as proteins are concerned, stabilization could be obtained thanks to disulphide bridges [276]. In this respect, insect OBPs could be of particular interest, since they naturally fold thanks to six cysteines [279] (Figure C-2 (a)). Artificial binding proteins, or affitins, are another class of robust proteins that could be worth exploring [330] (Figure C-2 (b)). Similarly, when it comes to peptides, cyclic peptides flanked with two cysteines could be used. Indeed, the loop in these sequences could act as a “binding pocket” for VOC molecules. Libraries of cyclic peptides exist for phage display [331,332]. Nevertheless, we would probably have to change the surface chemistry used for the immobilization of these probes, since the disulphide bridges are likely to break when they are in close vicinity to the gold surface. Besides, in this thesis, all the probes that we used were peptides or proteins. However, DNA or RNA probes could also be considered. Even though there is a much smaller variety of nucleic acids than amino acids, it may be easier to control their grafting on a surface and their regeneration, as well as their structuring. Notably, hairpin DNA [325] could be promising, as we showed during a preliminary study [326] (see Appendix A-2). The multiple nucleic acids, well oriented in this structure, could indeed interact simultaneously with a VOC molecule (Figure C-2 (d)). One could go as far as to consider integrating several loops in the last two types of probes cited to broaden the linear detection range of the associated biosensors.

Interestingly, all these structure-constrained probes would be compatible with phage display (or SELEX in the case of DNA and RNA probes). Affitins and OBPs are small proteins, which makes it possible to display them onto phages [333]. Besides, commercial phage display libraries with cyclic peptides of various loop length are available (Figure C-2 (c)).

Alternatively, to overcome the robustness problems associated with large probes, it would be possible to increase the number of probe-to-target bounds (O) through the cooperation between probes (J). This could be achieved by using a single type of probe in a given sensing material (multivalency), or by mixing different probes. One could notably think of mixing several peptide segments of OBPs or ORs known to be cooperatively involved in VOC binding. On top of that, we previously showed that mixing two different kind of probes was also interesting to fabricate combinatorial sensing materials (Figure C-2 (e)) [334]. However, this strategy would require a homogeneous mixture on the sensor surface, which could be hard to verify. Branched structures (Figure C-2 (f)) or dendrimer could bring a solution to this problem [335,336].

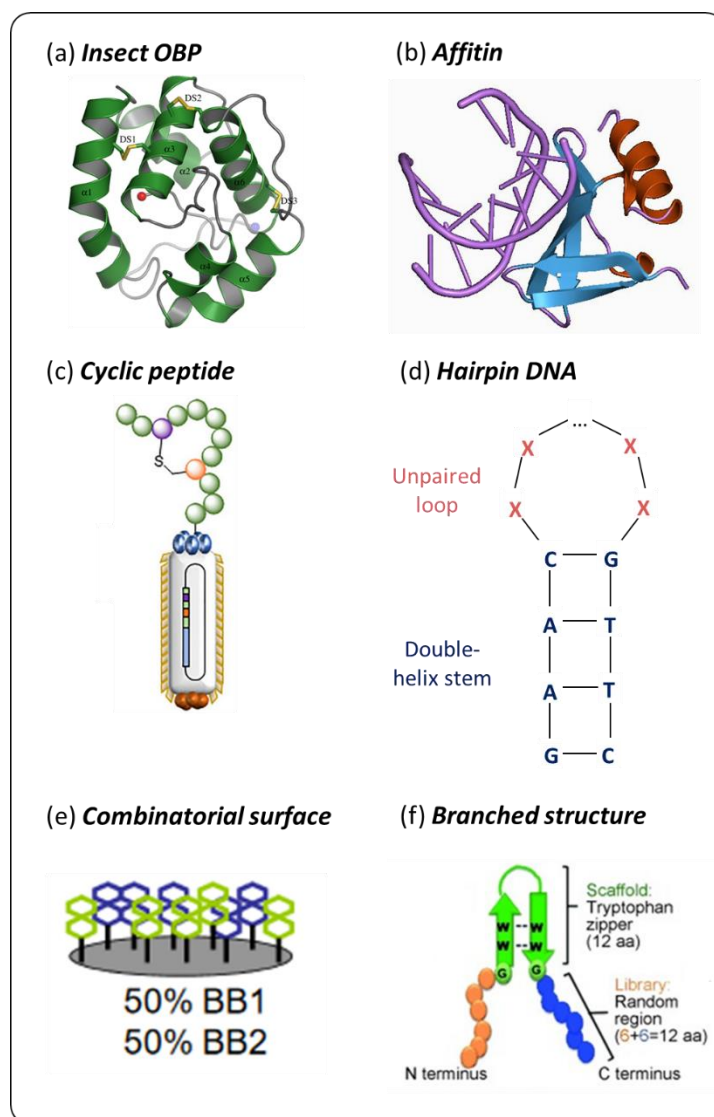


Figure C-2 Example of various structures that would favor the multiple interactions of a sensing material with its target VOC. (a) Insect OBP [337]. (b) Affitin: wild-type Sac7d is in blue and orange, bound to DNA in lilac. PDB: 1AZP. (c) Cyclic peptide, adapted from [331]. (d) Hairpin DNA, adapted from [325]. (e) Combinatorial surface adapted from [338]. (f) Branched structure, adapted from [339].

In the wake of this thesis, Marielle El Kazzy stated a PhD in November 2019, co-funded by the ANR project OBP-Optinose and Labex Lanef. She will explore some of those perspectives.



# Appendix

## A-1 Angular sensitivity

In the literature, the physical sensitivity is often approximated by the angular sensitivity  $\frac{\partial R}{\partial \theta}$ , through the following equation.

$$\frac{\partial R}{\partial n} = \frac{\partial R}{\partial \theta} \times \frac{\partial \theta}{\partial n}$$

The angular sensitivity quantifies the shift of the plasmon curve due to a bulk phase variation of the refractive index. We can get an estimation of the angular sensitivity of the different sensing materials. It corresponds to the derivative of the plasmon curve at the working angle  $\theta_w$  (Figure A-1 (a)), which is approached experimentally by:

$$\frac{\partial R}{\partial \theta} \approx \frac{\Delta R}{\Delta \theta} = \frac{R(\theta_w + 0.25^\circ) - R(\theta_w - 0.25^\circ)}{0.5^\circ}$$

This was a good approximation as far as we stayed in the linear region of the plasmon curve. It implied that  $\Delta R$  resulted only from the translation in angle of the plasmon curve, whereas in reality, the amplitude of this curve could also be crushed or stretched by optical effects.

An example is proposed in Figure A-1. In practice, the different sensing materials had slightly different refractive index. As a result, their plasmon curves were shifted in relation to each other. Consequently, there was no perfect angle setting. The choice of a working angle promoted the angular sensitivity of some of the sensing materials, to the detriment of others.

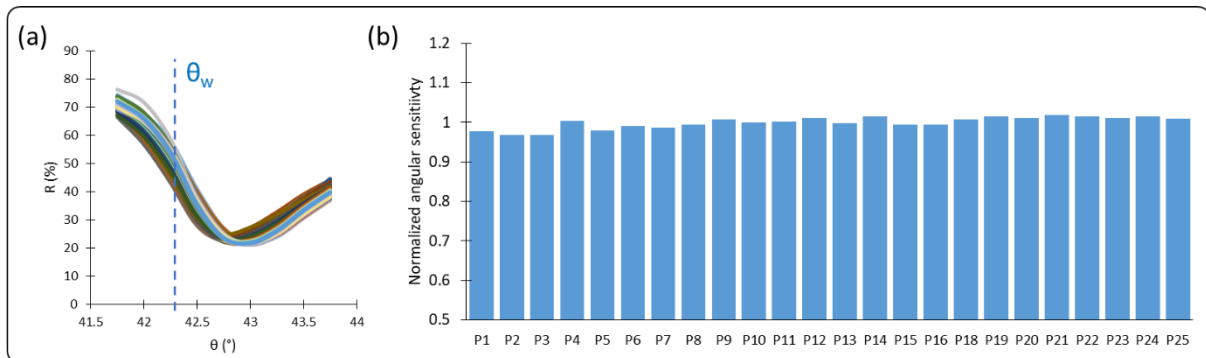


Figure A-1 (a) Plasmon curves for all the sensing materials with the working angle  $\theta_w$ . (b) Normalized angular sensitivity of all the sensing materials.

This calculation enabled to check if the setting was right. We aimed to minimize the variations in angular sensitivity between the sensing materials. However, it works only if we can fix a working angle in the linear region of all the plasmon curves. For this reason, it was unfeasible to mix sensing materials with radically different molecular weight (like proteins and peptides) on the same chip.

## A-2 *In silico* screening of hpDNA

The *in silico* screening procedure of hpDNA was described in details in [325]. It aimed at testing the virtual binding affinities of all possible hairpin DNA with a tetramer, pentamer or hexamer single strand DNA in their loop for fifty different VOCs. Only the four natural bases adenine (A), cytosine (C), guanine (G) and thymine (T) were used. To reduce the calculation time, only the variable part (the loop) was modeled. The VOCs from four chemical classes (14 alcohols, 13 aldehydes, 5 ketones and 18 esters) were selected in order to have different functional groups and carbon chain length.

The entire DNA library was generated using the Hyperchem software. Tools from OpenEye Scientific Software package under academic license, were used for the *in silico* screening procedure. Notably, multi-conformer rigid body docking was carried out using OEDocking [340]. In this model, like with Autodock, the probe and the VOC were considered rigid. The entire DNA molecular surface was included in the active site box defining the area where VOCs were expected to bind. Ten conformers per hpDNA and a maximum of 200 conformers for each of the 50 VOCs were considered. The binding score average for each probe was calculated over all the conformers. The entire process was automated using a bash script.

Since the final aim is the use of these probes in cross-reactive sensors, the hpDNA used in this study were selected taking into account not the absolute “best” binding scores but the minimum cross reactivity. This was done looking at the largest differences among the chemical classes.

The oligonucleotides virtual binding score trend was correlated to the oligonucleotide size for all chemical classes, with values increasing of about 25% from tetramer to hexamer. All oligonucleotides had common trend with best binding scores for alcohols followed by esters, aldehydes and ketones. In all libraries, alcohols affinities were 2 times higher than ketones ones. The minimum-maximum dynamic range for each chemical class was quite narrow for tetramers becoming relevant only for the hexamer DNA library (-3.07 kcal/mol). In all cases, average and median were very close to each other demonstrating a good symmetry in normal distribution.

Tetramer DNA that would become the unpaired loops in hpDNA probed were purchased from Thermo Fischer Scientifics (Italy), while, pentamer and hexamer were purchased from Integrated DNA Technologies (USA). The nine single-stranded DNA loops were then extended and synthesized with the same double helix stem of four base pair DNA (GAAG to 5' end and CTTC to 3' end). The purified oligonucleotides also had a thiol spacer with six carbons (C6) attached to 5' phosphate end of the hpDNA.

Each hpDNA secondary structure was analyzed using the Mfold Web Server (unafold.rna.albany.edu) to check the stem-loop intramolecular base pairing. The Figure A-2 (a) shows the most thermodynamically favorable structures of hpDNA at 25°C, obtained by the Mfold

Web Server. This temperature was the one kept in experimental testing. At this temperature, all selected DNA should have the desired structure in solution. The shape of these sequences was particularly interesting because the loop could act as a “binding pocket” for the VOC molecules. The multiple nucleic acids, well oriented in this structure, could indeed interact simultaneously with a VOC molecule (Figure A-2 (b)).

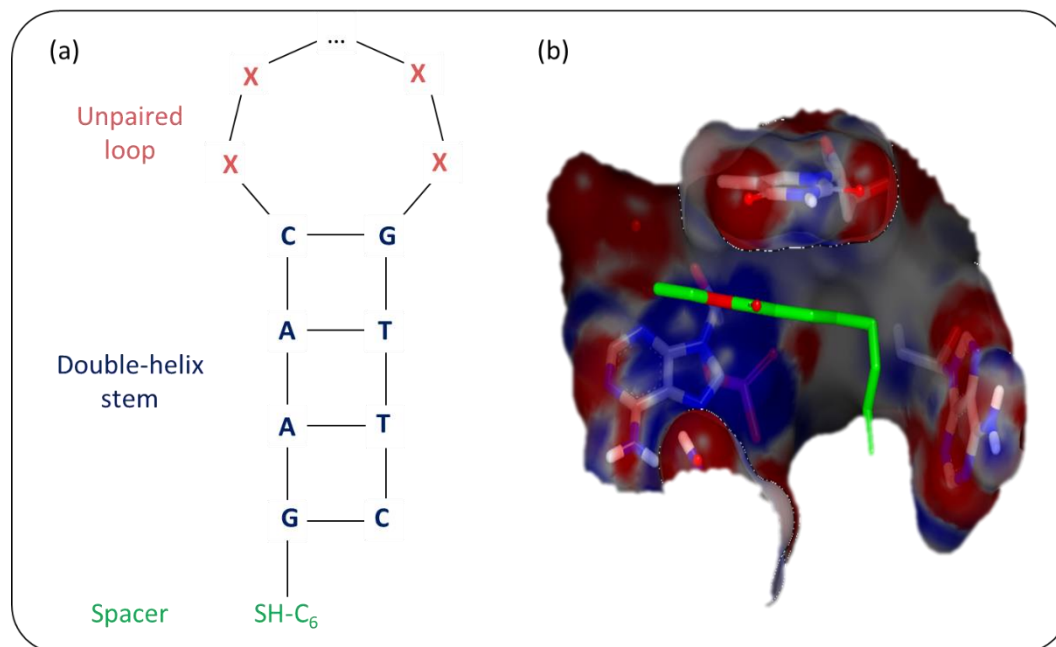


Figure A-2 (a) Typical structure of a hairpin DNA probe at 25°C. (b) Example of docking simulation for octanal and 6hpDNA2. Adapted from [325].

The tetramer loops showed a good affinity towards small aldehydes while the pentamer and hexamer loops demonstrated stronger interaction with alcohols [325].

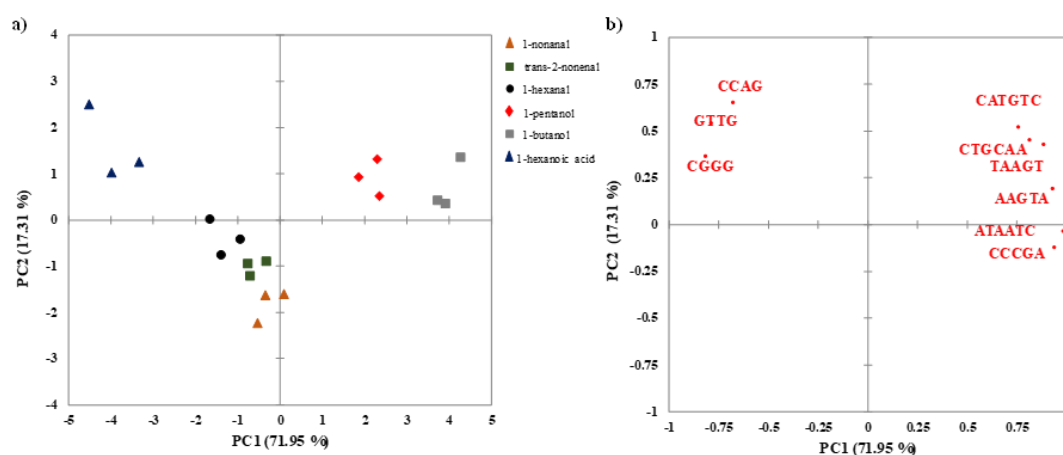


Figure A-3 PCA for the discrimination of different VOCs with different hpDNA. On the left, the individual plot reporting analyzed VOCs. On the right, the variable plot reporting the contribution of the different hpDNA.

For the hpDNA-based optoelectronic nose, a good separation was obtained for the three chemical classes but not among aldehydes. The variable plot was consistent with the simulations: hpDNA with pentamer and hexamer loops had a stronger affinity with alcohols (butanol and

pentanol) and correlated positively with PC1, while tetramer loops had more affinity for aldehydes (hexanal, nonanal and trans-2-nonanal) and correlated negatively with PC1.

These results demonstrated that the optoelectronic nose consisting of either short peptides or hpDNA with different loop size, allowed to discriminate between different chemical classes. The better performance of peptides in classification could be justified by the higher diversity of their physicochemical properties thanks to greater combinations of diverse amino acids as basic brick when compared to DNA, composed of only four bases. In the latter case the selectivity was related to the size of the loop and not to a particular combination of the bases.

Clearly, the performances of the optoelectronic nose was improved with better discrimination capacity for tested VOCs thanks to their complementarity of the response.

## References

1. Ju, S.; Lee, K.Y.; Min, S.J.; Yoo, Y.K.; Hwang, K.S.; Kim, S.K.; Yi, H. Single-carbon discrimination by selected peptides for individual detection of volatile organic compounds. *Sci Rep* **2015**, *5*, 9196, doi:10.1038/srep09196.
2. Gardner, J.W.; Bartlett, P.N. A brief history of electronic noses. *Sens. Actuators B Chem.* **1994**, *18*, 210–211, doi:10.1016/0925-4005(94)87085-3.
3. Council Directive 1999/13/EC of 11 March 1999 on the limitation of emissions of volatile organic compounds due to the use of organic solvents in certain activities and installations; **1999**; Vol. L 085, pp. 0001–0022.
4. Holopainen, J.K.; Blande, J.D. Molecular plant volatile communication. In *Sensing in nature*; Springer, **2012**; pp. 17–31, doi: 10.1007/978-1-4614-1704-0\_2.
5. Schiestl, F.P. The evolution of floral scent and insect chemical communication: Evolution of floral scent. *Ecol. Lett.* **2010**, *13*, 643–656, doi:10.1111/j.1461-0248.2010.01451.x.
6. von Mérey, G.E.; Veyrat, N.; D'Alessandro, M.; Turlings, T.C.J. Herbivore-induced maize leaf volatiles affect attraction and feeding behavior of *Spodoptera littoralis* caterpillars. *Front. Plant Sci.* **2013**, *4*, doi:10.3389/fpls.2013.00209.
7. Amann, A.; Costello, B. de L.; Miekisch, W.; Schubert, J.; Buszewski, B.; Pleil, J.; Ratcliffe, N.; Risby, T. The human volatilome: volatile organic compounds (VOCs) in exhaled breath, skin emanations, urine, feces and saliva. *J. Breath Res.* **2014**, *8*, 034001, doi:10.1088/1752-7155/8/3/034001.
8. Mazzatenta, A.; Di Giulio, C.; Pokorski, M. Pathologies currently identified by exhaled biomarkers. *Respir. Physiol. Neurobiol.* **2013**, *187*, 128–134, doi:10.1016/j.resp.2013.02.016.
9. Sanaeifar, A.; ZakiDizaji, H.; Jafari, A.; Guardia, M. de la Early detection of contamination and defect in foodstuffs by electronic nose: A review. *TrAC Trends Anal. Chem.* **2017**, *97*, 257–271, doi:10.1016/j.trac.2017.09.014.
10. Wojnowski, W.; Dymerski, T.; Gębicki, J.; Namieśnik, J. Electronic Noses in Medical Diagnostics. *Curr. Med. Chem.* **2019**, *26*, 197–215, doi:10.2174/0929867324666171004164636.
11. Eusebio, L.; Capelli, L.; Sironi, S. Electronic Nose Testing Procedure for the Definition of Minimum Performance Requirements for Environmental Odor Monitoring. *Sensors* **2016**, *16*, 1548, doi:10.3390/s16091548.
12. Buck, L.; Axel, R. A novel multigene family may encode odorant receptors: A molecular basis for odor recognition. *Cell* **1991**, *65*, 175–187, doi:10.1016/0092-8674(91)90418-X.
13. Pelosi, P. Perireceptor events in olfaction. *J. Neurobiol.* **1996**, *30*, 3–19, doi:10.1002/(SICI)1097-4695(199605)30:1<3::AID-NEU2>3.0.CO;2-A.
14. Wilson, A.; Baietto, M. Applications and Advances in Electronic-Nose Technologies. *Sensors* **2009**, *9*, 5099–5148, doi:10.3390/s90705099.
15. Li, Z.; Askim, J.R.; Suslick, K.S. The Optoelectronic Nose: Colorimetric and Fluorometric Sensor Arrays. *Chem. Rev.* **2019**, *119*, 231–292, doi:10.1021/acs.chemrev.8b00226.



16. Cuypers, W.; Lieberzeit, P.A. Combining Two Selection Principles: Sensor Arrays Based on Both Biomimetic Recognition and Chemometrics. *Front. Chem.* **2018**, *6*, 268, doi:10.3389/fchem.2018.00268.
17. Cave, J.W.; Wickiser, J.K.; Mitropoulos, A.N. Progress in the development of olfactory-based bioelectronic chemosensors. *Biosens. Bioelectron.* **2019**, *123*, 211–222, doi:10.1016/j.bios.2018.08.063.
18. Wu, C.; Lillehoj, P.B.; Wang, P. Bioanalytical and chemical sensors using living taste, olfactory, and neural cells and tissues: a short review. *The Analyst* **2015**, *140*, 7048–7061, doi:10.1039/C5AN01288K.
19. Bhalla, N.; Jolly, P.; Formisano, N.; Estrela, P. Introduction to biosensors. *Essays Biochem.* **2016**, *60*, 1–8, doi:10.1042/EBC20150001.
20. Jalal, A.H.; Alam, F.; Roychoudhury, S.; Umasankar, Y.; Pala, N.; Bhansali, S. Prospects and Challenges of Volatile Organic Compound Sensors in Human Healthcare. *ACS Sens.* **2018**, *3*, 1246–1263, doi:10.1021/acssensors.8b00400.
21. Malnic, B.; Hirono, J.; Sato, T.; Buck, L.B. Combinatorial Receptor Codes for Odors. *Cell* **1999**, *96*, 713–723, doi:10.1016/S0092-8674(00)80581-4.
22. Niimura, Y.; Matsui, A.; Touhara, K. Extreme expansion of the olfactory receptor gene repertoire in African elephants and evolutionary dynamics of orthologous gene groups in 13 placental mammals. *Genome Res.* **2014**, *24*, 1485–1496, doi:10.1101/gr.169532.113.
23. Araneda, R.C.; Kini, A.D.; Firestein, S. The molecular receptive range of an odorant receptor. *Nat. Neurosci.* **2000**, *3*, 1248–1255, doi:10.1038/81774.
24. Barbosa, A.J.M.; Oliveira, A.R.; Roque, A.C.A. Protein- and Peptide-Based Biosensors in Artificial Olfaction. *Trends Biotechnol.* **2018**, *36*, 1244–1258, doi:10.1016/j.tibtech.2018.07.004.
25. Wasilewski, T.; Gębicki, J.; Kamysz, W. Advances in olfaction-inspired biomaterials applied to bioelectronic noses. *Sens. Actuators B Chem.* **2018**, *257*, 511–537, doi:10.1016/j.snb.2017.10.086.
26. Gralapp, A.K.; Powers, W.J.; Bundy, D.S. Comparison of olfactometry, gas chromatography, and electronic nose technology for measurement of indoor air from swine facilities. *Trans. ASAE* **2001**, *44*, 1283–1290, doi:10.13031/2013.6433.
27. Du, L.; Wu, C.; Liu, Q.; Huang, L.; Wang, P. Recent advances in olfactory receptor-based biosensors. *Biosens. Bioelectron.* **2013**, *42*, 570–580, doi:10.1016/j.bios.2012.09.001.
28. Lee, S.H.; Jin, H.J.; Song, H.S.; Hong, S.; Park, T.H. Bioelectronic nose with high sensitivity and selectivity using chemically functionalized carbon nanotube combined with human olfactory receptor. *J. Biotechnol.* **2012**, *157*, 467–472, doi:10.1016/j.jbiotec.2011.09.011.
29. Sung, J.H.; Ko, H.J.; Park, T.H. Piezoelectric biosensor using olfactory receptor protein expressed in *Escherichia coli*. *Biosens. Bioelectron.* **2006**, *21*, 1981–1986, doi:10.1016/j.bios.2005.10.002.
30. Hou, Y.; Jaffrezic-Renault, N.; Martelet, C.; Zhang, A.; Minic-Vidic, J.; Gorojankina, T.; Persuy, M.-A.; Pajot-Augy, E.; Salesse, R.; Akimov, V.; et al. A novel detection strategy for odorant molecules based on controlled bioengineering of rat olfactory receptor I7. *Biosens Bioelectron* **2007**, *22*, 1550–1555, doi:10.1016/j.bios.2006.06.018.

31. Vidic, J.M.; Grosclaude, J.; Persuy, M.-A.; Aioun, J.; Salesse, R.; Pajot-Augy, E. Quantitative assessment of olfactory receptors activity in immobilized nanosomes: a novel concept for bioelectronic nose. *Lab. Chip* **2006**, *6*, 1026, doi:10.1039/b603189g.
32. Jin, H.J.; Lee, S.H.; Kim, T.H.; Park, J.; Song, H.S.; Park, T.H.; Hong, S. Nanovesicle-based bioelectronic nose platform mimicking human olfactory signal transduction. *Biosens. Bioelectron.* **2012**, *35*, 335–341, doi:10.1016/j.bios.2012.03.012.
33. Lim, J.H.; Park, J.; Oh, E.H.; Ko, H.J.; Hong, S.; Park, T.H. Nanovesicle-Based Bioelectronic Nose for the Diagnosis of Lung Cancer from Human Blood. *Adv. Healthc. Mater.* **2014**, *3*, 360–366, doi:10.1002/adhm.201300174.
34. Khadka, R.; Aydemir, N.; Carraher, C.; Hamiaux, C.; Colbert, D.; Cheema, J.; Malmström, J.; Kralicek, A.; Travas-Sejdic, J. An ultrasensitive electrochemical impedance-based biosensor using insect odorant receptors to detect odorants. *Biosens. Bioelectron.* **2019**, *126*, 207–213, doi:10.1016/j.bios.2018.10.043.
35. Oh, J.; Yang, H.; Jeong, G.E.; Moon, D.; Kwon, O.S.; Phyo, S.; Lee, J.; Song, H.S.; Park, T.H.; Jang, J. Ultrasensitive, Selective, and Highly Stable Bioelectronic Nose That Detects the Liquid and Gaseous Cadaverine. *Anal. Chem.* **2019**, *91*, 12181–12190, doi:10.1021/acs.analchem.9b01068.
36. Goldsmith, B.R.; Mitala, J.J.; Josue, J.; Castro, A.; Lerner, M.B.; Bayburt, T.H.; Khamis, S.M.; Jones, R.A.; Brand, J.G.; Sligar, S.G.; et al. Biomimetic Chemical Sensors Using Nanoelectronic Readout of Olfactory Receptor Proteins. *ACS Nano* **2011**, *5*, 5408–5416, doi:10.1021/nn200489j.
37. Murugathas, T.; Zheng, H.Y.; Colbert, D.; Kralicek, A.V.; Carraher, C.; Plank, N.O.V. Biosensing with Insect Odorant Receptor Nanodiscs and Carbon Nanotube Field-Effect Transistors. *ACS Appl. Mater. Interfaces* **2019**, *11*, 9530–9538, doi:10.1021/acsami.8b19433.
38. Song, H.S.; Lee, S.H.; Oh, E.H.; Park, T.H. Expression, Solubilization and Purification of a Human Olfactory Receptor from Escherichia coli. *Curr. Microbiol.* **2009**, *59*, 309–314, doi:10.1007/s00284-009-9435-6.
39. Michalke, K.; Gravière, M.-E.; Huyghe, C.; Vincentelli, R.; Wagner, R.; Pattus, F.; Schroeder, K.; Oschmann, J.; Rudolph, R.; Cambillau, C.; et al. Mammalian G-protein-coupled receptor expression in Escherichia coli: I. High-throughput large-scale production as inclusion bodies. *Anal. Biochem.* **2009**, *386*, 147–155, doi:10.1016/j.ab.2008.12.016.
40. Michalke, K.; Huyghe, C.; Lichière, J.; Gravière, M.-E.; Siponen, M.; Sciara, G.; Lepaul, I.; Wagner, R.; Magg, C.; Rudolph, R.; et al. Mammalian G protein-coupled receptor expression in Escherichia coli: II. Refolding and biophysical characterization of mouse cannabinoid receptor 1 and human parathyroid hormone receptor 1. *Anal. Biochem.* **2010**, *401*, 74–80, doi:10.1016/j.ab.2010.02.017.
41. Hamana, H.; Shou-xin, L.; Breuils, L.; Hirono, J.; Sato, T. Heterologous functional expression system for odorant receptors. *J. Neurosci. Methods* **2010**, *185*, 213–220, doi:10.1016/j.jneumeth.2009.09.024.
42. Kaiser, L.; Graveland-Bikker, J.; Steuerwald, D.; Vanberghem, M.; Herlihy, K.; Zhang, S. Efficient cell-free production of olfactory receptors: Detergent optimization, structure, and ligand binding analyses. *Proc. Natl. Acad. Sci.* **2008**, *105*, 15726–15731, doi:10.1073/pnas.0804766105.

43. Chen, F.; Wang, J.; Du, L.; Zhang, X.; Zhang, F.; Chen, W.; Cai, W.; Wu, C.; Wang, P. Functional expression of olfactory receptors using cell-free expression system for biomimetic sensors towards odorant detection. *Biosens. Bioelectron.* **2019**, *130*, 382–388, doi:10.1016/j.bios.2018.09.032.
44. Di Pietrantonio, F.; Cannatà, D.; Benetti, M.; Verona, E.; Varriale, A.; Staiano, M.; D'Auria, S. Detection of odorant molecules via surface acoustic wave biosensor array based on odorant-binding proteins. *Biosens. Bioelectron.* **2013**, *41*, 328–334, doi:10.1016/j.bios.2012.08.046.
45. Arakawa, T.; Suzuki, T.; Tsujii, M.; Iitani, K.; Chien, P.-J.; Ye, M.; Toma, K.; Iwasaki, Y.; Mitsubayashi, K. Real-time monitoring of skin ethanol gas by a high-sensitivity gas phase biosensor (bio-sniffer) for the non-invasive evaluation of volatile blood compounds. *Biosens. Bioelectron.* **2019**, *129*, 245–253, doi:10.1016/j.bios.2018.09.070.
46. Heydel, J.-M.; Coelho, A.; Thiebaud, N.; Legendre, A.; Bon, A.-M.L.; Faure, P.; Neiers, F.; Artur, Y.; Golebiowski, J.; Briand, L. Odorant-Binding Proteins and Xenobiotic Metabolizing Enzymes: Implications in Olfactory Perireceptor Events. *Anat. Rec.* **2013**, *296*, 1333–1345, doi:10.1002/ar.22735.
47. Pelosi, P.; Mastrogiacomo, R.; Iovinella, I.; Tuccori, E.; Persaud, K.C. Structure and biotechnological applications of odorant-binding proteins. *Appl. Microbiol. Biotechnol.* **2014**, *98*, 61–70, doi:10.1007/s00253-013-5383-y.
48. Pelosi, P.; Zhu, J.; Knoll, W. Odorant-Binding Proteins as Sensing Elements for Odour Monitoring. *Sens. Basel* **2018**, *18*, doi:Artn 3248 10.3390/S18103248.
49. Hurot, C.; Brenet, S.; Buhot, A.; Barou, E.; Belloir, C.; Briand, L.; Hou, Y. Highly sensitive olfactory biosensors for the detection of volatile organic compounds by surface plasmon resonance imaging. *Biosens. Bioelectron.* **2019**, *123*, 230–236, doi:10.1016/j.bios.2018.08.072.
50. Brito, N.F.; Moreira, M.F.; Melo, A.C.A. A look inside odorant-binding proteins in insect chemoreception. *J. Insect Physiol.* **2016**, *95*, 51–65, doi:10.1016/j.jinsphys.2016.09.008.
51. Hou, Y.; Jaffrezic-Renault, N.; Martelet, C.; Tlili, C.; Zhang, A.; Pernollet, J.-C.; Briand, L.; Gomila, G.; Errachid, A.; Samitier, J.; et al. Study of Langmuir and Langmuir–Blodgett Films of Odorant-Binding Protein/Amphiphile for Odorant Biosensors. *Langmuir* **2005**, *21*, 4058–4065, doi:10.1021/la0471801.
52. Cannata, D.; Benetti, M.; Verona, E.; Varriale, A.; Staiano, M.; D'Auria, S.; Di Pietrantonio, F. Odorant detection via Solidly Mounted Resonator biosensor. In *Proceedings of the 2012 IEEE International Ultrasonics Symposium*; IEEE: Dresden, Germany, **2012**; pp. 1537–1540, doi: 10.1109/ULTSYM.2012.0384.
53. Hurot, C.; Buhot, A.; Barou, E.; Belloir, C.; Briand, L.; Hou, Y. Odorant-binding protein-based optoelectronic tongue and nose for sensing volatile organic compounds. In *Proceedings of the 2019 IEEE International Symposium on Olfaction and Electronic Nose (ISOEN)*; IEEE: Fukuoka, Japan, **2019**; pp. 1–4, doi: 10.1109/ISOEN.2019.8823179.
54. Gao, A.; Wang, Y.; Zhang, D.; He, Y.; Zhang, L.; Liu, Y.; Wang, Y.; Song, H.; Li, T. Highly sensitive and selective detection of human-derived volatile organic compounds based on odorant binding proteins functionalized silicon nanowire array. *Sens. Actuators B Chem.* **2020**, *309*, 127762, doi:10.1016/j.snb.2020.127762.

55. Di Pietrantonio, F.; Benetti, M.; Cannatà, D.; Verona, E.; Palla-Papavlu, A.; Fernández-Pradas, J.M.; Serra, P.; Staiano, M.; Varriale, A.; D'Auria, S. A surface acoustic wave bio-electronic nose for detection of volatile odorant molecules. *Biosens. Bioelectron.* **2015**, *67*, 516–523, doi:10.1016/j.bios.2014.09.027.
56. Busch, J.L.H.C.; Hrnčirik, K.; Bulukin, E.; Boucon, C.; Mascini, M. Biosensor Measurements of Polar Phenolics for the Assessment of the Bitterness and Pungency of Virgin Olive Oil. *J. Agric. Food Chem.* **2006**, *54*, 4371–4377, doi:10.1021/jf060103m.
57. Pauliukaite, R.; Zhylyak, G.; Citterio, D.; Spichiger-Keller, U.E. l-Glutamate biosensor for estimation of the taste of tomato specimens. *Anal. Bioanal. Chem.* **2006**, *386*, 220–227, doi:10.1007/s00216-006-0656-2.
58. Tønning, E.; Sapelnikova, S.; Christensen, J.; Carlsson, C.; Winther-Nielsen, M.; Dock, E.; Solna, R.; Skladal, P.; Nørgaard, L.; Ruzgas, T.; et al. Chemometric exploration of an amperometric biosensor array for fast determination of wastewater quality. *Biosens. Bioelectron.* **2005**, *21*, 608–617, doi:10.1016/j.bios.2004.12.023.
59. Pavan, S.; Berti, F. Short peptides as biosensor transducers. *Anal. Bioanal. Chem.* **2012**, *402*, 3055–3070, doi:10.1007/s00216-011-5589-8.
60. Ramírez, D. Computational Methods Applied to Rational Drug Design. *Open Med. Chem. J.* **2016**, *10*, 7–20, doi:10.2174/1874104501610010007.
61. Wu, T.-Z.; Lo, Y.-R. Synthetic peptide mimicking of binding sites on olfactory receptor protein for use in 'electronic nose.' *J. Biotechnol.* **2000**, *80*, 63–73, doi:10.1016/S0168-1656(00)00228-5.
62. Wu, T.-Z.; Lo, Y.-R.; Chan, E.-C. Exploring the recognized bio-mimicry materials for gas sensing. *Biosens. Bioelectron.* **2001**, *16*, 945–953, doi: 10.1016/S0956-5663(01)00215-9.
63. Lin, Y.-J.; Guo, H.-R.; Chang, Y.-H.; Kao, M.-T.; Wang, H.-H.; Hong, R.-I. Application of the electronic nose for uremia diagnosis. *Sens. Actuators B Chem.* **2001**, *76*, 177–180, doi:10.1016/S0925-4005(01)00625-6.
64. Sankaran, S.; Panigrahi, S.; Mallik, S. Olfactory receptor based piezoelectric biosensors for detection of alcohols related to food safety applications. *Sens. Actuators B Chem.* **2011**, *155*, 8–18, doi:10.1016/j.snb.2010.08.003.
65. Panigrahi, S.; Sankaran, S.; Mallik, S.; Gaddam, B.; Hanson, A.A. Olfactory receptor-based polypeptide sensor for acetic acid VOC detection. *Mater. Sci. Eng. C* **2012**, *32*, 1307–1313, doi:10.1016/j.msec.2011.11.003.
66. Kruse, S.W.; Zhao, R.; Smith, D.P.; Jones, D.N.M. Structure of a specific alcohol-binding site defined by the odorant binding protein LUSH from *Drosophila melanogaster*. *Nat. Struct. Mol. Biol.* **2003**, *10*, 694–700, doi:10.1038/nsb960.
67. Sankaran, S.; Panigrahi, S.; Mallik, S. Odorant binding protein based biomimetic sensors for detection of alcohols associated with *Salmonella* contamination in packaged beef. *Biosens. Bioelectron.* **2011**, *26*, 3103–3109, doi:10.1016/j.msec.2011.11.003.
68. Son, M.; Kim, D.; Kang, J.; Lim, J.H.; Lee, S.H.; Ko, H.J.; Hong, S.; Park, T.H. Bioelectronic nose using odorant binding protein-derived peptide and carbon nanotube field-effect transistor for the assessment of salmonella contamination of food. *Anal. Chem.* **2016**, *88*, 11283–11287, doi: 10.1021/acs.analchem.6b03284.

69. Wasilewski, T.; Szulczyński, B.; Wojciechowski, M.; Kamysz, W.; Gębicki, J. A Highly Selective Biosensor Based on Peptide Directly Derived from the HarmOBP7 Aldehyde Binding Site. *Sensors* **2019**, *19*, 4284, doi:10.3390/s19194284.
70. Okochi, M.; Muto, M.; Yanai, K.; Tanaka, M.; Onodera, T.; Wang, J.; Ueda, H.; Toko, K. Array-Based Rational Design of Short Peptide Probe-Derived from an Anti-TNT Monoclonal Antibody. *ACS Comb. Sci.* **2017**, *19*, 625–632, doi:10.1021/acscombsci.7b00035.
71. Yuan, S.; Dahoun, T.; Brugarolas, M.; Pick, H.; Filipek, S.; Vogel, H. Computational modeling of the olfactory receptor Olfr73 suggests a molecular basis for low potency of olfactory receptor-activating compounds. *Commun. Biol.* **2019**, *2*, 141, doi:10.1038/s42003-019-0384-8.
72. Blanco, M.; McAlpine, M.C.; Heath, J.R. First Principles Molecular Modeling of Sensing Material Selection for Hybrid Biomimetic Nanosensors. In *Computational Methods for Sensor Material Selection*; Ryan, M.A., Shevade, A.V., Taylor, C.J., Homer, M.L., Blanco, M., Stetter, J.R., Eds.; Springer US: New York, NY, **2010**; pp. 135–148, doi:10.1007/978-0-387-73715-7\_6.
73. Pizzoni, D.; Mascini, M.; Lanzone, V.; Del Carlo, M.; Di Natale, C.; Compagnone, D. Selection of peptide ligands for piezoelectric peptide based gas sensors arrays using a virtual screening approach. *Biosens. Bioelectron.* **2014**, *52*, 247–254, doi:10.1016/j.bios.2013.08.044.
74. Esfandiari, A.; Kybert, N.J.; Dattoli, E.N.; Hee Han, G.; Lerner, M.B.; Akhavan, O.; Irajizad, A.; Charlie Johnson, A.T. DNA-decorated graphene nanomesh for detection of chemical vapors. *Appl. Phys. Lett.* **2013**, *103*, 183110, doi:10.1063/1.4827811.
75. Kybert, N.J.; Lerner, M.B.; Yodh, J.S.; Preti, G.; Johnson, A.T.C. Differentiation of Complex Vapor Mixtures Using Versatile DNA–Carbon Nanotube Chemical Sensor Arrays. *ACS Nano* **2013**, *7*, 2800–2807, doi:10.1021/nn400359c.
76. Kybert, N.J.; Han, G.H.; Lerner, M.B.; Dattoli, E.N.; Esfandiari, A.; Charlie Johnson, A.T. Scalable arrays of chemical vapor sensors based on DNA-decorated graphene. *Nano Res.* **2014**, *7*, 95–103, doi:10.1007/s12274-013-0376-9.
77. Fu, K.; Willis, B.G. Characterization of DNA as a solid-state sorptive vapor sensing material. *Sens. Actuators B Chem.* **2015**, *220*, 1023–1032, doi:10.1016/j.snb.2015.05.132.
78. Mascini, M.; Gaggiotti, S.; Della Pelle, F.; Wang, J.; Pingarrón, J.M.; Compagnone, D. Hairpin DNA-AuNPs as molecular binding elements for the detection of volatile organic compounds. *Biosens. Bioelectron.* **2019**, *123*, 124–130, doi:https://doi.org/10.1016/j.bios.2018.07.028.
79. Gaggiotti, S.; Mascini, M.; Pittia, P.; Della Pelle, F.; Compagnone, D. Headspace Volatile Evaluation of Carrot Samples—Comparison of GC/MS and AuNPs-hpDNA-Based E-Nose. *Foods* **2019**, *8*, 293, doi:10.3390/foods8080293.
80. Smith, G.P. Phage Display: Simple Evolution in a Petri Dish (Nobel Lecture). *Angew. Chem. Int. Ed.* **2019**, doi:10.1002/anie.201908308.
81. Galán, A.; Comor, L.; Horvatić, A.; Kuleš, J.; Guillemin, N.; Mrljak, V.; Bhide, M. Library-based display technologies: where do we stand? *Mol. Biosyst.* **2016**, *12*, 2342–2358, doi:10.1039/C6MB00219F.
82. Rodi, D.J.; Makowski, L. Phage-display technology – finding a needle in a vast molecular haystack. *Curr. Opin. Biotechnol.* **1999**, *10*, 87–93, doi:10.1016/S0958-1669(99)80016-0.

83. Tan, Y.; Tian, T.; Liu, W.; Zhu, Z.; J. Yang, C. Advance in phage display technology for bioanalysis. *Biotechnol. J.* **2016**, *11*, 732–745, doi:10.1002/biot.201500458.
84. Goldman, E.R.; Pazirandeh, M.P.; Charles, P.T.; Balighian, E.D.; Anderson, G.P. Selection of phage displayed peptides for the detection of 2,4,6-trinitrotoluene in seawater. *Anal. Chim. Acta* **2002**, *457*, 13–19, doi:10.1016/S0003-2670(01)01246-6.
85. Jaworski, J.W.; Raorane, D.; Huh, J.H.; Majumdar, A.; Lee, S.-W. Evolutionary Screening of Biomimetic Coatings for Selective Detection of Explosives. *Langmuir* **2008**, *24*, 4938–4943, doi:10.1021/la7035289.
86. Jang, H.J.; Na, J.H.; Jin, B.S.; Lee, W.K.; Lee, W.H.; Jung, H.J.; Kim, S.C.; Lim, S.H.; Yu, Y.G. Identification of dinitrotoluene selective peptides by phage display cloning. *Bull. Korean Chem. Soc.* **2010**, *31*, 3703–3706, doi:10.5012/bkcs.2010.31.12.3703.
87. Kubas, G.; Rees, W.; Caguiat, J.; Asch, D.; Fagan, D.; Cortes, P. Identification of peptide sequences that selectively bind to pentaerythritol trinitrate hemisuccinate—a surrogate of PETN, via phage display technology. *Pept. Sci.* **2017**, *108*, e22997, doi:10.1002/bip.22997.
88. Liu, Z.; Liu, J.; Wang, K.; Li, W.; Shelver, W.L.; Li, Q.X.; Li, J.; Xu, T. Selection of phage-displayed peptides for the detection of imidacloprid in water and soil. *Anal. Biochem.* **2015**, *485*, 28–33, doi:10.1016/j.ab.2015.05.014.
89. Ding, X.; Yang, K.-L. Development of an Oligopeptide Functionalized Surface Plasmon Resonance Biosensor for Online Detection of Glyphosate. *Anal. Chem.* **2013**, *85*, 5727–5733, doi:10.1021/ac400273g.
90. Sawada, T.; Okeya, Y.; Hashizume, M.; Serizawa, T. Screening of peptides recognizing simple polycyclic aromatic hydrocarbons. *Chem. Commun.* **2013**, *49*, 5088, doi:10.1039/c3cc38907c.
91. Ju, S.; Lee, K.Y.; Min, S.J.; Yoo, Y.K.; Hwang, K.S.; Kim, S.K.; Yi, H. Single-carbon discrimination by selected peptides for individual detection of volatile organic compounds. *Sci Rep* **2015**, *5*, 9196, doi:10.1038/srep09196.
92. Fukunaga, K.; Taki, M. Practical Tips for Construction of Custom Peptide Libraries and Affinity Selection by Using Commercially Available Phage Display Cloning Systems. *J. Nucleic Acids* **2012**, *2012*, 9, doi:10.1155/2012/295719.
93. Knez, K.; Noppe, W.; Geukens, N.; Janssen, K.P.F.; Spasic, D.; Heyligen, J.; Vriens, K.; Thevissen, K.; Cammue, B.P.A.; Petrenko, V.; et al. Affinity Comparison of p3 and p8 Peptide Displaying Bacteriophages Using Surface Plasmon Resonance. *Anal. Chem.* **2013**, *85*, 10075–10082, doi:10.1021/ac402192k.
94. Tanaka, M.; Minamide, T.; Takahashi, Y.; Hanai, Y.; Yanagida, T.; Okochi, M. Peptide Screening from a Phage Display Library for Benzaldehyde Recognition. *Chem. Lett.* **2019**, *48*, 978–981, doi:10.1246/cl.190318.
95. Watt, P.M.; Milech, N.; Stone, S.R. Structure-diverse Phylomer libraries as a rich source of bioactive hits from phenotypic and target directed screens against intracellular proteins. *Curr. Opin. Chem. Biol.* **2017**, *38*, 127–133, doi:10.1016/j.cbpa.2017.03.016.
96. Nakamura, C.; Inuyama, Y.; Goto, H.; Obataya, I.; Kaneko, N.; Nakamura, N.; Santo, N.; Miyake, J. Dioxin-Binding Pentapeptide for Use in a High-Sensitivity On-Bead Detection Assay. *Anal. Chem.* **2005**, *77*, 7750–7757, doi:10.1021/ac051151t.

97. Ilgu, M.; Nilsen-Hamilton, M. Aptamers in analytics. *The Analyst* **2016**, *141*, 1551–1568, doi:10.1039/C5AN01824B.
98. Tuerk, C.; Gold, L. Systematic evolution of ligands by exponential enrichment: RNA ligands to bacteriophage T4 DNA polymerase. *Science* **1990**, *249*, 505–510, doi:10.1126/science.2200121.
99. Stoltenburg, R.; Nikolaus, N.; Strehlitz, B. Capture-SELEX: Selection of DNA Aptamers for Aminoglycoside Antibiotics. *J. Anal. Methods Chem.* **2012**, *2012*, 1–14, doi:10.1155/2012/415697.
100. Komarova, N.; Andrianova, M.; Glukhov, S.; Kuznetsov, A. Selection, Characterization, and Application of ssDNA Aptamer against Furaneol. *Molecules* **2018**, *23*, 3159, doi:10.3390/molecules23123159.
101. Kuznetsov, A.E.; Komarova, N.V.; Kuznetsov, E.V.; Andrianova, M.S.; Grudtsov, V.P.; Rybachek, E.N.; Puchnin, K.V.; Ryazantsev, D.V.; Saurov, A.N. Integration of a field effect transistor-based aptasensor under a hydrophobic membrane for bioelectronic nose applications. *Biosens. Bioelectron.* **2019**, *129*, 29–35, doi:10.1016/j.bios.2019.01.013.
102. Goode, J.A.; Rushworth, J.V.H.; Millner, P.A. Biosensor Regeneration: A Review of Common Techniques and Outcomes. *Langmuir* **2015**, *31*, 6267–6276, doi:10.1021/la503533g.
103. Giebel, L.B.; Cass, R.T.; Milligan, D.L.; Young, D.C.; Arze, R.; Johnson, C.R. Screening of Cyclic Peptide Phage Libraries Identifies Ligands That Bind Streptavidin with High Affinities. *Biochemistry* **1995**, *34*, 15430–15435, doi:10.1021/Bi00047a006.
104. Deyle, K.; Kong, X.-D.; Heinis, C. Phage Selection of Cyclic Peptides for Application in Research and Drug Development. *Acc. Chem. Res.* **2017**, *50*, 1866–1874, doi:10.1021/acs.accounts.7b00184.
105. Liu, W.; Wu, C. A mini-review and perspective on multicyclic peptide mimics of antibodies. *Chin. Chem. Lett.* **2018**, *29*, 1063–1066, doi:10.1016/j.ccllet.2018.03.015.
106. Kim, S.; Kim, D.; Jung, H.H.; Lee, I.-H.; Kim, J.I.; Suh, J.-Y.; Jon, S. Bio-Inspired Design and Potential Biomedical Applications of a Novel Class of High-Affinity Peptides. *Angew. Chem. Int. Ed.* **2012**, *51*, 1890–1894, doi:10.1002/anie.201107894.
107. Sankaran, S.; Khot, L.R.; Panigrahi, S. Biology and applications of olfactory sensing system: A review. *Sens. Actuators B Chem.* **2012**, *171–172*, 1–17, doi:10.1016/j.snb.2012.03.029.
108. Kotlowski, C.; Larisika, M.; Guerin, P.M.; Kleber, C.; Kröber, T.; Mastrogiacomo, R.; Nowak, C.; Pelosi, P.; Schütz, S.; Schwaighofer, A.; et al. Fine discrimination of volatile compounds by graphene-immobilized odorant-binding proteins. *Sens. Actuators B Chem.* **2018**, *256*, 564–572, doi:10.1016/j.snb.2017.10.093.
109. Hou, Y.; Genua, M.; Tada Batista, D.; Calemczuk, R.; Buhot, A.; Fornarelli, P.; Koubachi, J.; Bonnaffé, D.; Saesen, E.; Laguri, C.; et al. Continuous Evolution Profiles for Electronic-Tongue-Based Analysis. *Angew. Chem.* **2012**, *124*, 10540–10544, doi:10.1002/ange.201205346.
110. Hou, Y.; Genua, M.; Garcon, L.A.; Buhot, A.; Calemczuk, R.; Bonnaffe, D.; Lortat-Jacob, H.; Livache, T. Electronic tongue generating continuous recognition patterns for protein analysis. *J Vis Exp* **2014**, 51901, doi:10.3791/51901.

111. Genua, M.; Garçon, L.-A.; Mounier, V.; Wehry, H.; Buhot, A.; Billon, M.; Calemczuk, R.; Bonnaffé, D.; Hou, Y.; Livache, T. SPR imaging based electronic tongue via landscape images for complex mixture analysis. *Talanta* **2014**, *130*, 49–54, doi:10.1016/j.talanta.2014.06.038.
112. Garçon, L.-A.; Hou, Y.; Genua, M.; Buhot, A.; Calemczuk, R.; Bonnaffé, D.; Hou, Y.; Livache, T. Landscapes of Taste by a Novel Electronic Tongue for the Analysis of Complex Mixtures. *Sens. Lett.* **2014**, *12*, 1059–1064, doi:10.1166/sl.2014.3164.
113. Doty, R.L. Olfaction. *Annu. Rev. Psychol.* **2001**, *52*, 423–452, doi:10.1146/annurev.psych.52.1.423.
114. Compagnone, D.; Fusella, G.C.; Del Carlo, M.; Pittia, P.; Martinelli, E.; Tortora, L.; Paolesse, R.; Di Natale, C. Gold nanoparticles-peptide based gas sensor arrays for the detection of foodaromas. *Biosens. Bioelectron.* **2013**, *42*, 618–625, doi:10.1016/j.bios.2012.10.096.
115. Mascini, M.; Gaggiotti, S.; Della Pelle, F.; Di Natale, C.; Qakala, S.; Iwuoha, E.; Pittia, P.; Compagnone, D. Peptide Modified ZnO Nanoparticles as Gas Sensors Array for Volatile Organic Compounds (VOCs). *Front. Chem.* **2018**, *6*, 105, doi:10.3389/fchem.2018.00105.
116. Zine, N.; Pajot, E.; Persuy, M.A.; Korri-Youssoufi, H.; Chebil, S.; Errachid, A.; Jaffrezic-Renault, N. Amplification of the Electrochemical Signal of an Olfactory Receptor Based Biosensor by in Situ Generated Gold Nanoparticles. *Procedia Eng.* **2011**, *25*, 920–923, doi:10.1016/j.proeng.2011.12.226.
117. Kaissling, K.-E. The Sensitivity of the Insect Nose: The Example of *Bombyx Mori*. In *Biologically Inspired Signal Processing for Chemical Sensing*; Gutiérrez, A., Marco, S., Eds.; Springer Berlin Heidelberg: Berlin, Heidelberg, **2009**; Vol. 188, pp. 45–52, doi: 10.1007/978-3-642-00176-5\_3.
118. Wang, Q.; Shang, Y.; Hilton, D.S.; Inthavong, K.; Zhang, D.; Elgar, M.A. Antennal scales improve signal detection efficiency in moths. *Proc. R. Soc. B Biol. Sci.* **2018**, *285*, 20172832, doi:10.1098/rspb.2017.2832.
119. Spencer, T.L.; Lavrik, N.; Hu, D.L. Synthetic moth antennae fabricated as preconcentrator for odor collection. In *Proceedings of the 2017 ISOCS/IEEE International Symposium on Olfaction and Electronic Nose (ISOEN)*; IEEE: Montreal, QC, Canada, **2017**; pp. 1–3, doi: 10.1109/ISOEN.2017.7968911.
120. Jaffar-Bandjee, M.; Casas, J.; Krijnen, G. Additive manufacturing: state of the art and potential for insect science. *Curr. Opin. Insect Sci.* **2018**, *30*, 79–85, doi:10.1016/j.cois.2018.09.011.
121. Gray, B.P.; Li, S.; Brown, K.C. From Phage Display to Nanoparticle Delivery: Functionalizing Liposomes with Multivalent Peptides Improves Targeting to a Cancer Biomarker. *Bioconjug. Chem.* **2013**, *24*, 85–96, doi:10.1021/bc300498d.
122. Larisika, M.; Kotlowski, C.; Steininger, C.; Mastrogiacomo, R.; Pelosi, P.; Schütz, S.; Peteu, S.F.; Kleber, C.; Reiner-Rozman, C.; Nowak, C.; et al. Electronic olfactory sensor based on *A. mellifera* odorant-binding protein 14 on a reduced graphene oxide field-effect transistor. *Angew Chem* **2015**, *127*, 13443–13446, doi:10.1002/anie.201505712.
123. Mammen, M.; Choi, S.-K.; Whitesides, G.M. Polyvalent Interactions in Biological Systems: Implications for Design and Use of Multivalent Ligands and Inhibitors. *Angew. Chem. Int. Ed.* **1998**, *37*, 2754–2794, doi:10.1002/(SICI)1521-3773(19981102)37:20<2754::AID-ANIE2754>3.0.CO;2-3.



124. Mani, V.; Wasalathanthri, D.P.; Joshi, A.A.; Kumar, C.V.; Rusling, J.F. Highly Efficient Binding of Paramagnetic Beads Bioconjugated with 100 000 or More Antibodies to Protein-Coated Surfaces. *Anal. Chem.* **2012**, *84*, 10485–10491, doi:10.1021/ac3028257.
125. Helms, B.A.; Reulen, S.W.A.; Nijhuis, S.; Graaf-Heuvelmans, P.T.H.M. de; Merckx, M.; Meijer, E.W. High-Affinity Peptide-Based Collagen Targeting Using Synthetic Phage Mimics: From Phage Display to Dendrimer Display. *J. Am. Chem. Soc.* **2009**, *131*, 11683–11685, doi:10.1021/ja902285m.
126. Manai, R.; Scorsone, E.; Rousseau, L.; Ghassemi, F.; Possas Abreu, M.; Lissorgues, G.; Tremillon, N.; Ginisty, H.; Arnault, J.C.; Tuccori, E.; et al. Grafting odorant binding proteins on diamond bio-MEMS. *Biosens. Bioelectron.* **2014**, *60*, 311–317, doi:10.1016/j.bios.2014.04.020.
127. Zhang, D.; Lu, Y.; Zhang, Q.; Yao, Y.; Li, S.; Li, H.; Zhuang, S.; Jiang, J.; Liu, G.L.; Liu, Q. Nanoplasmonic monitoring of odorants binding to olfactory proteins from honeybee as biosensor for chemical detection. *Sens. Actuators B Chem.* **2015**, *221*, 341–349, doi:10.1016/j.snb.2015.06.091.
128. Du, L.; Wu, C.; Peng, H.; Zou, L.; Zhao, L.; Huang, L.; Wang, P. Piezoelectric olfactory receptor biosensor prepared by aptamer-assisted immobilization. *Sens. Actuators B Chem.* **2013**, *187*, 481–487, doi:10.1016/j.snb.2013.02.009.
129. Kuang, Z.; Kim, S.N.; Crookes-Goodson, W.J.; Farmer, B.L.; Naik, R.R. Biomimetic Chemosensor: Designing Peptide Recognition Elements for Surface Functionalization of Carbon Nanotube Field Effect Transistors. *ACS Nano* **2010**, *4*, 452–458, doi:10.1021/nn901365g.
130. Staymates, M.E.; MacCrehan, W.A.; Staymates, J.L.; Kunz, R.R.; Mendum, T.; Ong, T.-H.; Geurtsen, G.; Gillen, G.J.; Craven, B.A. Biomimetic Sniffing Improves the Detection Performance of a 3D Printed Nose of a Dog and a Commercial Trace Vapor Detector. *Sci. Rep.* **2016**, *6*, 36876, doi:10.1038/srep36876.
131. Warden, A.C.; Trowell, S.C.; Gel, M. A Miniature Gas Sampling Interface with Open Microfluidic Channels: Characterization of Gas-to-Liquid Extraction Efficiency of Volatile Organic Compounds. *Micromachines* **2019**, *10*, 486, doi:10.3390/mi10070486.
132. Che Harun, F.K.; Taylor, J.E.; Covington, J.A.; Gardner, J.W. An electronic nose employing dual-channel odour separation columns with large chemosensor arrays for advanced odour discrimination. *Sens. Actuators B Chem.* **2009**, *141*, 134–140, doi:10.1016/j.snb.2009.05.036.
133. Burlachenko, J.; Kruglenko, I.; Snopok, B.; Persaud, K. Sample handling for electronic nose technology: State of the art and future trends. *TrAC Trends Anal. Chem.* **2016**, *82*, 222–236, doi:10.1016/j.trac.2016.06.007.
134. Elad, D.; Liebenthal, R.; Wenig, B.L.; Einav, S. Analysis of air flow patterns in the human nose. *Med. Biol. Eng. Comput.* **1993**, *31*, 585–592, doi:10.1007/BF02441806.
135. Craven, B.A.; Paterson, E.G.; Settles, G.S. The fluid dynamics of canine olfaction: Unique nasal airflow patterns as an explanation of macrosmia. *J. R. Soc. Interface* **2010**, *7*, 933–943, doi:10.1098/rsif.2009.0490.
136. Stitzel, S.E.; Stein, D.R.; Walt, D.R. Enhancing Vapor Sensor Discrimination by Mimicking a Canine Nasal Cavity Flow Environment. *J. Am. Chem. Soc.* **2003**, *125*, 3684–3685, doi:10.1021/ja028239y.

137. Chang, Z.; Sun, Y.; Zhang, Y.; Gao, Y.; Weng, X.; Chen, D.; David, L.; Xie, J. Bionic Optimization Design of Electronic Nose Chamber for Oil and Gas Detection. *J. Bionic Eng.* **2018**, *15*, 533–544, doi:10.1007/s42235-018-0044-6.
138. Scott, S.M.; James, D.; Ali, Z.; O'Hare, W.T. Optimising of the sensing chamber of an array of a volatile detection system. *J. Therm. Anal. Calorim.* **2004**, *76*, 693–708, doi:10.1023/B:JTAN.0000034891.68585.4a.
139. Di Francesco, F.; Falcitelli, M.; Marano, L.; Pioggia, G. A radially symmetric measurement chamber for electronic noses. *Sens. Actuators B Chem.* **2005**, *105*, 295–303, doi:10.1016/j.snb.2004.06.013.
140. El Barbri, N.; Duran, C.; Brezmes, J.; Cañellas, N.; Ramírez, J.; Bouchikhi, B.; Llobet, E. Selectivity Enhancement in Multisensor Systems Using Flow Modulation Techniques. *Sensors* **2008**, *8*, 7369–7379, doi:10.3390/s8117369.
141. Wang, Y.; Xing, J.; Qian, S. Selectivity Enhancement in Electronic Nose Based on an Optimized DQN. *Sensors* **2017**, *17*, 2356, doi:10.3390/s17102356.
142. Ziyatdinov, A.; Fonollosa, J.; Fernández, L.; Gutierrez-Gálvez, A.; Marco, S.; Perera, A. Bioinspired early detection through gas flow modulation in chemo-sensory systems. *Sens. Actuators B Chem.* **2015**, *206*, 538–547, doi:10.1016/j.snb.2014.09.001.
143. Hui Kim, S.; Kyoung Yoo, Y.; Chae, M.S.; Yoon Kang, J.; Song Kim, T.; Seon Hwang, K.; Hoon Lee, J. Effects of water molecules on binding kinetics of peptide receptor on a piezoelectric microcantilever. *Appl. Phys. Lett.* **2012**, *101*, doi:10.1063/1.4769969.
144. Lee, S.H.; Oh, E.H.; Park, T.H. Cell-based microfluidic platform for mimicking human olfactory system. *Biosens. Bioelectron.* **2015**, *74*, 554–561, doi:10.1016/j.bios.2015.06.072.
145. Nogueira, J.M.F. Novel sorption-based methodologies for static microextraction analysis: A review on SBSE and related techniques. *Anal. Chim. Acta* **2012**, *757*, 1–10, doi:10.1016/j.aca.2012.10.033.
146. Pena-Pereira, F.; Duarte, R.; Duarte, A. Considerations on the application of miniaturized sample preparation approaches for the analysis of organic compounds in environmental matrices. *Open Chem.* **2012**, *10*, doi:10.2478/s11532-011-0114-7.
147. Mozell, M.M.; Jagodowicz, M. Chromatographic separation of odorants by the nose: Retention times measured across in vivo olfactory mucosa. *Science* **1973**, *181*, 1247–1249, doi:10.1126/science.181.4106.1247.
148. Moulton, D.G. Spatial patterning of response to odors in the peripheral olfactory system. *Physiol. Rev.* **1976**, *56*, 578–593, doi:10.1152/physrev.1976.56.3.578.
149. Scott, J.W.; Shannon, D.E.; Charpentier, J.; Davis, L.M.; Kaplan, C. Spatially organized response zones in rat olfactory epithelium. *J. Neurophysiol.* **1997**, *77*, 1950–1962, doi:10.1152/jn.1997.77.4.1950.
150. Nolvachai, Y.; Kulsing, C.; Marriott, P.J. Multidimensional gas chromatography in food analysis. *TrAC Trends Anal. Chem.* **2017**, *96*, 124–137, doi:10.1016/j.trac.2017.05.001.
151. Tranchida, P.Q.; Sciarrone, D.; Dugo, P.; Mondello, L. Heart-cutting multidimensional gas chromatography: A review of recent evolution, applications, and future prospects. *Anal. Chim. Acta* **2012**, *716*, 66–75, doi:10.1016/j.aca.2011.12.015.

152. Gliszczyńska-Świgło, A.; Chmielewski, J. Electronic nose as a tool for monitoring the authenticity of food. A review. *Food Anal. Methods* **2017**, *10*, 1800–1816, doi: 10.1007/s12161-016-0739-4.
153. Covington, J.A.; Gardner, J.W.; Hamilton, A.; Pearce, T.C.; Tan, S.L. Towards a truly biomimetic olfactory microsystem: an artificial olfactory mucosa. *IET Nanobiotechnol.* **2007**, *1*, 15, doi:10.1049/iet-nbt:20060015.
154. Che Harun, F.K.; Covington, J.A.; Gardner, J.W. Mimicking the biological olfactory system: a Portable electronic Mucosa. *IET Nanobiotechnol.* **2012**, *6*, 45, doi:10.1049/iet-nbt.2010.0032.
155. Yabuki, M.; Scott, D.J.; Briand, L.; Taylor, A.J. Dynamics of Odorant Binding to Thin Aqueous Films of Rat-OBP3. *Chem. Senses* **2011**, *36*, 659–671, doi:10.1093/chemse/bjr037.
156. Woodka, M.D.; Brunschwig, B.S.; Lewis, N.S. Use of Spatiotemporal Response Information from Sorption-Based Sensor Arrays to Identify and Quantify the Composition of Analyte Mixtures. *Langmuir* **2007**, *23*, 13232–13241, doi:10.1021/la7026708.
157. Meyer, M.R.; Angele, A.; Kremmer, E.; Kaupp, U.B.; Muller, F. A cGMP-signaling pathway in a subset of olfactory sensory neurons. *Proc. Natl. Acad. Sci.* **2000**, *97*, 10595–10600, doi:10.1073/pnas.97.19.10595.
158. Frings, S. Chemoelectrical signal transduction in olfactory sensory neurons of air-breathing vertebrates. *Cell. Mol. Life Sci.* **2001**, *58*, 510–519, doi:10.1007/PL00000876.
159. Liu, Q.; Wu, C.; Cai, H.; Hu, N.; Zhou, J.; Wang, P. Cell-based biosensors and their application in biomedicine. *Chem. Rev.* **2014**, *114*, 6423–6461, doi:10.1021/cr2003129.
160. Schiffman, S.; Pearce, T. Handbook of machine olfaction. *Electron. Nose Technol. Eds TC Pearce SS Schiffman HT Nagle JW Gardner Darmstadt Wiley-VCH* **2003**, doi: 10.1002/3527601597.
161. Zhang, X.; Cheng, J.; Wu, L.; Mei, Y.; Jaffrezic-Renault, N.; Guo, Z. An overview of an artificial nose system. *Talanta* **2018**, *184*, 93–102, doi:10.1016/j.talanta.2018.02.113.
162. Dickinson, T.A.; White, J.; Kauer, J.S.; Walt, D.R. Current trends in 'artificial-nose' technology. *Trends Biotechnol.* **1998**, *16*, 250–258, doi:10.1016/S0167-7799(98)01185-8.
163. Röck, F.; Barsan, N.; Weimar, U. Electronic Nose: Current Status and Future Trends. *Chem. Rev.* **2008**, *108*, 705–725, doi:10.1021/cr068121q.
164. Pervez, N.; Ham, H.-G.; Kim, S. Interplay of Signaling Molecules in Olfactory Sensory Neuron toward Signal Amplification. *Hanyang Med. Rev.* **2014**, *34*, 137, doi:10.7599/hmr.2014.34.3.137.
165. Oh, E.H.; Lee, S.H.; Ko, H.J.; Lim, J.H.; Park, T.H. Coupling of olfactory receptor and ion channel for rapid and sensitive visualization of odorant response. *Acta Biomater.* **2015**, *22*, 1–7, doi:10.1016/j.actbio.2015.04.034.
166. Lu, D.; Lu, F.; Geng, L.; Pang, G. Recent Advances in Olfactory Receptor (OR) Biosensors and Cell Signaling Cascade Amplification Systems. *Sens. Mater.* **2018**, *67*, doi:10.18494/SAM.2018.1607.

167. Hajjar, E.; Perahia, D.; Debat, H.; Nespoulous, C.; Robert, C.H. Odorant binding and conformational dynamics in the odorant-binding protein. *J Biol Chem* **2006**, *281*, 29929–37, doi:10.1074/jbc.M604869200.
168. Nespoulous, C.; Briand, L.; Delage, M.-M.; Tran, V.; Pernollet, J.-C. Odorant binding and conformational changes of a rat odorant-binding protein. *Chem. Senses* **2004**, *29*, 189–198, doi:10.1093/chemse/bjh017.
169. Gestwicki, J.E.; Hsieh, H.V.; Pitner, J.B. Using receptor conformational change to detect low molecular weight analytes by surface plasmon resonance. *Anal. Chem.* **2001**, *73*, 5732–5737, doi:10.1021/ac0105888.
170. Wei, Y.; Brandazza, A.; Pelosi, P. Binding of polycyclic aromatic hydrocarbons to mutants of odorant-binding protein: A first step towards biosensors for environmental monitoring. *Biochim. Biophys. Acta-Proteins Proteomics* **2008**, *1784*, 666–671, doi:10.1016/j.bbapap.2008.01.012.
171. Vidic, J.; Grosclaude, J.; Monnerie, R.; Persuy, M.-A.; Badonnel, K.; Baly, C.B.; Caillol, M.; Briand, L.; Salessea, R.; Pajot-Augy, E. On a chip demonstration of a functional role for odorant binding protein in the preservation of olfactory receptor activity at high odorant concentration. *Lab. Chip* **2008**, *8*, 678–688, doi:10.1039/B717724K.
172. Andrianova, M.; Komarova, N.; Grudtsov, V.; Kuznetsov, E.; Kuznetsov, A. Amplified Detection of the Aptamer–Vanillin Complex with the Use of Bsm DNA Polymerase. *Sensors* **2017**, *18*, 49, doi:10.3390/s18010049.
173. Raman, B.; Stopfer, M.; Semancik, S. Mimicking biological design and computing principles in artificial olfaction. *ACS Chem Neurosci* **2011**, *2*, 487–499, doi:10.1021/cn200027r.
174. Dickinson, T.A.; Michael, K.L.; Kauer, J.S.; Walt, D.R. Convergent, Self-Encoded Bead Sensor Arrays in the Design of an Artificial Nose. *Anal. Chem.* **1999**, *71*, 2192–2198, doi:10.1021/ac981457i.
175. Brenet, S.; John-Herpin, A.; Gallat, F.X.; Musnier, B.; Buhot, A.; Herrier, C.; Rousselle, T.; Livache, T.; Hou, Y. Highly-Selective Optoelectronic Nose Based on Surface Plasmon Resonance Imaging for Sensing Volatile Organic Compounds. *Anal. Chem.* **2018**, *90*, 9879–9887, doi:10.1021/acs.analchem.8b02036.
176. LaFratta, C.N.; Walt, D.R. Very High Density Sensing Arrays. *Chem. Rev.* **2008**, *108*, 614–637, doi:10.1021/cr0681142.
177. Walt, D.R. Bead-based optical fiber arrays for artificial olfaction. *Curr. Opin. Chem. Biol.* **2010**, *14*, 767–770, doi:10.1016/j.cbpa.2010.06.181.
178. Hyun, S.; Park, T.H. Integration of biomolecules and nanomaterials: Towards highly selective and sensitive biosensors. *Biotechnol. J.* **2011**, *6*, 1310–1316, doi:10.1002/biot.201100006.
179. Zhang, A.; Lieber, C.M. Nano-Bioelectronics. *Chem. Rev.* **2016**, *116*, 215–257, doi:10.1021/acs.chemrev.5b00608.
180. Ellis, J.E.; Star, A. Carbon Nanotube Based Gas Sensors toward Breath Analysis. *ChemPlusChem* **2016**, *81*, 1248–1265, doi:10.1002/cplu.201600478.
181. Rao, S.G.; Huang, L.; Setyawan, W.; Hong, S. Large-scale assembly of carbon nanotubes. *Nature* **2003**, *425*, 36–37, doi:10.1038/425036a.

182. Gao, A.; Wang, Y.; Yang, X.; Wang, Y.; Li, T. Ultrasensitive bioelectronic nose based on CMOS-compatible silicon nanowire array. In *Proceedings of IEEE Sensors*; **2017**; Vol. 2017-December, pp. 1–3, doi:10.1109/ICSENS.2017.8234347.
183. Gutierrez-Osuna, R. Pattern analysis for machine olfaction: a review. *IEEE Sens. J.* **2002**, *2*, 189–202, doi:10.1109/JSEN.2002.800688.
184. Marco, S.; Gutierrez-Galvez, A. Signal and Data Processing for Machine Olfaction and Chemical Sensing: A Review. *IEEE Sens. J.* **2012**, *12*, 3189–3214, doi:10.1109/JSEN.2012.2192920.
185. Vanarse, A.; Osseiran, A.; Rassau, A. An Investigation into Spike-Based Neuromorphic Approaches for Artificial Olfactory Systems. *Sensors* **2017**, *17*, 2591, doi:10.3390/s17112591.
186. Hu, W.; Wan, L.; Jian, Y.; Ren, C.; Jin, K.; Su, X.; Bai, X.; Haick, H.; Yao, M.; Wu, W. Electronic Noses: From Advanced Materials to Sensors Aided with Data Processing. *Adv. Mater. Technol.* **2018**, 1800488, doi:10.1002/admt.201800488.
187. Narusuye, K.; Kawai, F.; Miyachi, E. Spike encoding of olfactory receptor cells. *Neurosci. Res.* **2003**, *46*, 407–413, doi:10.1016/S0168-0102(03)00131-7.
188. Płociniczak, Ł.; Maciejewska, M.; Szczurek, A. Regularization and the inflection point method for sensor signal in gas concentration measurement. *Inverse Probl. Sci. Eng.* **2017**, *25*, 555–579, doi:10.1080/17415977.2016.1172225.
189. Muezzinoglu, M.K.; Vergara, A.; Huerta, R.; Rulkov, N.; Rabinovich, M.I.; Selverston, A.; Abarbanel, H.D.I. Acceleration of chemo-sensory information processing using transient features. *Sens. Actuators B Chem.* **2009**, *137*, 507–512, doi:10.1016/j.snb.2008.10.065.
190. Luo, Y.; Ye, W.; Zhao, X.; Pan, X.; Cao, Y. Classification of Data from Electronic Nose Using Gradient Tree Boosting Algorithm. *Sensors* **2017**, *17*, 2376, doi:10.3390/s17102376.
191. Rodriguez Gamboa, J.C.; Albarracin E, E.S.; da Silva, A.J.; L. de Andrade Lima, L.; E. Ferreira, T.A. Wine quality rapid detection using a compact electronic nose system: Application focused on spoilage thresholds by acetic acid. *LWT* **2019**, *108*, 377–384, doi:10.1016/j.lwt.2019.03.074.
192. Munoz-Mata, J.L.; Osorio-Arrieta, D.L.; Jimenez-Arellano, J.J.; Beltran-Perez, G.; Castillo-Mixcoatl, J.; Munoz-Aguirre, S. Comparison of Two Methods to Reduce Time Measurement of Quartz Crystal Microbalance Gas Sensors. In *Proceedings of the 2019 IEEE International Symposium on Olfaction and Electronic Nose (ISOEN)*; IEEE: Fukuoka, Japan, **2019**; pp. 1–4, doi:10.1109/ISOEN.2019.8823192.
193. Thriumani, R.; Zakaria, A.; Hashim, Y.Z.H.-Y.; Helmy, K.M.; Omar, M.I.; Jeffree, A.; Adom, A.H.; Shakaff, A.Y.M.; Kamarudin, L.M. Feature extraction techniques using multivariate analysis for identification of lung cancer volatile organic compounds. In *AIP Conference Proceedings*; *1808*, Penang, Malaysia, **2017**; p. 020054, doi:10.1063/1.4975287.
194. Zhan, X.; Guan, X.; Wu, R.; Wang, Z.; Wang, Y.; Li, G. Discrimination between Alternative Herbal Medicines from Different Categories with the Electronic Nose. *Sensors* **2018**, *18*, 2936, doi:10.3390/s18092936.
195. Perera, A.; Yamanaka, T.; Gutiérrez-Gálvez, A.; Raman, B.; Gutiérrez-Osuna, R. A dimensionality-reduction technique inspired by receptor convergence in the olfactory system. *Sens. Actuators B Chem.* **2006**, *116*, 17–22, doi:10.1016/j.snb.2005.11.082.

196. Magna, G.; Mosciano, F.; Martinelli, E.; Di Natale, C. Unsupervised On-Line Selection of Training Features for a robust classification with drifting and faulty gas sensors. *Sens. Actuators B Chem.* **2018**, *258*, 1242–1251, doi:10.1016/j.snb.2017.12.005.
197. Ur Rehman, A.; Bermak, A. Drift-Insensitive Features for Learning Artificial Olfaction in E-Nose System. *IEEE Sens. J.* **2018**, *18*, 7173–7182, doi:10.1109/JSEN.2018.2853674.
198. Magna, G.; Di Natale, C.; Martinelli, E. Self-repairing Classification Algorithms for Chemical Sensor Array. *Sens. Actuators B Chem.* **2019**, *297*, 126721, doi: 10.1016/j.snb.2019.126721.
199. Persaud, K.C., Marco, S., Gutiérrez-Gálvez, A. *Neuromorphic Olfaction*; Eds.; Frontiers in Neuroengineering; CRC Press/Taylor & Francis: Boca Raton (FL), **2013**; ISBN 978-1-4398-7171-3.
200. Pearce, T.C. Computational parallels between the biological olfactory pathway and its analogue 'The Electronic Nose': *Biosystems* **1997**, *41*, 43–67, doi:10.1016/S0303-2647(96)01661-9.
201. Sakamoto, M.; Kageyama, R.; Imayoshi, I. The functional significance of newly born neurons integrated into olfactory bulb circuits. *Front. Neurosci.* **2014**, *8*, doi:10.3389/fnins.2014.00121.
202. Ramdya, P.; Benton, R. Evolving olfactory systems on the fly. *Trends Genet.* **2010**, *26*, 307–316, doi:10.1016/j.tig.2010.04.004.
203. Pfeil, T.; Grübl, A.; Jeltsch, S.; Müller, E.; Müller, P.; Petrovici, M.A.; Schmuker, M.; Brüderle, D.; Schemmel, J.; Meier, K. Six Networks on a Universal Neuromorphic Computing Substrate. *Front. Neurosci.* **2013**, *7*, doi:10.3389/fnins.2013.00011.
204. Liu, Y.-J.; Zeng, M.; Meng, Q.-H. Electronic nose using a bio-inspired neural network modeled on mammalian olfactory system for Chinese liquor classification. *Rev. Sci. Instrum.* **2019**, *90*, 025001, doi:10.1063/1.5064540.
205. White, J.; Kauer, J.S. Odor recognition in an artificial nose by spatio-temporal processing using an olfactory neuronal network. *Neurocomputing* **1999**, *26–27*, 919–924, doi:10.1016/S0925-2312(98)00137-4.
206. Pearce, T.; Verschure, P.; White, J.; Kauer, J. Robust Stimulus Encoding in Olfactory Processing: Hyperacuity and Efficient Signal Transmission. In *Emergent Neural Computational Architectures Based on Neuroscience*; Wermter, S., Austin, J., Willshaw, D., Eds.; Springer Berlin Heidelberg: Berlin, Heidelberg, **2001**; Vol. 2036, pp. 461–479, doi: 10.1007/3-540-44597-8\_33.
207. Raman, B.; Sun, P.A.; Gutierrez-Galvez, A.; Gutierrez-Osuna, R. Processing of Chemical Sensor Arrays With a Biologically Inspired Model of Olfactory Coding. *IEEE Trans. Neural Netw.* **2006**, *17*, 1015–1024, doi:10.1109/TNN.2006.875975.
208. Martinelli, E.; Polese, D.; Dini, F.; Paolesse, R.; Filippini, D.; Lundström, I.; Di Natale, C. An Investigation on the Role of Spike Latency in an Artificial Olfactory System. *Front. Neuroengineering* **2011**, *4*, doi:10.3389/fneng.2011.00016.
209. Jing, Y.-Q.; Meng, Q.-H.; Qi, P.-F.; Cao, M.-L.; Zeng, M.; Ma, S.-G. A Bioinspired Neural Network for Data Processing in an Electronic Nose. *IEEE Trans. Instrum. Meas.* **2016**, *65*, 2369–2380, doi:10.1109/TIM.2016.2578618.

210. Koickal, T.J.; Hamilton, A.; Tan, S.L.; Covington, J.A.; Gardner, J.W.; Pearce, T.C. Analog VLSI Circuit Implementation of an Adaptive Neuromorphic Olfaction Chip. *IEEE Trans. Circuits Syst. Regul. Pap.* **2007**, *54*, 60–73, doi:10.1109/TCSI.2006.888677.
211. Hung-Yi Hsieh; Kea-Tiong Tang VLSI Implementation of a Bio-Inspired Olfactory Spiking Neural Network. *IEEE Trans. Neural Netw. Learn. Syst.* **2012**, *23*, 1065–1073, doi:10.1109/TNNLS.2012.2195329.
212. Vanarse, A.; Osseiran, A.; Rassau, A.; van der Made, P. A Hardware-Deployable Neuromorphic Solution for Encoding and Classification of Electronic Nose Data. *Sensors* **2019**, *19*, 4831, doi:10.3390/s19224831.
213. Ratton, L.; Kunt, T.; McAvoy, T.; Fuja, T.; Cavicchi, R.; Semancik, S. A comparative study of signal processing techniques for clustering microsensor data (a first step towards an artificial nose). *Sens. Actuators B Chem.* **1997**, *41*, 105–120, doi:10.1016/S0925-4005(97)80283-3.
214. Marco, S.; Gutiérrez-Gálvez, A.; Lansner, A.; Martinez, D.; Rospars, J.P.; Beccherelli, R.; Perera, A.; Pearce, T.C.; Verschure, P.F.M.J.; Persaud, K. A biomimetic approach to machine olfaction, featuring a very large-scale chemical sensor array and embedded neuro-bio-inspired computation. *Microsyst. Technol.* **2014**, *20*, 729–742, doi:10.1007/s00542-013-2020-8.
215. Diamond, A.; Schmuker, M.; Berna, A.Z.; Trowell, S.; Nowotny, T. Classifying continuous, real-time e-nose sensor data using a bio-inspired spiking network modelled on the insect olfactory system. *Bioinspir. Biomim.* **2016**, *11*, 026002, doi:10.1088/1748-3190/11/2/026002.
216. Borthakur, A.; Cleland, T.A. A Spike Time-Dependent Online Learning Algorithm Derived From Biological Olfaction. *Front. Neurosci.* **2019**, *13*, 656, doi:10.3389/fnins.2019.00656.
217. Li, Z.; Hertz, J. Odour recognition and segmentation by a model olfactory bulb and cortex. *Netw. Comput. Neural Syst.* **2000**, *11*, 83–102, doi:10.1088/0954-898X\_11\_1\_305.
218. Gutierrez-Osuna, R.; Gutierrez-Galvez, A. Habituation in the kiii olfactory model with chemical sensor arrays. *IEEE Trans. Neural Netw.* **2003**, *14*, 1565–1568, doi:10.1109/TNN.2003.820438.
219. Gutierrez-Osuna, R.; Powar, N.U. ODOR MIXTURES AND CHEMOSENSORY ADAPTATION IN GAS SENSOR ARRAYS. *Int. J. Artif. Intell. Tools* **2003**, *12*, 1–16, doi:10.1142/S0218213003001083.
220. Buhot, A.; Bonnaffé, D.; Hou-Broutin, Y.; Livache, T. Electronic nose or tongue sensor, **2013**, (patent WO213124810).
221. Hou-Broutin, Y.; Brenet, S.; Livache, T.; Herrier, C.; Rousselle, T. Composés chimiques mis en oeuvre comme surfaces de référence pour déterminer le bruit d'un capteur multipléxé de type nez électronique et en diminuer la dérive, **2017**, (patent FR1758547).
222. Hou-Broutin, Y.; Brenet, S.; Buhot, A.; Herrier, C.; Rousselle, T.; Livache, T. Système de détection pour nez électronique permettant une classification physicochimique des odeurs et nez électronique comprenant un tel système, **2019**, (patent FR1907884).
223. Livache, T.; Gallat, F.-X.; Hou-Broutin, Y.; Herrier, C.; Rousselle, T. Procédé de calibration d'un nez électronique, **2017**, (patent FR1751751).

224. Hardware solutions - NeOse Pro Available online: <https://aryballe.com/solutions/device-solutions/> (accessed on Apr 7, 2020).
225. Horton, H.R. *Principes de biochimie*; De Boeck University: Bruxelles, **1994**; ISBN 2-8041-1578-X.
226. Merrifield, R.B. Solid Phase Peptide Synthesis. I. The Synthesis of a Tetrapeptide. *J. Am. Chem. Soc.* **1963**, *85*, 2149–2154, doi:10.1021/ja00897a025.
227. Compound, I. A Brief Guide to the Twenty Common Amino Acids Available online: <https://www.compoundchem.com/2014/09/16/aminoacids/> (accessed on Mar 19, 2020).
228. Brenet, S. Développement et optimisation d'un nez électronique basé sur l'imagerie de résonance de plasmons de surface, Communauté université Grenoble Alpes, 2018 (Thèse).
229. sciFLEXARRAYER - ultra-low volume dispensing systems for R&D and manufacturing Available online: [www.scienion.com](http://www.scienion.com) (accessed on Jul 1, 2017).
230. Lichtenberg, J.Y.; Ling, Y.; Kim, S. Non-Specific Adsorption Reduction Methods in Biosensing. *Sensors* **2019**, *19*, 2488, doi:10.3390/s19112488.
231. Dahlgran, J. Dilution of volatile organic compounds with light oils for solvent encapsulation to create VOCs in soil performance evaluation standards. *Am. Lab.*, **2002**, *34* (19), 24–26.
232. Weerakkody, J.S.; Hurot, C.; Brenet, S.; Mathey, R.; Herrier, C.; Livache, T.; Buhot, A.; Hou, Y. Surface plasmon resonance imaging-based optoelectronic nose: fundamental study on the effects of temperature and humidity. In *Proceedings of the Optical Sensing and Detection VI*; Berghmans, F., Mignani, A.G., Eds.; SPIE: Online Only, France, **2020**; p. 44, doi: 10.1117/12.2555450.
233. Thomson, G.; Oddy, W.A.; Lintrum, D. *The Museum Environment*; Butterworth Heinemann Ltd: London, **2013**; ISBN 978-1-4831-0271-9.
234. Homola, J. Surface plasmon resonance sensors for detection of chemical and biological species. *Chem. Rev.* **2008**, *108*, 462–493, doi:10.1021/cr068107d.
235. Maillart, E.; Livache, T.; Leroy, L. *Biological Applications of Surface Plasmon Resonance Imaging*; **2012**; ISBN 978-3-642-25497-0.
236. Campbell, C.T.; Kim, G. SPR microscopy and its applications to high-throughput analyses of biomolecular binding events and their kinetics. *Biomaterials* **2007**, *28*, 2380–2392, doi:10.1016/j.biomaterials.2007.01.047.
237. Schasfoort, R.B. *Handbook of surface plasmon resonance*; Royal Society of Chemistry, **2017**; ISBN 1-78262-730-8.
238. Scarano, S.; Scuffi, C.; Mascini, M.; Minunni, M. Surface plasmon resonance imaging (SPRI)-based sensing: A new approach in signal sampling and management. *Biosens. Bioelectron.* **2010**, *26*, 1380–1385, doi:10.1016/j.bios.2010.07.056.
239. Lê, S.; Josse, J.; Husson, F. FactoMineR: An R Package for Multivariate Analysis. *J. Stat. Softw.* **2008**, *25*, 1–18, doi: 10.18637/jss.v025.i01.



240. Lamiable, A.; Thévenet, P.; Rey, J.; Vavrusa, M.; Derreumaux, P.; Tufféry, P. PEP-FOLD3: faster *de novo* structure prediction for linear peptides in solution and in complex. *Nucleic Acids Res.* **2016**, *44*, W449–W454, doi:10.1093/nar/gkw329.
241. Thevenet, P.; Shen, Y.; Maupetit, J.; Guyon, F.; Derreumaux, P.; Tuffery, P. PEP-FOLD: an updated *de novo* structure prediction server for both linear and disulfide bonded cyclic peptides. *Nucleic Acids Res.* **2012**, *40*, W288–W293, doi:10.1093/nar/gks419.
242. Kim, S.; Chen, J.; Cheng, T.; Gindulyte, A.; He, J.; He, S.; Li, Q.; Shoemaker, B.A.; Thiessen, P.A.; Yu, B.; et al. PubChem 2019 update: improved access to chemical data. *Nucleic Acids Res.* **2019**, *47*, D1102–D1109, doi:10.1093/nar/gky1033.
243. Trott, O.; Olson, A.J. AutoDock Vina: Improving the speed and accuracy of docking with a new scoring function, efficient optimization, and multithreading. *J. Comput. Chem.* **2009**, *31*(2), 455–461, doi:10.1002/jcc.21334.
244. Verde, A.V.; Acres, J.M.; Maranas, J.K. Investigating the Specificity of Peptide Adsorption on Gold Using Molecular Dynamics Simulations. *Biomacromolecules* **2009**, *10*, 2118–2128, doi:10.1021/bm9002464.
245. Raut, V.P.; Agashe, M.A.; Stuart, S.J.; Latour, R.A. Molecular Dynamics Simulations of Peptide–Surface Interactions. *Langmuir* **2005**, *21*, 1629–1639, doi:10.1021/la047807f.
246. Jaworski, J.W.; Raorane, D.; Huh, J.H.; Majumdar, A.; Lee, S.-W. Evolutionary Screening of Biomimetic Coatings for Selective Detection of Explosives. *Langmuir* **2008**, *24*, 4938–4943, doi:10.1021/la7035289.
247. Kaye, G.; Laby, T. Tables of physical and chemical constants. **2018**, ISBN 0 582 46354 8.
248. Weerakkody, J.S.; Brenet, S.; Livache, T.; Herrier, C.; Hou, Y.; Buhot, A. Optical Index Prism Sensitivity of Surface Plasmon Resonance Imaging in Gas Phase: Experiment versus Theory. *J. Phys. Chem. C* **2020**, *124*, 3756–3767, doi:10.1021/acs.jpcc.9b09973.
249. Campbell, C.T.; Kim, G. SPR microscopy and its applications to high-throughput analyses of biomolecular binding events and their kinetics. *Biomaterials* **2007**, *28*, 2380–2392, doi:10.1016/j.biomaterials.2007.01.047.
250. Wen, X.; Linton, R.W.; Formaggio, F.; Toniolo, C.; Samulski, E.T. Self-Assembled Monolayers of Hexapeptides on Gold: Surface Characterization and Orientation Distribution Analysis. *J. Phys. Chem. A* **2004**, *108*, 9673–9681, doi:10.1021/jp047922z.
251. Cho, Y.; Ivanisevic, A. TAT Peptide Immobilization on Gold Surfaces: A Comparison Study with a Thiolated Peptide and Alkylthiols Using AFM, XPS, and FT-IRRAS. *J. Phys. Chem. B* **2005**, *109*, 6225–6232, doi:10.1021/jp045731q.
252. Nowinski, A.K.; Sun, F.; White, A.D.; Keefe, A.J.; Jiang, S.Y. Sequence, Structure, and Function of Peptide Self-Assembled Monolayers. *J. Am. Chem. Soc.* **2012**, *134*, 6000–6005, doi:10.1021/ja3006868.
253. Heller, D.A.; Garga, V.; Kelleher, K.J.; Lee, T.-C.; Mahbubani, S.; Sigworth, L.A.; Lee, T.R.; Rea, M.A. Patterned networks of mouse hippocampal neurons on peptide-coated gold surfaces. *Biomaterials* **2005**, *26*, 883–889, doi:10.1016/j.biomaterials.2004.03.029.
254. Feldner, J.C.; Ostrop, M.; Friedrichs, O.; Sohn, S.; Lipinsky, D.; Gunst, U.; Arlinghaus, H.F. TOF-SIMS investigation of the immobilization process of peptide nucleic acids. *Appl. Surf. Sci.* **2003**, *203–204*, 722–725, doi:10.1016/S0169-4332(02)00805-X.

255. Leufgen, K.; Mutter, M.; Vogel, H.; Szymczak, W. Orientation Modulation of a Synthetic Polypeptide in Self-Assembled Monolayers: A TOF-SIMS Study. *J. Am. Chem. Soc.* **2003**, *125*, 8911–8915, doi:10.1021/ja0210749.
256. La plate-forme de Nanocaractérisation (PFNC) Available online: <https://www.minatec.org/fr/recherche/plates-formes-dediees/plate-forme-nanocaracterisation/> (accessed on May 7, 2020).
257. Ohnesorge, F.; Binnig, G. True Atomic Resolution by Atomic Force Microscopy Through Repulsive and Attractive Forces. *Science* **1993**, *260*, 1451–1456, doi:10.1126/science.260.5113.1451.
258. Cleveland, J.P.; Anczykowski, B.; Schmid, A.E.; Elings, V.B. Energy dissipation in tapping-mode atomic force microscopy. *Appl. Phys. Lett.* **1998**, *72*, 2613–2615, doi:10.1063/1.121434.
259. Barth, C.; Hynninen, T.; Bielecki, M.; Henry, C.R.; Foster, A.S.; Esch, F.; Heiz, U. AFM tip characterization by Kelvin probe force microscopy. *New J. Phys.* **2010**, *12*, 093024, doi:10.1088/1367-2630/12/9/093024.
260. Kaja, K. Development of nano-probe techniques for work function assessment and application to materials for microelectronics, Université Grenoble Alpes, 2010 (Thèse).
261. Canesson, P.; Brundle, C.R.; Baker, A.D. Electron Spectroscopy: Theory, Techniques and Applications. *Acad. Press N. Y. Lond.* **1982**, *4*.
262. Vickerman, J.C., Brown, A.A., Reed, N.M. *Secondary ion mass spectrometry: principles and applications*; Eds.; The International series of monographs on chemistry; Clarendon Press ; Oxford University Press: Oxford : Oxford ; New York, **1989**; ISBN 978-0-19-855625-1.
263. Fiche, J.-B. Etudes thermiques des puces à ADN par imagerie de résonance des plasmons de surface (SPRi): vers la détection de mutations ponctuelles. **2006** (Thèse).
264. Hajjar, E.; Perahia, D.; Debat, H.; Nespoulous, C.; Robert, C.H. Odorant binding and conformational dynamics in the odorant-binding protein. *J Biol Chem* **2006**, *281*, 29929–37, doi:10.1074/jbc.M604869200.
265. Nespoulous, C.; Briand, L.; Delage, M.-M.; Tran, V.; Pernollet, J.-C. Odorant binding and conformational changes of a rat odorant-binding protein. *Chem. Senses* **2004**, *29*, 189–198, doi:10.1093/chemse/bjh017..
266. Gestwicki, J.E.; Hsieh, H.V.; Pitner, J.B. Using receptor conformational change to detect low molecular weight analytes by surface plasmon resonance. *Anal. Chem.* **2001**, *73*, 5732–5737, doi:10.1021/ac0105888.
267. Hurot, C.; Brenet, S.; Buhot, A.; Barou, E.; Belloir, C.; Briand, L.; Hou, Y. Highly sensitive olfactory biosensors for the detection of volatile organic compounds by surface plasmon resonance imaging. *Biosens. Bioelectron.* **2019**, *123*, 230–236, doi:10.1016/j.bios.2018.08.072.
268. Mitchell, J.S.; Wu, Y.; Cook, C.J.; Main, L. Sensitivity enhancement of surface plasmon resonance biosensing of small molecules. *Anal. Biochem.* **2005**, *343*, 125–135, doi:10.1016/j.ab.2005.05.001.
269. Bécherrawy, T. *Optique géométrique: cours et exercices corrigés*; De Boeck: Bruxelles, **2006**; ISBN 978-2-8041-4912-3.

270. Wasilewski, T.; Gebicki, J.; Kamysz, W. Bioelectronic nose: Current status and perspectives. *Biosens Bioelectron* **2017**, *87*, 480–494, doi:10.1016/j.bios.2016.08.080.
271. Wasilewski, T.; Gębicki, J.; Kamysz, W. Advances in olfaction-inspired biomaterials applied to bioelectronic noses. *Sens. Actuators B Chem.* **2018**, *257*, 511–537, doi:10.1016/j.snb.2017.10.086.
272. Du, L.; Wu, C.; Liu, Q.; Huang, L.; Wang, P. Recent advances in olfactory receptor-based biosensors. *Biosens. Bioelectron.* **2013**, *42*, 570–580, doi:10.1016/j.bios.2012.09.001.
273. Gomila, G.; Casuso, I.; Errachid, A.; Ruiz, O.; Pajot, E.; Minic, J.; Gorjankina, T.; Persuy, M.A.; Aioun, J.; Salesse, R.; et al. Advances in the production, immobilization, and electrical characterization of olfactory receptors for olfactory nanobiosensor development. *Sens. Actuators B Chem.* **2006**, *116*, 66–71, doi:10.1016/j.snb.2005.11.083.
274. Hou, Y.; Jaffrezic-Renault, N.; Martelet, C.; Zhang, A.; Minic-Vidic, J.; Gorjankina, T.; Persuy, M.-A.; Pajot-Augy, E.; Salesse, R.; Akimov, V.; et al. A novel detection strategy for odorant molecules based on controlled bioengineering of rat olfactory receptor 17. *Biosens. Bioelectron.* **2007**, *22*, 1550–1555, doi:10.1016/j.bios.2006.06.018.
275. Barou, E.; Sigoillot, M.; Bouvet, M.; Briand, L.; Meunier-Prest, R. Electrochemical detection of the 2-isobutyl-3-methoxypyrazine model odorant based on odorant-binding proteins: The proof of concept. *Bioelectrochemistry* **2015**, *101*, 28–34, doi:10.1016/j.bioelechem.2014.06.006.
276. Kotlowski, C.; Larisika, M.; Guerin, P.M.; Kleber, C.; Kröber, T.; Mastrogiacomo, R.; Nowak, C.; Pelosi, P.; Schütz, S.; Schwaighofer, A.; et al. Fine discrimination of volatile compounds by graphene-immobilized odorant-binding proteins. *Sens. Actuators B Chem.* **2018**, *256*, 564–572, doi:10.1016/j.snb.2017.10.093.
277. Lu, Y.; Yao, Y.; Li, S.; Zhang, Q.; Liu, Q. Olfactory biosensor based on odorant-binding proteins of *Bactrocera dorsalis* with electrochemical impedance sensing for pest management. *Sens. Rev.* **2017**, *37*, 396–403, doi:10.1108/SR-03-2017-0044.
278. Manai, R.; Scorsone, E.; Rousseau, L.; Ghassemi, F.; Possas Abreu, M.; Lissorgues, G.; Tremillon, N.; Ginisty, H.; Arnault, J.C.; Tuccori, E.; et al. Grafting odorant binding proteins on diamond bio-MEMS. *Biosens. Bioelectron.* **2014**, *60*, 311–317, doi:10.1016/j.bios.2014.04.020.
279. Pelosi, P.; Mastrogiacomo, R.; Iovinella, I.; Tuccori, E.; Persaud, K.C. Structure and biotechnological applications of odorant-binding proteins. *Appl. Microbiol. Biotechnol.* **2014**, *98*, 61–70, doi:10.1007/s00253-013-5383-y.
280. Heydel, J.-M.; Coelho, A.; Thiebaud, N.; Legendre, A.; Bon, A.-M.L.; Faure, P.; Neiers, F.; Artur, Y.; Golebiowski, J.; Briand, L. Odorant-Binding Proteins and Xenobiotic Metabolizing Enzymes: Implications in Olfactory Perireceptor Events. *Anat. Rec.* **2013**, *296*, 1333–1345, doi:10.1002/ar.22735.
281. Löbel, D.; Jacob, M.; Völkner, M.; Breer, H. Odorants of Different Chemical Classes Interact with Distinct Odorant Binding Protein Subtypes. *Chem. Senses* **2002**, *27*, 39–44, doi:10.1093/chemse/27.1.39.
282. Zhao, X.; Ashley, G.M.; Garcia-Gancedo, L.; Jin, H.; Luo, J.; Flewitt, A.J.; Lu, J.R. Protein functionalized ZnO thin film bulk acoustic resonator as an odorant biosensor. *Sens. Actuators B Chem.* **2012**, *163*, 242–246, doi:10.1016/j.snb.2012.01.046.

283. Lu, Y.; Li, H.; Zhuang, S.; Zhang, D.; Zhang, Q.; Zhou, J.; Dong, S.; Liu, Q.; Wang, P. Olfactory biosensor using odorant-binding proteins from honeybee: Ligands of floral odors and pheromones detection by electrochemical impedance. *Sens. Actuators B Chem.* **2014**, *193*, 420–427, doi:10.1016/j.snb.2013.11.045.
284. Lu, Y.; Yao, Y.; Zhang, Q.; Zhang, D.; Zhuang, S.; Li, H.; Liu, Q. Olfactory biosensor for insect semiochemicals analysis by impedance sensing of odorant-binding proteins on interdigitated electrodes. *Biosens. Bioelectron.* **2015**, *67*, 662–669, doi: 10.1016/j.bios.2014.09.098.
285. Lu, Y.; Zhang, D.; Zhang, Q.; Huang, Y.; Luo, S.; Yao, Y.; Li, S.; Liu, Q. Impedance spectroscopy analysis of human odorant binding proteins immobilized on nanopore arrays for biochemical detection. *Biosens. Bioelectron.* **2016**, *79*, 251–257, doi:10.1016/j.bios.2015.12.047.
286. Lu, Y.; Huang, Y.; Li, S.; Zhang, Q.; Wu, J.; Xiong, Z.; Xiong, L.; Wan, Q.; Liu, Q. Fat taste detection with odorant-binding proteins (OBPs) on screen-printed electrodes modified by reduced graphene oxide. *Sens. Actuators B Chem.* **2017**, *252*, 973–982, doi:10.1016/j.snb.2017.06.100.
287. Larisika, M.; Kotlowski, C.; Steininger, C.; Mastrogiacomo, R.; Pelosi, P.; Schütz, S.; Peteu, S.F.; Kleber, C.; Reiner-Rozman, C.; Nowak, C.; et al. Electronic olfactory sensor based on *A. mellifera* odorant-binding protein 14 on a reduced graphene oxide field-effect transistor. *Angew Chem* **2015**, *127*, 13443–13446, doi:10.1002/anie.201505712.
288. Mulla, M.Y.; Tuccori, E.; Magliulo, M.; Lattanzi, G.; Palazzo, G.; Persaud, K.; Torsi, L. Capacitance-modulated transistor detects odorant binding protein chiral interactions. *Nat. Commun.* **2015**, *6*, 6010, doi:10.1038/ncomms7010.
289. Zhang, D.; Lu, Y.; Zhang, Q.; Yao, Y.; Li, S.; Li, H.; Zhuang, S.; Jiang, J.; Liu, G.L.; Liu, Q. Nanoplasmonic monitoring of odorants binding to olfactory proteins from honeybee as biosensor for chemical detection. *Sens. Actuators B Chem.* **2015**, *221*, 341–349, doi: 10.1016/j.snb.2015.06.091.
290. Hurot, C.; Buhot, A.; Barou, E.; Belloir, C.; Briand, L.; Hou, Y. Odorant-binding protein-based optoelectronic tongue and nose for sensing volatile organic compounds. In *Proceedings of the 2019 IEEE International Symposium on Olfaction and Electronic Nose (ISOEN)*; IEEE: Fukuoka, Japan, **2019**; pp. 1–4, doi:10.1109/ISOEN.2019.8823179.
291. Hurot, C.; Brenet, S.; Buhot, A.; Barou, E.; Belloir, C.; Briand, L.; Hou, Y. Development of a novel olfactory biosensor based on surface plasmon resonance imaging. In *Proceedings of the 3. Journées Plénières du GDR "Bio-Ingénierie des Interfaces"*; Besançon, France, **2018**.
292. Hurot, C.; Weerakkody, J.; Brenet, S.; Buhot, A.; Hou, Y. Electronic noses: Novel sensing materials for better performances. In *Proceedings of the 4th Annual Meeting of GDR O3*; Nice, France, **2018**.
293. Brenet, S.; Hurot, C.; Buhot, A.; Barou, E.; Belloir, C.; Briand, L.; Hou, Y. Surface plasmon resonance imaging for sensing volatile organic compounds: biomimetic olfactory biosensors & optoelectronic nose. In *Proceedings of the Biosensors*; Miami, United States, **2018**.
294. Tcatchoff, L.; Nespoulous, C.; Pernollet, J.C.; Briand, L. A single lysyl residue defines the binding specificity of a human odorant-binding protein for aldehydes. *FEBS Lett.* **2006**, *580*, 2102–2108, doi:10.1016/j.febslet.2006.03.017.

295. Brulé, M.; Glaz, M.; Belloir, C.; Poirier, N.; Moitrier, L.; Neiers, F.; Briand, L. Bacterial expression and purification of vertebrate odorant-binding proteins. In *Methods in Enzymology*; Elsevier, **2020**; p. S0076687920302135, doi: 10.1016/bs.mie.2020.05.002.
296. Daniel, C.; Mélaïne, F.; Roupioz, Y.; Livache, T.; Buhot, A. Real time monitoring of thrombin interactions with its aptamers: Insights into the sandwich complex formation. *Biosens. Bioelectron.* **2013**, *40*, 186–192, doi:10.1016/j.bios.2012.07.016.
297. Lu, C.; Saint-Pierre, C.; Gasparutto, D.; Roupioz, Y.; Peyrin, E.; Buhot, A. Linear Chain Formation of Split-Aptamer Dimers on Surfaces Triggered by Adenosine. *Langmuir* **2017**, *33*, 12785–12792, doi:10.1021/acs.langmuir.7b02104.
298. Sota, H.; Hasegawa, Y.; Iwakura, M. Detection of conformational changes in an immobilized protein using surface plasmon resonance. *Anal. Chem.* **1998**, *70*, 2019–2024, doi: 10.1021/ac9713666.
299. Miyazaki, C.M.; Shimizu, F.M.; Mejía-Salazar, J.R.; Oliveira, O.N.; Ferreira, M. Surface plasmon resonance biosensor for enzymatic detection of small analytes. *Nanotechnology* **2017**, *28*, doi:10.1088/1361-6528/aa6284.
300. Dell’Orco, D.; Sulmann, S.; Linse, S.; Koch, K.-W. Dynamics of Conformational Ca<sup>2+</sup>-Switches in Signaling Networks Detected by a Planar Plasmonic Device. *Anal. Chem.* **2012**, *84*, 2982–2989, doi:10.1021/ac300213j.
301. Kim, M.; Jung, S.O.; Park, K.; Jeong, E.J.; Joung, H.A.; Kim, T.H.; Seol, D.W.; Chung, B.H. Detection of Bax protein conformational change using a surface plasmon resonance imaging-based antibody chip. *Biochem. Biophys. Res. Commun.* **2005**, *338*, 1834–1838, doi:10.1016/j.bbrc.2005.10.155.
302. Bozdogan, A.; Hageneder, S.; Dostalek, J. Plasmonic biosensors relying on biomolecular conformational changes: Case of odorant binding proteins. In *Methods in Enzymology*; Elsevier, **2020**; p. S007668792030207X, doi:10.1016/bs.mie.2020.04.068.
303. Branden, C.; Tooze, J.; Lubochinsky, B. *Introduction à la structure des protéines*; De Boeck Université: Paris; Bruxelles, **1996**; ISBN 978-2-8041-2109-9.
304. Smith, G. Filamentous fusion phage: novel expression vectors that display cloned antigens on the virion surface. *Science* **1985**, *228*, 1315–1317, doi:10.1126/science.4001944.
305. Smith, G.P. Phage Display: Simple Evolution in a Petri Dish (Nobel Lecture). *Angew. Chem. Int. Ed.* **2019**, *58*, 14428–14437, doi:10.1002/anie.201908308.
306. Naik, R.R.; Stringer, S.J.; Agarwal, G.; Jones, S.E.; Stone, M.O. Biomimetic synthesis and patterning of silver nanoparticles. *Nat. Mater.* **2002**, *1*, 169–172, doi:10.1038/nmat758.
307. Whaley, S.R.; English, D.S.; Hu, E.L.; Barbara, P.F.; Belcher, A.M. Selection of peptides with semiconductor binding specificity for directed nanocrystal assembly. *Nature* **2000**, *405*, 665–668, doi:10.1038/35015043.
308. Slonczewski, J.L.; Foster, J.W. The Filamentous Phage M13: Vaccines and Nanowires Available online: <https://wwnorton.com> (accessed on Apr 9, 2020).
309. Hess, G.T.; Cragolini, J.J.; Popp, M.W.; Allen, M.A.; Dougan, S.K.; Spooner, E.; Ploegh, H.L.; Belcher, A.M.; Guimaraes, C.P. M13 Bacteriophage Display Framework That Allows Sortase-Mediated Modification of Surface-Accessible Phage Proteins. *Bioconjug. Chem.* **2012**, *23*, 1478–1487, doi:10.1021/bc300130z.

310. Knez, K.; Noppe, W.; Geukens, N.; Janssen, K.P.F.; Spasic, D.; Heyligen, J.; Vriens, K.; Thevissen, K.; Cammue, B.P.A.; Petrenko, V.; et al. Affinity Comparison of p3 and p8 Peptide Displaying Bacteriophages Using Surface Plasmon Resonance. *Anal. Chem.* **2013**, *85*, 10075–10082, doi:10.1021/ac402192k.
311. Fukunaga, K.; Taki, M. Practical Tips for Construction of Custom Peptide Libraries and Affinity Selection by Using Commercially Available Phage Display Cloning Systems. *J. Nucleic Acids* **2012**, *2012*, 1–9, doi:10.1155/2012/295719.
312. Tanaka, M.; Minamide, T.; Takahashi, Y.; Hanai, Y.; Yanagida, T.; Okochi, M. Peptide Screening from a Phage Display Library for Benzaldehyde Recognition. *Chem. Lett.* **2019**, *48*, 978–981, doi:10.1246/cl.190318.
313. *Bioconjugate Techniques*; Elsevier, 2013; ISBN 978-0-12-382239-0.
314. Kubas, G.; Rees, W.; Caguiat, J.; Asch, D.; Fagan, D.; Cortes, P. Identification of peptide sequences that selectively bind to pentaerythritol trinitrate hemisuccinate—a surrogate of PETN, via phage display technology. *Pept. Sci.* **2017**, *108*, e22997, doi:10.1002/bip.22997.
315. Johnson, M. Detergents: Triton X-100, Tween-20, and More. *Mater. Methods* **2013**, *3*, doi:10.13070/mm.en.3.163.
316. Bhardwaj, D.; Singh, S.S.; Abrol, S.; Chaudhary, V.K. Monoclonal antibodies against a minor and the major coat proteins of filamentous phage M13: their application in phage display. *J. Immunol. Methods* **1995**, *179*, 165–175, doi:10.1016/0022-1759(94)00280-A.
317. Liu, X.; Atwater, M.; Wang, J.; Huo, Q. Extinction coefficient of gold nanoparticles with different sizes and different capping ligands. *Colloids Surf. B Biointerfaces* **2007**, *58*, 3–7, doi:10.1016/j.colsurfb.2006.08.005.
318. Weerakkody, J.S.; Hurot, C.; Brenet, S.; Mathey, R.; Raillon, C.; Livache, T.; Buhot, A.; Hou, Y. Opto-electronic nose - temperature and VOC concentration effects on the equilibrium response. In *Proceedings of the 2019 IEEE International Symposium on Olfaction and Electronic Nose (ISOEN)*; IEEE: Fukuoka, Japan, **2019**; pp. 1–3, doi: 10.1109/ISOEN.2019.8823292.
319. Gordiichuk, P.; Pesce, D.; Ocampo, O.E.C.; Marcozzi, A.; Wetzelaer, G.J.A.H.; Paul, A.; Loznik, M.; Gloukhikh, E.; Richter, S.; Chiechi, R.C.; et al. Orientation and Incorporation of Photosystem I in Bioelectronics Devices Enabled by Phage Display. *Adv. Sci.* **2017**, *4*, doi:Artn 1600393 10.1002/Adv.201600393.
320. Khedkar, S.A.; Malde, A.K.; Coutinho, E.C. In silico screening of ligand databases: Methods and applications. *Indian J. Pharm. Sci.* **2006**, *68*, 689, doi:10.4103/0250-474X.30998.
321. Del Carlo, M.; Fusella, G.C.; Pepe, A.; Sergi, M.; Di Martino, M.; Mascini, M.; Martino, G.; Cichelli, A.; Di Natale, C.; Compagnone, D. Novel oligopeptides based e-nose for food quality control: application to extra-virgin olive samples. *Qual. Assur. Saf. Crops Foods* **2014**, *6*, 309–317, doi:10.3920/QAS2013.0377.
322. Compagnone, D.; Faieta, M.; Pizzoni, D.; Di Natale, C.; Paolesse, R.; Van Caelenberg, T.; Beheydt, B.; Pittia, P. Quartz crystal microbalance gas sensor arrays for the quality control of chocolate. *Sens. Actuators B Chem.* **2015**, *207*, 1114–1120, doi:10.1016/j.snb.2014.10.049.
323. Pizzoni, D.; Compagnone, D.; Di Natale, C.; D'Alessandro, N.; Pittia, P. Evaluation of aroma release of gummy candies added with strawberry flavours by gas-chromatography/mass-

- spectrometry and gas sensors arrays. *J. Food Eng.* **2015**, *167*, 77–86, doi:10.1016/j.jfoodeng.2015.03.003.
324. Mascini, M.; Gaggiotti, S.; Della Pelle, F.; Di Natale, C.; Qakala, S.; Iwuoha, E.; Pittia, P.; Compagnone, D. Peptide Modified ZnO Nanoparticles as Gas Sensors Array for Volatile Organic Compounds (VOCs). *Front. Chem.* **2018**, *6*, 105, doi:10.3389/fchem.2018.00105.
325. Mascini, M.; Gaggiotti, S.; Della Pelle, F.; Wang, J.; Pingarrón, J.M.; Compagnone, D. Hairpin DNA-AuNPs as molecular binding elements for the detection of volatile organic compounds. *Biosens. Bioelectron.* **2019**, *123*, 124–130, doi:10.1016/j.bios.2018.07.028.
326. Gaggiotti, S.; Hurot, C.; Weerakkody, J.S.; Mathey, R.; Buhot, A.; Mascini, M.; Hou, Y.; Compagnone, D. Development of an optoelectronic nose based on surface plasmon resonance imaging with peptide and hairpin DNA for sensing volatile organic compounds. *Sens. Actuators B Chem.* **2020**, *303*, 127188, doi:10.1016/j.snb.2019.127188.
327. Mascini, M.; Pizzoni, D.; Perez, G.; Chiarappa, E.; Di Natale, C.; Pittia, P.; Compagnone, D. Tailoring gas sensor arrays via the design of short peptides sequences as binding elements. *Biosens. Bioelectron.* **2017**, *93*, 161–169, doi:10.1016/j.bios.2016.09.028.
328. Okochi, M.; Muto, M.; Yanai, K.; Tanaka, M.; Onodera, T.; Wang, J.; Ueda, H.; Toko, K. Array-Based Rational Design of Short Peptide Probe-Derived from an Anti-TNT Monoclonal Antibody. *ACS Comb. Sci.* **2017**, *19*, 625–632, doi:10.1021/acscmbosci.7b00035.
329. Brenet, S.; John-Herpin, A.; Gallat, F.-X.; Musnier, B.; Buhot, A.; Herrier, C.; Rousselle, T.; Livache, T.; Hou, Y. Highly-Selective Optoelectronic Nose Based on Surface Plasmon Resonance Imaging for Sensing Volatile Organic Compounds. *Anal. Chem.* **2018**, *90*, 9879–9887, doi:10.1021/acs.analchem.8b02036.
330. Krehenbrink, M.; Chami, M.; Guilvout, I.; Alzari, P.M.; Pécorari, F.; Pugsley, A.P. Artificial Binding Proteins (Affitins) as Probes for Conformational Changes in Secretin PulD. *J. Mol. Biol.* **2008**, *383*, 1058–1068, doi:10.1016/j.jmb.2008.09.016.
331. Owens, A.E.; Iannuzzelli, J.A.; Gu, Y.; Fasan, R. MORPH-PhD: An Integrated Phage Display Platform for the Discovery of Functional Genetically Encoded Peptide Macrocycles. *ACS Cent. Sci.* **2020**, *6*, 368–381, doi:10.1021/acscentsci.9b00927.
332. Simonetti, L.; Ivarsson, Y. Genetically Encoded Cyclic Peptide Phage Display Libraries. *ACS Cent. Sci.* **2020**, *6*, 336–338, doi:10.1021/acscentsci.0c00087.
333. Simeon, R.; Chen, Z. In vitro-engineered non-antibody protein therapeutics. *Protein Cell* **2018**, *9*, 3–14, doi:10.1007/s13238-017-0386-6.
334. Hou, Y.; Genua, M.; Tada Batista, D.; Calemczuk, R.; Buhot, A.; Fornarelli, P.; Koubachi, J.; Bonnaffé, D.; Saesen, E.; Laguri, C.; et al. Continuous Evolution Profiles for Electronic-Tongue-Based Analysis. *Angew. Chem.* **2012**, *124*, 10540–10544, doi:10.1002/ange.201205346.
335. Kim, S.; Kim, D.; Jung, H.H.; Lee, I.-H.; Kim, J.I.; Suh, J.-Y.; Jon, S. Bio-Inspired Design and Potential Biomedical Applications of a Novel Class of High-Affinity Peptides. *Angew. Chem. Int. Ed.* **2012**, *51*, 1890–1894, doi:10.1002/anie.201107894.
336. Gray, B.P.; Li, S.; Brown, K.C. From Phage Display to Nanoparticle Delivery: Functionalizing Liposomes with Multivalent Peptides Improves Targeting to a Cancer Biomarker. *Bioconjug. Chem.* **2013**, *24*, 85–96, doi:10.1021/bc300498d.

337. Sun, J.S.; Xiao, S.; Carlson, J.R. The diverse small proteins called odorant-binding proteins. *Open Biol.* **2018**, *8*, 180208, doi:10.1098/rsob.180208.
338. Genua, M. Combinatorial surface-based electronic tongue development: Analytical applications and conception of 2D and 3D biomimetic surfaces, **2013** (Thèse).
339. Kim, S.; Kim, D.; Jung, H.H.; Lee, I.-H.; Kim, J.I.; Suh, J.-Y.; Jon, S. Bio-Inspired Design and Potential Biomedical Applications of a Novel Class of High-Affinity Peptides. *Angew. Chem. Int. Ed.* **2012**, *51*, 1890–1894, doi:10.1002/anie.201107894.
340. McGann, M. FRED Pose Prediction and Virtual Screening Accuracy. *J. Chem. Inf. Model.* **2011**, *51*, 578–596, doi:10.1021/ci100436p.





## List of scientific production

### Papers

1. A. Delices, D. Moodelly, **C. Hurot**, Y. Hou, W. L. Ling, C. Saint-Pierre, D. Gasparutto, G. Nogues, P. Reiss, K. Kheng\*, "Aqueous synthesis of DNA-Functionalized Near-Infrared AgInS<sub>2</sub>/ZnS Core/Shell Quantum Dots", **2020**, submitted.
2. **C. Hurot**, N. Scaramozzino, A. Buhot, Y. Hou\*, "Bio-Inspired Strategies for Improving the Selectivity and Sensitivity of Artificial Noses: A Review", *Sensors*, **2020**, 20, 1803. DOI:10.3390/s20061803 (IF 3.031)
3. S. Gaggiotti, **C. Hurot**, J. S. Weerakkody, R. Mathey, A. Buhot, M. Mascini, Y. Hou\*, D. Compagnone\*, "Development of an optoelectronic nose based on surface plasmon resonance imaging with peptide and hairpin DNA for sensing volatile organic compounds", *Sensors and Actuators: B. Chemical*, **2020**, 127188. DOI: 10.1016/j.snb.2019.127188 (IF 6.393, cited 5 times)
4. **C. Hurot**, S. Brenet, A. Buhot, E. Barou, C. Belloir, L. Briand, Y. Hou\*, "Highly sensitive olfactory biosensors for the detection of volatile organic compounds by surface plasmon resonance imaging", *Biosensors and Bioelectronics*, **2019**, 123, 230-236. DOI: 10.1016/j.bios.2018.08.072 (IF 9.518, cited 11 times)

### Book chapter

1. M. El Kazzy, **C. Hurot**, Jonathan S. Weerakkody, A. Buhot, Y. Hou, "Biomimetic olfactory biosensors and bioelectronic noses", *Advances in Biosensors: Reviews, Book Series, Vol. 3*, **2020**, accepted.

### Proceeding papers

1. J. S. Weerakkody, **C. Hurot**, S. Brenet, R. Mathey, C. Herrier, T. Livache, A. Buhot\*, Y. Hou\*, "Surface plasmon resonance imaging-based optoelectronic nose: fundamental study on the effects of temperature and humidity," *Proc. SPIE 2020*, 11354, *Optical Sensing and Detection VI*, 2555450, **2020**. DOI: 10.1117/12
2. **C. Hurot**, A. Buhot, É. Barou, C. Belloir, L. Briand, Y. Hou\*, "Odorant-binding protein-based optoelectronic tongue and nose for sensing volatile organic compounds", *2019 IEEE International Symposium on Olfaction and Electronic Nose (ISOEN)*, **2019**, page 1-4. DOI: 10.1109/ISOEN.2019.8823179 (peer reviewed with a double-blind evaluation procedure)
3. J. S. Weerakkody, **C. Hurot**, S. Brenet, R. Mathey, C. Raillon, T. Livache, A. Buhot\*, Y. Hou\*, "Optoelectronic nose-Temperature and VOC concentration effects on the equilibrium response", *2019 IEEE International Symposium on Olfaction and Electronic Nose (ISOEN)*, **2019**, page 1-3. DOI: 10.1109/ISOEN.2019.8823292 (peer reviewed with a double-blind evaluation procedure)

## Oral presentations

1. Y. Hou, S. Brenet, **C. Hurot**, J. Weerakkody, R. Mathey, A. Buhot, "Biomimetic optoelectronic nose for analysis of volatile organic compounds", *AnalytiX-2019*, **13<sup>th</sup>-15<sup>th</sup> November 2019**, Berlin, Germany.
2. **C. Hurot**, A. Buhot, É. Barou, C. Belloir, L. Briand, Y. Hou, "Odorant-binding protein-based optoelectronic tongue and nose for sensing volatile organic compounds", *18th International Symposium on Olfaction & Electronic Nose*, **26<sup>th</sup>-29<sup>th</sup> May 2019**, Fukuoka, Japan.
3. S. Gaggiotti, **C. Hurot**, J. Weerakkody, R. Mathey, A. Buhot, Y. Hou, M. Mascini, D. Compagnone, "Surface plasmon resonance imaging based on peptide and HpDNA for sensing volatile organic compounds", *XX AISEM*, **11<sup>th</sup>-13<sup>th</sup> February**, 2019, Napoli, Italy.
4. S. Brenet, **C. Hurot**, A. Buhot, E. Barou, C. Belloir, L. Briand, Y. Hou, "Surface plasmon resonance imaging for sensing volatile organic compounds: biomimetic olfactory biosensors & optoelectronic nose", *Biosensors*, **12<sup>th</sup>-15<sup>th</sup> June 2018**, Miami, USA.
5. **C. Hurot**, J. Weerakkody, S. Brenet, A. Buhot, Y. Hou, "Electronic noses: Novel sensing materials for better performances", *4th Annual Meeting of GDR O3*, **3<sup>rd</sup>-4<sup>th</sup> December 2018**, Nice, France.
6. S. Brenet, **C. Hurot**, J. Weerakkody, A. Buhot, C. Belloir, L. Briand, Y. Hou, "Biomimetic electronic noses for odor detection", *Journée Scientifique de la Division de Chimie Physique*, **20<sup>th</sup> December 2018**, Paris, France. (invited talk)
7. **C. Hurot**, S. Brenet, A. Buhot, E. Barou, C. Belloir, L. Briand, Y. Hou, "Development of novel olfactory biosensors based on surface plasmon resonance imaging", *Journées plénières du GDR "bio-ingénierie des interfaces"*, **25<sup>th</sup>-26<sup>th</sup> June, 2018**, Besançon, France. (best oral presentation award)

## Posters

1. **C. Hurot**, S. Brenet, A. Buhot, E. Barou, C. Belloir, L. Briand, N. Scaramozzino, Y. Hou, « Matériaux sensibles biomimétiques pour le développement de nez optoélectroniques », *Ecole thématique BIOSURF*, **June 2019**, Porquerolles, France.
2. J. S. Weerakkody, **C. Hurot**, S. Brenet, R. Mathey, C. Raillon, T. Livache, A. Buhot, Y. Hou, "Opto-electronic nose-Temperature and VOC concentration effects on the equilibrium response", *18th International Symposium on Olfaction & Electronic Nose*, **26<sup>th</sup>-29<sup>th</sup> May, 2019**, Fukuoka, Japan.
3. **C. Hurot**, S. Brenet, A. Buhot, E. Barou, C. Belloir, L. Briand, Y. Hou, "Biomimetic olfactory sensors for the detection of small molecules by surface plasmon resonance imaging", *Journée microcapteurs optiques Minalogic*, **March 2018**, Grenoble, France.



## Résumé

Les nez artificiels ont un grand potentiel applicatif dans divers domaines industriels, du contrôle qualité au diagnostic médical. Nombre de ces applications requièrent de détecter une molécule cible avec certitude dans un environnement complexe, parfois à très faible concentration. Cependant, la sensibilité et la sélectivité des nez artificiels actuels sont encore loin d'égaliser celles du nez biologique dont ils s'inspirent. Dans ce contexte, notre équipe développe depuis 2012 un nez optoélectronique pour la détection de composés organiques volatils en phase gazeuse. Il s'appuie sur un réseau de matériaux sensibles peptidiques et une transduction par imagerie par résonance de plasmons de surface. Cette thèse explore trois stratégies pour le développement de nouveaux matériaux sensibles biomimétiques permettant d'en améliorer les performances. Nous proposons, premièrement, d'intégrer des protéines naturellement présentes dans le nez au système, deuxièmement, de sélectionner *in vitro* des peptides par *phage display*, et troisièmement d'utiliser le criblage virtuel. L'implémentation de ces trois méthodes prometteuses permet de mieux comprendre leurs différents enjeux techniques pour pouvoir à l'avenir adapter rapidement notre dispositif aux besoins de ses utilisateurs.

**Mots clés :** Nez artificiel, nez optoélectronique, composé organique volatil, imagerie par résonance de plasmons de surface, protéines liant les odorants, peptide, *phage display*, criblage virtuel, sensibilité, sélectivité.

## Summary

Artificial noses have a great application potential in various industrial fields, from quality control to medical diagnosis. Many of these applications require the detection of a target molecule with certainty in a complex environment, sometimes at a very low concentration. However, the sensitivity and selectivity of today's artificial noses are still far from matching those of their biological source of inspiration. In this context, our team has been developing since 2012 an optoelectronic nose for the detection of volatile organic compounds in the gas phase. It is based on an array of peptide sensing materials and a transduction by surface plasmon resonance imaging. This thesis explores three strategies for the development of new biomimetic sensing materials to improve its performance. We propose, firstly, to integrate proteins naturally present in the nose into the system, secondly, to select peptides *in vitro* by phage display, and thirdly, to use virtual screening. The implementation of these three promising methods allows a better understanding of their different technical issues in order to be able to adapt promptly our device to the needs of its final users in the future.

**Keywords:** Artificial nose, optoelectronic nose, volatile organic compound, surface plasmon resonance imaging, odorant binding proteins, peptide, phage display, virtual screening, sensitivity, selectivity.